DOCTEUR EN SCIENCES

Long term dynamics of space debris orbits including Earth's shadows

Hubaux, Charles

Award date:
2013

Awarding institution:
Universite de Namur

UNIVERSITE DE NAMUR

FACULTE DES SCIENCES

DEPARTEMENT DE MATHEMATIQUE

Long term dynamics of space debris orbits including Earth's shadows

Thèse présentée par
Charles Hubaux
pour l'obtention du grade
de Docteur en Sciences

Composition du Jury:

Timoteo Carletti (Président du Jury)
Florent Deleflie
Jean-Charles Delvenne
Anne Lemaître (Promoteur)
Klaus Merz
Alessandro Rossi

Juin 2013

Imprimé en Belgique

ISBN : 978-2-87037 -801 -4
Dépôt légal: D / 2013 / 1881 / 28

Université de Namur
Faculté des Sciences
Rue de Bruxelles, 61, B-5000 Namur (Belgique)

Dynamique à long terme de l'orbite des débris spatiaux considérant l'ombre de la Terre

par Charles Hubaux

Résumé: De très nombreux débris spatiaux sont actuellement en orbite autour de la Terre. Le risque permanent de collisions entre ces objets incontrôlables et les sondes spatiales actives (habitées ou non) requiert la connaissance précise de leur trajectoire. Cette thèse propose un intégrateur symplectique permettant de propager numériquement et rapidement les orbites des débris sur de longs intervalles de temps. Les perturbations agissant sur leurs trajectoires sont nombreuses. En particulier, la pression de radiation solaire devient prédominante pour les objets dont le rapport surface sur masse est important. Les passages dans l'ombre de la Terre ne peuvent alors plus être négligés. Ce travail présente une méthode innovante de modélisation de ces passages dans l'ombre (cylindrique ou conique) dont la formulation permet de conserver le caractère symplectique du propagateur. Les résultats prouvent qu'une ombre cylindrique représente une mauvaise approximation de la réalité, et préconisent une formulation conique, particulièrement pour les grands rapports surface sur masse. Des méthodes numérique et semi-analytique sont ensuite développées pour expliquer les importantes déviations périodiques (observées sur les orbites) provoquées par ces passages dans l'ombre, avec des périodes allant de 1 à 10000 ans. Enfin, une étude systématique de la stabilité autour de l'altitude géostationnaire prouve la présence de chaos, dont l'intensité et l'étendue sont renforcées par les passages dans l'ombre.

Long term dynamics of space debris orbits including Earth's shadows

by Charles Hubaux

Abstract: A huge amount of space debris are currently orbiting the Earth. Understanding the motion of such uncontrolled objects is of great importance in order to reduce the risks of hypervelocity impacts with manned and unmanned spacecraft. In this work, we present an accurate symplectic integration scheme to numerically propagate space debris orbits over long periods of time. Among the perturbations that influence debris motion, this thesis mainly brings new results about the effects of solar radiation pressure on debris characterized by high area-to-mass ratios. In this case, Earth's shadow crossings cannot be neglected. Hence we propose an innovative method that successfully models shadow crossings and does not break the symplectic properties of our propagator. Both cylindrical and conical shadows are considered. We show that the cylindrical model is only a poor approximation of the more realistic conical model, especially for high area-to-mass ratios. Thanks to both numerical and semi-analytical techniques, we then explain how shadow crossings are responsible for large periodic deviations from the initial condition. Finally an analysis is presented to highlight the strong influence of shadow crossings on the stability of high area-to-mass space debris located around the geostationary altitude.

Thèse de doctorat en Sciences mathématiques (Ph.D. thesis in Mathematics)
Date : 17-06-2013
Département de Mathématique
Promoteur (Advisor): Prof. A. Lemaître

Remerciements
Acknowledgements

Je tiens à exprimer ma gratitude envers l'Université de Namur pour m'avoir permis de réaliser cette thèse. Je remercie également le Fonds de la Recherche Scientifique (FNRS) pour le mandat d'aspirant qui m'a été octroyé et le soutien financier indispensable à la réussite de ce projet.

I would like to thank this thesis jury for the helpful comments and pertinent questions that have improved the quality and accuracy of this manuscript.

Je remercie chaleureusement ma promotrice de thèse, Anne Lemaître, pour l'énorme investissement qu'a représenté l'encadrement de ma thèse. Outre l'excellente contribution scientifique apportée à mes travaux, les conseils toujours judicieux et le soutien constant dont j'ai pu bénéficier m'ont placé dans des conditions optimales à la réalisation d'un travail de qualité et à mon épanouïssement personnel lors de ces quatre années de thèse.

L'aide précieuse de la part des membres de mon comité d'accompagnement se doit d'être soulignée. En particulier, je remercie Florent Deleflie pour les discussions fructueuses et l'invitation à la conférence organisée à Lille en 2011. Le séjour organisé à Pise avec Alessandro Rossi m'a permis de tester mon propagateur et d'améliorer ma compréhension de la problématique des débris spatiaux. Finalement, de nombreuses discussions avec Timoteo Carletti ainsi qu'une collaboration constante m'ont permis d'envisager de nouvelles directions de recherche, d'améliorer la qualité de mon travail et de produire des résultats innovants.

Furthermore I would like to acknowledge the Space Debris Office at ESA/ESOC for having accepted to host me during two weeks. This short stay let me discover a very welcoming and helpful team.

The last and longest stay abroad took place in the celestial mechanics group of the University of Pisa. I really appreciated the pertinent discussions with Andrea Milani about my results and the efficient collaboration with Giovanni F. Gronchi. A special thanks goes to Chiara Tardioli and Giulio Baù for the enjoyable time spent together in Pisa.

Je remercie vivement tous mes collègues académiques et scientifiques du département de mathématique pour ces quatre années passées en leur compagnie. Je remercie en particulier Nicolas et Anne-Sophie pour leur aide scientifique et leurs nombreux conseils. Un grand merci à Jérémy pour avoir partagé mon bureau et veillé à me laisser un espace de travail suffisant. Je garderai de nombreux souvenirs de ces moments passés dans le bureau de Jonathan et Jérémy (l'autre) qui ont certainement contribué à libérer la pression dans les moments difficiles. Sans pouvoir citer tout le monde, je tiens à remercier entre autres Emilie, Charlotte, Benoît, Audrey, Jehan, Jojo et toute(s) l'(es) équipe(s) du GRT pour tous ces petits instants agréables de la vie du département.

Un projet de cette envergure n'aurait jamais été possible sans le soutien et les encouragements perpétuels de ma famille et de ma belle-famille. Je tiens à exprimer toute ma fierté et ma reconnaissance envers eux pour tout ce qu'ils m'ont apporté jusqu'à présent et leur témoigner toute ma confiance pour le futur.

A Eve, pour l'amour dont elle me témoigne tous les jours.

Contents

Chapter 1
Introduction

1.1 Context

Since the first artificial satellite was launched by the Soviet Union in 1957, around 6000 satellites have been put into orbit around the Earth. However, recent figures (ESA official website) reveal that only about 800 of them are still operational today. Meanwhile, the total number of space debris has dramatically increased. As defined in the Inter-Agency Space Debris Coordination Committee (IADC) Space Debris Mitigation Guidelines (IADC 2007), space debris are "*all man made objects including fragments and elements thereof, in Earth orbit or re-entering the atmosphere, that are non functional*". While operational spacecraft account for 6 percent of the catalogued orbits, 38 percent are made of decommissioned satellites, spent upper stages and mission-related objects. The remaining part consists in pieces resulting from fragmentations and explosions of spacecraft and upper stages.

Understanding the motion of such uncontrolled objects is of great importance in order to reduce the risks of hypervelocity impacts with manned and unmanned spacecraft. Lots of impacts between small objects and spacecraft have already been listed and laboratory experiments have been performed (see a hypervelocity impact reproduction in Fig. 1.1) to analyse this threat. Moreover, while the small ones burn up as they enter the Earth's atmosphere, fragments of larger objects manage to reach the ground intact and potentially represent a strong hazard for the population. Recent cases have been reported. For example the approximately 20 year old ROSAT satellite re-entered Earth's atmosphere on 23 October 2011, falling over the Bay of Bengal, east of India.

While most debris originate from in-orbit break-ups, an important amount of them results from collisions (10 of them have been reported until now). The first accidental in-orbit collision between two satellites occurred on 10 February 2009, at 776 km altitude above Siberia, between an American privately owned

Figure 1.1 • *Laboratory test of the impact area between a small aluminium sphere (*1.2 *cm in diameter and* 1.7 *g) moving to* 6.8 *km/s against an aluminum block,* 18 *cm thick. ESA website.*

communication satellite, Iridium 33, and a Russian military satellite, Kosmos-2251. The collision happened at a relative speed of 11.7 km/s and produced a large amount of debris. Three years before, the French military satellite Cerise had already been hit by a catalogued space debris object from an Ariane rocket. Such unfortunate events obviously emphasize the need for mitigation (the International Space Station often performs debris avoidance maneuvers), protection, removal and risk assessment techniques (see for instance Rossi and Valsecchi 2006).

Only biggest debris (of the order of 5 to 10 cm in low Earth orbit (LEO) and 30 cm to 1 m at geostationary altitudes (GEO)) can be tracked, allowing the US Space Surveillance Network (SSN) to build a catalogue of objects orbiting the Earth (more information in Klinkrad 2006). As shown in Fig. 1.2, more than 16000 objects are currently being traced back in the maintained catalogue and their number keeps on steadily increasing. Let us point out the net increase in debris population in 2007 and 2009 corresponding to the intentional destruction by China of one of their satellites (FY-1C) and the aforementioned collision between Iridium 33 and Kosmos-2251. Small-size debris (resulting primarily from fragmentations or slag and dust residues from solid rocket motor firings) are much more difficult to detect. Various approaches described in Rossi (2005) have been used to assess

their number. The estimated number of debris is around 29000 for sizes larger than 10 cm, 670000 for sizes larger than 1 cm and more than 170 million for sizes larger than 1 mm. Debris distribution is not uniform across orbit altitudes. Several zones showing different dynamical properties have been identified (see e.g. IADC 2007):

LEO A Low Earth Orbit lies in a spherical region that extends from the Earth's surface up to an altitude of 2000 km. Most orbiting objects can be found in this region. High density and large relative velocities make it a region of major concern which has already been extensively studied.

MEO A Medium Earth Orbit is situated between LEO and GEO. Most navigation satellites like the Global Positioning System (GPS) are located in this region. In light of their crucial abilities in everyday life, the protection of the MEO zone is also an important issue.

GEO A Geostationary Earth Orbit has zero inclination and zero eccentricity and its orbital period is equal to the Earth's sidereal period. The altitude of this unique circular orbit is close to 35786 km. These properties make it remain at a fixed position with respect to any observer on Earth. This advantage makes the geostationary region a crucial zone populated with a lot of telecommunication and weather satellites. A GEO is a particular case of geosynchronous orbit for which the inclination can vary from 0 to 15 deg. One can also define a geostationary ring as a toroidal region of space close to the equatorial plane at about 36000 km of altitude (see e.g. Rossi 2005).

GTO A Geostationary Transfer Orbit is or can be used to transfer spacecraft or orbital stages from lower orbits to the geosynchronous region. Such orbits typically have perigees within LEO region and apogees near or above GEO.

As shown in Rossi (2005) (see Fig. 1.3), the population of debris presents obvious peaks of density at LEO, MEO and GEO altitudes. Data used in this figure come from the MASTER 2001 model developed by ESA (Bendisch et al. 2004). MASTER 2001 reproduces the population environment by modelling known phenomena that create and eliminate debris. The MASTER 2009 software is now available on the ESA website[1].

[1]The MASTER website is available at `http://www.master-model.de/`.

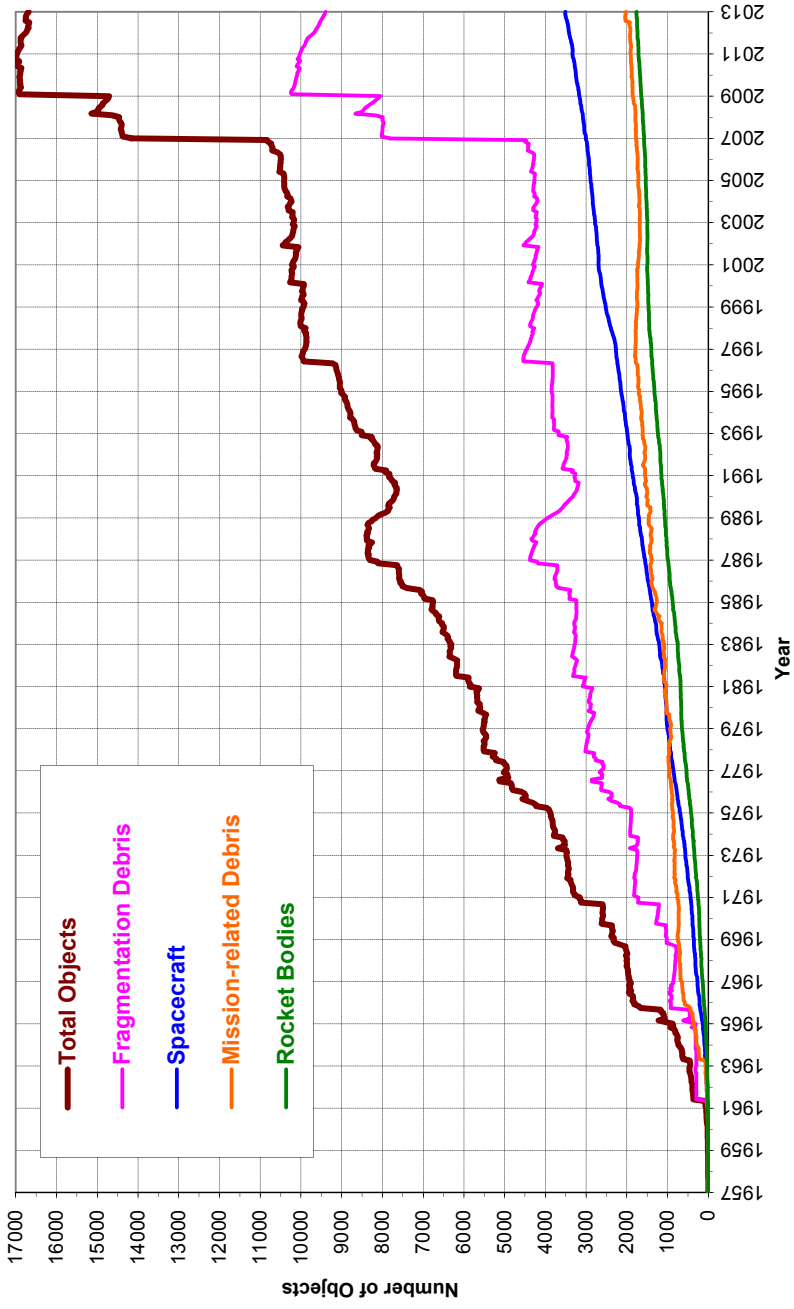

Figure 1.2 • *Caption from NASA (2013). Monthly Number of Cataloged Objects in Earth Orbit by Object Type. This chart displays a summary of all objects in Earth orbit officially cataloged by the U.S. Space Surveillance Network. "Fragmentation debris" includes satellite breakup debris and anomalous event debris, while "mission-related debris" includes all objects dispensed, separated, or released as part of the planned mission.*

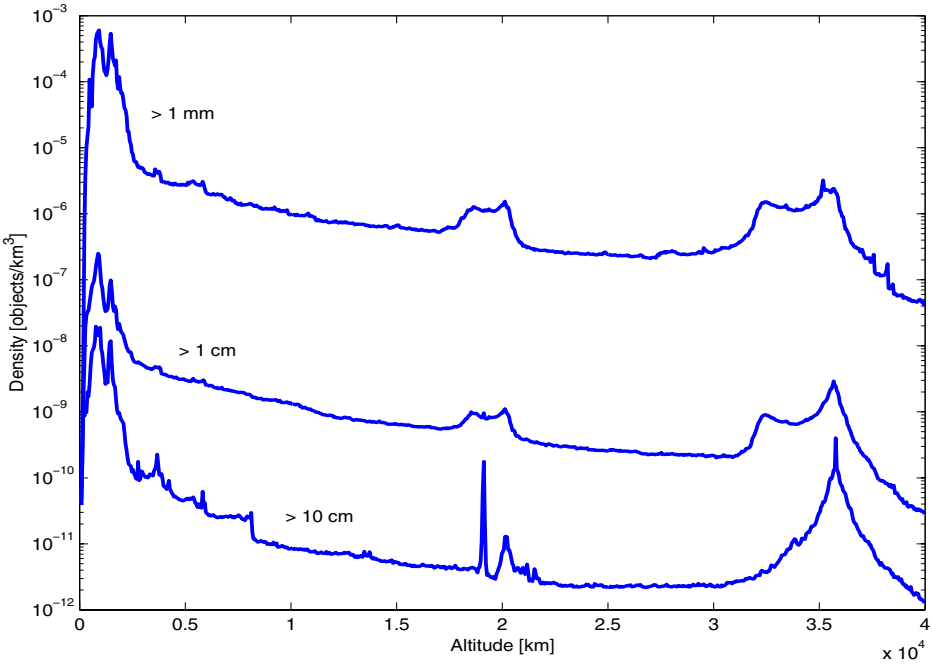

Figure 1.3 • *Caption from Rossi (2005). Density of objects as a function of altitude for objects diameter larger than* 1 *mm,* 1 *cm and* 10 *cm.*

1.2 High area-to-mass ratio

Focus will be put in this thesis on the long term evolution of debris located in the geostationary ring. At these altitudes, objects smaller than 1 m are extremely difficult to detect. Lots of works from the Astronomical Institute of the University of Bern (AIUB) have already been dedicated to this task. In particular, debris characterized by extremely high area-to-mass ratio (AMR) are presented in Schildknecht et al. (2010). The AMR of 274 uncorrelated objects from the AIUB/ESA catalogue is shown in Fig. 1.4. Surprisingly a significant population of objects with AMR larger than 1 m^2/kg and as high as 86.7 m^2/kg can be found. As a point of comparison, the AMR of a GPS (Block II) satellite is only of 0.02 m^2/kg. Such high AMR values correspond to particular debris types like e.g. pieces of multi-layer insulation material or solar panels. Moreover, it turns out that the majority of the objects with AMR larger than 1 m^2/kg have a mean motion near 1 revolution per day and eccentricities ranging from 0.05 to 0.5. Such objects correspond to the red cloud dispersed around one revolution per day mean motion in Fig. 1.5.

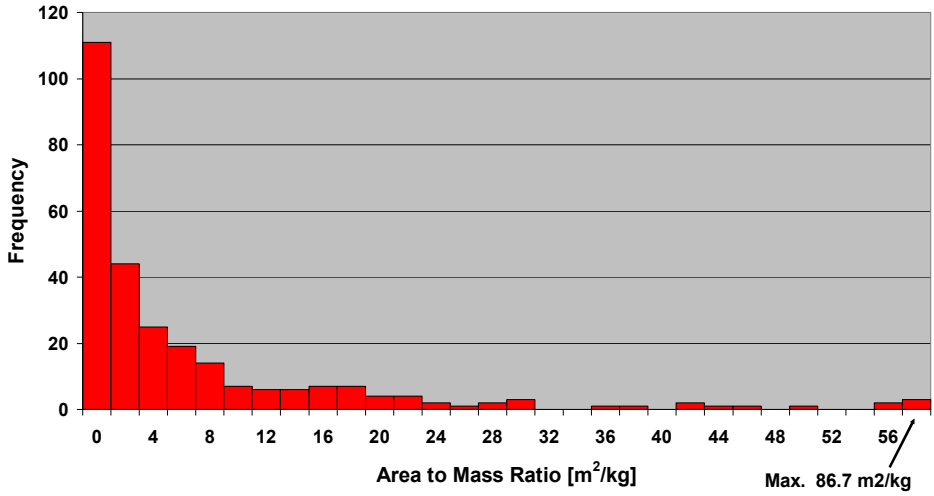

Figure 1.4 • *Caption from Schildknecht et al. (2010). Distribution of the AMR of* 274 *uncorrelated objects in the AIUB/ESA catalogue.*

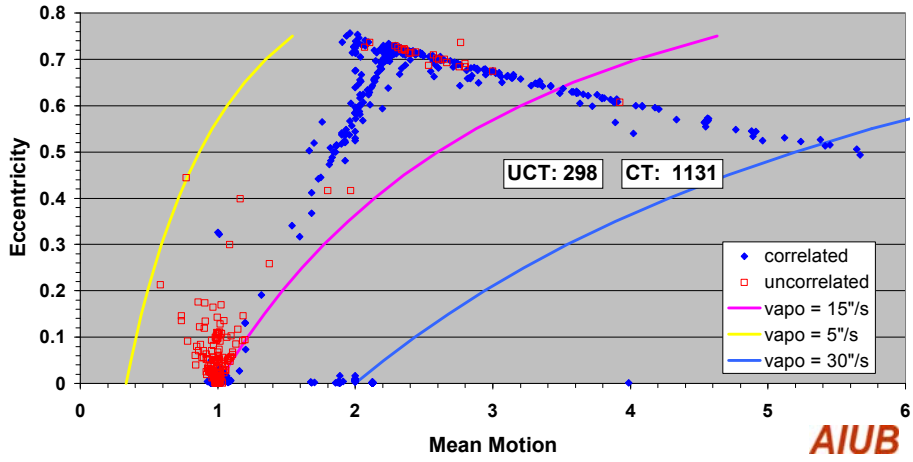

Figure 1.5 • *Caption from Schildknecht et al. (2010). Eccentricity as a function of the mean motion for* 1217 *objects for which* 6*-parameter orbits were determined. UCT and CT respectively denote the number of correlated and uncorrelated objects. The velocity in right ascension is noted* vapo.

Historically, Liou and Weaver (2005) was the first work to point out that such high AMR could possibly originate from the GEO ring and see their orbits strongly perturbed by the solar radiation pressure (SRP), resulting in periodically varying eccentricities and inclinations. Shortly thereafter Schildknecht et al. (2005) confirmed that guess by determining the first AMR values for 28 objects, surprisingly ranged from 1 to 28 m^2/kg. Following that discovery, a lot of papers

have been published in order to understand the long term evolution of high AMR space debris in the geostationary belt. The aim of this thesis is to present new results related to this challenging topic.

1.3 Existing studies and contributions

Different physical effects have to be considered in order to accurately model artificial satellite and space debris orbits. Several orders of magnitude corresponding to the main perturbations acting on space debris are shown in Fig. 1.6. The acceleration norms[2] are computed from formulae presented in Montenbruck and Gill (2005). It turns out that the oblateness of the Earth (J_2) and luni-solar gravitational attractions are of the same order, six orders of magnitude below the central gravitational attraction of the Earth. Moreover, large AMR values can lead to similar or even higher levels of perturbation. Indeed, AMR values higher than 1 m^2/kg correspond to orders of magnitude above the other perturbations and become the major perturbation.

In particular, several works have already shown the great importance of the solar radiation pressure (SRP) effects on space debris motion with high AMR. We have already mentioned the precursor role of Liou and Weaver (2005). Consequently, simplified averaged equations of motion resulting from the SRP have been proposed in Chao (2005) and Chao (2006), revealing large eccentricity evolutions. Numerical investigations performed in Anselmo and Pardini (2005) on mid term (54 yr) also confirmed results from Liou and Weaver (2005), the higher the AMR, the larger the eccentricity and inclination amplitudes. Semi-analytical methods developed in Valk et al. (2008) are in agreement with Chao (2005), Anselmo and Pardini (2005), Chao (2006) and improved the previous models by working on the Hamiltonian formulation of space debris motion. Simple relations grasp the averaged behaviour of the eccentricity and inclination. This general scheme is not tied to the specific GEO region and is not sensitive to zero eccentricities. Further work devoted to the identification of various resonances in the GEO ring was also published in Lemaitre et al. (2009). Meanwhile, some authors have pointed out that Earth's shadowing effects should not be neglected and that these phenomena could lead to significant short-periodic perturbations. See for instance Kozai (1961) and Aksnes (1976) who give the perturbation to be added to each orbital element and at each revolution due to cylindrical Earth's shadow crossings. The variation of orbital elements is also investigated in Ferraz-Mello (1972), based on a canonical approximation of the shadow function. The semi-analytical approach developed in Valk et al. (2008) has been extended and numerical simulations are performed in Valk and Lemaitre (2008) to describe the evolution of space debris over 25 yr.

[2]No distinction is made between the radial and tangential components of the accelerations.

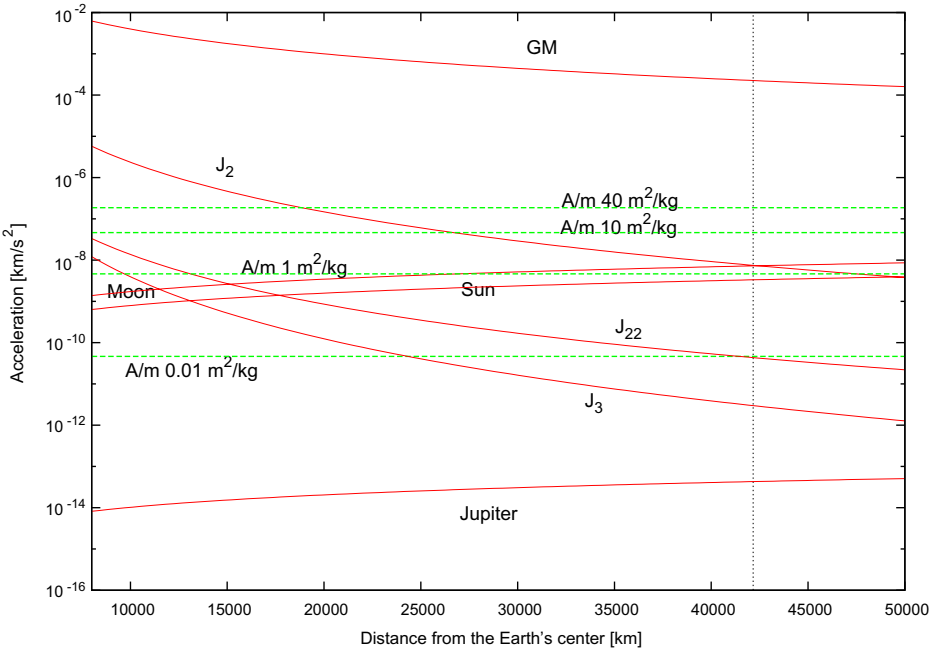

Figure 1.6 • *Caption from Valk (2008). Order of magnitude of the main perturbations acting on space debris orbits (red solid curves) and of the SRP for AMR values equal to* 0.01, 1, 10, 40 m^2/kg *(green dashed curves). The vertical dotter line represents the GEO altitude.*

A first aspect of space debris dynamics that we decided to take into account in our analysis is their possible long lifetimes. While the efficiency of the drag forces cleans lower LEO area in few years, it is different for higher orbits, especially geostationary ones, on which the objects can stay for hundreds of years (see aforementioned papers). Up to now the numerical simulations concerning debris have been performed using a wide variety of numerical integrators for short timescales. Resorting to a symplectic (or quasi-symplectic) integration scheme to compute the orbit of space debris has rarely been done despite their excellent energy preservation properties on long time scales and the fact of being less time-consuming than non-symplectic schemes (mainly because of the possibility to use larger time steps). To the best of our knowledge, only few authors have already discussed the use of symplectic mappings to propagate the orbit of artificial satellites, among which we can cite Jackson (1996), Breiter (1999) and Breiter et al. (2005a) for applications of symplectic integrators of the Wisdom-Holman type, Mikkola and Innanen (1999) for the presentation of time transformations in the framework of symplectic integrators and Mikkola et al. (2002) for an implementation of the logarithmic Hamiltonian method. In this work, we will describe a general high order explicit symplectic scheme based on Laskar and Robutel (2001).

Secondly, modelling Earth's shadow crossings in this context is a challenging problem. Indeed, the actual direct SRP reaching the satellite has to be computed with a sufficiently smooth function and included directly in the equations of motion in order not to introduce numerical errors in the symplectic scheme. We will present an innovative theory to model both cylindrical and conical shadow (umbra-penumbra transitions) crossings. Our model being totally included in the equations of motion of the space debris, it will thus be well adapted to our symplectic integration scheme.

This thesis also aims to describe the evolution of space debris orbits due to Earth's shadow crossings on long time scales. Unexpected periodic motions appear with periods of time of the order of 1000 yr which directly depend on the AMR. Such behaviour has never been addressed in the literature. We will present both numerical and analytical results that help understand how Earth's shadow crossings disturb the long term evolution of space debris orbits. To that purpose, only the Earth's gravitational attraction as a single mass point and SRP are considered. The resulting simplified model will highlight a new frequency which is responsible for this periodic motion. This frequency should be understood as a new theoretical contribution to more complete models including other important perturbations such as the gravitational attraction of the Sun and Moon, the geopotential or the Poynting-Robertson effect.

Based on our symplectic integrator we assess the stability (i.e. the predictability) of high AMR debris, especially at the geostationary altitude. For the first time, the Mean Exponential Growth factor of Nearby Orbits (MEGNO) chaos indicator has been used by Breiter et al. (2005b) to study the predictability of debris orbits in the near-geostationary region. Still using the MEGNO criterion, Valk et al. (2009) analyzed the influence of the direct SRP on high AMR. Until now, Earth's shadowing effects have never been included in such studies. In light of this, we present an analysis of the influence of the Earth's shadowing effects on the stability of GEO space debris motion. To do so, we will resort to stability maps realized with the MEGNO criterion computed in a symplectic framework. Based on the GSI method developed in Libert et al. (2011) and MEGNO criterion, we will compare the cylindrical shadow model to the conical one and present some results about the influence of shadowing effects on the regular or chaotic behaviour of space debris orbits.

For the sake of completeness, let us mention recent papers that also dealt with the influence of SRP in different situations. The impact of the object attitude and Earth's oblateness was investigated in Rosengren (2011) by studying the evolution of eccentricity and angular momentum vectors up to 100 yr. In McMahon (2010), secular orbit variations are described when SRP acts on a rotating asymmetric body. Another paper (Scheeres 2012) deals with long-term perturbations in the framework of small bodies orbiting the Sun.

1.4 Tools

Unless explicitely stated, each result presented in this thesis was obtained by means of self-coded Fortran 90 software using double-precision floating-point format. Numerical computations were either performed on a local computer or on the Interuniversity Scientific Computing Facility (ISCF) located at the University of Namur, Belgium, which is supported by the F.R.S.-FNRS under convention No. 2.4617.07. In particular, chaos maps presented in Chap. 5 were obtained as array jobs on the ISCF. Most charts were realized with MATLAB.

1.5 Outline

This thesis is organized as follows. Chap. 2 is devoted to the description of the symplectic schemes that will be used in this work and the presentation of the model that we consider to propagate space debris orbits. In Chap. 3 a theory is developed to efficiently model Earth's shadow crossings in the framework of symplectic integration. A semi-analytical theory is thereafter presented in Chap. 4 to point out the influence of Earth's shadow crossings on the secular evolution of space debris orbits. Then, the stability of space debris considering Earth's shadow crossings is analyzed in Chap. 5. First, we adress the problem of computing a chaos criterion with symplectic schemes. Then, we validate our tools and apply it to the case of interest. Eventually, we conclude in Chap. 6.

Main acronyms, units and notations are described in Appx. A. Appendices B, C, D and F present useful technical details and are referred to in the text. Some work in progress about the related Stark problem is also presented in Appx. E.

1.6 Publications

Key results appearing in this document have already been published in peer-reviewed journals. In particular, the propagation technique (Chap. 2) and shadow crossing models (Chap. 3) can be found in Hubaux et al. (2012). The formulation of the GSI method to compute chaos indicators with symplectic integrators (Chap. 5) was described in Libert et al. (2011) and improved further in Hubaux et al. (2013). Chaos maps showing stability results of high AMR space debris around geostationary altitudes were also published in Hubaux et al. (2013). Finally, Hubaux and Lemaitre (2013) presents the semi-analytical method allowing to describe the secular evolution of debris motion.

Chapter 2
Integrator

Contents

This chapter is devoted to the description of the numerical propagator. Even if various symplectic schemes have already been proposed to integrate artificial satellites (and thus space debris), it has been decided to rely on the symmetric integrator families proposed in Laskar and Robutel (2001) and Yoshida (1990). These present the great advantage to be explicit, of high order and not restricted to a particular physical application. The description of these families of integrator and their implementation are first described in Sec. 2.1.
Then, the physical contributions taken into account into our model are detailed in Sec. 2.2. Some practical information is also given on the way that the symplectic integrator was adapted to the characteristics of space debris motion (Sec. 2.3). In Sec. 2.4, our propagator is compared to other methods in other to assess the accuracy of this scheme. Concluding remarks are given in the last part of this chapter (Sec. 2.5).

2.1 Symplectic integration

Symplectic integration methods are defined in the framework of Hamiltonian mechanics. Let $\mathcal{H}(\vec{p},\vec{q})$ be an autonomous (i.e. explicitely not dependent on time) Hamiltonian with N degrees of freedom where $\vec{p},\vec{q} \in \mathbb{R}^N$ are respectively the momentum and coordinate vectors. Equations of motion can then be written as

$$\dot{p}_i = -\frac{\partial \mathcal{H}}{\partial q_i}(\vec{p},\vec{q}) \quad \text{and} \quad \dot{q}_i = \frac{\partial \mathcal{H}}{\partial p_i}(\vec{p},\vec{q}) \quad \forall i = 1,...,N \tag{2.1}$$

where p_i and q_i denote the ith component of respectively $\vec{p}$ and $\vec{q}$ vectors. The point of using a symplectic integrator is to preserve two well-known properties of Hamiltonian systems. On the one hand, the solutions preserve the Hamiltonian $\mathcal{H}(\vec{p},\vec{q})$, which is a first integral of the system (2.1). On the other hand, the symplecticity of the flow is also preserved (see Hairer et al. 2006). Most generic numerical methods used to solve differential equations (2.1) ignore this symplectic structure and distort the phase space. A symplectic map will conserve these geometrical invariants, leading to accurate integrations even on long time scales.

Various symplectic methods exist. A comprehensive list of these techniques can be found in Hairer et al. (2006). In the following, we will focus on explicit symplectic schemes based on the Campbell-Baker-Hausdorff (CBH) theorem. In particular, we will describe both methods presented in Yoshida (1990) and Laskar and Robutel (2001).

2.1.1 Explicit symmetric high order symplectic integrators

Combining $\vec{p}$ and $\vec{q}$ into a single vector

$$\vec{x} = \begin{pmatrix} \vec{p} \\ \vec{q} \end{pmatrix} \in \mathbb{R}^{2N},$$

equations of motion (2.1) (also called Hamiltonian vector field) can be written as

$$\dot{\vec{x}} = L_{\mathcal{H}}\vec{x} = \{\mathcal{H}, \vec{x}\} = \sum_{j=1}^{N} \left(\frac{\partial \mathcal{H}}{\partial p_j}\frac{\partial \vec{x}}{\partial q_j} - \frac{\partial \mathcal{H}}{\partial q_j}\frac{\partial \vec{x}}{\partial p_j} \right).$$

The operator $L_{\mathcal{H}}\bullet$ is used as another notation for Poisson brackets $\{\mathcal{H}, \bullet\}$. The solution of this differential equation can be formally expressed as

$$\vec{x}(t) = e^{\tau L_{\mathcal{H}}}\vec{x}(t_0) = \sum_{j=0}^{\infty} \frac{\tau^j}{j!} L^j_{\mathcal{H}}\vec{x}(t_0) \tag{2.2}$$

where t_0 is the initial time, t is the time where $\vec{x}$ needs to be evaluated and $\tau = t - t_0$. Families of symplectic integrators that will be used afterwards are nothing but approximations of the exponential operator appearing in eq. (2.2).

From now on, let us assume that the Hamiltonian $\mathcal{H}$ can be split into two integrable parts

$$\mathcal{H}(\vec{p}, \vec{q}) = A(\vec{p}, \vec{q}) + B(\vec{p}, \vec{q}).$$

If τ is small enough, an approximation of the solution (2.2) at order n will be found if we are able to define two sets of real coefficients

$$(c_1, c_2, ..., c_k) \quad \text{and} \quad (d_1, d_2, ..., d_k) \tag{2.3}$$

such that

$$\begin{aligned} e^{\tau L_{\mathcal{H}}}\vec{x}(t_0) &= e^{\tau L_{A+B}}\vec{x}(t_0) \\ &= e^{\tau (L_A + L_B)}\vec{x}(t_0) \\ &= \prod_{j=1}^{k} e^{c_j \tau L_A} e^{d_j \tau L_B}\vec{x}(t_0) + \mathcal{O}(\tau^{n+1}) \\ &=: S_n(\tau)\vec{x}(t_0) + \mathcal{O}(\tau^{n+1}). \end{aligned} \tag{2.4}$$

That means that we exactly evaluate $\mathcal{E}$ where

$$\mathcal{E} = A + B + \mathcal{O}(\tau^{n+1}). \tag{2.5}$$

When n is small, a solution can be found by hand. For example, with $n = 2$, $c_1 = c_2 = 1/2$, $d_1 = 1$ and $d_2 = 0$ is a convenient choice. Indeed,

$$e^{\tau(L_A+L_B)} = \mathbb{1} + \tau(L_A + L_B) + \frac{\tau^2}{2}(L_A + L_B)^2 + ... \tag{2.6}$$

and

$$\begin{aligned} & e^{c_1\tau L_A} e^{d_1\tau L_B} e^{c_2\tau L_A} e^{d_2\tau L_B} \\ = & \left(\mathbb{1} + c_1\tau L_A + \frac{c_1^2\tau^2}{2}L_A^2 + ...\right)\left(\mathbb{1} + d_1\tau L_B + \frac{d_1^2\tau^2}{2}L_B^2 + ...\right) \times \\ & \left(\mathbb{1} + c_2\tau L_A + \frac{c_2^2\tau^2}{2}L_A^2 + ...\right)\left(\mathbb{1} + d_2\tau L_B + \frac{d_2^2\tau^2}{2}L_B^2 + ...\right). \end{aligned} \tag{2.7}$$

Equating coefficients of same power in eq. (2.6) and (2.7), one obtains the following conditions

$$\begin{cases} c_1 + c_2 = 1 \\ d_1 + d_2 = 1 \end{cases} \quad \text{and} \quad \begin{cases} c_1^2 + c_2^2 + 2c_1c_2 = 1 \\ d_1^2 + d_2^2 + 2d_1d_2 = 1 \end{cases}$$

allowing the combination $c_1 = c_2 = 1/2$, $d_1 = 1$ and $d_2 = 0$ and yielding the following second order explicit symplectic integrator

$$S_2(\tau)\vec{x}(t_0) = e^{\tau(L_A+L_B)}\vec{x}(t_0) = e^{\frac{\tau}{2}L_A} e^{\tau L_B} e^{\frac{\tau}{2}L_A} + \mathcal{O}(\tau^3),$$

also known as Störmer-Verlet/Leap Frog scheme (Hairer et al. 2006). Difficulty naturally increases in finding the right coefficients for higher orders. We now briefly describe the approach used in Yoshida (1990).

The keystone is the CBH formula (see e.g. Hairer et al. 2006 or Forest and Ruth 1990) which lets us write

$$e^{\tau L_A} e^{\tau L_B} = e^{\alpha_1\tau + \alpha_2\tau^2 + \alpha_3\tau^3 + \alpha_4\tau^4 + ...}$$

with

$$\begin{aligned} \alpha_1 &= L_A + L_B \\ \alpha_2 &= \frac{1}{2}[L_A, L_B] \\ \alpha_3 &= \frac{1}{12}([L_A, [L_A, L_B]] + [L_B, [L_B, L_A]]) \\ \alpha_4 &= \frac{1}{24}[L_A, [L_B, [L_B, L_A]]] \end{aligned}$$

where $[A, B]$ is the commutator of A and B. Applying twice the CBH formula, the second order integrator S_2 is expressed as

$$S_2(\tau) = e^{\frac{\tau}{2}L_A} e^{\tau L_B} e^{\frac{\tau}{2}L_A} = e^{\beta_1\tau + \beta_3\tau^3 + \beta_5\tau^5 + ...}$$

where

$$\begin{aligned}\beta_1 &= L_A + L_B \\ \beta_3 &= \frac{1}{12}[L_B,[L_B,L_A]] - \frac{1}{24}[L_A,[L_A,L_B]] \\ \beta_5 &= \frac{7}{5760}[L_A,[L_A,[L_A,[L_A,L_B]]]].\end{aligned}$$

Moreover it can easily be shown that any operator S_n defined as in eq. (2.4) which is symmetric, i.e.

$$S_n(\tau)^{-1} = S_n(-\tau),$$

contains only terms of odd powers of τ. From that point, symplectic integrators of higher even order can be built by applying several times the S_2 integrator and c_i and d_i coefficients can be explicitely computed. For example, a fourth-order integrator is obtained as

$$S_4(\tau) = S_2(\gamma_0\tau)S_2(\gamma_1\tau)S_2(\gamma_0\tau)$$

where two applications of the CBH formula let us determine γ_0 and γ_1 values as

$$\gamma_0 = -\frac{2^{1/3}}{2-2^{1/3}} \quad \text{and} \quad \gamma_1 = \frac{1}{2-2^{1/3}}.$$

We can then go back to eq. (2.4) to get the values of c_i and d_i coefficients. In the same way, a sixth-order integrator is given by

$$S_6(\tau) = S_4(\gamma_2\tau)S_4(\gamma_3\tau)S_4(\gamma_2\tau)$$

where

$$\gamma_2 = -\frac{2^{1/5}}{2-2^{1/5}} \quad \text{and} \quad \gamma_3 = \frac{1}{2-2^{1/5}}.$$

One could build symplectic integrators of higher order using the same technique, but a $(2n)$th-order integrator would require 3^{n-1} evaluations of S_2. A method allowing fewer steps for 6th- and 8th-order integrators is described in Yoshida (1990) but no further details will be given here.

Now, if we assume that the Hamiltonian $\mathcal{H}(\vec{p},\vec{q})$ has the form of a perturbed one, i.e. there exists a small parameter ε such that

$$\mathcal{H}(\vec{p},\vec{q}) = A(\vec{p},\vec{q}) + \varepsilon B(\vec{p},\vec{q}),$$

Laskar and Robutel (2001) showed that one can find two appropriate sets of positive coefficients c_i and d_i such that the error is of order $\mathcal{O}(\tau^{2n}\varepsilon + \tau^2\varepsilon^2)$. The positivity of the coefficients prevents negative time progression during the time step that could lead to numerical errors (see e.g. Hairer et al. 2006). To achieve

this, the CBH formula is used and the existence of the small parameter is taken into account. Four classes of symmetric symplectic integrators are presented:

$$\begin{aligned}
&\mathrm{SABA}_{2n}(\tau)\\
=\;& e^{c_1\tau L_A}e^{d_1\tau L_{\varepsilon B}}...e^{c_n\tau L_A}e^{d_n\tau L_{\varepsilon B}}e^{c_{n+1}\tau L_A}e^{d_n\tau L_{\varepsilon B}}e^{c_n\tau L_A}...e^{d_1\tau L_{\varepsilon B}}e^{c_1\tau L_A}\\
&\mathrm{SABA}_{2n+1}(\tau)\\
=\;& e^{c_1\tau L_A}e^{d_1\tau L_{\varepsilon B}}...e^{c_{n+1}\tau L_A}e^{d_{n+1}\tau L_{\varepsilon B}}e^{c_{n+1}\tau L_A}...e^{d_1\tau L_{\varepsilon B}}e^{c_1\tau L_A}\\
&\mathrm{SBAB}_{2n}(\tau)\\
=\;& e^{d_1\tau L_{\varepsilon B}}e^{c_2\tau L_A}e^{d_2\tau L_{\varepsilon B}}...e^{c_{n+1}\tau L_A}e^{d_{n+1}\tau L_{\varepsilon B}}e^{c_{n+1}\tau L_A}...e^{d_2\tau L_{\varepsilon B}}e^{c_2\tau L_A}e^{d_1\tau L_{\varepsilon B}}\\
&\mathrm{SBAB}_{2n+1}(\tau)\\
=\;& e^{d_1\tau L_{\varepsilon B}}e^{c_2\tau L_A}...e^{d_{n+1}\tau L_{\varepsilon B}}e^{c_{n+2}\tau L_A}e^{d_{n+1}\tau L_{\varepsilon B}}...e^{c_2\tau L_A}e^{d_1\tau L_{\varepsilon B}}
\end{aligned}$$

Coefficients c_i and d_i are given in Laskar and Robutel (2001). The algebraic equations developed to compute these values become trickier as the order of the integrator increases. Hence the coefficient values are given in the form of analytical formulae for the first orders and of figures with 36 significant digits for the higher orders. As the approximation error depends on the small parameter ε, these classes of integrators are well suited for Hamiltonian systems that are perturbations of integrable ones.

In the following, both families of integrators will be considered. In particular, S_2, S_4 and SABA_2, SABA_4, SABA_8, SABA_8 and SBAB_4 will be extensively used.

2.1.2 Implementation

In order to illustrate the implementation of the integration process, let us consider

$$\mathrm{SABA}_2(\tau) = e^{c_1\tau L_A}e^{d_1\tau L_{\varepsilon B}}e^{c_2\tau L_A}e^{d_1\tau L_{\varepsilon B}}e^{c_1\tau L_A}.$$

Starting from $\vec{x}_k := \vec{x}(t_k)$, one obtains

$$\begin{aligned}
\vec{x}_{k+1} &= \mathrm{SABA}_2(\tau)\vec{x}_k\\
t_{k+1} &= t_k + \tau
\end{aligned}$$

Hence, at each time step, one needs to compute

$$\begin{aligned}
\vec{x}_{k_1} &= e^{c_1 \tau L_A} \vec{x}_k \\
\vec{x}_{k_2} &= e^{d_1 \tau L_{\varepsilon B}} \vec{x}_{k_1} \\
\vec{x}_{k_3} &= e^{c_2 \tau L_A} \vec{x}_{k_2} \\
\vec{x}_{k_4} &= e^{d_1 \tau L_{\varepsilon B}} \vec{x}_{k_3} \\
\vec{x}_{k+1} &= \vec{x}_{k_5} = e^{c_1 \tau L_A} \vec{x}_{k_4} \\
t_{k+1} &= t_k + \tau.
\end{aligned}$$

That requires three evaluations of the exponential operator $e^{c_i \tau L_A}$ and two evaluations of $e^{d_i \tau L_{\varepsilon B}}$, meaning that one must solve three times equations of motion associated to the A-part and two times equations of motion for the B-part of the Hamiltonian. In particular, these evaluations are easy if we assume that $\mathcal{H}$ can be split into two separate integrable parts which depend only on either momenta or coordinates

$$\mathcal{H}(\vec{p}, \vec{q}) = A(\vec{p}) + \varepsilon B(\vec{q}).$$

Then, in order to compute $e^{c_1 \tau L_A} \vec{x}_k$, equations of motion are written as

$$\left\{ \begin{array}{l} \dot{\vec{p}}_{k_1} = -c_1 \vec{\nabla}_{\vec{q}} A(\vec{p}_k) = 0 \\ \dot{\vec{q}}_{k_1} = c_1 \vec{\nabla}_{\vec{p}} A(\vec{p}_k) \end{array} \right.$$

The $\vec{\nabla}_{\vec{q}} f$ symbol denotes the gradient vector containing derivatives of f with respect to each element of $\vec{q}$. Hence,

$$\begin{pmatrix} \vec{p}_{k_1} \\ \vec{q}_{k_1} \end{pmatrix} = e^{c_1 \tau L_A} \begin{pmatrix} \vec{p}_k \\ \vec{q}_k \end{pmatrix} = \begin{pmatrix} \vec{p}_k \\ \vec{q}_k + c_1 \tau \vec{\nabla}_{\vec{p}} A(\vec{p}_k) \end{pmatrix}.$$

Similarly, applying $e^{d_1 \tau L_{\varepsilon B}} \vec{x}_{k_1}$ requires to solve the following equations of motion

$$\left\{ \begin{array}{l} \dot{\vec{p}}_{k_2} = -d_1 \varepsilon \vec{\nabla}_{\vec{q}} B(\vec{q}_{k_1}) \\ \dot{\vec{q}}_{k_2} = d_1 \varepsilon \vec{\nabla}_{\vec{p}} B(\vec{q}_{k_1}) = 0 \end{array} \right.$$

It follows that

$$\begin{pmatrix} \vec{p}_{k_2} \\ \vec{q}_{k_2} \end{pmatrix} = e^{d_1 \tau L_{\varepsilon B}} \begin{pmatrix} \vec{p}_{k_1} \\ \vec{q}_{k_1} \end{pmatrix} = \begin{pmatrix} \vec{p}_{k_1} - d_1 \varepsilon \tau \vec{\nabla}_{\vec{q}} B(\vec{q}_{k_1}) \\ \vec{q}_{k_1} \end{pmatrix}.$$

2.2 Model

Let us now consider the following autonomous Hamiltonian made of both space debris kinetic and potential energies:

$$\mathcal{H}_{\text{debris}}(\vec{v},\Lambda,\vec{r},\theta) = \mathcal{H}_{\text{kepl}}(\vec{v},\vec{r}) + \mathcal{H}_{\text{rot}}(\Lambda) + \mathcal{H}_{\text{geopot}}(\vec{r},\theta) + \mathcal{H}_{\text{3body}}(\vec{r}) + \mathcal{H}_{\text{srp}}(\vec{r}) \tag{2.8}$$

where $\vec{r} := (x, y, z)$ and $\vec{v}$ are respectively the Cartesian geocentric coordinates and velocities of the satellite in the inertial equatorial geocentric frame, θ is the Greenwich sidereal time and Λ is its associated momentum. Our model takes into account the attraction of the Earth as a point mass central body ($\mathcal{H}_{\text{kepl}}$), the constant rotation of the Earth around itself ($\mathcal{H}_{\text{rot}}$) and the perturbations due to the Earth gravity field ($\mathcal{H}_{\text{geopot}}$), third bodies (mainly the Sun and the Moon) ($\mathcal{H}_{\text{3body}}$) and the solar radiation pressure ($\mathcal{H}_{\text{srp}}$).

The attraction of the Earth as a central body is accounted for as

$$\mathcal{H}_{\text{kepl}} = \frac{v^2}{2} - \frac{\mu}{r}$$

where $r := \|\vec{r}\|$, $v := \|\vec{v}\|$ and $\mu = \mathcal{G}M_\oplus$ is the standard Earth's gravitational coefficient.

The rotation of the Earth around its axis of smallest inertia is modeled as

$$\mathcal{H}_{\text{rot}} = \dot{\theta}\Lambda$$

where $\dot{\theta}$ is assumed constant.

The complete Earth's potential expressed in the frame rotating around the Earth's axis of smallest inertia and with the same angular speed can be written as

$$U_{\text{geopot}}(r,\lambda,\phi) = -\frac{\mu}{r}\sum_{n=1}^{\infty}\sum_{m=0}^{n}\left(\frac{R_\oplus}{r}\right)^n \mathcal{P}_{nm}(\sin\phi)(C_{nm}\cos m\lambda + S_{nm}\sin m\lambda)$$

where (r, λ, ϕ) are the geocentric spherical coordinates of the satellite, $R_\oplus$ represents the equatorial radius of the Earth, $\mathcal{P}_{nm}$ are Legendre functions and C_{nm} and S_{nm} are the spherical harmonics coefficients (see e.g. Kaula 1966).

Thanks to formulae presented in Cunningham (1970) and later in Montenbruck and Gill (2005), we are able to write U_{geopot} as a function of $\vec{r}$

$$U_{\text{geopot}}(\vec{r}) = -\frac{\mu}{R_\oplus}\sum_{n=1}^{\infty}\sum_{m=0}^{n}(C_{nm}V_{nm}(\vec{r}) + S_{nm}W_{nm}(\vec{r})).$$

Let us remark that V_{nm} and W_{nm} depend directly on Cartesian coordinates and are recursively defined. Also note that U_{geopot} is still written in the same rotating frame as the one described above. The following simple change of variable

$$\begin{aligned} x &\mapsto x\cos\theta + y\sin\theta \\ y &\mapsto -x\sin\theta + y\cos\theta \end{aligned}$$

lets us express U_{geopot} in the fixed inertial geocentric frame. Recursive relations for V_{nm} and W_{nm} functions with the change of variables are given in Sec. B.1.

Also note that the zero degree is already present in $\mathcal{H}_{\text{kepl}}$. Moreover, given that the center of mass coincides with the origin of the reference frame $C_{10} = C_{11} = S_{11} = 0$, while the coefficient S_{10} is null by construction. Hence, the sum in U_{geopot} must start at $n = 2$. It follows that

$$\mathcal{H}_{\text{geopot}}(\mathbf{r}) = -\frac{\mu}{R_\oplus}\sum_{n=2}^{\infty}\sum_{m=0}^{n}(C_{nm}V_{nm}(\mathbf{r},\theta) + S_{nm}W_{nm}(\mathbf{r},\theta)).$$

The Earth's gravity model is the *EGM96* one described in Lemoine et al. (1998).

Perturbations due to third bodies (the Sun, the Moon and planets of the solar system) are introduced in the Hamiltonian function as

$$\mathcal{H}_{\text{3body}} = -\sum_i \mu_i \left(\frac{1}{\|\vec{r} - \vec{r}_i\|} - \frac{\vec{r}\cdot\vec{r}_i}{\|\vec{r}_i\|^3}\right)$$

where $\mu_i = \mathcal{G}M_i$ and $\vec{r}_i$ is the geocentric Cartesian coordinates of any third body of mass M_i. Position and velocity of the latter are time dependent and computed either by means of Jet Propulsion Laboratory (JPL)[1] planetary and lunar ephemeris (Standish 1998) when the integration time span is short (below 1000 yr) or from a subroutine created by P. Exertier (OCA)[2] for secular propagations. This external contribution introduces an implicit time dependence in the Hamiltonian, formulated as a quasi periodic function. For simpler models of the solar orbit, limited to three frequencies for example, we could have introduced three new variables (linear functions of time) and associated conjugated momenta (as it has been done with Λ in $\mathcal{H}_{\text{rot}}$ for the rotation of the Earth). However it would have increased the number of differential equations to deal with (and hence the computational cost), and the model would stay approximate (the position of disturbing bodies would be less accurately determined than with JPL ephemeris).

[1] More precisely, we worked with the following JPL ephemerides:

- *de405* : from JD 2305424.5 (1599/09/12) to JD 2513360.5 (2169/03/31)
- *de406* : from JD 0625360.50 (-3000/02/23) to JD 2816912.50 (3000/05/06).

.

[2] This model is based on Brown's theory of the mean motion of both Moon and Sun (Meeus 1988).

This is the reason for which we have chosen to work on with a quasi-symplectic formulation in this context.

Eventually, the direct SRP is included. We use three standard physical models: the absorption, the reflection and the diffusion. The force induced by the SRP is obtained by adding together the elementary forces accounting for each effect. The model assumes that space debris are spherical objects and that there is no radiation from the surface of the Earth. Detailed information about the model can be found in Milani and Gronchi (2009). It leads to the following potential:

$$\mathcal{H}_{\text{srp}} = -C_r \frac{1}{\|\vec{r} - \vec{r}_\odot\|} P_r \frac{\mathbb{A}}{\mathbb{M}} a_\odot^2 \tag{2.9}$$

where C_r (fixed to one in this work) is a dimension-free reflectivity coefficient, $\vec{r}_\odot$ is the geocentric Cartesian position of the Sun, $P_r = 4.56 \times 10^{-6}\, N/m^2$ is the radiation pressure for an object located at a distance of 1 AU from the Sun, $\mathbb{A}/\mathbb{M}$ is the AMR of the space debris and $a_\odot$ is equal to the mean distance between the Sun and the Earth (i.e. $a_\odot = 1$ AU). The construction of this potential is also explained in e.g. Montenbruck and Gill (2005). Let us remark, that, making some assumptions, $\mathcal{H}_{\text{srp}}$ is written under its conservative form. Moreover, the shadow of the Sun by the Earth is not yet considered.

2.3 Numerical computation

Applying the aforementioned symplectic integrators to the Hamiltonian describing space debris motion is quite straightforward. Nevertheless, some technical points need to be discussed.

2.3.1 Choice of integrator and Hamiltonian splitting

The right splitting of the Hamiltonian (2.8) and the choice of symplectic integrator (from Yoshida 1990 or Laskar and Robutel 2001) can significantly improve the propagator accuracy. As explained in Sec. 2.1.2, computations are easier when the Hamiltonian can be split into two parts A and B depending respectively only on momenta and coordinates. We could do it with $\mathcal{H}_{\text{debris}}$ by removing the gravitational attraction of the Earth as a single mass point from $\mathcal{H}_{\text{kepl}}$ and putting it in $\mathcal{H}_{\text{geopot}}$. By doing this we obtain the following subdivision

$$\begin{aligned} \mathcal{H}(\vec{v}, \Lambda, \vec{r}, \theta) &= \mathcal{H}_{\text{kin}}(\vec{v}) + \mathcal{H}_{\text{rot}}(\Lambda) + \mathcal{H}_{\text{geopot'}}(\vec{r}, \theta) + \mathcal{H}_{\text{3body}}(\vec{r}) + \mathcal{H}_{\text{srp}}(\vec{r}) \\ &= A(\vec{v}, \Lambda) + B(\vec{r}, \theta) \end{aligned}$$

with

$$\begin{aligned}\mathcal{H}_{\text{kin}} &= \frac{v^2}{2} \\ \mathcal{H}_{\text{geopot'}} &= -\frac{\mu}{R_\oplus}\sum_{n=0}^{\infty}\sum_{m=0}^{n}(C_{nm}V_{nm}(\vec{r},\theta)+S_{nm}W_{nm}(\vec{r},\theta)).\end{aligned}$$

Anyway, some numerical simulations confirmed that this splitting does not yield efficient results. Indeed, such a scheme does not imply that the B-part is always smaller than the A-part (i.e. $\varepsilon \simeq |B|/|A|$ is not small enough) and we do not take advantage of the perturbed form of $\mathcal{H}_{\text{debris}}$, as expressed in eq. (2.8). Starting directly from eq. (2.8), we can choose

$$\begin{aligned}\mathcal{H}_{\text{debris}}(\vec{v},\Lambda,\vec{r},\theta) &= \mathcal{H}_{\text{kepl}}(\vec{v},\vec{r})+\mathcal{H}_{\text{rot}}(\Lambda)+\mathcal{H}_{\text{geopot}}(\vec{r},\theta)+\mathcal{H}_{\text{3body}}(\vec{r})+\mathcal{H}_{\text{srp}}(\vec{r}) \\ &= A(\vec{v},\vec{r},\Lambda)+B(\vec{r},\theta). \qquad (2.10)\end{aligned}$$

With this form, the B-part only contains perturbations. The main contribution to debris dynamics (the two-body problem) lies entirely in A. Hence, using any symplectic integrator proposed by Laskar and Robutel (2001) in this context is highly relevant. As the error of these integrators takes into account the small parameter ε, the accuracy of the propagator will prove to be excellent. Unfortunately, since we have splitted $\mathcal{H}_{\text{debris}}$ in such a way, we can not use the same method as in Sec. 2.1.2. In particular the evaluation of exponential operators involving the A-part of $\mathcal{H}_{\text{debris}}$ will be different.

2.3.2 Computation of $e^{c_i\tau L_A}$

In equation (2.10), we clearly see that A only depends on $\vec{v}$, $\vec{r}$ and Λ:

$$A(\vec{v},\vec{r},\Lambda)=\frac{v^2}{2}-\frac{\mu}{r}+\dot{\theta}\Lambda.$$

The first part of A corresponds to the Hamiltonian of a classic two-body problem. Moreover, as $\dot{\theta}$ is assumed to be constant and Λ is a constant parameter, equations of motion of A do not need to be numerically integrated. An analytical solution can be given, as explained below.

In the framework of orbital motion, the position and velocity of the orbiting body is usually given in terms of Keplerian elements (a,e,i,Ω,ω,f). The shape of the elliptic trajectory is determined by its semi-major axis a and eccentricity e. As illustrated in Fig. 2.1, the position of this ellipse with respect to a reference frame (in our case the Earth's equatorial plane) is given by the inclination i, the longitude of the ascending node Ω (also called right ascension of the ascending node) and the argument of the pericenter ω which is the angle between the point

of closest approach to the central point and the orbit ascending node. The last element is the true anomaly f, giving the position of the orbiting object on the ellipse. Other kinds of anomalies exist and will be described below. In a simple two-body problem, only the anomaly evolves with time, the other elements remaining constant.

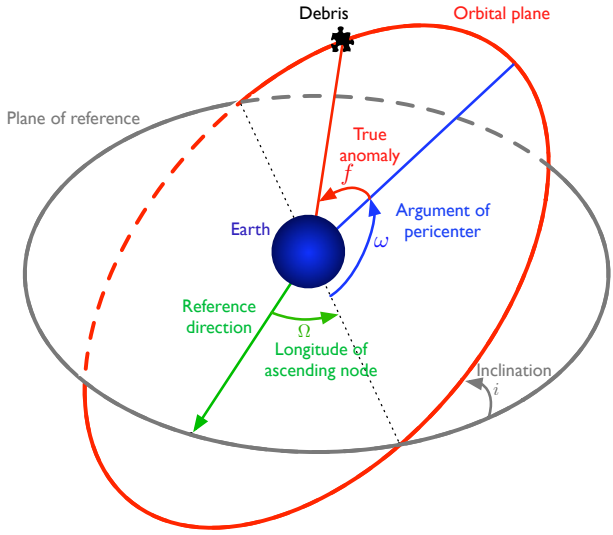

Figure 2.1 • *Keplerian elements of space debris orbiting the Earth*

Starting from the debris orbital elements, it is possible to express their position in geocentric Cartesian coordinates. We briefly explain the change of coordinates[3].

First, the cartesian position of the body in the orbital plane is given by

$$\begin{cases} x' &= r\cos f \\ y' &= r\sin f \\ z' &= 0 \end{cases}$$

where

$$r = \frac{a(1-e^2)}{1+e\cos f} = a(1-e\cos E)$$

[3]These are classic developments that can be found in e.g. Murray and Dermott (1999).

with E the eccentric anomaly. Thanks to Euler's angles, we are now able to write the position of the orbiting body in geocentric Cartesian coordinates:

$$
\begin{aligned}
&\begin{pmatrix} x \\ y \\ z \end{pmatrix} \\
= &\begin{pmatrix} \cos\Omega\cos\omega - \sin\Omega\cos i\sin\omega & -\cos\Omega\sin\omega - \sin\Omega\cos i\cos\omega & \sin\Omega\sin i \\ \sin\Omega\cos\omega + \cos\Omega\cos i\sin\omega & -\sin\Omega\sin\omega + \cos\Omega\cos i\cos\omega & -\cos\Omega\sin i \\ \sin i\sin\omega & \sin i\cos\omega & \cos i \end{pmatrix} \begin{pmatrix} x' \\ y' \\ z' \end{pmatrix} \\
= &\; r\begin{pmatrix} \cos\Omega\cos(\omega+f) - \sin\Omega\cos i\sin(\omega+f) \\ \sin\Omega\cos(\omega+f) + \cos\Omega\cos i\sin(\omega+f) \\ \sin i\sin(\omega+f) \end{pmatrix} \\
= &\; r\begin{pmatrix} \cos(V-2\Omega)\sin^2(i/2) + \cos V\cos^2(i/2) \\ -\sin(V-2\Omega)\sin^2(i/2) + \sin V\cos^2(i/2) \\ \sin i\sin(V-\Omega) \end{pmatrix}
\end{aligned}
\tag{2.11}
$$

where $V = \Omega + \omega + f$ is called the true longitude. This variable is introduced to avoid undefined variables. Indeed, when $e = 0$, ω and f are not well defined and we have to use their sum $\omega + f$ instead. Similarly, if $i = 0$, Ω and ω are not well defined but their sum is. The true longitude (or equivalently the mean and eccentric longitudes) is the only element which remains well defined even for singular eccentricity and inclination.
The velocity can be computed easily in the same way.

During one evaluation of $e^{c_i\tau L_A}$, only the true anomaly needs to be modified according to τ. To that end, we need to use the mean anomaly M. This quantity is proportional to the area swept by the focus-to-body line from the pericenter and is computed as

$$M = M_0 + c_i\tau n$$

where n is the mean motion, M_0 is the initial mean anomaly and c_i is the integrator coefficient (2.3). The mean motion is easily obtained from the third Kepler's law which asserts that

$$n = \mu^{1/2}a^{-3/2}.$$

Coming back to the true anomaly is not straightforward. We first have to solve the so-called Kepler's equation

$$M = E - e\sin E. \tag{2.12}$$

giving the value of E w.r.t. M and then compute the true anomaly f as

$$f = \arctan\frac{\sqrt{1-e^2}\sin E}{\cos E - e}.$$

In this work, Kepler's equation (2.12) is solved by means of Danby's method (see Danby and Burkardt 1983, Burkardt and Danby 1983 or Danby 1987). The

algorithm is

$$
\begin{array}{l}
g = E - e\sin E - M \\
\textbf{while } |g| \geq \zeta \\
\quad \left|\begin{array}{l}
g' = 1 - e\cos E \\
g'' = e\sin E \\
g''' = e\cos E \\
\Delta_1 = -g/g' \\
\Delta_2 = -g/(g' + \frac{1}{2}\Delta_1 g'') \\
\Delta_3 = -g/(g' + \frac{1}{2}\Delta_1 g'' + \frac{1}{6}\Delta_2^2 g''') \\
E = E + \Delta_3 \\
g = E - e\sin E - M
\end{array}\right.
\end{array}
$$

where the initial condition depends on the values of the eccentricity and mean anomaly:

$$
\begin{array}{rcl}
0.8 < e < 1 & \Rightarrow & E = \pi \\
e \leq 0.8 \quad \text{and} \quad M < 0.1 & \Rightarrow & E = M + [(6M)^{1/3} - M]e^2 \\
e \leq 0.8 \quad \text{and} \quad M \geq 0.1 & \Rightarrow & E = M + 0.85e.
\end{array}
$$

The precision threshold is given by ζ which must be a small enough number, e.g. $\zeta = 10^{-9}$.

Let us summarize how to compute $\vec{x}_{k_i} = e^{c_i \tau L_A}\vec{x}_k$. First, $\vec{x}_k$ is expressed in terms of Keplerian elements:

$$
(\vec{r}_k, \vec{v}_k) \rightsquigarrow (a_k, e_k, i_k, \Omega_k, \omega_k, f_k)
$$

and the next vector $\vec{x}_{k_i}$ is given by

$$
\left\{
\begin{array}{rcl}
\vec{v}_{k_i} & = & \vec{v}(a_k, e_k, i_k, \Omega_k, \omega_k, f_{k_i}) \\
\Lambda_{k_i} & = & \Lambda_k \\
\vec{r}_{k_i} & = & \vec{r}(a_k, e_k, i_k, \Omega_k, \omega_k, f_{k_i}) \\
\theta_{k_i} & = & \theta_k + c_i \tau \dot{\theta}
\end{array}
\right.
$$

where f_{k_i} is updated from f_k according to the previous formulae.

This approach seems efficient even for near zero eccentricity and inclination. However, described formulae to update the true anomaly are theoretically sensitive to undefined orbital elements. Hence in practice another similar method has been used. Instead of using eq. (2.11) to compute Cartesian position and velocity from Keplerian elements, we have used a subroutine of the MSLIB library made by CNES which works with the following non-singular orbital elements:

$$
\begin{array}{lll}
a & e\cos(\Omega + \omega) & 2\sin(i/2)\cos\Omega \\
M + \Omega + \omega & e\sin(\Omega + \omega) & 2\sin(i/2)\sin\Omega.
\end{array}
$$

where $\lambda := M + \Omega + \omega$ is the mean longitude. It can be updated more easily than the true anomaly as

$$\lambda = \lambda_0 + c_i \tau n.$$

Singularities are avoided and the computation of $e^{c_i \tau L_A} \vec{x}_k$ is more robust.

2.3.3 Computation of $e^{d_i \tau L_B}$

Given that B only depends on $\vec{r}$ and θ, the solution of $e^{d_i \tau L_B} \vec{x}_k$ is computed exactly as the solution of the set of differential equations

$$\left\{ \begin{array}{rcrcl} \dot{\vec{v}} & = & -d_i \vec{\nabla}_{\vec{r}} B(\vec{r}, \theta) & & \\ \dot{\Lambda} & = & -d_i \vec{\nabla}_{\theta} B(\vec{r}, \theta) & & \\ \dot{\vec{r}} & = & d_i \vec{\nabla}_{\vec{v}} B(\vec{r}, \theta) & = & \vec{0} \\ \dot{\theta} & = & d_i \vec{\nabla}_{\Lambda} B(\vec{r}, \theta) & = & 0 \end{array} \right. .$$

It follows that

$$e^{d_i \tau L_B} \begin{pmatrix} \vec{v}_k \\ \Lambda_k \\ \vec{r}_k \\ \theta_k \end{pmatrix} = \begin{pmatrix} \vec{v}(t_0) - d_i \tau \vec{\nabla}_{\vec{r}} B(\vec{r}_k, \theta_k) \\ \Lambda(t_0) - d_i \tau \vec{\nabla}_{\theta} B(\vec{r}_k, \theta_k) \\ \vec{r}_k \\ \theta_k \end{pmatrix}.$$

Gradients of V_{nm} and W_{nm} required in the computation of $\vec{\nabla}_{\vec{r}} B$ and $\vec{\nabla}_{\theta} B$ are presented in Sec. B.2.

2.3.4 Units

Units have been chosen so that the distance unit is close to 1 for near-geostationary orbits. Hence we avoid both huge and tiny values during the propagation. The unit of time has been set to

$$1\,\mathbf{UT} = \frac{1}{2\pi} \text{ sidereal day}.$$

This directly comes from the following relation

$$n = \frac{2\pi}{T} = \frac{1}{\mathbf{UT}}$$

where n is the mean motion and T is the orbital period, i.e., 1 sidereal day.

The mass unit **UM** is equal to one Earth's mass, i.e. 5.9737×10^{24} kg.

The distance unit **UD** has been fixed so that the universal gravitational constant is equal to 1 $\mathbf{UD}^3\ \mathbf{UM}^{-1}\ \mathbf{UT}^{-2}$:

$$\mathcal{G} = 6.6742867 \times 10^{-11} \frac{\mathrm{m}^3}{\mathrm{kg\ s}^2} = 1 \frac{\mathbf{UD}^3}{\mathbf{UM}\ \mathbf{UT}^2}.$$

With previous unit choices, the unit of distance turns out to be close to the geostationary semi-major axis

$$\begin{aligned} 1\,\mathbf{UD} &= \left[6.6742867 \times 10^{-11} \times 5.9737 \times 10^{24} \times \frac{86164.09^2}{4\pi^2}\right]^{1/3} \mathrm{m} \\ &= 42164.1697748545\,\mathrm{km}. \end{aligned}$$

Note that one sidereal day equals 86164.09 s. Also remark that, in such units, the gravitational parameter μ becomes $\mu = 1\ \mathbf{UD}^3\ \mathbf{UT}^{-2}$.

2.3.5 Julian Days

The time scale for third body ephemerides is built on Julian Days. Hence, some transformations are needed to convert Julian Days to Calendar Dates and vice versa. As presented with many details in Montenbruck and Gill (2005), the Julian Day (JD) is the number of days since noon January 1, 4713 BC. Because this number is presently actually large, one has also defined the Modified Julian Day (MJD) as follows:

$$\mathrm{MJD} = \mathrm{JD} - 2400000.5.$$

This corresponds to the number of days since 0h November 17, 1858.

How to compute the MJD from the Calendar Date ? Let the civil time be expressed in year Y, month M and day D. Then, we need to define the following auxiliary quantities:

$$\begin{aligned} y &= \begin{cases} Y - 1 & \text{if } M \leq 2 \\ Y & \text{otherwise} \end{cases} \\ m &= \begin{cases} M + 12 & \text{if } M \leq 2 \\ M & \text{otherwise} \end{cases} \\ B &= \begin{cases} -2 + \lfloor (Y + 4716)/4 \rfloor - 1179 & \text{until 4 Oct. 1582} \\ \lfloor Y/400 \rfloor - \lfloor Y/100 \rfloor + \lfloor Y/4 \rfloor & \text{from 10 Oct. 1582} \end{cases} \end{aligned}$$

where $\lfloor x \rfloor$ denotes the integer part of x. Let us point out that, in the Gregorian Calendar, days from 5 Oct. 1582 to 9 Oct. 1582 do not exist. This has been

introduced to account for the leap years. Eventually, the MJD is given by

$$\text{MJD} = 365y - 679004 + B + \lfloor 30.6001(m+1) \rfloor + D.$$

The inverse transformation also needs some auxiliary variables:

$$\begin{cases} a &= \lfloor \text{MJD} \rfloor + 2400001 \\ q &= \text{MJD} - \lfloor \text{MJD} \rfloor \\ b &= \begin{cases} 0 & \text{if } a < 2299161 \\ \lfloor (a - 1867216.25)/36524.25 \rfloor & \text{otherwise} \end{cases} \\ c &= \begin{cases} a + 1524 & \text{if } a < 2299161 \\ a + b - \lfloor b/4 \rfloor + 1525 & \text{otherwise} \end{cases} \\ d &= \lfloor (c - 121.1)/365.25 \rfloor \\ e &= \lfloor 365.25d \rfloor \\ f &= \lfloor (c - e)/30.6001 \rfloor. \end{cases}$$

Finally, the calendar date is given by the following three quantities:

$$\begin{cases} D &= c - e - \lfloor 30.6001f \rfloor + q \\ M &= f - 1 - 12\lfloor f/14 \rfloor \\ Y &= d - 4715 - \lfloor (7 + M)/10 \rfloor. \end{cases}$$

2.4 Validation

Different tests are now presented to evaluate the accuracy of our propagator. First, we show that the energy is well preserved even on long periods of time. Then we compare our symplectic integrator to a non-symplectic one, another symplectic one and to orbits retrieved from Two-Line Elements.

2.4.1 Energy

We show in Fig. 2.2 (top) the maximum relative error in energy and CPU time required by our symplectic scheme to propagate the orbit of an object on a long time span (500 yr), depending on several time steps and integrator orders. The formula used to compute the relative error in energy at time t is given by

$$\Delta E(t) := |\mathcal{H}_t - \mathcal{H}_{t_0}|/\mathcal{H}_{t_0}$$

where $\mathcal{H}_t$ and $\mathcal{H}_{t_0}$ denote respectively the values of the Hamiltonian $\mathcal{H}_{\text{debris}}$ at times t and t_0. Initial conditions are $a = 42164.140$ km, $e = 0.1$, $i = 0.1$ rad, $\Omega = \omega = M = 0$ rad and the initial JD is 2455194.5 days. The model includes the geopotential up to degree and order 4. Time steps for these simulations have been set to 24, 12, 4, 1 and 1/2 hours. Several observations can be made from Fig. 2.2. On the one hand, the system being fully symplectic in this case (no implicit time dependence), the energy is accurately preserved even with large time steps. On the other hand, CPU times are really small, keeping in mind that the orbit has been propagated over 500 yr. Computations have been performed on a E5440 Intel Xeon CPU (2.83 GHz) with 6144 KB cache size.

The introduction of the gravitational perturbation of the Sun does not prevent the energy from being preserved on long time scales. However, the quasi-symplecticity (implicit time dependence through ephemerides) of our integrator means that relative variations of the energy are about 10^{-6} for the third body and solar radiation pressure perturbations, which is the amplitude of the quasi periodic solar motion. Out of curiosity, the relative energy error associated to two different orbits has been computed. The model still includes the geopotential up to degree and order 4 and we add the solar graviational perturbation. The difference appears in the computation of the Cartesian position of the Sun. On the one hand, we use JPL ephemerides and, on the other hand, we consider a Keplerian solar motion with null eccentricity and inclination (part of the ephemeris module of the NIMASTEP software described below). This lets us reduce the quasi periodic motion of the Sun. Results are shown in Fig. 2.3, where the $SABA_4$ integrator has been used. Obviously, a circular and coplanar solar orbit reduces the relative error in energy to order 10^{-9}. Fig. 2.3 also emphasizes the excellent energy preservation over the years, even when JPL ephemerides are used.

Let us mention that the introduction of JPL ephemerides greatly increases the computation cost. As a point of comparison, the CPU time needed for this simulation after 500 years with a time step of 4 hours and the SABA_4 integrator is 22 seconds. It roughly corresponds to twice the amount of CPU time needed for the same propagation without the computation of Sun's position.

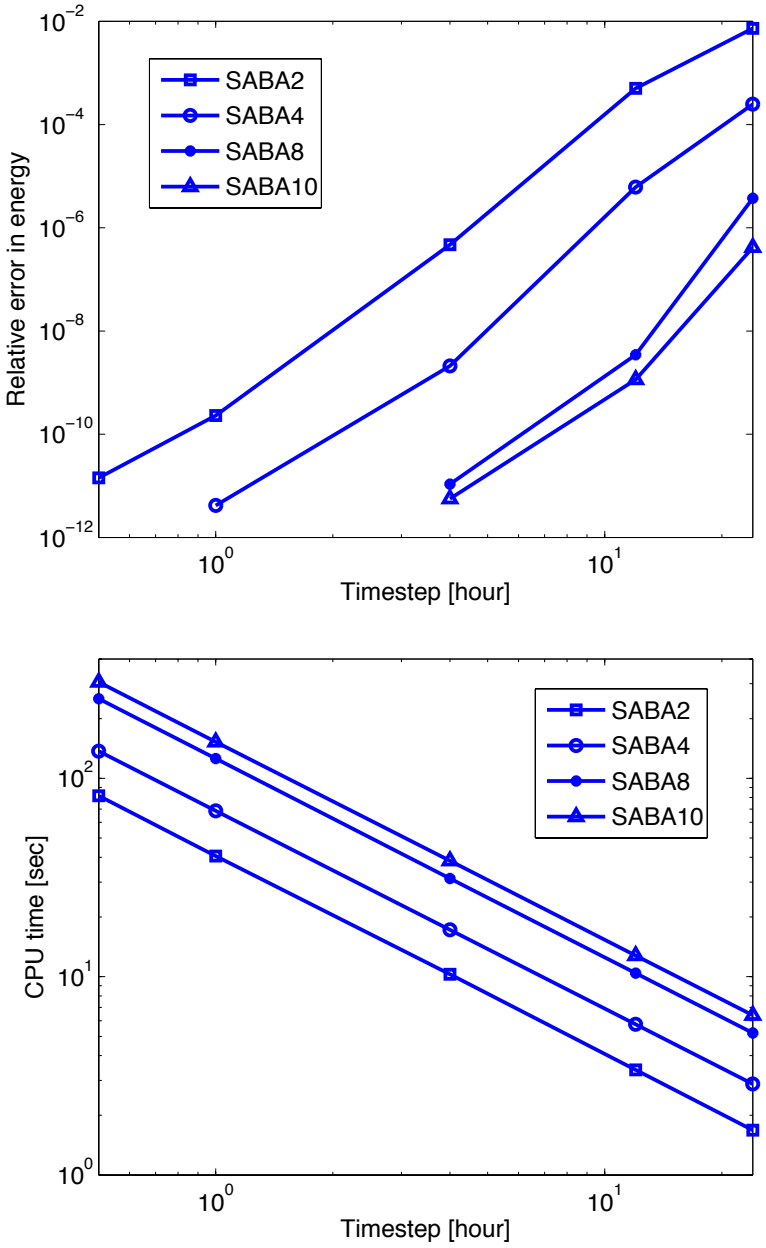

Figure 2.2 • *Maximum relative errors in energy (top) and CPU times (bottom) for different integrator orders, as a function of the time step. Initial conditions are* $a = 42164.140$ *km,* $e = 0.1$*,* $i = 0.1$ *rad,* $\Omega = \omega = M = 0$ *rad and the initial JD is* 2455194.5 *days. The model includes the geopotential up to degree and order* 4*. The integration has been performed on a time span of* 500 *years.*

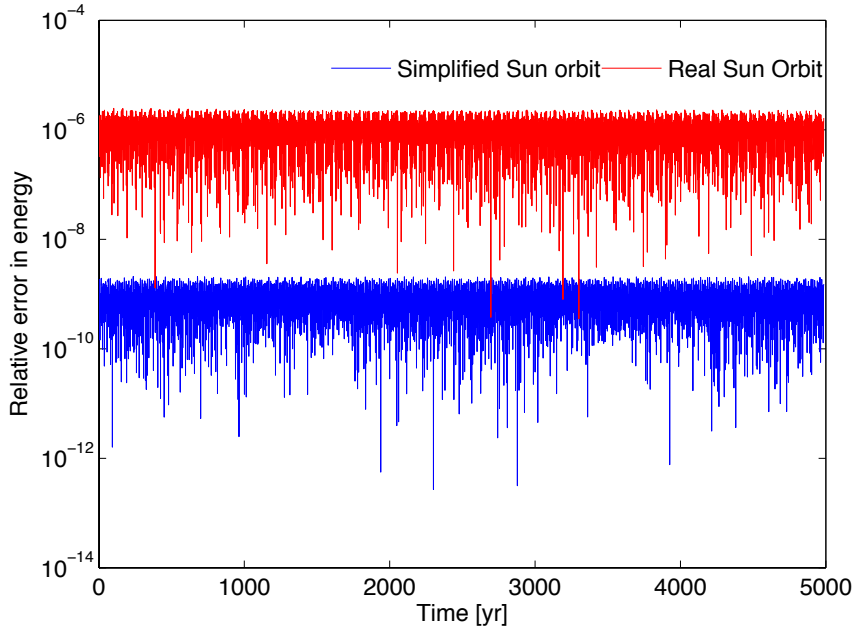

Figure 2.3 • *Comparison of the relative errors in energy as a function of time. Both real (upper curve) and simplified (i.e.* $e_\odot = 0$ *and* $i_\odot = 0$ *rad, lower curve) orbits of the Sun are considered. Initial conditions are* $a = 42164.140$ *km,* $e = 0.1$*,* $i = 0.1$ *rad,* $\Omega = \omega = M = 0$ *rad and the initial JD is* 698382.5 *days. The model includes the geopotential up to degree and order* 4 *and the gravitational perturbation of the Sun. The simulation has been run with the* $SABA_4$ *integrator and time steps set to* 1 *day*$/2\pi$*.*

The energy is an important indicator of the global accuracy of the integration. However it does not give much information about the degree of accuracy for each individual degree of freedom. Hence in Fig. 2.4 we show, for each orbital element, the absolute difference between the orbit propagated over 100 yr and the backward orbit propagated with negative time steps from 100 yr to 0 yr. Initial conditions are $a = 42164.140$ km, $e = 0.1$, $i = 0.1$ rad, $\Omega = \omega = M = 0$ rad and the initial JD is 2455194.5 days. The model includes the geopotential up to degree and order 4, luni-solar gravitational perturbations and the SRP with a large AMR equal to 1 m^2/kg. This test emphasizes very small errors for the eccentricity, inclination, longitude of node and argument of pericenter. Unsurprisingly, the biggest error occurs for the semi-major axis which is very sensitive to accuracy losses. Even if the error increases as we are getting closer to the initial time epoch, it remains very small for such a long integration time span.

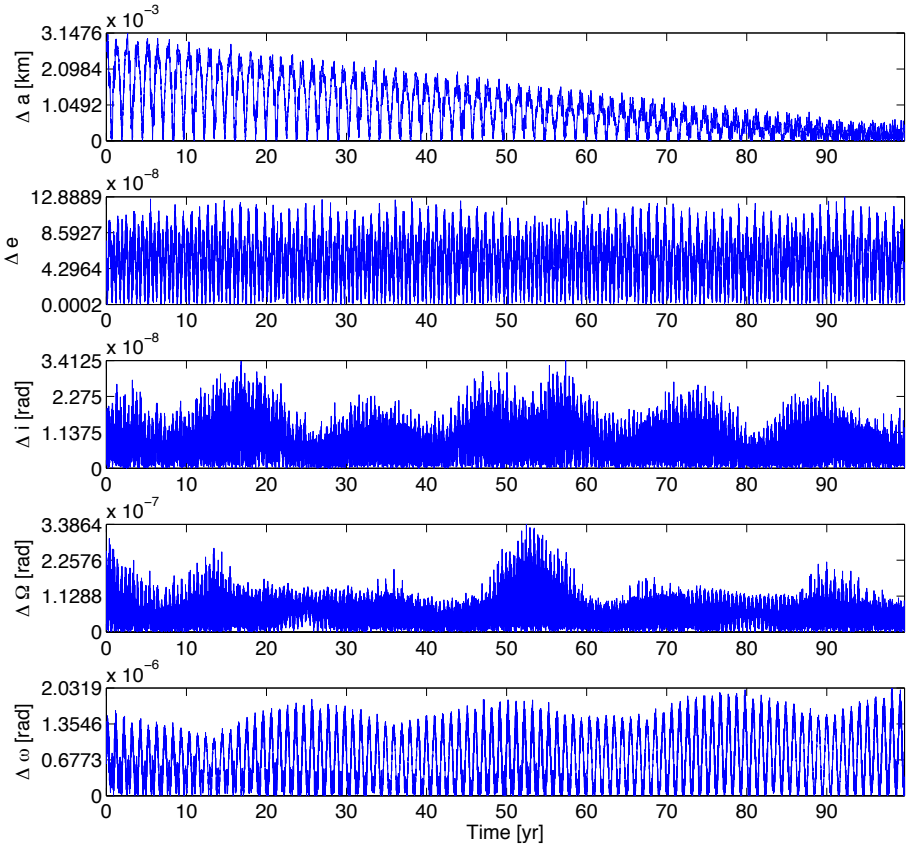

Figure 2.4 • *Absolute difference between each Keplerian element of the forward and backward orbits. Initial conditions are* $a = 42164.140$ *km,* $e = 0.1$*,* $i = 0.1$ *rad,* $\Omega = \omega = M = 0$ *rad and the initial JD is* 2455194.5 *days. The model includes the geopotential up to degree and order* 4*, luni-solar gravitational perturbations and the SRP with the AMR set to* 1 m^2/kg*. The simulation has been run with the* $SABA_4$ *integrator and time steps set to* 0.01 *day*$/2\pi$*.*

Step size [day]	Step size [s]	CPU time [s]
1/200	432	142.01
1/100	864	79.31
1/86	1004.65	70.73
1/75	1152	66.83

Table 2.1 • *CPU times required by* NIMASTEP *(with ABM10) with respect to time steps.*

2.4.2 Comparison with a non-symplectic scheme

We then compare our integration scheme to the NIMASTEP software (Delsate and Compère 2012). NIMASTEP (Numerical Integration of the Motion of Artificial Satellites orbiting a TElluric Planet) is an extensive tool that allows to integrate numerically the osculating motion of an arbitrary object (natural or artificial satellite, space debris...) orbiting a central body ((dwarf-) planets or asteroids of the Solar System) taking into account a large number of forces, integrators and options. This software has been successfully validated and compared to other external software like STELA[4]. In the following comparisons, NIMASTEP is used with the Adams-Bashforth-Moulton integrator of order ten (Hairer et al. 1993), hereafter referred to as ABM_{10}. Both integrators have propagated the same initial conditions. For the sake of completeness, all kinds of perturbations have been considered. Hence, we take into account the geopotential up to degree and order 4, luni-solar perturbations and the solar radiation pressure with AMR equal to 0.01 m^2/kg. In this case, the fourth order SABA integrator has been used with time steps equal to 4 hours. The CPU time required by the propagation over 190 yr with this method is 11.54 s. Table 2.1 lists each CPU time required by NIMASTEP for different time steps. To get more insight of the number of steps per revolution (about one day for these initial conditions), time steps are given in terms of fractions of one day and in seconds. Even if NIMASTEP quickly performs the numerical integration, the fact that our symplectic scheme can use large (ten times bigger) time steps naturally makes it a faster algorithm.

Given that both orbits obtained with our symplectic scheme and NIMASTEP are very close to each other, we show the absolute difference between each Keplerian element and for each time step. Results can be seen in Fig. 2.5. For each time step and orbital element, the absolute difference has been computed each day. Both software having been developed using different units of time and

[4]Semi-analytic Tool for End of Life Analysis (STELA) has been designed by CNES to support the French Space Operations Act (see Fraysse et al. 2012). STELA performs efficient long-term propagations of LEO, GEO, and GTO based on semi-analytical models and assessment of protected regions criteria. It also offers useful tools like the conversion of TLE. It is available online at
`http://logiciels.cnes.fr/STELA/en/logiciel.htm`.

distance, residual errors could have been introduced artificially. From Fig. 2.5, we see that absolute errors are quite small for the eccentricity, inclination, longitude of ascending node and argument of pericenter, no matter which time step is considered. The situation is slightly different for the semi-major axis and the mean anomaly. In this case, the error is clearly bigger for larger time steps and increases linearly with time. This can be explained by the non-symplecticity of NIMASTEP which does not fully preserve the energy. As explained previously, it is well known that the energy of a two-body problem is closely related to the semi-major axis, making this kind of discrepancy between both schemes unsurprising. While both integrators turn out to be really efficient on short time scales, our symplectic integrator does not suffer from a slight drift on the semi-major axis on long time scales. Nevertheless, let us remark that NIMASTEP with time steps equal to 432 and 864 s yields excellent results, the drift on the semi-major axis being reasonably low after 190 years (8.4443×10^{-2} km and 2.9404×10^{-1} km respectively with times steps 432 and 864 s). One of the main advantages of our integrator is its ability to obtain accurate results even with big time steps. As a comparison point, it turns out that NIMASTEP cannot be used with time steps larger than 1160 s for this particular set of initial conditions and perturbations.

2.4.3 Comparison with another symplectic scheme

Another symplectic scheme has been tested during a short stay at the Space Debris Office at ESOC/ESA. This integrator[5] is considered experimental and pending some validation. It was a good opportunity to compare our propagator with this one, hereafter called LTOP (Long-term Orbit Propagator). While no details are publicly available about the method, some information can be found in Wnuk et al. (2010). More precisely, LTOP is based on the logarithmic form of Hamiltonian equations of motion presented in Mikkola et al. (2002). The integration process takes place in the J2000 dynamical reference frame and the perturbing forces taken into account are the geopotential, gravitational potential of the Moon and the Sun and SRP.

The following perturbing factors have been considered for this cross-comparison: geopotential up to degree and order 20, SRP without shadows and luni-solar perturbations. The initial JD is 2455194.5 days. Please note that, unlike the previous comparison (Sec. 2.4.2), output data were not obtained at identical time steps. Hence, we only show orbital elements comparisons and do not produce an accurate absolute difference between these elements. Let us also mention that some artificial discrepancies are also due to the number of output time steps which is different for both propagators.

[5]This integrator was developed under the ESA contract Space debris orbits - observation, determination and evolution, PECS Project No. 98088 WP 1, ESA, 2010.

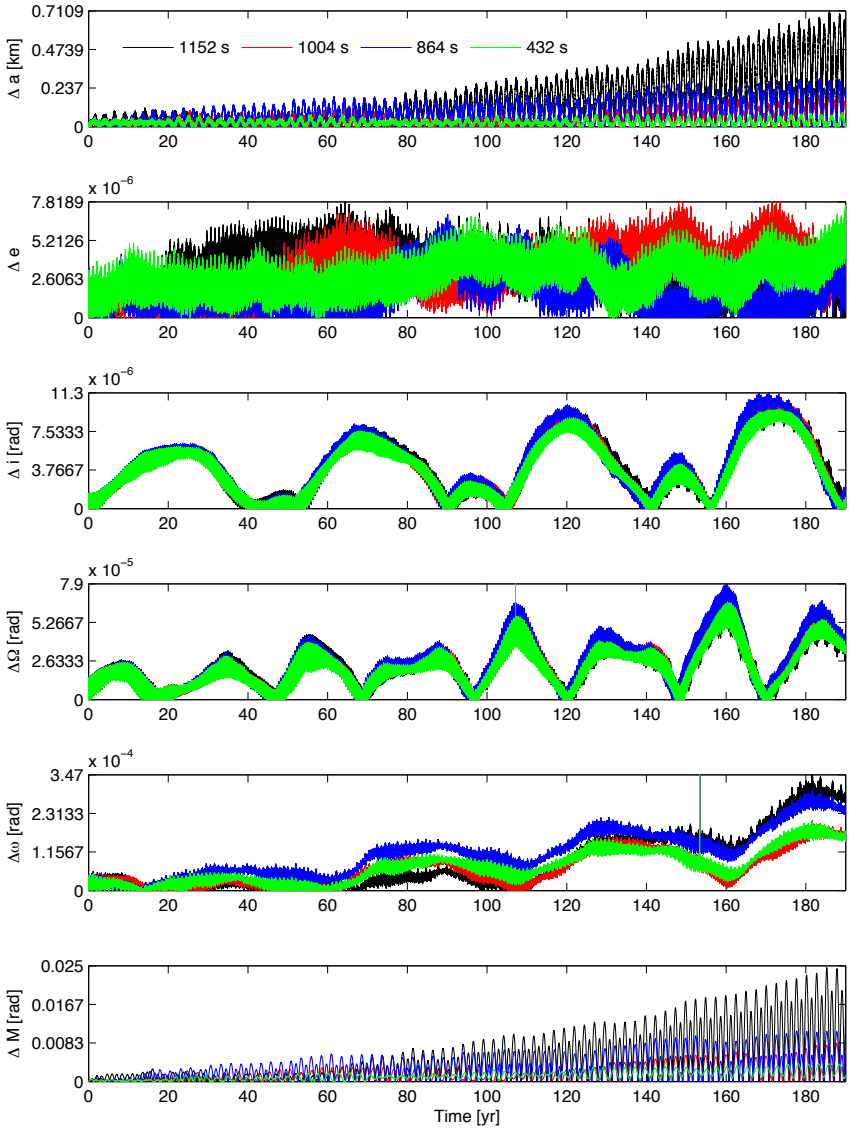

Figure 2.5 • *Absolute difference between each Keplerian element of the orbit obtained by our scheme ($SABA_4$ integrator and time step equal to 4 hours) and by the* NIMASTEP *software (with ABM10). Several time steps have been used with* NIMASTEP*:* 432 *s (green),* 864 *s (red),* 1004.65 *s (blue) and* 1152 *s (black) (Color online). Initial conditions are* $a = 42164.140$ *km,* $e = 0.1$ *,* $i = 0.1$ *rad,* $\Omega = \omega = M = 0$ *rad. The model includes the geopotential up to degree and order* 4*, solar radiation pression (with AMR equal to* 0.01 m^2/kg*) and luni-solar perturbations. The initial JD is* 2455194.5 *days.*

Five types of orbits have been propagated with both $SBAB_4$ and LTOP. These five cases were inspired from different scenarii proposed in the documentation of LTOP. The first one is a GEO. The comparison is shown in Fig. 2.6. Both orbits are in excellent agreement. Differences are visible for the argument of pericenter that come from 2π-modulo transformations. The second type is a GTO, a transfer orbit used to reach a geostationary one. From Fig. 2.7, we conclude that no significant difference appears even with high eccentricity values. Then, we test both schemes on a MEO (Fig. 2.8), characterized by a semi-major axis below geostationary ones and large enough to neglect the atmospheric drag. Again, the agreement is excellent between both element evolutions. However, important discrepancies are clearly visible for the semi-major axis after 130 yr. As will be explained in Sec. 5.4.4, this comes from the chaotic behaviour of this orbit. The same conclusion holds for the last orbit types where we took initial conditions close to the ones of ESA's X-ray Multi-Mirror Mission (XMM-Newton) and INTErnational Gamma-Ray Astrophysics Laboratory (INTEGRAL) satellites (see Fig. 2.9 and 2.10).

2.4.4 Comparison with Two-Line Element data

During a two-week collaboration with Dr. A. Rossi at the IFAC-CNR (Sesto Fiorentino, Italy), our propagator has been compared to observation data. Such data are publicly available[6] in the form of Two-Line Element (TLE) sets. The TLE is a format specified by the North American Aerospace Defense Command (NORAD).

The elements in the TLE sets are mean elements calculated to fit a set of observations using a specific SGP4/SDP4 orbital model (Hoots and Roehrich 1980). Hence, reformatting the data to obtain osculating orbital elements (like the Keplerian elements described in Sec. 2.3.2) needs to be carefully done. Osculating elements used in the following comparison were passed on to me directly by A. Rossi. First the SGP4 theory was used to convert the TLE to osculating elements. Then integrations were performed using a special perturbations propagator based on Cowell's method (Lyddane and Cohen 1962) for the numerical integration of the equations of motion. The force model includes the zonal and tesseral harmonics of the Earth's gravity potential, the luni-solar gravitational perturbation, SRP with eclipses and several thermospheric density models for airdrag computation. This propagator was assembled in Pisa, at ISTI, based on the old NASA

[6]TLE are available on the CELESTRAK website `http://celestrak.com`. A detailed description of the TLE format can be found in the documentation page.

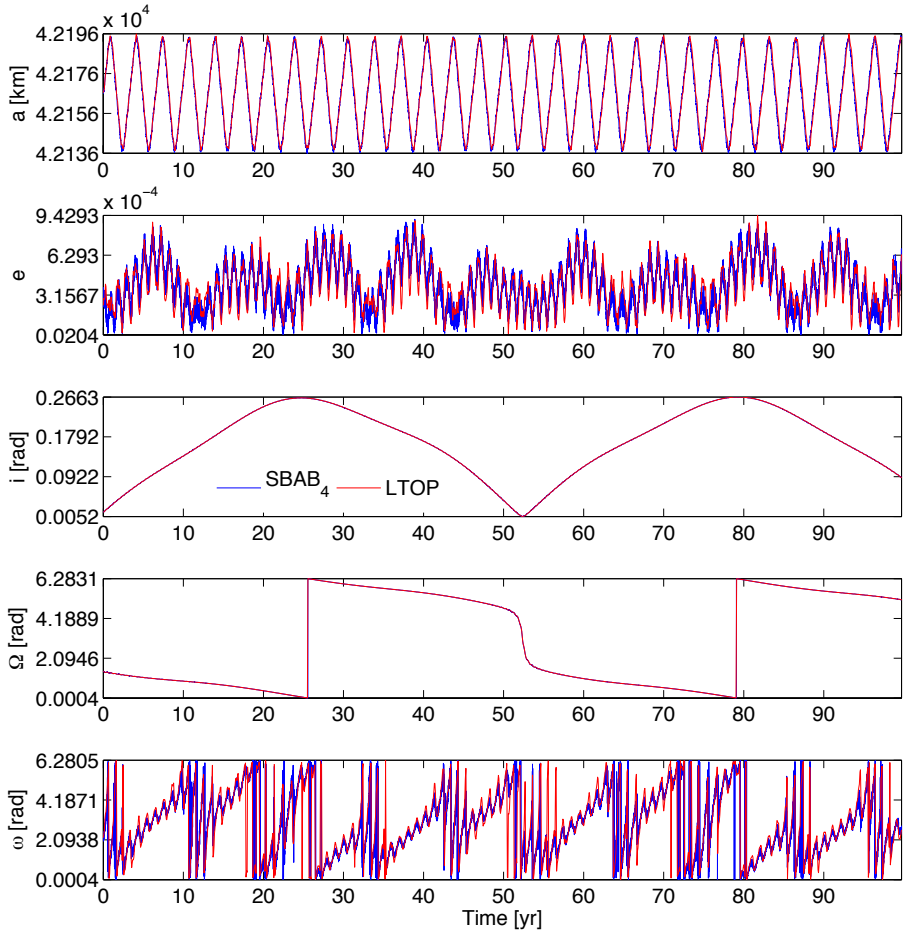

Figure 2.6 • *GEO debris orbital evolution obtained with $SBAB_8$ (in blue) and LTOP (in red). Initial conditions are $a = 42166.49250917766$ km, $e = 0.00023450$, $i = 0.0144999332771152$ deg, $\Omega = 1.41637816239974$ deg, $\omega = 2.20551812147257$ deg and $M = 1.93365266048441$ deg. Time steps used with $SBAB_4$ are equal to 1 day/2π. The AMR has been fixed to 0.01442821 m^2/kg.*

program called Artificial Satellite Analysis Program (ASAP) (Kwok 1987). Some propagations performed with the propagator are presented in Rossi (2008).

Orbital trajectories for different objects have been tested (mostly GLONASS, MOLNIYA and ETALON satellites). However, one must keep in mind that actual orbits are regularly modified by maneuvers. That means that an accurate comparison between TLE data and propagated orbits can only be performed between such operations. Comparison results proved to be excellent. In this work,

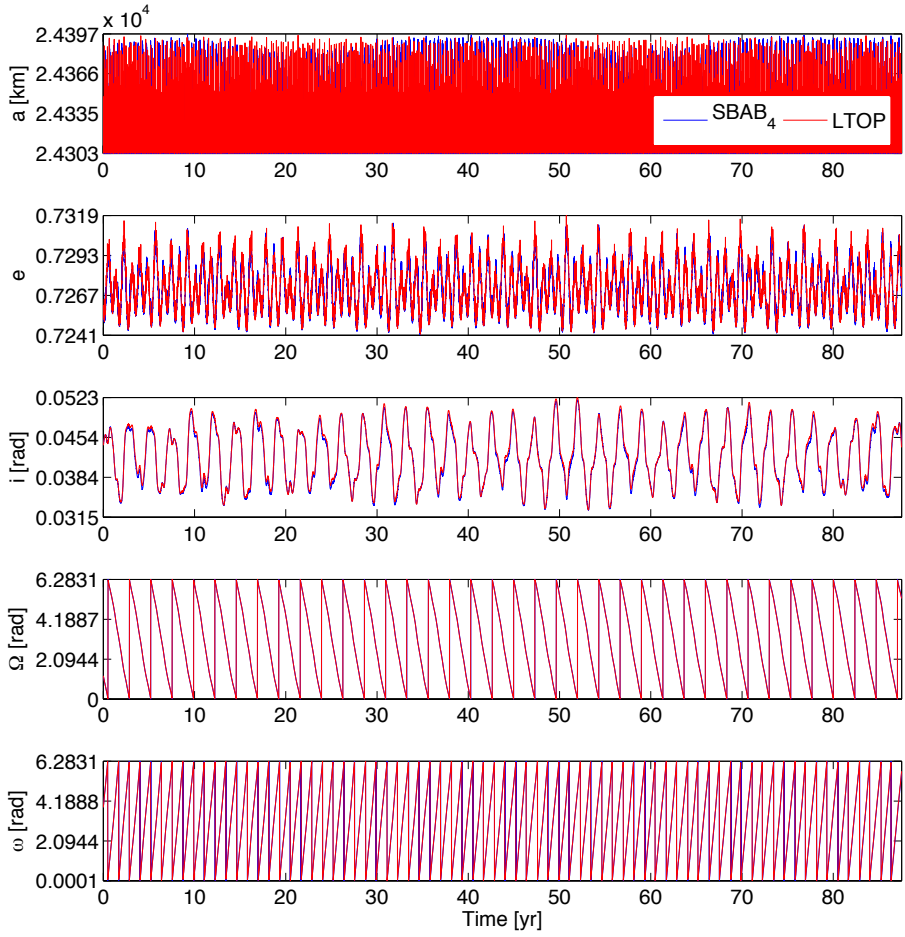

Figure 2.7 • *GTO debris orbital evolution obtained with $SBAB_8$ (in blue) and LTOP (in red). Initial conditions are* $a = 24304.9223156395$ *km,* $e = 0.7259043136$*,* $i = 0.0440146509329572$ *deg,* $\Omega = 1.21622727033479$ *deg,* $\omega = 3.85766404408082$ *deg and* $M = 0.889361796265728$ *deg. Time steps used with $SBAB_4$ are equal to* 1 *day*$/2\pi$*. The AMR has been fixed to* 0.06468090 m^2/kg*.*

we will only show them for one satellite: Etalon 1. Etalon is a geodetic passive satellite family of two identical Russian spacecrafts. Etalon is entirely dedicated to satellite laser ranging to permit solid Earth studies: geodynamic processes, development of high accuracy global references, long-period disturbances, geopotential modelling,...). Fortunately, no maneuver is supposed to occur during Etalon satellites flight. Moreover, Etalon 1 being a spherical shaped object, its AMR can be roughly estimated. The comparison between orbital elements for Etalon 1, obtained with the $SBAB_4$ integrator and with A. Rossi's software is shown in Fig. 2.11. Time steps used with $SBAB_4$ are 0.1 day$/2\pi$. The model includes the

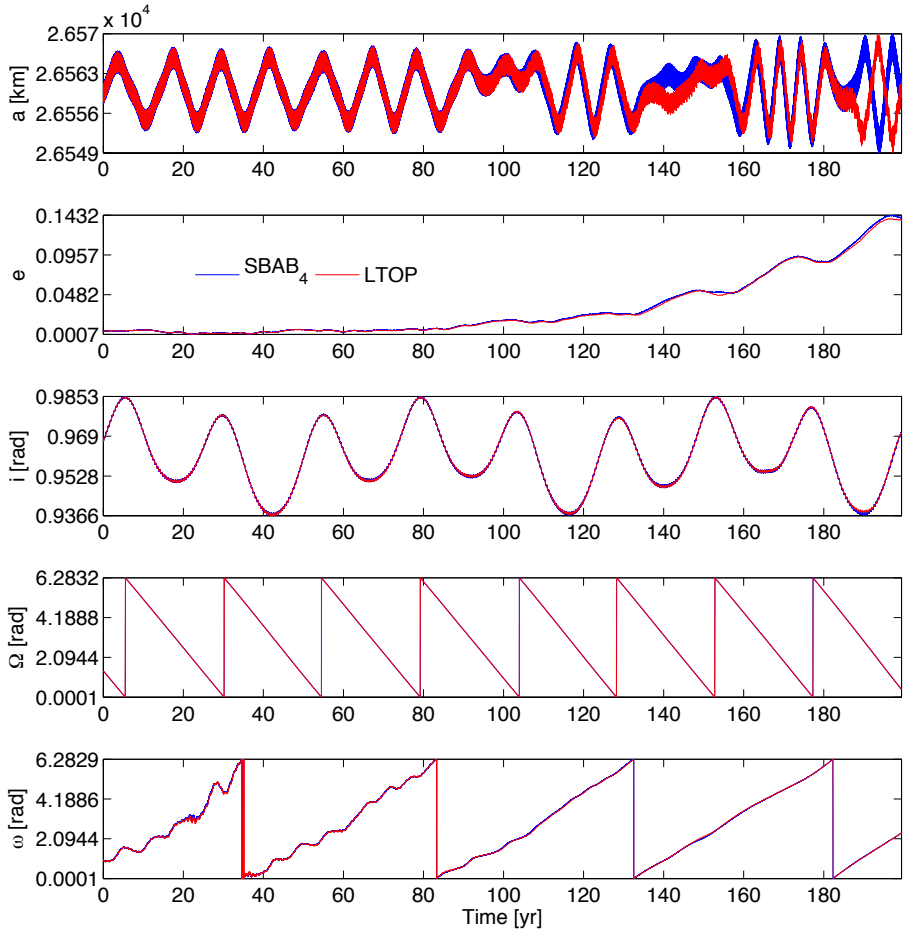

Figure 2.8 • *MEO debris orbital evolution obtained with $SBAB_8$ (in blue) and LTOP (in red). Initial conditions are a = 26561.50234949912 km, e = 0.00450962279279, i = 0.966840549730 deg, Ω = 1.38509409064 deg, ω = 0.948470412222 deg and M = 5.34171486198 deg. Time steps used with $SBAB_4$ are equal to 0.1 day/2π. The AMR has been fixed to 0.01205276 m^2/kg.*

geopotential up to degree and order 20, luni-solar perturbations and SRP (AMR equal to 0.001 m^2/kg) with shadows. More details about it are given in Chap. 3. Note that the small AMR makes Earth's shadows nearly insignificant in this simulation. The initial JD is 2448135.5 days. The agreement between both orbits is excellent. Only a small shift is visible at the end of the time interval for the inclination. That could arise from a slightly different AMR. One should also keep in mind that TLE are mean elements that might also present some uncertainties in their determination (see e.g. Flohrer et al. 2009).

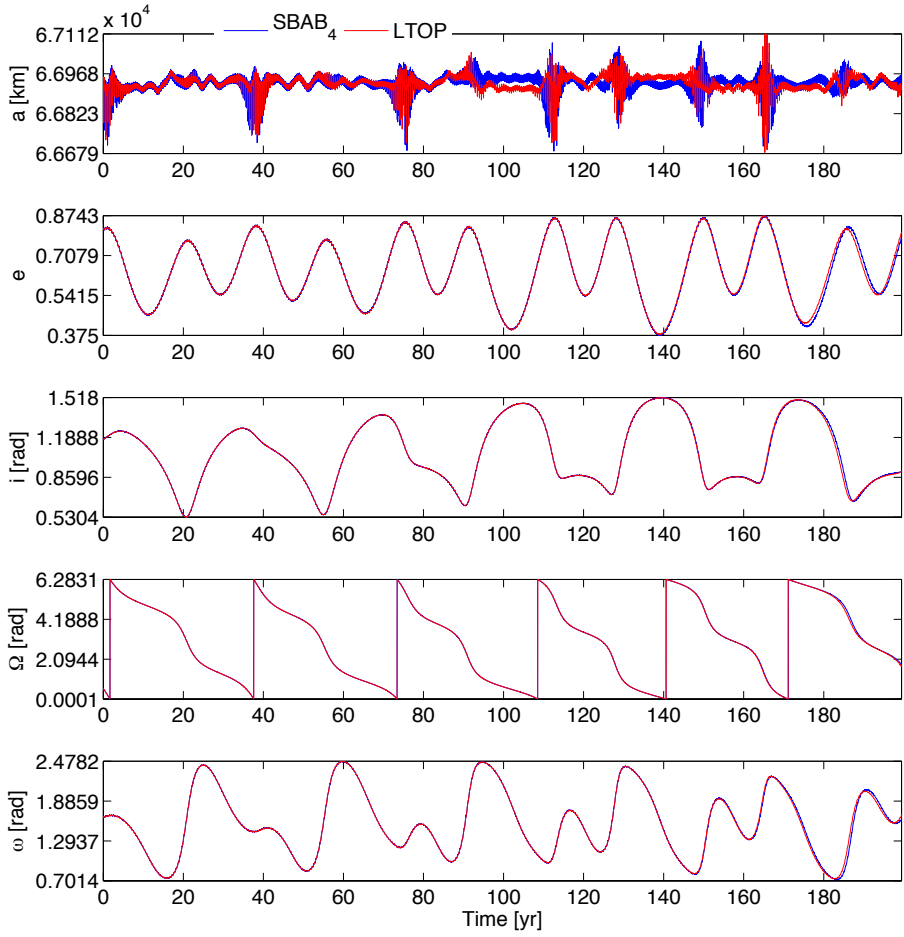

Figure 2.9 • *XMM-Newton-like orbital evolution obtained with* $SBAB_8$ *(in blue) and LTOP (in red). Initial conditions are* $a = 66934.833329141$ *km,* $e = 0.817460399$, $i = 1.17107997187960$ *deg,* $\Omega = 0.558535960536030$ *deg,* $\omega = 1.64483432165334$ *deg and* $M = 1.64483432165334$ *deg. Time steps used with* $SBAB_4$ *are equal to* 0.1 *day*$/2\pi$. *The AMR has been fixed to* 0.0119119 m^2/kg.

2.5 Conclusion

An efficient symplectic integration scheme has been built to propagate space debris orbits. The underlying algorithm has been described and the accuracy of the integrator has been demonstrated by means of numerical comparisons. It has been pointed out that large time steps could be used and that the relative error

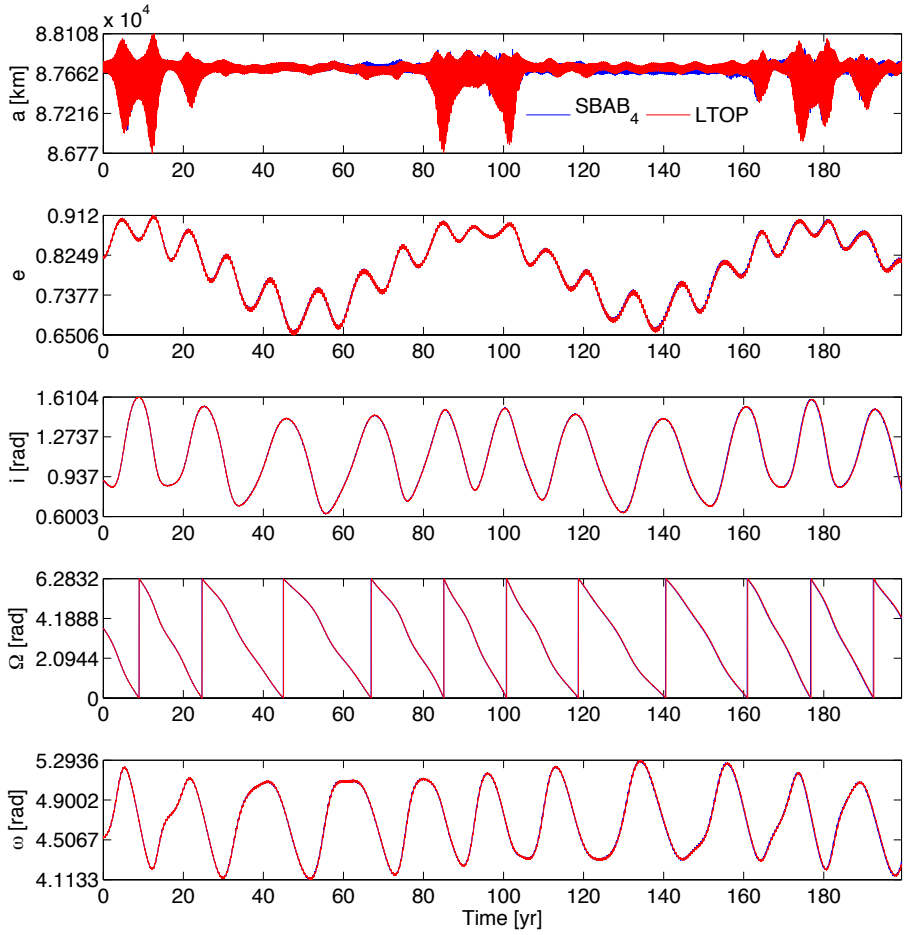

Figure 2.10 • *INTEGRAL-like orbital evolution obtained with $SBAB_8$ (in blue) and LTOP (in red). Initial conditions are $a = 87777.928856932$ km, $e = 0.820673671$, $i = 52.007475192$ deg, $\Omega = 210.912732145$ deg, $\omega = 259.251239584$ deg and $M = 353.046797176$ deg. Time steps used with $SBAB_4$ are equal to 0.1 day$/2\pi$. The AMR has been fixed to 0.0119119 m^2/kg.*

in energy was not increasing with time, even on huge time spans. Our method is not stuck to one particular order and it can be adapted to the complexity of the perturbations and to the desired precision. Our integration scheme is able to take into account the Earth's gravitational potential, luni-solar and planetary gravitational perturbations and SRP. While the symplectic propagator is fast and reliable on long time scales, it has been shown that it was also accurate on smaller time spans.

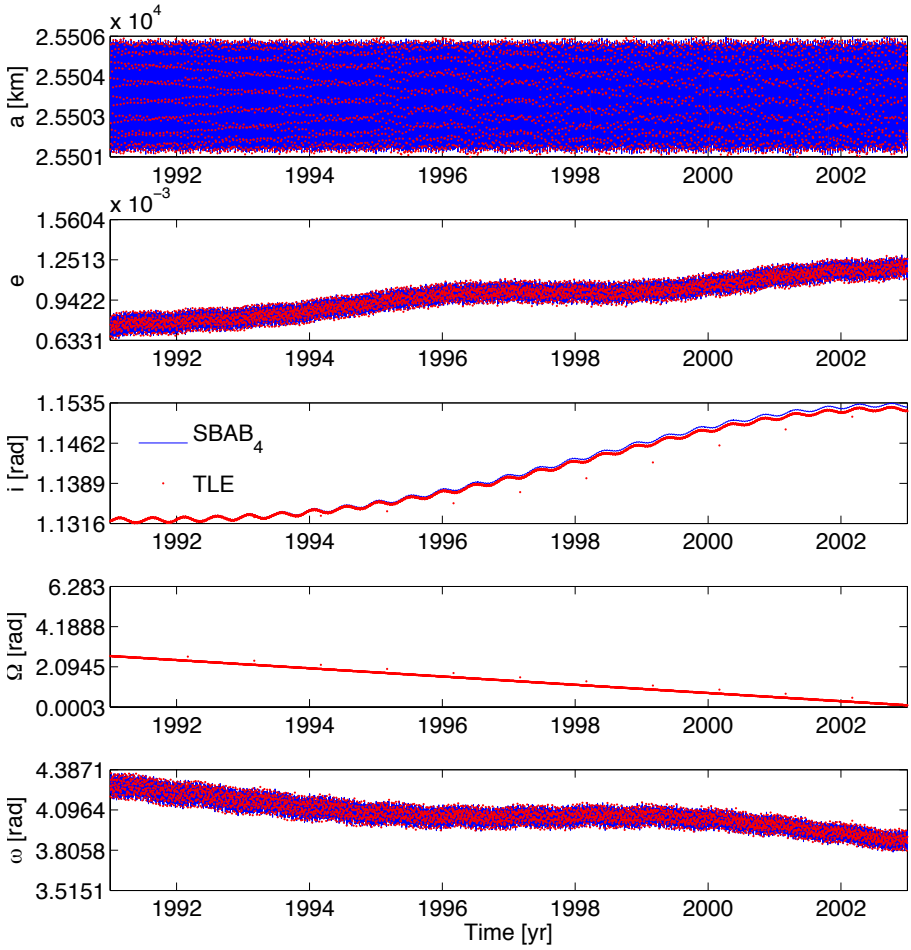

Figure 2.11 • *Etalon* 1 *orbital evolution obtained with* $SBAB_4$ *(in blue) and with A. Rossi's software (in red). Initial conditions are* $a = 25501.226477215$ *km,* $e = 6.4277342743962 \times 10^{-4}$*,* $i = 64.8926918456919$ *deg,* $\Omega = 156.2287368375213$ *deg,* $\omega = 245.4831550716323$ *deg and* $M = 13.9439761054335$ *deg.*

However, two drawbacks appear. First, shorter time steps are obviously required when propagating highly eccentric orbits. Indeed, using adaptive time steps with symplectic integrators is a very hard task. Some works dealing with this issue have been published for particular situations and mappings (see Skeel and Gear 1992, Skeel and Biesiadecki 1994). This problem has not be solved during this thesis and we decided to focus on other topics.
Second, our propagator is not able to deal with the atmospheric drag. Indeed, an explicit non-periodic time dependence would appear in the Hamiltonian and break the preserving properties of this scheme. That limitation implies that no LEO

(altitude below approximately 2000 km) can be modelled with our tool. Some clues exist to perform symplectic integrations with drag forces (Mueller et al. 1979, Breiter and Métris 1999) but it is not directly applicable to our general splitting method.
Hopefully, we managed to include another tricky phenomenon into our symplectic scheme: Earth's shadow crossings. All details are given in Chap. 3.

Chapter 3
Earth's shadows

Contents

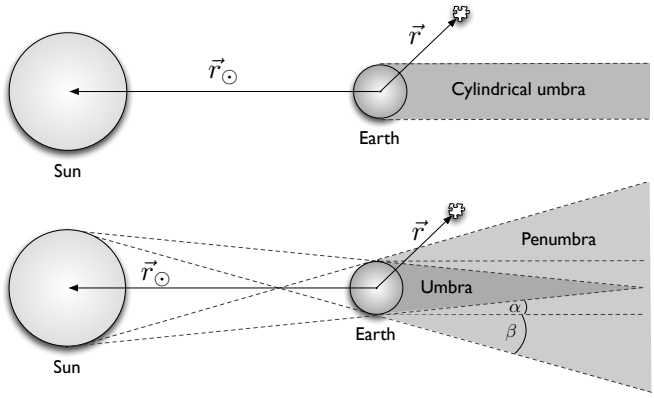

Figure 3.1 • *Top panel: cylindrical Earth shadow with solar rays assumed to be parallel when reaching the Earth. Bottom panel: Umbra-penumbra model including partial eclipses. Angles α and β give the geometric difference between both cylindrical and conical models.*

A first approximation of Earth's shadows consists in modelling it as simple cylinder. In this case, the Sun is assumed to be infinitely far away from the Earth and the solar rays are supposed to be parallel. The geometry of this problem is illustrated in Fig. 3.1 (top). However, a more realistic model includes the penumbra transitions which let us model partial eclipses (see Fig. 3.1, bottom). In this case, the distance to the Sun and diameters of both Earth and Sun have to be considered to compute the amount of sunlight actually reaching parts of space debris.

The idea of the introduction of a continuous shadow function equal to one in direct sunlight and zero otherwise has first been proposed in Ferraz-Mello (1964) and Ferraz-Mello (1965). This function depends on the angle formed by the geocentric Cartesian position of space debris and the dark pole of the Earth's terminator (i.e. the locus of points where the sunrays are tangent). Another numerical approximation of the same shadow function has been proposed later on in Lála and Sehnal (1969). Then, a way of computing shadow entrance and exit anomalies along the orbit has been proposed in Escobal (1976). It has to be noted that such approximations were only able to model cylindrical shaped Earth's shadows. Hence, these solutions have been improved further in order to take into account penumbra transitions. For example, umbra and penumbra cone boundaries have been computed in Escobal (1976). Other detailed studies exist. For example, penumbra transitions and several physical atmospheric processes have been numerically studied in Vokrouhlický et al. (1993) to provide a realistic shadow crossing model. In particular, it was shown that the refraction phenomena could be taken into account when modelling the penumbra transition curve. Faced with the complexity of its implementation in our symplectic algorithm, it has

been decided to neglect this effect. Let us mention that an approximate version (and less time consuming) of Vokrouhlický et al. (1993) has been presented in Vokrouhlický et al. (1994a). Penumbra phenomena induced by the SRP from the Earth-reflected sunlight have also been studied in Vokrouhlický et al. (1994b), leading to the conclusion that these effects were much less important than the direct SRP. A further numerical investigation (Vokrouhlický et al. 1996) has also shown that the oblateness of the Earth was nearly insignificant. Eventually, we can find another geometrical model of the penumbra transition in Montenbruck and Gill (2005), where the computation of the degree of occultation of the Sun by the Earth is performed by means of apparent radii in geocentric Cartesian coordinates.

The aim of this chapter is to present a new shadow crossing model. As we intend to primarily use it with the symplectic propagation scheme, the shadow function has to be smooth enough and included directly in the equations of motion. Any other alternative would introduce numerical errors in the symplectic scheme and cause an important drift in some orbital elements (mostly the semi-major axis, closely related to the energy) even on a short term. Our theory is able to model both cylindrical and conical shadow (umbra-penumbra transitions) crossings. Even if the formulation makes it perfectly suitable for symplectic propagators, no restriction applies for any other non-symplectic integrator.

In the following, we start from an existing method to model cylindrical shadows and present our solution (Sec. 3.1.2). Then, our method is extended to the case of penumbra transition models (Sec. 3.2). In Sec. 3.3, we numerically compare our model with the solution from Escobal (1976) and Montenbruck and Gill (2005) and analyze the differences between orbits obtained with both our cylindrical and conical shadow models. Finally, we conclude in Sec. 3.4

3.1 Cylindrical shadow models

3.1.1 Orbital entrance and exit from Earth's shadows

In Escobal (1976), a method is proposed to find the orbital entrance and exit of a satellite from the shadow of the Earth. Two non-spurious roots of a quartic polynomial in the cosine of the true anomaly correspond to the shadow entrance and exit. Then the effect of the SRP can be switched on and off, depending on the angular position of debris on their orbits.

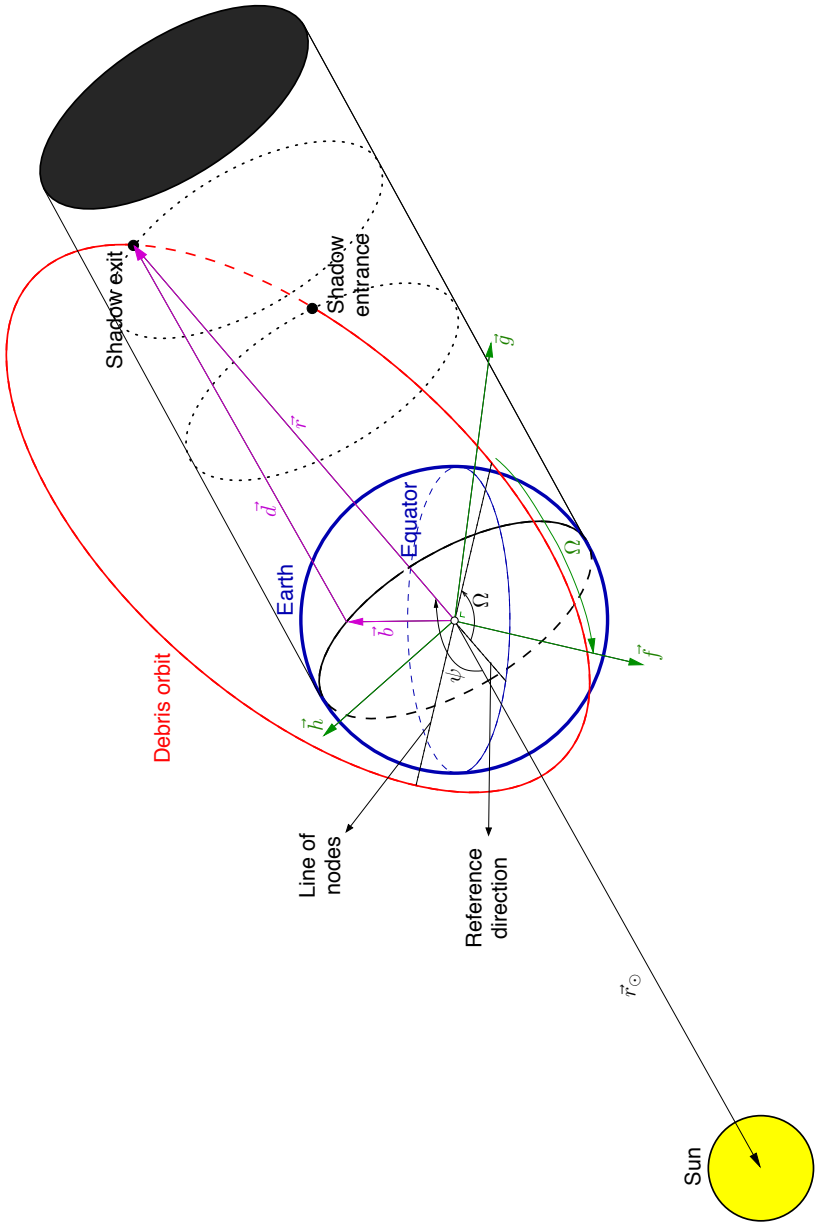

Figure 3.2 • *Geometric description of angles, vectors and frames used to determine when debris enter and exit Earth's cylindrical umbra. Inspired from Valk and Lemaitre (2008)*

Let $\vec{b}$ and $\vec{d}$ be defined as in Fig. 3.2. The vector $\vec{d}$ is positioned on the surface of the cylinder, starts from the Earth's terminator and points either to the entrance in or exit from the cylindrical shadow. Then, $\vec{b}$ is the vector from the Earth's center to the beginning of $\vec{d}$. When debris enter or exit the umbra, $\vec{b}$ and $\vec{r}_\odot$ are orthogonal and such that

$$\vec{r}_\odot \cdot \vec{d} = \vec{r}_\odot \cdot (\vec{r} - \vec{b}) = \vec{r}_\odot \cdot \vec{r}. \tag{3.1}$$

Let ψ be the angle between $\vec{r}$ and $\vec{r}_\odot$. At shadow entrance and exit, $\vec{b}$ and $\vec{d}$ also being orthogonal, eq. (3.1) becomes

$$-\sqrt{r^2 - R_\oplus^2} = - \parallel d \parallel = r \cos\psi. \tag{3.2}$$

Instead of working with Keplerian elements, we will use the same non-singular *equinoctial* orbital elements and method developed in Valk and Lemaitre (2008) and defined as

$$\begin{array}{lll} a & h_e = e\sin(\Omega+\omega) & p_e = \tan\frac{i}{2}\sin\Omega \\ \lambda = \Omega + \omega + M & k_e = e\cos(\Omega+\omega) & q_e = \tan\frac{i}{2}\cos\Omega \end{array} \tag{3.3}$$

where λ is the mean longitude. We also define the frame centered at the Earth's center and given by vectors $(\vec{f}, \vec{g}, \vec{h})$ (see Fig. 3.2). While $\vec{f}$ and $\vec{g}$ are contained in the orbital plane, $\vec{h}$ is orthogonal to previous vectors and orbital plane. The angle between the line of nodes and $\vec{f}$ is equal to Ω and $\vec{g}$ is positioned at an angle of $\pi/2$ with respect to $\vec{f}$ in the orbital plane.

Using Euler's angles as in eq. (2.11), debris position can be expressed in $(\vec{f}, \vec{g}, \vec{h})$ as

$$\vec{r} = \begin{pmatrix} x \\ y \\ z \end{pmatrix} = \begin{pmatrix} \vec{f} & \vec{g} & \vec{h} \end{pmatrix} \begin{pmatrix} x' \\ y' \\ 0 \end{pmatrix} \tag{3.4}$$

where x' and y' give debris position in the $(\vec{f}, \vec{g})$ orbital plane. Let V be defined as debris true longitude

$$V = \Omega + \omega + f.$$

Then,

$$\begin{cases} x' &= r\cos V \\ y' &= r\sin V \end{cases}$$

and $\vec{r}$ is given by

$$\begin{cases} x &= r\cos\Omega\cos(\omega+f) - r\sin\Omega\sin(\omega+f)\cos i \\ &= \dfrac{1}{1+p_e^2+q_e^2}\left[x'(1+q_e^2-p_e^2)+2y'p_eq_e\right] \\ y &= r\sin\Omega\cos(\omega+f) + r\cos\Omega\sin(\omega+f)\cos i \\ &= \dfrac{1}{1+p_e^2+q_e^2}\left[2x'p_eq_e+y'(1+p_e^2-q_e^2)\right] \\ z &= r\sin i\sin(\omega+f) \\ &= \dfrac{1}{1+p_e^2+q_e^2}\left[-2x'p_e+2y'q_e\right]. \end{cases}$$

Looking back at eq. (3.4), one easily obtains $\vec{f}$ and $\vec{g}$ as

$$\vec{f} = \frac{1}{1+p_e^2+q_e^2}\begin{pmatrix} 1+q_e^2-p_e^2 \\ 2p_eq_e \\ -2p_e \end{pmatrix} \quad \vec{g} = \frac{1}{1+p_e^2+q_e^2}\begin{pmatrix} 2p_eq_e \\ 1+p_e^2-q_e^2 \\ 2q_e \end{pmatrix}.$$

The value of $\vec{h}$ is not useful for its components will always be multiplied by zero.

With this new expression, the cosine of ψ can be written as

$$\cos\psi = \frac{\vec{r}\cdot\vec{r}_\odot}{r\,r_\odot} = \frac{(x'\vec{f}+y'\vec{g})\cdot\vec{r}_\odot}{r\,r_\odot} = f_\odot\cos V + g_\odot\sin V \tag{3.5}$$

where

$$f_\odot = \frac{\vec{f}\cdot\vec{r}_\odot}{r_\odot} \quad \text{and} \quad g_\odot = \frac{\vec{g}\cdot\vec{r}_\odot}{r_\odot}.$$

Eventually, starting from eq. (3.2) and using both eq. (3.5) and *semi-latus rectum* variable

$$p := a(1-e^2) = r(1+k_e\cos V + h_e\sin V),$$

we find the following shadow function which is equal to zero when debris cross Earth's shadows:

$$\Sigma := R_\oplus^2(1+k_e\cos V+h_e\sin V)^2 + p^2(f_\odot\cos V+g_\odot\sin V)^2 - p^2. \tag{3.6}$$

Entrance and exit true longitudes from the Earth's shadows are found to be the non-spurious solutions of $\Sigma = 0$. Unfeasible solutions are spotted by noting that any shadow crossing should normally occur when $\psi \in [\pi/2, 3\pi/2]$, i.e. $\cos\psi < 0$.

In Escobal (1976), classic Keplerian elements are used, yielding a simpler function

$$\Sigma' := R_\oplus^2(1+e\cos f)^2 + p^2(f_\odot\cos f+g_\odot\sin f)^2 - p^2.$$

It corresponds to a quartic polynomial in the cosine of the true anomaly. This function is transformed to standard form to find a new quartic polynomial in f which is solved in closed form by quadratic radicals (see Descartes' rule presented in Escobal 1976).

In Valk and Lemaitre (2008), the solutions of $\Sigma = 0$ are found using the so-called *resultant method* (see Gronchi 2005 for another application example). The latter lets us solve analytically the problem as a system of two algebraic equations in two variables.

We hereby propose a further improvement in the computation of the solutions of (3.6). By defining $T := \tan(V/2)$, (3.6) $\Sigma = 0$ becomes

$$R_\oplus^2\left(1+k_e\frac{1-T^2}{1+T^2}+h_e\frac{2T}{1+T^2}\right)^2+p^2\left(f_\odot\frac{1-T^2}{1+T^2}+g_\odot\frac{2T}{1+T^2}\right)^2-p^2=0$$

or, equivalently,

$$\begin{aligned} & T^4[p^2f_\odot^2-p^2+R_\oplus^2-2k_eR_\oplus^2+k_e^2R_\oplus^2]+T^3[-4f_\odot g_\odot p^2+4h_eR_\oplus^2-4h_ek_eR_\oplus^2] \\ + \quad & T^2[4g_\odot^2p^2-2p^2f_\odot^2-2p^2+4h_e^2R_\oplus^2+2R_\oplus^2-2k_e^2R_\oplus^2] \\ + \quad & T[4f_\odot g_\odot p^2+4h_eR_\oplus^2+4h_ek_eR_\oplus^2]+[p^2f_\odot^2-p^2+R_\oplus^2+2k_eR_\oplus^2+k_e^2R_\oplus^2] \\ = \quad & 0. \end{aligned}$$

Descartes' rule can then be used to find orbital entrance and exit true longitudes. The advantage of this method is twofold. First, the use of the tangent function directly indicates the right quadrant for the true anomaly. Then, the resultant method is not necessary anymore.

As will be shown in Sec. 3.3, this method cannot be used directly with the symplectic scheme. That is why a new shadow crossing model has been developed.

3.1.2 Smooth cylindrical shadow model

Eq. (3.2) turns out to be a very simple relation telling us that debris are situated in the cylindrical shadow of the Earth when

$$s_c(\vec{r}) := \frac{\vec{r}\cdot\vec{r}_\odot}{r_\odot}+\sqrt{r^2-R_\oplus^2}\leq 0. \tag{3.7}$$

In order to avoid numerical errors in the integration process, it is necessary to find a smooth function $\nu(\vec{r})$ approximately equal to one when debris are in

direct sunlight and zero otherwise. Then, $\vec{\nabla}_{\vec{r}}\mathcal{H}_{\rm srp}(\vec{r})$ can be multiplied by $\nu(\vec{r})$ in equations of motion so that each shadow crossing is taken into account.

We introduce a new shadow function defined as

$$\nu_{\rm c}(\vec{r}) := \frac{1}{2}\Big\{1+\tanh[\gamma\, s_{\rm c}(\vec{r})]\Big\} \simeq \left\{ \begin{array}{ll} 0 & \text{in cylindrical umbra} \\ 1 & \text{otherwise} \end{array} \right. \tag{3.8}$$

where the constant γ has to be fixed according to the required precision. The shape of this function is shown for different values of γ in Fig. 3.3 (top). It can be seen that, the bigger γ, the sharper the function $\nu_{\rm c}$. As a matter of fact, a perfect cylindrical shadow model would require γ to be infinite. However, considering double precision floating point standard, Fig. 3.3 (bottom) shows that taking $\gamma = 10^9$ is sufficient to represent cylindrical shadow crossings. Indeed, the absolute difference between 1 and the function $\nu_{\rm c}$ with $s_{\rm c}(\vec{r}) = 10^{-8}$ is already of order 10^{-9}. This explains the $\simeq$ symbol in above equation.

As explained above, replacing $\vec{\nabla}_{\vec{r}}\mathcal{H}_{\rm srp}(\vec{r})$ by $\nu_{\rm c}(\vec{r})\vec{\nabla}_{\vec{r}}\mathcal{H}_{\rm srp}(\vec{r})$ in equations of motion turns out to be an efficient way to use the fully symplectic integration scheme and consider cylindrical-shaped shadows of the Earth. In this case, a special attention has to be paid to the integration time step. The latter must be small enough to perform some steps inside the umbra zone, which only represents a small part of the total revolution time. As illustrated in Fig. 3.6, the cylindrical shadow on a geostationary orbit only lasts around half an hour. While this drawback cannot be neglected, it makes possible the use of low order symplectic integrators. In particular, the $SBAB_4$ and even $SBAB_2$ integrator can be used when the shadowing effects are enabled, still keeping highly accurate results.

3.2 Conical shadow model

Several attempts have been made to model the penumbra transition. A solution is proposed in Escobal (1976) to add umbra-penumbra corrections. Basically, one ends up with a more accurate but also trickier shadow function which still induces numerical errors in our symplectic integration scheme because the SRP does not include Earth's shadows as a smooth function.

Another kind of shadow crossing model can be found in Montenbruck and Gill (2005). In this case, a coefficient ν_M corresponds to the fraction of sunlight reaching the debris, based on the angular separation and diameters of the Sun and the Earth. Hence, ν_M is equal respectively to zero and one when the debris is in direct sunlight and umbra and corresponds to the remaining ratio of sunlight in the penumbra transition phase. Unfortunately this fraction can only be defined in the penumbra cone. It is not possible to write the function ν_M as a smooth

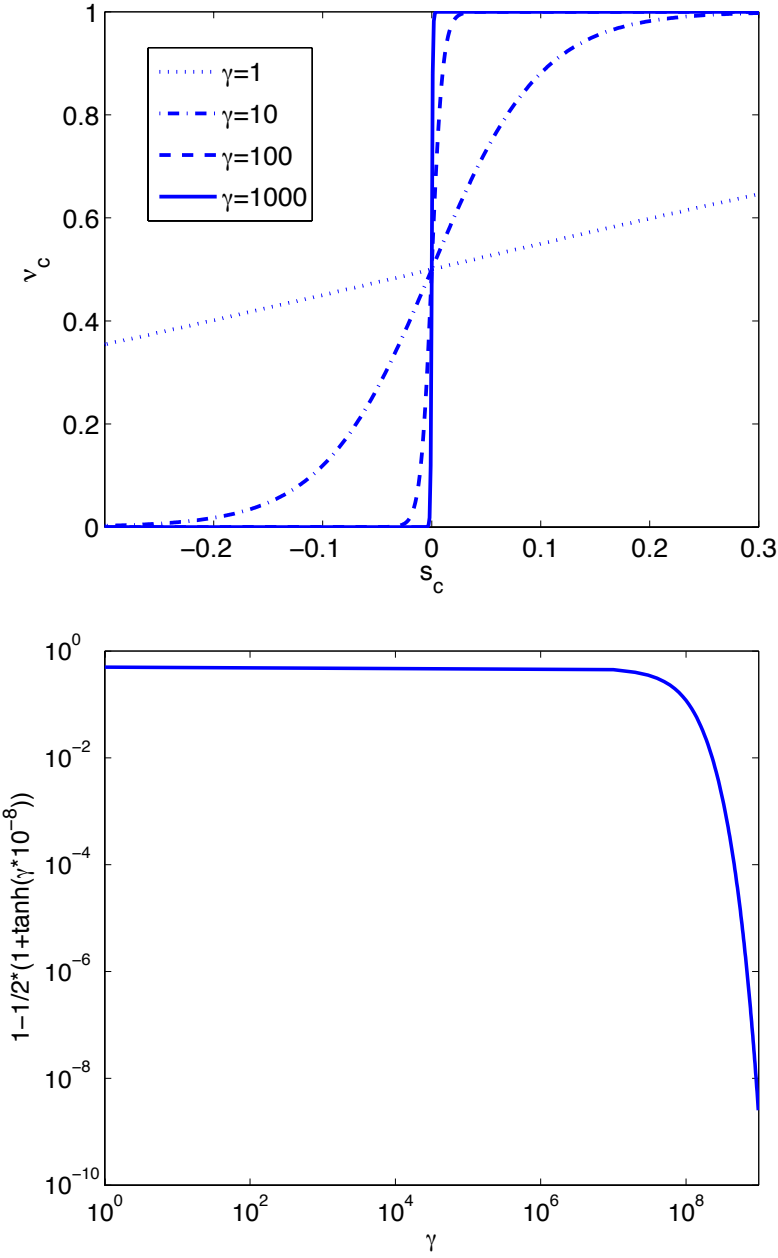

Figure 3.3 • *Top panel: evolution of the function ν_c for different values of s_c and of the parameter γ. Bottom panel: absolute difference between* 1 *and the function ν_c evaluated at $s_c(\vec{r}) = 10^{-8}$ for different values of the parameter γ.*

function and it cannot be used directly within our symplectic scheme. Moreover, any stability study requiring the computation of deviation vectors (see Chap. 5) could not be used with this method, ν_M being a piecewise-defined function. Nevertheless, ν_M is kept back as a comparison criterion for our further developments.

In the following, we present an original way of modelling umbra and penumbra cones crossings during the numerical integration of space debris orbit. First, simple geometry lets us introduce α and β angles representing the difference between the umbra cylinder and respectively the umbra and penumbra cones (see Fig. 3.1)

$$\alpha = \operatorname{atan} \frac{R_\odot - R_\oplus}{\|\vec{r} - \vec{r}_\odot\|} \quad \text{and} \quad \beta = \operatorname{atan} \frac{R_\odot + R_\oplus}{\|\vec{r} - \vec{r}_\odot\|}$$

with $R_\odot$ the radius of the Sun. Extending relation (3.7), it follows that space debris are in the umbra cone when

$$s_{\mathrm{u}}(\vec{r}) := \frac{\vec{r} \cdot \vec{r}_\odot}{r_\odot} + \cos\alpha \left[\sqrt{r^2 - R_\oplus^2 \cos^2\alpha} + R_\oplus \sin\alpha \right] \leq 0$$

and in the penumbra cone when

$$s_{\mathrm{p}}(\vec{r}) := \frac{\vec{r} \cdot \vec{r}_\odot}{r_\odot} + \cos\beta \left[\sqrt{r^2 - R_\oplus^2 \cos^2\beta} - R_\oplus \sin\beta \right] \leq 0.$$

An example of the evolution of functions s_{c}, s_{u} and s_{p} depending on time is shown in Fig. 3.4. Logically, as time goes on, s_{p} is the first quantity to become negative (we first enter the penumbra cone), followed by s_{c} (we cross the cylindrical umbra) and finally s_{u}. The same functions become positive in the reverse order as we leave the umbra cone, cross again the cylindrical umbra and then leave the penumbra cone.

Now, we will show that the function ν_{c} can be adapted to include the penumbra transition. As a matter of fact, the parameter γ will not be constant anymore but will be chosen so that the new shadow function ν_{p} is equal to one in direct sunlight, starts to decrease in the penumbra cone and is equal to zero in the umbra cone. The value of $1 - \nu_{\mathrm{p}}$ when the penumbra cone is crossed has to be fixed to attain a given precision threshold, denoted σ. Hence, we define the constant

$$\delta := \operatorname{atanh}(1 - \sigma). \tag{3.9}$$

In this chapter, δ is set equal to 8, meaning that the precision threshold $\sigma \simeq 2.25 \times 10^{-7}$.

Then, assuming that the time spent in the penumbra transition, Δt, is known, we can play with the tanh function using simple function manipulations. By setting γ equal to $\delta/\Delta t$

$$\nu_{\mathrm{p}}(\vec{r}) := \frac{1}{2} \left\{ 1 + \tanh \left[\frac{\delta}{\Delta t} s_{\mathrm{c}}(\vec{r}) \right] \right\} \tag{3.10}$$

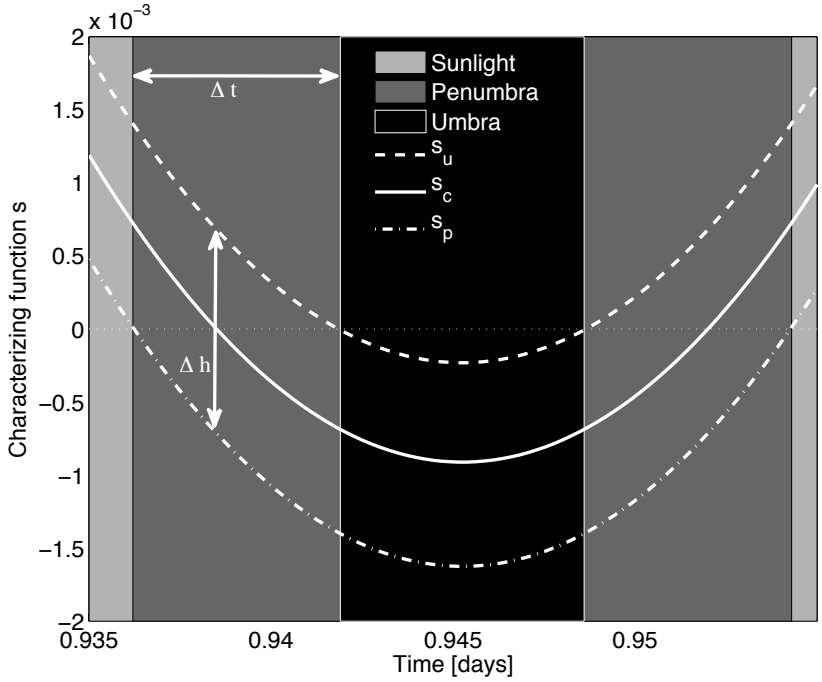

Figure 3.4 • *Evolution of the functions s_c, s_u and s_p during a shadow crossing on a geostationary orbit. The penumbra and umbra cones are crossed respectively when s_p is negative and s_u is negative. The time spent in the penumbra transition is noted Δt and the difference between s_u and s_p at the entrance of the cylindrical shadow is denoted by Δh.*

is smooth and such that

$$\left\{\begin{array}{rlll} \nu_{\rm p}(\vec{r}) \simeq 1 & \text{if} & s_{\rm p}(\vec{r}) > 0 & \\ \nu_{\rm p}(\vec{r}) = 1-\sigma & \text{if} & s_{\rm p}(\vec{r}) = 0 & \\ \sigma < \nu_{\rm p}(\vec{r}) < 1-\sigma & \text{if} & s_{\rm p}(\vec{r}) < 0 & \text{and} \quad s_{\rm u}(\vec{r}) > 0 \\ \nu_{\rm p}(\vec{r}) = \sigma & \text{if} & s_{\rm u}(\vec{r}) = 0 & \\ \nu_{\rm p}(\vec{r}) \simeq 0 & \text{if} & s_{\rm u}(\vec{r}) < 0 & \end{array}\right. .$$

The main difficulty lies in the way to assess Δt. As a matter of fact, this quantity cannot be estimated before each shadow crossing[1]. However, we will show that it can be replaced by a quantity depending only on debris position. Both entrance and exit times spent in the penumbra cone being computed exactly in the same fashion, we will only explain our method in the entrance case.

In the following developments, each quantity $s_{\rm c}$, $s_{\rm u}$ and $s_{\rm p}$ will be expressed as functions of the angle ψ between $\vec{r}$ and $\vec{r}_\odot$. As a first step, we assume that r does not depend on ψ (i.e. the orbit is assumed circular). It yields

$$s_{\rm c}(\psi) = r\cos\psi + \sqrt{r^2 - R_\oplus^2} \tag{3.11}$$

$$s_{\rm u}(\psi) = r\cos\psi + \cos\alpha\left[\sqrt{r^2 - R_\oplus^2\cos^2\alpha} + R_\oplus \sin\alpha\right] \tag{3.12}$$

$$s_{\rm p}(\psi) = r\cos\psi + \cos\beta\left[\sqrt{r^2 - R_\oplus^2\cos^2\beta} - R_\oplus \sin\beta\right]. \tag{3.13}$$

Let us also define ψ_1, ψ_2 and ψ_3 respectively as the value of ψ at the entrance the cylindrical shadow, umbra and penumbra cones. Hence, the following relations hold:

$$s_{\rm c}(\psi_1) = s_{\rm u}(\psi_2) = s_{\rm p}(\psi_3) = 0. \tag{3.14}$$

The difference $(\Delta\psi)$ between ψ_2 and ψ_3 will help us to characterize Δt. It is computed as follows. First, eq. (3.14) tells us that

$$\cos\psi_2 + \cos\alpha\left[\sqrt{1 - \frac{R_\oplus^2}{r^2}\cos^2\alpha} + \frac{R_\oplus}{r}\sin\alpha\right] = 0 \tag{3.15}$$

$$\cos\psi_3 + \cos\beta\left[\sqrt{1 - \frac{R_\oplus^2}{r^2}\cos^2\beta} - \frac{R_\oplus}{r}\sin\beta\right] = 0. \tag{3.16}$$

Then, we denote by ρ the small quantity $r/r_\odot$. It leads to the following simplified expression

$$\frac{\|\vec{r} - \vec{r}_\odot\|^2}{r_\odot^2} = 1 - 2\rho\cos\psi + \rho^2 \simeq 1 - 2\rho\cos\psi$$

[1] A possible alternative could be to set Δt to the time spent in the penumbra transition during the previous shadow crossing.

where the small term ρ^2 has been neglected. Then, keeping only terms of order ρ,

$$\begin{aligned}
\tan\alpha &= \frac{R_\odot - R_\oplus}{r_\odot}\frac{r_\odot}{\|\vec{r}-\vec{r}_\odot\|} \\
&\simeq \frac{R_\odot - R_\oplus}{r_\odot}(1-2\rho\cos\psi)^{-1/2} \\
&\simeq \frac{R_\odot - R_\oplus}{r_\odot}(1+\rho\cos\psi) \\
&\simeq \frac{\rho(R_\odot - R_\oplus)}{r}(1+\rho\cos\psi) \\
&\simeq \frac{\rho(R_\odot - R_\oplus)}{r}.
\end{aligned}$$

As $\tan\alpha$ is small sine and cosine functions of α can be approximated as

$$\sin\alpha \simeq \tan\alpha \simeq \rho\,\frac{R_\odot - R_\oplus}{r} \quad \text{and} \quad \cos\alpha \simeq 1 \tag{3.17}$$

Similarly, one obtains

$$\sin\beta \simeq \tan\beta \simeq \rho\,\frac{R_\odot + R_\oplus}{r} \quad \text{and} \quad \cos\beta \simeq 1. \tag{3.18}$$

Replacing (3.17) and (3.18) values in (3.15) and (3.16), one obtains

$$\cos\psi_2 + \sqrt{1-\frac{R_\oplus^2}{r^2}} + \rho R_\oplus\,\frac{R_\odot - R_\oplus}{r^2} = 0 \tag{3.19}$$

$$\cos\psi_3 + \sqrt{1-\frac{R_\oplus^2}{r^2}} - \rho R_\oplus\,\frac{R_\odot + R_\oplus}{r^2} = 0. \tag{3.20}$$

By (3.19) and (3.20), we get

$$\cos\psi_3 - \cos\psi_2 = 2\rho\,\frac{R_\oplus R_\odot}{r^2}. \tag{3.21}$$

Eventually, a first order Taylor series of $\cos\psi$ centered at ψ_2 and evaluated at ψ_3 shows that

$$\cos\psi_3 - \cos\psi_2 = -\sin\psi_2(\psi_3-\psi_2) + ... = \sin\psi_2\Delta\psi + ... \tag{3.22}$$

Hence, eq. (3.21) and (3.22) yield

$$\Delta\psi := \psi_2 - \psi_3 = 2\rho\frac{R_\odot}{r} + \mathcal{O}(\rho(\psi_3-\psi_2)^2) \tag{3.23}$$

where $\psi_3 - \psi_2$ is small at the shadow entrance.

Then it is worth noting that the link between $\Delta\psi$ and Δt can be expressed as

$$\Delta\psi = \dot{\psi}\Delta t \simeq \frac{2\pi}{\text{day}}\Delta t.$$

Hence,

$$\Delta t \simeq \frac{\Delta\psi}{2\pi}\,\text{day} \simeq \frac{\rho R_\odot}{\pi r}\,\text{day}. \tag{3.24}$$

This approximation is efficient for nearly geosynchronous orbits. If other orbits are considered, the orbital period can be evaluated and Δt can be easily adapted.

The final step consists in showing that the difference between s_u and s_p at the entrance of the cylindrical shadow, denoted by Δh, can be used instead of Δt. At the cylindrical shadow entrance, angle ψ is equal to ψ_1. From (3.12) and (3.13), one obtains

$$s_\text{u}(\psi_1) = r\cos\psi_1 + \cos\alpha\left[\sqrt{r^2 - R_\oplus^2\cos^2\alpha} + R_\oplus\sin\alpha\right]$$

$$s_\text{p}(\psi_1) = r\cos\psi_1 + \cos\beta\left[\sqrt{r^2 - R_\oplus^2\cos^2\beta} - R_\oplus\sin\beta\right].$$

Then, from (3.17) and (3.18), it follows that

$$s_\text{u}(\psi_1) = r\cos\psi_1 + \sqrt{r^2 - R_\oplus^2} + R_\oplus\rho\,\frac{R_\odot - R_\oplus}{r} + \mathcal{O}(\rho^2)$$

$$s_\text{p}(\psi_1) = r\cos\psi_1 + \sqrt{r^2 - R_\oplus^2} - R_\oplus\rho\,\frac{R_\odot + R_\oplus}{r} + \mathcal{O}(\rho^2).$$

Eventually, (3.14) yields

$$s_\text{u}(\psi_1) = R_\oplus\rho\,\frac{R_\odot - R_\oplus}{r} + \mathcal{O}(\rho^2)$$

$$s_\text{p}(\psi_1) = -R_\oplus\rho\,\frac{R_\odot + R_\oplus}{r} + \mathcal{O}(\rho^2).$$

In conclusion, we can write

$$\Delta h = s_\text{u}(\psi_1) - s_\text{p}(\psi_1) \simeq 2\rho R_\oplus\frac{R_\odot}{r}. \tag{3.25}$$

To summarize, we have shown through eq. (3.24) and (3.25) that Δt can be approximated as

$$\Delta t \simeq \frac{\Delta h}{R_\oplus 2\pi}.$$

From a geometrical point of view, our approximation means that the slope of each curve s_u, s_c and s_p is close to -1 at the shadow entrance and to 1 at the shadow exit with our particular choice of units.

The same mathematical developments can be achieved in the case of non-circular space debris orbits. The only difference with the circular case is given by the dependence of r on ψ. Expressing r in terms of Keplerian elements, one has

$$r(\psi) = \frac{a(1-e^2)}{1+e\cos f(\psi)}$$

where f is the true anomaly. Expanding this relation (see e.g. Murray and Dermott 1999) and keeping only terms of first order in eccentricity, r can be finally written as

$$r(\psi) \simeq a(1-e\cos M(\psi)) = a(1-e\cos(\psi+\phi_0))$$

where M is the mean anomaly and ϕ_0 is the appropriate phasing. Following the same scheme as for the circular case, we end up with

$$\Delta t = \frac{\rho R_\odot}{a\pi}(1+e\cos(\psi+\phi_0)) + \mathcal{O}(\rho^2 e + \rho e^2 + \rho^2 e^2) \quad \text{days}$$

and

$$\Delta h = \frac{2\rho R_\oplus R_\odot}{a}(1+e\cos(\psi+\phi_0)) + \mathcal{O}(\rho^2 e + \rho e^2 + \rho^2 e^2).$$

Going back to equation (3.10), the shadow function can now be written as

$$\nu_{\rm p}(\vec{r}) = \frac{1}{2}\left\{1+\tanh\left[\frac{\delta 2\pi R_\oplus}{\Delta h(\vec{r})}s_{\rm c}(\vec{r})\right]\right\} \tag{3.26}$$

Let us remark that, in practice, Δh is computed with actual values of α and β :

$$\begin{aligned}\Delta h(\vec{r}) &= s_{\rm u}(\vec{r}) - s_{\rm p}(\vec{r}) \\ &= \cos\alpha(\vec{r})\left[\sqrt{r^2 - R_\oplus^2\cos^2\alpha(\vec{r})} + R_\oplus\sin\alpha(\vec{r})\right] \\ &\quad -\cos\beta(\vec{r})\left[\sqrt{r^2 - R_\oplus^2\cos^2\beta(\vec{r})} - R_\oplus\sin\beta(\vec{r})\right].\end{aligned}$$

Also note that, with $\alpha=\beta=0$, $\nu_{\rm p}$ is equal to $\nu_{\rm c}$.

3.3 Numerical comparisons

Different numerical comparisons have been performed to assess the accuracy of our shadow crossing models. All propagations were performed with time steps equal to 0.01 day/2π to correctly handle short eclipses.

First, we show in Fig. 3.5 that using the shadow crossing model from Escobal (1976) with our symplectic integrator gives totally wrong results. During the

propagation, the time step is adjusted so as to stop exactly at the shadow entrance, switch off SRP effects inside the shadow, stop again at the shadow exit and switch on SRP for the next steps. More details about this process are given in Appx. C. The comparison is made with respect to ν_c shadow function. The $SBAB_4$ symplectic integrator has been used for both propagations. The error with Escobal (1976) does not depend on the step size (very small steps have been tested) and is certainly due to the great sensitivity of the symplectic scheme to external contributions and variable step size (see Sec. 2.5). Other initial conditions and/or AMR value give totally different error patterns. The loss of accuracy is mainly visible with the semi-major axis evolution. Let us mention that the tendency of the semi-major axis evolution to decrease with ν_c function is not an error and will find an explanation in Chap. 4.

Then, it is interesting to study the shape of the shadow functions on a single shadow crossing. Considering a geostationary orbit, we show the evolution of ν_c, ν_p and ν_M during a typical shadow crossing in Fig. 3.6. Even if the shapes of ν_p and ν_M are different, both share common properties. It can be seen that both shadow functions cross the cylindrical shadow limit at $\nu_c = \nu_p = \nu_M \simeq 0.5$, start to decrease when entering the penumbra cone, are equal to zero in the umbra cone and increase again in the penumbra exit transition.

Short-periodic effects of Earth's cylindrical shadows on the orbital elements of space debris have already been studied in Valk and Lemaitre (2008). For example, the evolution of the semi-major axis and eccentricity for space debris disturbed by SRP and an AMR equal to 5 m^2/kg is described in Valk and Lemaitre (2008) (Fig. 3). The same simulation has been performed in Fig. 3.7 with our conical shadow model. At first sight, one could not detect any significant discrepancies between the semi-major axis and eccentricity evolutions. We obtain the typical increase and decrease of the semi-major axis and eccentricty occuring twice a year and corresponding to both shadow seasons that happen each year at this altitude. The inclination also increases according to the analysis performed in Valk and Lemaitre (2008). The weird behaviour of the other orbital elements is explained by the near zero initial eccentricity and inclination causing undetermined longitude of the ascending node and argument of pericenter before 0.5 yr. Anyway we wanted to use the same initial conditions as in Valk and Lemaitre (2008) to compare the same orbits.

However, this naive interpretation proves wrong and both shadow models lead to significantly different debris trajectories. To support that claim, we compare one propagation obtained with $SBAB_4$ and ν_p to a *reference* orbit where cylindrical shadows are modelled. Yet one has to choose which integrator and model should be used to get a reference orbit. To that aim, we resorted to the shadow model from Escobal (1976). We use the on/off switching technique detailed in Appx. C which seems to be the most realistic way of modelling cylindrical shadow

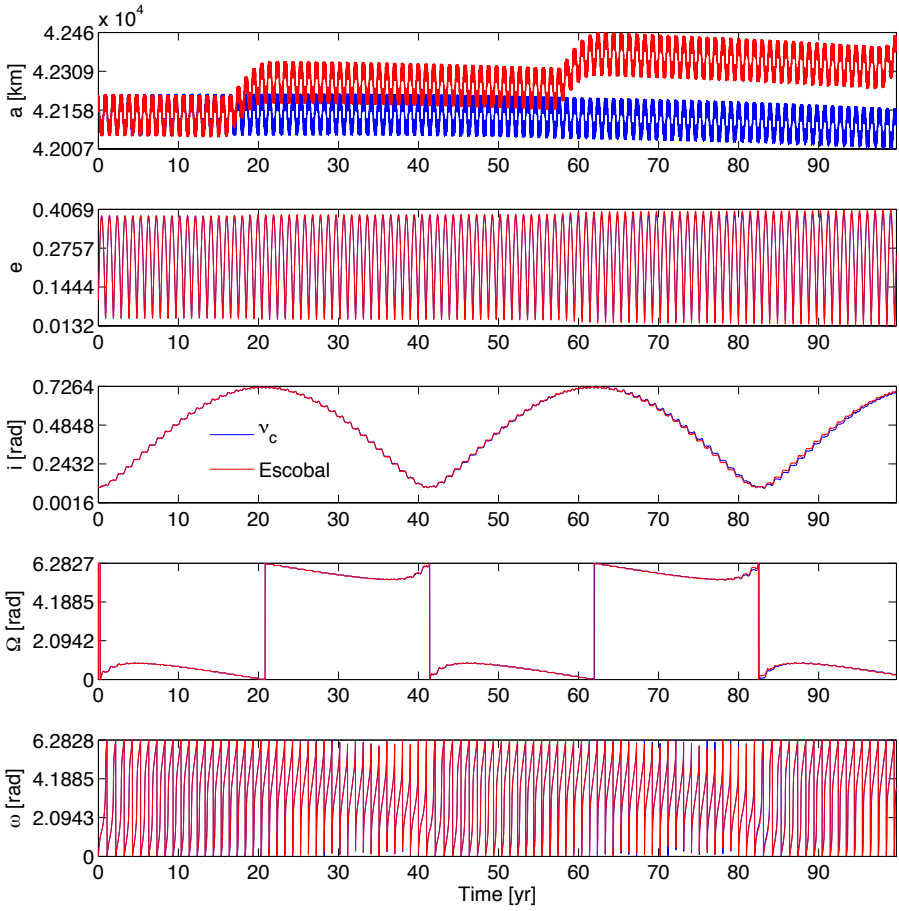

Figure 3.5 • *Evolution of Keplerian elements of space debris orbit subject to the Earth's central attraction and SRP with ν_c shadow function (in blue) and the method from Escobal (1976) (in red). The initial semi-major axis is set at* 42164 *km, the other elements are set equal to zero and the AMR is equal to* 20 m^2/kg. *Each numerical integration has been performed with $SBAB_4$ and time steps equal to* 0.01 $day/2\pi$.

crossings. Still, one should keep in mind that even this method is already an approximation. Indeed, at each time step, entrance and exit anomalies are computed and the step size is adjusted. However, perturbations are responsible for trajectory modifications during the time step. Hence, a small shift exists between the entrance or exit anomaly computed the step before and the actual one. The simple fourth-order non symplectic Runge-Kutta (RK_4) integrator (see Hairer et al. 1993) has been chosen. As the comparison will be performed on a single shadow season, the RK_4 is certainly accurate enough. Moreover, fixed steps are used, as

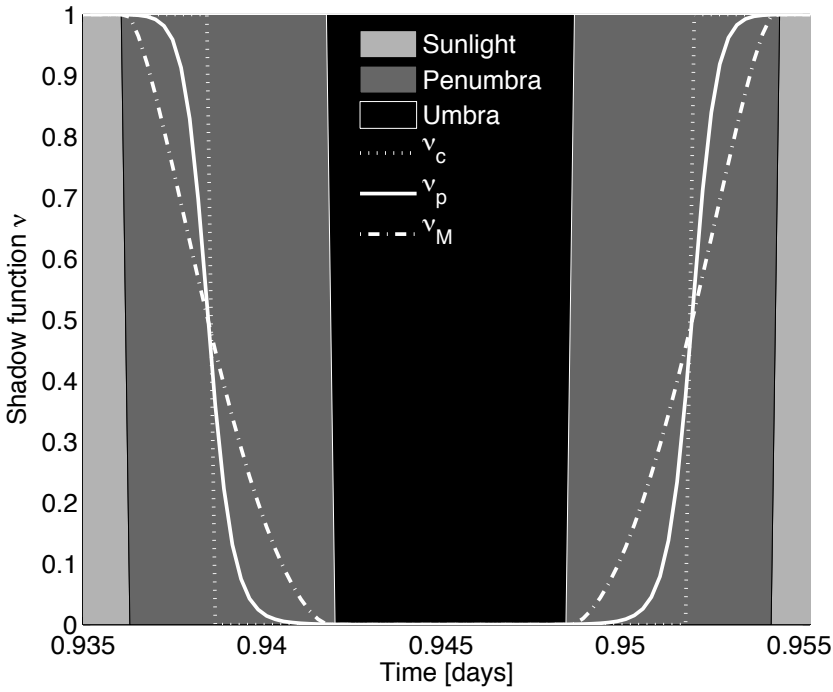

Figure 3.6 • *Typical shadow crossing on a geostationary orbit. Three shadow crossing models are compared as a function of time.*

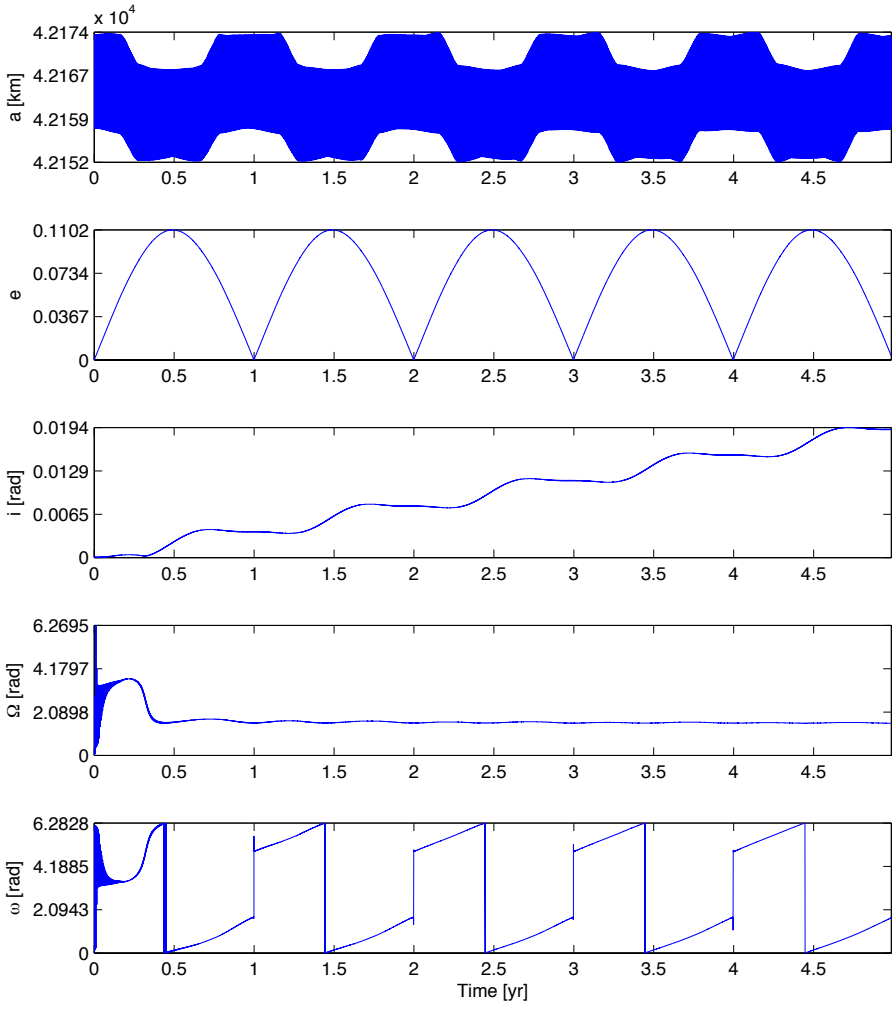

Figure 3.7 • *Evolution of Keplerian elements of space debris orbit subject to the Earth's central attraction and SRP. The initial semi-major axis is set at* 42164 *km, the other elements are set equal to zero and the AMR is equal to* 5 m^2/kg. *The shadow function* ν_p *is used to model the Earth's shadowing effects. The results are in agreement with what is proposed in Fig. 3 in Valk and Lemaitre (2008).*

for our symplectic propagator. As clearly shown in Fig. 3.8, the absolute difference between orbital elements obtained with both models is zero before the first shadow season and starts to increase after this period of time. A shadow season appears each time that the Sun moves through the orbital plane of motion, leading to a succession of shadow crossings. More information about such phenomena can be found in Valk and Lemaitre (2008).

After 15 years, the difference between both trajectories keeps on increasing and reaches high values, especially for the semi-major axis. This is illustrated in Fig. 3.9 (blue curve) where the model from Escobal (1976) has been replaced by the ν_{c} shadow function. In light of this, it turns out that cylindrical shadow models are not reliable approximations (at least on such short term propagation) of conical Earth's shadows, especially in the case of space debris with high AMR and situated at high altitudes, the higher the orbit, the larger the time spent in the penumbra transition. In Fig. 3.9, the results obtained with both shadow functions ν_{p} and ν_{M} are represented by the red curve. Given that ν_{M} cannot be used with our symplectic scheme, it has been included in NIMASTEP in order to perform the comparison between both methods. Differences between Keplerian elements in this case are clearly smaller than in the previous comparison involving ν_{c} and ν_{p} (Fig. 3.9, blue curve). Moreover, this difference between both conical shadow models does not increase linearly with time. Debris trajectories obtained with our symplectic integrator coupled to our smooth shadow function seem consistent with the ones computed by NIMASTEP (ABM_{10}) using ν_{M}.

Another test has been performed, proving that the symplecticity of our scheme does not lead to a loss of accuracy with the shadow function ν_{p}. The comparison in Fig. 3.10 shows that no significant difference appears between the orbits obtained with SBAB_4 and fixed step-size RK_4 integrators with the ν_{p} shadow function.

Eventually, a last remark is given about the energy conservation in the case of cylindrical and conical shadow models. The comments about the quasi-symplecticity are, of course, the same for the SRP than for the third body contributions. Hence, we are still limited in the computation of the relative variation of the energy. However, it is shown in Fig 3.11 that the relative error in energy does not increase with time, even on an extremely long time span (5000 yr). Let us remark that the computed energy takes into account the contribution of the SRP with permanent sunlight. Indeed, the part of the Hamiltonian function corresponding to the SRP cannot be retrieved from the equations of motion $\nu_{\mathrm{c,p}}(\vec{r})\,\vec{\nabla}_{\vec{r}}\mathcal{H}_{\mathrm{srp}}(\vec{r},\theta)$, the latter being impossible to integrate analytically. One must still keep in mind that the slope of the hyperbolic tangent in our cylindrical and conical shadow models increases the integrator error during a shadow crossing. Indeed it depends on Poisson brackets of A and B and thus it involves $\vec{\nabla}\nu_{c,p}$. A close look to the relative error in energy shows small perturbations during each shadow season but it does not result in a long term drift on the energy.

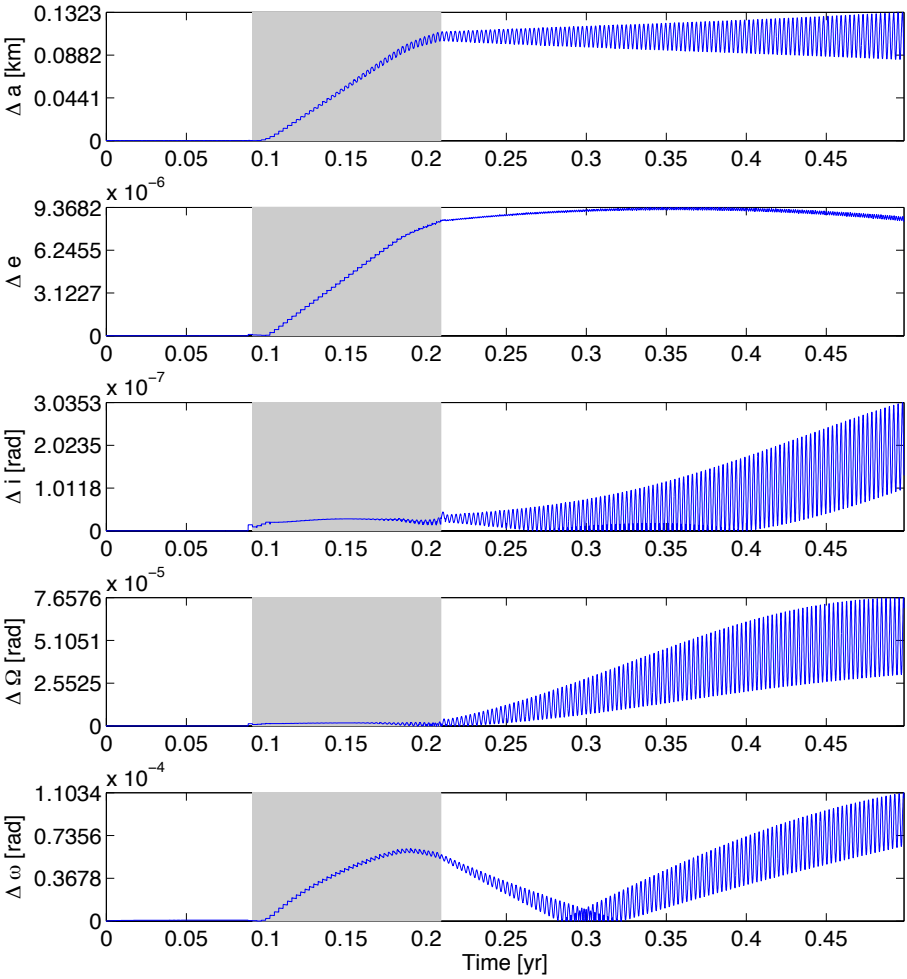

Figure 3.8 • *Absolute difference between the orbital elements of space debris subject to the Earth's central attraction and SRP with ν_c shadow function and the model from Escobal (1976). The initial semi-major axes are* 42164 *km, the other elements are set equal to zero and the AMR is equal to* 20 m^2/kg. *This figure emphasizes the beginning of the difference between both orbits during the first shadow season represented by the gray zone.*

3.4 Conclusion

We have built an innovative method to model both cylindrical and conical Earth's shadow crossings by means of smooth shadow functions. We have explained why

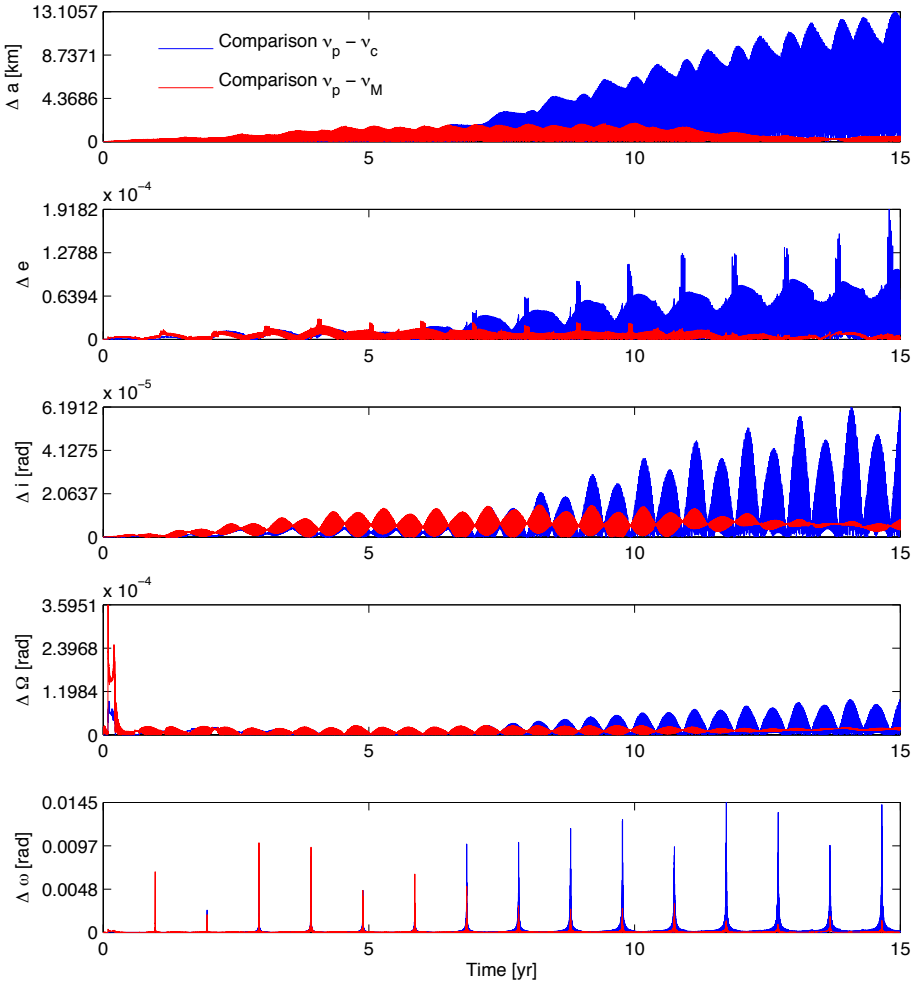

Figure 3.9 • *Absolute difference between the orbital elements of space debris subject to the Earth's central attraction and SRP with respectively ν_p and ν_c shadow functions (in blue) and ν_p and ν_M functions (in red). The orbit with ν_M has been computed by* NIMASTEP *(ABM10). The initial semi-major axes are* 42164 *km, the other elements are set equal to zero and the AMR is equal to* 20 m^2/kg. *Each numerical integration has been performed with time steps equal to* 150 *s.*

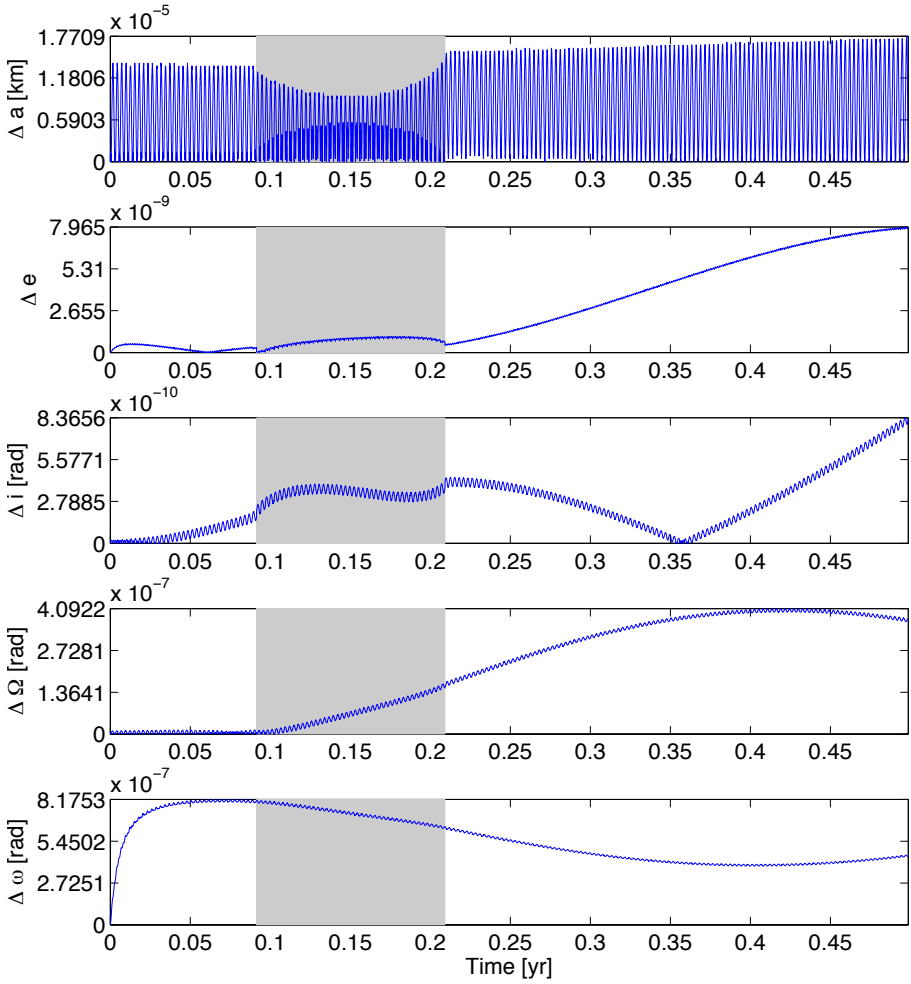

Figure 3.10 • *Absolute difference between the orbital elements of space debris subject to the Earth's central attraction and SRP with ν_p shadow function and $SBAB_4$ and RK_4 integrators. The initial semi-major axes are* 42164 *km, the other elements are set equal to zero and the AMR is equal to* 20 m^2/kg. *This figure emphasizes the beginning of the difference between both orbits after the first shadow season represented by the gray zone.*

these ones were particulary convenient in the framework of symplectic integration. It has been shown that the cylindrical model was not a suitable approximation of conical shadows, especially in the case of space debris associated to high AMR. Our formulation is consistent with the one from Montenbruck and Gill (2005), does not break the energy preservation property of the symplectic scheme but is not restricted to a symplectic scheme.

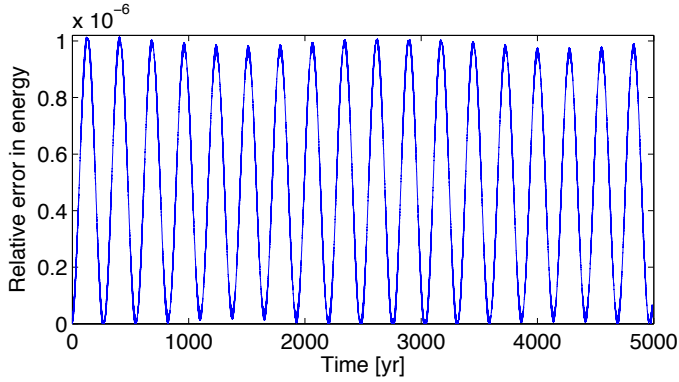

Figure 3.11 • *Evolution of the relative error in energy of space debris motion subject to SRP. The initial semi-major axis is set at* 42164 *km, the other elements are set equal to zero and the AMR is equal to* 0.1 m^2/kg. *The shadow function* ν_p *is used to model the Earth's shadowing effects.*

Another advantage of our shadow functions is that their derivatives are also smooth and easily computed. Hence, it makes possible stability studies explicitely requiring these derivatives to compute directly the solutions of the so-called variational equations. Full details about this topic are provided in Chap. 5.

It has been noticed that the computation of the shadow functions during the integration process requires reduced step sizes. Even if it can be considered as a limitation, one has to keep in mind that the order of the integrator can be reduced as well to speed up the propagations.

Chapter 4
Long term evolution

Contents

As explained in Chap. 1, the influence of the SRP on the trajectory of high AMR space debris is a well known topic. However, existing studies have always been performed on time spans of the order of 100 yr which is usually suitable as far as space debris lifetime is concerned. For example, Anselmo and Pardini (2005) described the evolution of geostationary space debris on a maximum period of 54 yr. Similarly, the SRP was identified as the possible cause of the highly eccentric objects observed in the geostationary belt in Liou and Weaver (2005). In this case numerical simulations were performed on time spans shorter than 30 yr. Other analytical and numerical approaches were developed on *long-term* time ranges smaller than 150 yr (Chao 2006, Valk 2008, Lemaitre et al. 2009, Rosengren and Scheeres 2012, Deleflie and et al. 2013).

Earth's shadows have also been investigated, still on relatively short periods of time. Indeed, shadow functions or perturbation theories have been used in studies limited to 1 yr (Kozai 1961, Aksnes 1976) or 40 yr (Valk and Lemaitre 2008). A very detailed analytical model including shadow functions can also be found in McMahon and Scheeres (2010). The radiation force is expressed as Fourier series with respect to the mean anomaly and takes into account the object attitude (assuming that its motion repeats each orbit). While analytical results are produced, no variation of the orbital elements is explicitely given on long time spans.

This chapter aims to describe the evolution of space debris orbits due to Earth's shadow crossing on longer time scales. Preliminary tests of the ν_{p} shadow function revealed unexpected periodic motion with periods of time of the order of 1000 yr. First, we believed that our approach was wrong and produced numerical errors (see the semi-major axis evolution in Fig. 3.5). Persuaded that this method should not fail, we started (semi-)analytical investigations that finally explain this phenomenon. To the best of our knowledge, such behaviour has never been addressed in the literature. Here we present both numerical and analytical results that help understand how Earth's shadow crossings disturb the long term evolution of space debris orbits. To that purpose, only the Earth's gravitational attraction as a single mass point and SRP are considered. The resulting simplified model lets us highlight a new frequency which is responsible for this periodic motion. This frequency must be seen as a new theoretical contribution to more complete models including other important perturbations such as the gravitational attraction of the Sun and Moon, the geopotential or the Poynting-Robertson effect.

First, we give an overview of the perturbation acting on orbital elements on long time scales in Sec. 4.1. Sec. 4.2 is devoted to the presentation of analytical and semi-analytical schemes that let us point out the significant parameters and angles associated to this long term periodic motion. To that end, we start from the work of Valk (2008) where shadows were not considered and extend this analytical model with a first order pertubation theory (see Sec. 4.2.1). Then, we

include Earth's shadows in the model and compare the numerical simulations to the new semi-analytical method in Sec. 4.2.2. We conclude in Sec. 4.3

4.1 Long term numerical propagation

Some insight is given about the behaviour of high AMR space debris on long time scales by showing the evolution of debris orbital elements up to 25000 yr without Earth's shadows. The $SABA_4$ is used to produce Fig. 4.1. The Earth's attraction as a single mass point and SRP as only perturbation are considered. On such a long time scale, no secular periodic motion is visible for any Keplerian element. Both eccentricity and inclination periods are in perfect agreement with what was determined in Valk (2008).

When including Earth's shadows, the semi-major axis, eccentricity and inclination are characterized by a new secular periodic motion that clearly depends on the value of the AMR. The semi-major axis of space debris with the AMR equal to 5 m^2/kg and 20 m^2/kg present an oscillatory motion whose amplitudes are respectively equal to 57.98 km and 309.58 km and with a period about respectively 13000 yr and 1200 yr. The eccentricity and inclination are also affected by Earth's shadows to a smaller extent. It should be noted that, even if these propagations are performed over 25000 yr, the large amplitudes observed in Fig. 4.2 induce an important drift from the geostationary altitude after several hundred years, the greater the AMR. Fig. 4.3 highlights the important discrepancies between semi-major axis evolutions obtained with and without shadows for an AMR equal to 5 m^2/kg.

The dependence of the amplitude and period of the semi-major axis evolution on the AMR value has then been studied further, still from a numerical point of view. For each initial value of the semi-major axis and AMR, a discrete Fourier transform has been applied on the semi-major axis to compute the associated period. The amplitude has also been stored. As illustrated in Fig. 4.4, the dependence on the initial semi-major axis (chosen around the geostationary one) is less obvious than the influence of the AMR. On the one hand, the amplitude increases linearly with respect to the AMR. On the other hand, the period increases as the AMR decreases, being asymptotically infinite when the AMR is zero.

These orbits have been checked with the reliable propagator ABM_{10}. Even if the computations could not be performed as long as with the $SABA_4$ integrator, the first years of the time interval showed similar orbital element evolutions. Another confirmation is brought by the semi-analytical method described in Sec. 4.2.

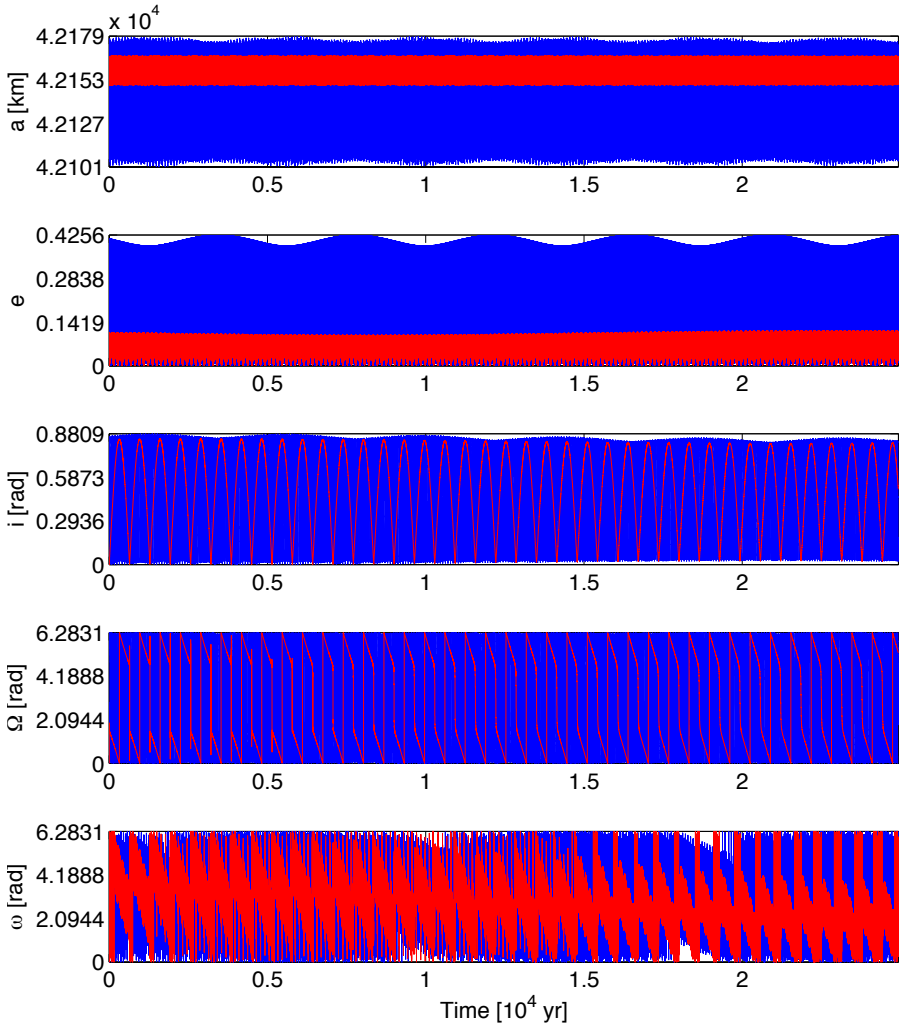

Figure 4.1 • *Space debris orbital evolution initially positioned at the geostationary altitude. Initial conditions are* $a = 42164.140$ *km,* $e = 0$*,* $i = \Omega = \omega = M = 0$ *rad, the initial time epoch is* 25 *January* 1991 *and the AMR are set to* 5 *(in red) and* 20 *(in blue)* m^2/kg*. The* $SABA_4$ *integrator has been used with time steps equal to* 1 $day/2\pi$*. The model includes the gravitational attraction of the Earth as a mass point and the SRP without Earth's shadows.*

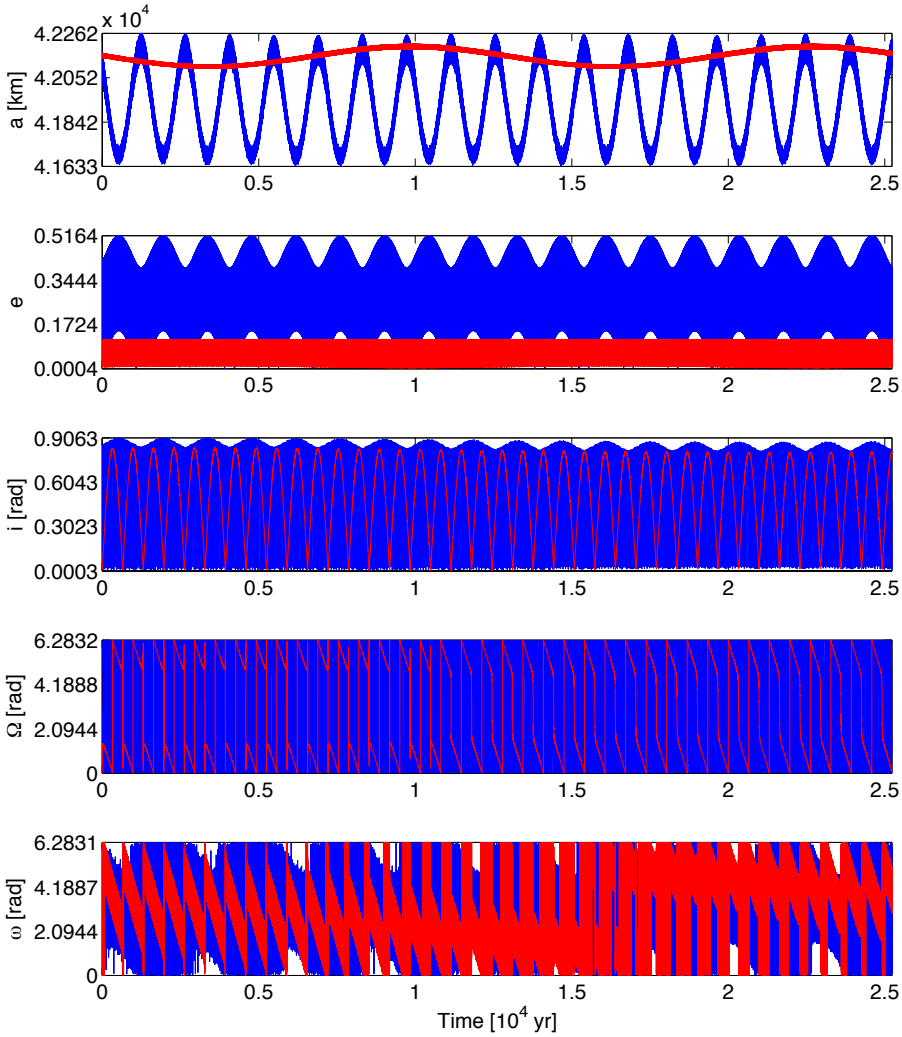

Figure 4.2 • *Space debris orbital evolution initially positioned at the geostationary altitude. Initial conditions are* $a = 42164.140$ *km,* $e = 0$*,* $i = \Omega = \omega = M = 0$ *rad, the initial time epoch is* 25 *January* 1991 *and the AMR are set to* 5 *(in red) and* 20 *(in blue)* m^2/kg*. The* $SABA_4$ *integrator has been used with time steps equal to* 0.01 *day*$/2\pi$*. The model includes the gravitational attraction of the Earth as a mass point and the SRP with Earth's shadows.*

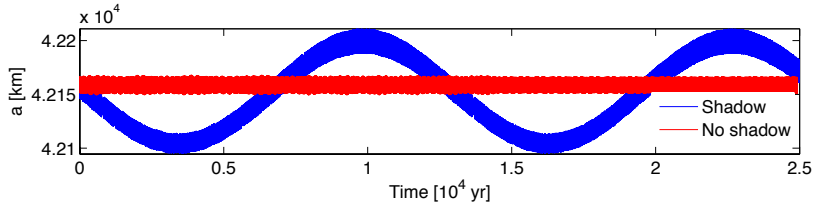

Figure 4.3 • *Space debris semi-major axis evolution. Initial conditions and propagator are the same as in Fig. 4.2. The AMR is equal to 5 m^2/kg. The model includes the gravitational attraction of the Earth as a mass point and the SRP with (in blue) and without (in red) Earth's shadows.*

4.2 Averaged orbit

In this section, we confirm the previous results by means of a semi-analytical approach. To that purpose, we will mainly average the Hamiltonian with respect to the fast mean anomaly angle. Its period (about 1 sidereal day) is very small compared to the targeted time span. We will also average the same Hamiltonian with respect to the Sun's mean longitude whose period is close to 1 year. It can still be considered as a fast angle in this context.

First, let us assume the Sun's orbit to be circular (i.e. $r_\odot = a_\odot$). Then, consider the Delaunay's variables which let us build a set of canonical action-angles variables defined as

$$\begin{array}{lll} l = M & g = \omega & h = \Omega \\ L = \sqrt{\mu a} & G = L\sqrt{1-e^2} & H = G\cos i. \end{array} \tag{4.1}$$

Then, the Hamiltonian, reduced to

$$\begin{aligned} \mathcal{H}_{\text{debris}}(\vec{v},\vec{r}) &= \mathcal{H}_{\text{kepl}}(\vec{v},\vec{r}) + \mathcal{H}_{\text{srp}}(\vec{r}) \\ &= \frac{\| \vec{v} \|^2}{2} - \frac{\mu}{r} - C_r \frac{1}{\|\vec{r}-\vec{r}_\odot\|} P_r \frac{\mathbb{A}}{\mathbb{M}} a_\odot^2, \end{aligned} \tag{4.2}$$

is replaced by

$$\mathcal{H}_{\text{debris}} = -\frac{\mu^2}{2L^2} + \begin{cases} C_r P_r \frac{\mathbb{A}}{\mathbb{M}} \frac{1}{a_\odot} r\, r_\odot \cos(\psi) & \text{outside Earth's shadows} \\ 0 & \text{inside Earth's shadows} \end{cases}, \tag{4.3}$$

ψ being the angle between $\vec{r}$ and $\vec{r}_\odot$. The first part $-\mu^2/(2L^2)$ accounts for the Keplerian part of the dynamics and only depends on L. Indeed, only the mean anomaly l will evolve, each angle g and h and momenta L, G and H remaining constant. It is consistent with the description of the two-body problem given in Sec. 2.3.2. It also reveals the link between the energy and the semi-major axis

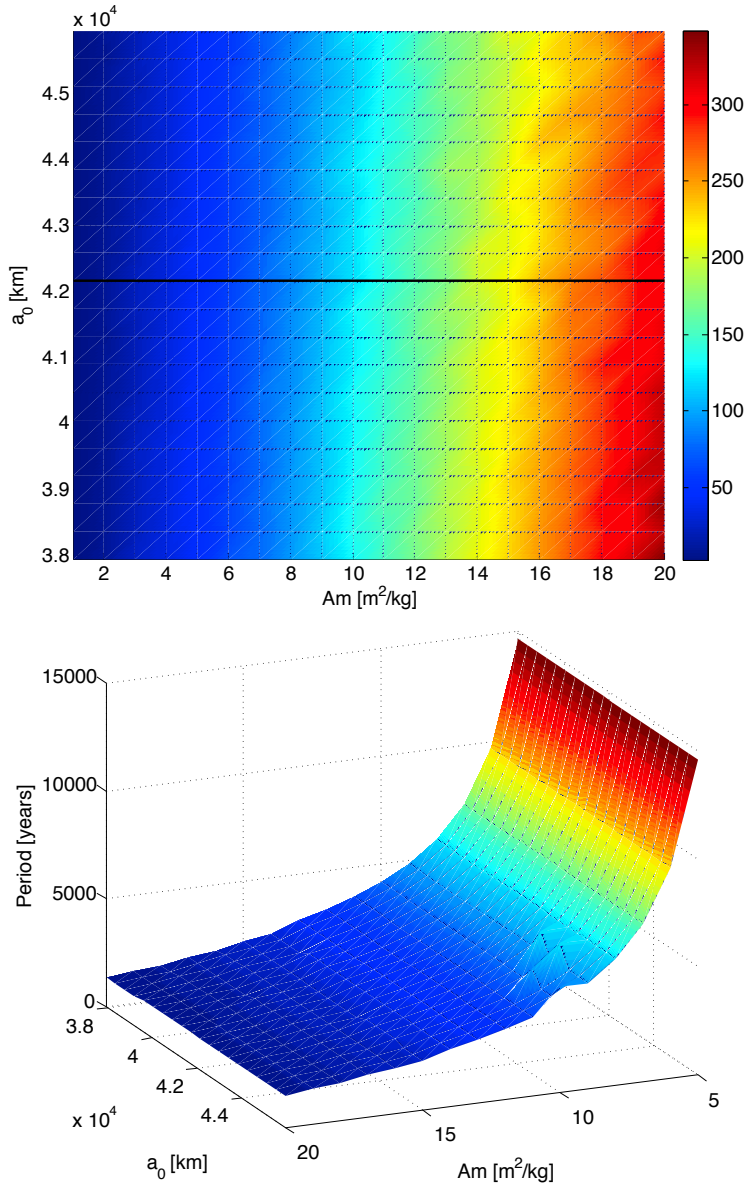

Figure 4.4 • *Evolution of the amplitude in km (top) and period (bottom) of the semi-major axis of space debris orbits with respect to initial semi-major axis and AMR. Other initial conditions are* $e = 0$, $i = \Omega = \omega = M = 0$ *rad and the initial time epoch is* 25 *January* 1991. *The* $SABA_4$ *integrator has been used with time steps equal to* 0.01 *day*$/2\pi$ *on* 30000 *yr. The model includes the gravitational attraction of the Earth as a mass point and the SRP with Earth's shadows. The black line (top) represents the nominal geostationary altitude.*

(through L) for this simple dynamics. The other part of eq (4.3) is a first order approximation of the rest of the Hamiltonian.

The dot product $r\, r_\odot \cos(\psi)$ in eq. (4.3) is then developed as

$$r\, r_\odot \cos(\psi) = a\, a_\odot \sum_{i=1}^{3} \overline{r}_i\, \overline{r}_{\odot,i}$$

where normalized debris and Sun's Cartesian coordinates are denoted respectively by $\overline{r}_1, \overline{r}_2, \overline{r}_3$ and $\overline{r}_{\odot,1}, \overline{r}_{\odot,2}, \overline{r}_{\odot,3}$. Hence, we end up with the following Hamiltonian

$$\mathcal{H}_{\text{debris}} = -\frac{\mu}{2a} + \begin{cases} C_r P_r \frac{\mathbb{A}}{\mathbb{M}} a(u\xi + v\eta) & \text{outside Earth's shadows} \\ 0 & \text{inside Earth's shadows} \end{cases}. \tag{4.4}$$

The functions u and v both depend on space debris eccentricity and eccentric anomaly E and are defined as

$$u = \cos E - e \quad \text{and} \quad v = \sin E \sqrt{1 - e^2}. \tag{4.5}$$

The variables ξ and η are computed as

$$\xi = \xi_1 \overline{r}_{\odot,1} + \xi_2 \overline{r}_{\odot,2} + \xi_3 \overline{r}_{\odot,3} \tag{4.6}$$

$$\eta = \eta_1 \overline{r}_{\odot,1} + \eta_2 \overline{r}_{\odot,2} + \eta_3 \overline{r}_{\odot,3} \tag{4.7}$$

with

$$\begin{aligned} \xi_1 &= \cos\Omega\cos\omega - \sin\Omega\cos i\sin\omega & \eta_1 &= -\cos\Omega\sin\omega - \sin\Omega\cos i\cos\omega \\ \xi_2 &= \sin\Omega\cos\omega + \cos\Omega\cos i\sin\omega & \eta_2 &= -\sin\Omega\sin\omega + \cos\Omega\cos i\cos\omega \\ \xi_3 &= \sin i\sin\omega & \eta_3 &= \sin i\cos\omega \end{aligned}$$

Following the same idea as in Aksnes (1976), the Hamiltonian function can now be averaged with respect to the mean anomaly, removing the contribution of the SRP when space debris cross any Earth's umbra. To that purpose, shadows entry and exit eccentric anomalies (respectively E_1 and E_2) are first computed as

in Sec. 3.1.1. It yields

$$\begin{aligned}
\overline{\mathcal{H}}_{\text{debris}} &= \frac{1}{2\pi}\int_0^{2\pi} \mathcal{H}_{\text{debris}}\, dM \\
&= -\frac{\mu}{2\overline{a}} + \frac{1}{2\pi} C_r P_r \frac{\mathbb{A}}{\mathfrak{m}} \overline{a} \times \\
&\quad \left[\int_0^{E_1} (u\xi + v\eta)(1 - e\cos E)\, dE + \int_{E_2}^{2\pi} (u\xi + v\eta)(1 - e\cos E)\, dE\right] \\
&= -\frac{\mu}{2\overline{a}} - \frac{3}{2} C_r P_r \frac{\mathbb{A}}{\mathfrak{m}} \overline{a}\, \overline{e}\xi + \frac{1}{2\pi} C_r P_r \frac{\mathbb{A}}{\mathfrak{m}} \overline{a} \times \\
&\quad \left[\xi\left(-2(1+\overline{e}^2)\cos\frac{S}{2}\sin\frac{D}{2} + \frac{3}{2}\overline{e}\, D + \frac{\overline{e}}{2}\cos S \sin D\right)\right. \\
&\quad \left. +\eta\sqrt{1-\overline{e}^2}\left(-2\,\sin\frac{S}{2}\sin\frac{D}{2} + \frac{\overline{e}}{2}\sin S\sin D\right)\right] \qquad (4.8)
\end{aligned}$$

with $S = E_1 + E_2$ and $D = E_2 - E_1$. It is worth noting that the first two terms of equation (4.8) correspond to the Keplerian problem and SRP perturbation, the rest accounting for shadow crossing perturbations. In the following, we will develop further this Hamiltonian formulation in two different situations. First, we will consider the case where space debris never cross Earth's shadows. Then, we will add the Earth's shadows in the averaged orbit.

4.2.1 Without Earth's shadows

Let us first recall the results of the classical problem, without shadowing effects, which corresponds to the case $E_1 = E_2$ in the Hamiltonian (4.8).

The analysis of this first part of the Hamiltonian was published in Valk (2008) and an analytical solution was provided, reproducing the main characteristics of the motion. We show here that it can be pushed further. Let us mention that we could also have used a different analytical approach published in Scheeres (2012).

The initial Hamiltonian has been averaged over the short periodic mean anomaly. Consequently the mean semi-major axis is constant as well as $L = \sqrt{\mu a}$. Only the mean inclination, eccentricity, argument of the pericenter and longitude of the node are involved in the averaged dynamics.

Following Valk (2008), we introduce canonical variables for the averaged motion in eccentricity and inclination, based on Delaunay's momenta (L, G and H),

and their corresponding Poincaré's Cartesian formulation x_1, y_1 and x_2, y_2.

$$\begin{array}{lcllcl} p & = & -\varpi = -\omega - \Omega & P & = & L - G \\ q & = & -\Omega & Q & = & G - H \\ x_1 & = & \sqrt{2P}\,\sin p & y_1 & = & \sqrt{2P}\,\cos p \\ x_2 & = & \sqrt{2Q}\,\sin q & y_2 & = & \sqrt{2Q}\,\cos q \end{array}$$

Angles p, q and momenta P, Q are introduced to avoid singularity problems with null eccentricities and inclinations. These variables behaving like polar coordinates, Poincaré's coordinates gather them in Cartesian-like canonical variables. Moreover, Poincaré's coordinates can be easily interpreted. Indeed, P is proportional to the square of the eccentricity e, and Q to the square of $\sin\frac{i}{2}$. At first order we can simply replace $e \simeq \sqrt{\frac{2P}{L}}$, $\cos^2\frac{i}{2} = 1 - \frac{Q}{2L}$ and $\sin\frac{i}{2} \simeq \sqrt{\frac{Q}{2L}}$.

A simplified circular motion is assumed for the Sun, only depending on its mean longitude $\lambda_\odot = n_\odot\, t + \lambda_{\odot,0}$ and on the Earth's obliquity ϵ, with $n_\odot = 2\pi/\text{year}$:

$$\left\{\begin{array}{lcl} \bar{r}_{\odot,1} & = & \cos\lambda_\odot \\ \bar{r}_{\odot,2} & = & \sin\lambda_\odot \cos\epsilon \\ \bar{r}_{\odot,3} & = & \sin\lambda_\odot \sin\epsilon. \end{array}\right.$$

We introduce five functions of x_2 and y_2 :

$$\begin{array}{lcl} R_1(x_2,y_2) & = & 1 - \dfrac{x_2^2}{2L} \\ R_2(x_2,y_2) & = & \dfrac{x_2 y_2}{2L} \\ R_3(x_2,y_2) & = & 1 - \dfrac{y_2^2}{2L} \\ R_4(x_2,y_2) & = & \dfrac{x_2}{\sqrt{L}} \\ R_5(x_2,y_2) & = & \dfrac{y_2}{\sqrt{L}} \end{array} \tag{4.9}$$

and a constant κ, defined by

$$n_\odot\,\kappa = \frac{3}{2}\,C_r P_r\,\frac{\mathbb{A}}{\mathbb{M}}\,\frac{a}{\sqrt{L}}.$$

The Hamiltonian $\overline{\mathcal{H}}_{\text{debris}}$ with this new set of variables writes

$$\begin{array}{rcl} \overline{\mathcal{H}}_{\text{debris}}(x_1,y_1,x_2,y_2,\lambda_\odot) & \simeq & -n_\odot\,\kappa\,\Big(\bar{r}_{\odot,1}\,(x_1\,R_2 + y_1\,R_1) - \bar{r}_{\odot,2}\,(x_1\,R_3 + y_1\,R_2) \\ & & -\bar{r}_{\odot,3}\,(x_1\,R_5 - y_1\,R_4)\Big) \end{array} \tag{4.10}$$

and the corresponding dynamical system is given by

$$\begin{array}{rclcrcl} \dot{x}_1 &=& \dfrac{\partial \overline{\mathcal{H}}_{\rm debris}}{\partial y_1} & & \dot{y}_1 &=& -\dfrac{\partial \overline{\mathcal{H}}_{\rm debris}}{\partial x_1} \\ \dot{x}_2 &=& \dfrac{\partial \overline{\mathcal{H}}_{\rm debris}}{\partial y_2} & & \dot{y}_2 &=& -\dfrac{\partial \overline{\mathcal{H}}_{\rm debris}}{\partial x_2}. \end{array} \tag{4.11}$$

By setting $x_2 = 0 = y_2$ in the equations, we easily deduce a short periodic motion in eccentricity solution of

$$\left\{ \begin{array}{rcl} \dot{x}_1 &=& -n_\odot \kappa\, \bar{r}_{\odot,1} \\ \dot{y}_1 &=& -n_\odot \kappa\, \bar{r}_{\odot,2} \end{array} \right.$$

and explicitly given by

$$\left\{ \begin{array}{rcccl} x_1 &=& -\kappa\, \sin\lambda_\odot + C_x &=& -\kappa\, (\sin\lambda_\odot - D_x) \\ y_1 &=& \kappa \cos\lambda_\odot \cos\epsilon + C_y &=& \kappa\, (\cos\lambda_\odot \cos\epsilon + D_y). \end{array} \right. \tag{4.12}$$

The constants D_x and D_y are determined by the initial conditions. The period of 1 yr associated to this motion in eccentricity is due to the angle $\lambda_\odot$. A detailed description of this motion is given in Valk (2008).

This solution is substituted in the dynamical equations of $\dot{x}_2$ and $\dot{y}_2$, which we now average over the angle $\lambda_\odot$. The doubly averaged dynamics is then given by

$$\left\{ \begin{array}{rcl} \dot{x}_2 &=& \rho_c\, y_2 - \rho_s \\ \dot{y}_2 &=& -\rho_c\, x_2 \end{array} \right.$$

where $\rho_c = n_\odot\, \kappa^2 \cos\epsilon \frac{1}{2L}$ and $\rho_s = n_\odot\, \kappa^2 \sin\epsilon \frac{1}{2\sqrt{L}}$. The solution of this linear system is immediate, denoted by $\bar{x}_2$ and $\bar{y}_2$

$$\left\{ \begin{array}{rcl} \bar{x}_2 &=& \mathcal{E} \sin\varphi \\ \bar{y}_2 &=& \mathcal{E} \cos\varphi + \dfrac{\rho_s}{\rho_c} = \mathcal{E} \cos\varphi + \tan\epsilon \sqrt{L} \end{array} \right. \tag{4.13}$$

with $\varphi = \rho_c\, t + \varphi_0$, the constants φ_0 and $\mathcal{E}$ being determined by the initial conditions. Again Valk (2008) contains more information about this particular motion.

Let us now go one step further. The averaging over $\lambda_\odot$ can be represented as a Lie transform associated to a first order generator, $\mathcal{W}$, which can be explicitly calculated. The method used below (only at first order) has been described in Deprit (1969), Henrard (1970) and a practical guide has been presented in Dufey (2010) (PhD thesis available online[1]).

[1]Thesis available on `http://dial.academielouvain.be/vital/access/services/Download/boreal:32801/PDF_01`

We rewrite the averaged Hamiltonian (4.10), in which the solutions of x_1 and x_1 have been substituted, as a summation of two terms: a periodic part in $\lambda_\odot$, called $\overline{\mathcal{H}}_1$, and a term independent of $\lambda_\odot$, called $\overline{\mathcal{H}}_0$, in which we have added an artificial momentum, $\Lambda_\odot$, conjugated to the fast angle $\lambda_\odot$

$$\begin{aligned}\overline{\mathcal{H}}_{\text{debris}}(\Lambda_\odot, y_2, \lambda_\odot, x_2) &= \overline{\mathcal{H}}_0(\Lambda_\odot, y_2, -, x_2) + \overline{\mathcal{H}}_1(\Lambda_\odot, y_2, \lambda_\odot, x_2) \\ &= n_\odot \Lambda_\odot - n_\odot \kappa^2 (f_0(x_2, y_2) + f_1(x_2, y_2, \lambda_\odot)).\end{aligned}$$

The functions f_0 and f_1 are given by

$$\begin{aligned}f_0(x_2, y_2) &= \frac{1}{2}\,(R_1 \cos\epsilon + R_3 \cos\epsilon + R_5 \sin\epsilon), \\ f_1(x_2, y_2, \lambda_\odot) &= g_1\ \cos\lambda_\odot + g_2\ \sin\lambda_\odot + g_3\ \cos 2\lambda_\odot + g_4\ \sin 2\lambda_\odot\end{aligned}$$

in which the functions g_1, g_2, g_3 and g_4 are functions of x_2 and y_2 :

$$\begin{aligned}g_1(x_2, y_2) &= D_y\ R_1 + D_x\ R_2 \\ g_2(x_2, y_2) &= -D_x\ \cos\epsilon\ R_3 - D_y\ \cos\epsilon\ R_2 - D_x\ \sin\epsilon\ R_5 + D_y\ \sin\epsilon\ R_4 \\ g_3(x_2, y_2) &= \frac{1}{2}\ \cos\epsilon\ R_1 - \frac{1}{2}\ \cos\epsilon\ R_3 - \frac{1}{2}\ \sin\epsilon\ R_5 \\ g_4(x_2, y_2) &= -\frac{1}{2}\ R_2 - \frac{1}{2}\ \cos^2\epsilon\ R_2 + \frac{1}{2}\ \sin\epsilon\ \cos\epsilon\ R_4\end{aligned}$$

where the functions $R_j(x_2, y_2)$ with $j = 1, \ldots, 4$, are given by (4.9).

The generator $\mathcal{W}$ of the canonical averaging transformation is defined by the first-order homological equation:

$$\overline{\overline{\mathcal{H}}}_1 = \overline{\mathcal{H}}_1 + \{\overline{\mathcal{H}}_0, \mathcal{W}\} = \overline{\mathcal{H}}_1 - \frac{\partial \overline{\mathcal{H}}_0}{\partial \Lambda_\odot}\ \frac{\partial \mathcal{W}}{\partial \lambda_\odot} \tag{4.14}$$

where $\{\overline{\mathcal{H}}_0, \mathcal{W}\}$ denotes the Poisson Bracket of $\overline{\mathcal{H}}_0$ and $\mathcal{W}$ (already defined in Sec. 2.1.1) and $\overline{\overline{\mathcal{H}}}_1$ stands for the double average of $\mathcal{H}_1$ with respect to the mean anomaly and Sun's mean longitude. In eq. (4.14), only $\mathcal{W}$ is unknown. From this equation, one obtains

$$\frac{\partial \mathcal{W}}{\partial \lambda_\odot} = -\kappa^2\ f_1(x_2, y_2, \lambda_\odot)$$

and the solution writes

$$\mathcal{W} = -\kappa^2 (g_1\ \sin\lambda_\odot - g_2\ \cos\lambda_\odot + \frac{1}{2}\ g_3\ \sin 2\lambda_\odot - \frac{1}{2}\ g_4\ \cos 2\lambda_\odot).$$

The partial derivatives of g_i, for $i = 1, \cdots, 4$, with respect to x_2 and y_2 are computed through very simple analytical formulae. The variables x_2 and y_2 can

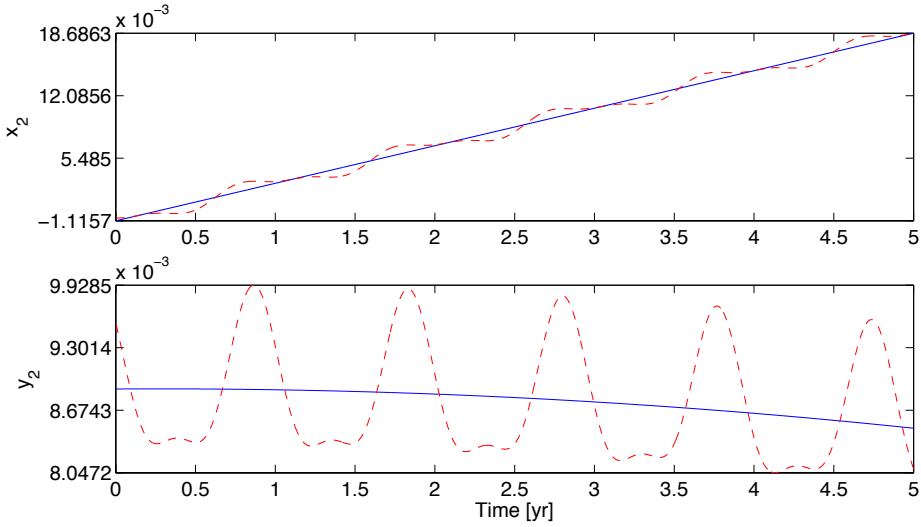

Figure 4.5 • *Comparison between the averaged evolution of (4.13) (blue plain curve) and the first order solution given by (4.15) (red dashed curve) over* 5 *yr. Initial conditions are* $a = 42164.140$ *km,* $e = 0$, $i = \Omega = \omega = M = 0$ *rad, the initial time epoch is* 25 *January* 1991 *and the AMR is set to* 5 m^2/kg.

be expressed as functions of their averaged values $\bar{x}_2$ and $\bar{y}_2$ and of the short periodic terms in $\lambda_\odot$ through the generator by the equations

$$\begin{cases} x_2 &= \bar{x}_2 + \dfrac{\partial \mathcal{W}}{\partial y_2} \\ y_2 &= \bar{y}_2 - \dfrac{\partial \mathcal{W}}{\partial x_2}. \end{cases} \tag{4.15}$$

In Fig. (4.5) we compare the averaged evolution of (4.13) with the first order solution given by (4.15) on a period of 5 yr. The short periodic motion in $\lambda_\odot$ is clearly visible around the averaged solution. Obviously, higher order perturbations would lead to a better approximation.

Then we compare in Fig. 4.6 the numerical solution of the complete model (4.2) with the averaged orbital elements retrieved from the evolution of x_1, y_1 (4.12) and $\bar{x}_2$, $\bar{y}_2$ (4.13). The Hamiltonian model is integrated with the SABA_4 symplectic integrator. The agreement is excellent between the complete model and the simple averaged analytical motion. In the same figure, the orbital elements computed from the evolution of x_1, y_1 (4.12) and the first order solution (4.15) are also plotted. The gain obtained with the introduction of the short periodic motion is obvious and leads to a more accurate analytical orbit.

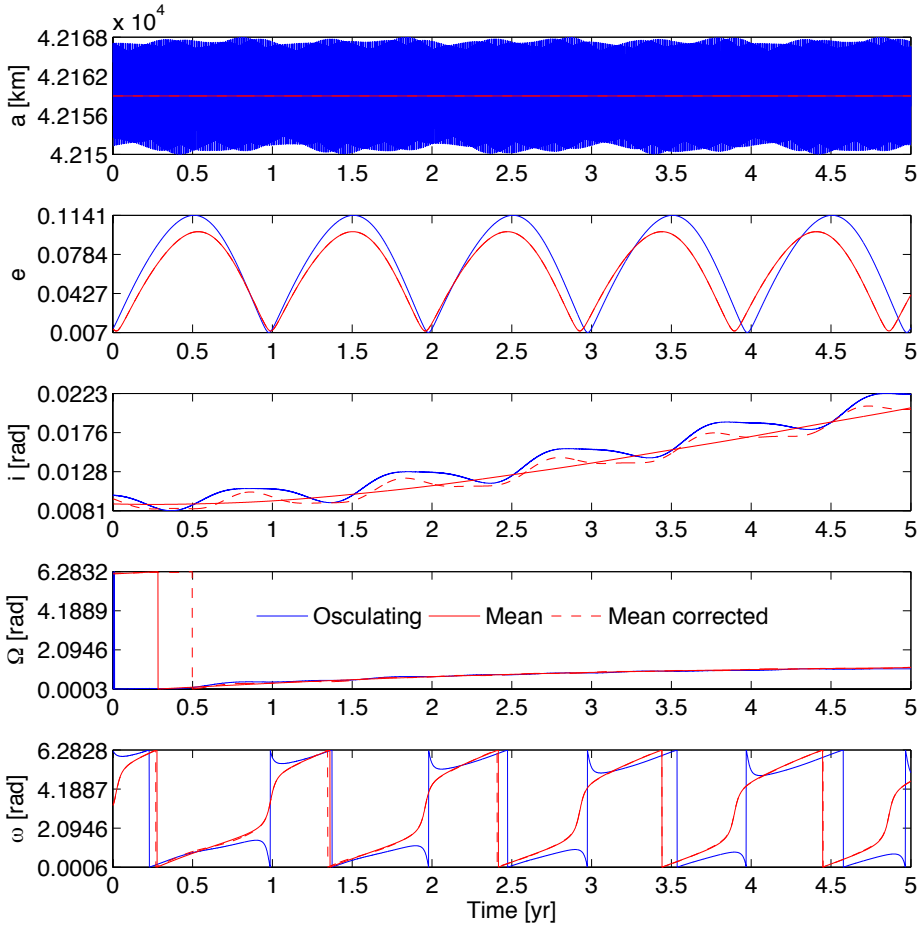

Figure 4.6 • *Comparison between the numerical solution of the complete Hamiltonian model (4.2) (blue plain curve), (4.12) and (4.13) (red plain curve) and (4.12) and (4.15) (red dashed line). Initial conditions are* $a = 42164.140$ *km,* $e = 0$, $i = \Omega = \omega = M = 0$ *rad, the initial time epoch is* 25 *January* 1991 *and the AMR is set to* 5 m^2/kg. *The* $SABA_4$ *integrator has been used with time steps equal to* 0.01 *day*$/2\pi$ *for the Hamiltonian model.*

4.2.2 With Earth's shadows

Due to the complexity of the Hamiltonian (4.8) when $E_1 \neq E_2$, the successive steps used in Sec. 4.2.1 will not be followed in this section. We will instead compute averaged Delaunay's variables G and H, Ω and ω time evolutions. One can either compute their time derivatives from $\overline{\mathcal{H}}_{\text{debris}}$ (4.8)

$$\begin{aligned} \dot{\overline{G}} &= -\frac{\partial \overline{\mathcal{H}}_{\text{debris}}}{\partial \overline{\omega}} \qquad \dot{\overline{\omega}} = \frac{\partial \overline{\mathcal{H}}_{\text{debris}}}{\partial \overline{G}} \\ \dot{\overline{H}} &= -\frac{\partial \overline{\mathcal{H}}_{\text{debris}}}{\partial \overline{\Omega}} \qquad \dot{\overline{\Omega}} = \frac{\partial \overline{\mathcal{H}}_{\text{debris}}}{\partial \overline{H}} \end{aligned} \tag{4.16}$$

or compute their time derivatives from $\mathcal{H}_{\text{debris}}$ (4.4)

$$\begin{aligned} \dot{G} &= -\frac{\partial \mathcal{H}_{\text{debris}}}{\partial \omega} \qquad \dot{\omega} = \frac{\partial \mathcal{H}_{\text{debris}}}{\partial G} \\ \dot{H} &= -\frac{\partial \mathcal{H}_{\text{debris}}}{\partial \Omega} \qquad \dot{\Omega} = \frac{\partial \mathcal{H}_{\text{debris}}}{\partial H} \end{aligned}$$

and then apply the averaging process. Both ways yield the same analytical expressions at first order. Obviously, the evolution of the averaged L variable can only be retrieved with the second method:

$$\begin{aligned} \dot{\overline{L}} &= \overline{\frac{\partial \mathcal{H}_{\text{debris}}}{\partial M}} = \frac{1}{2\pi}\int_0^{2\pi} \frac{\partial \mathcal{H}_{\text{debris}}}{\partial M}\, dM \\ &= \frac{1}{2\pi}\left[\int_0^{E_1} \frac{\partial \mathcal{H}_{\text{debris}}}{\partial M}(1 - e\cos E)\, dE + \int_{E_2}^{2\pi} \frac{\partial \mathcal{H}_{\text{debris}}}{\partial M}(1 - e\cos E)\, dE\right] \\ &= \frac{1}{\pi} C_r P_r \frac{\mathbb{A}}{\mathbb{M}} \overline{a}\left[\xi \sin\frac{S}{2} - \eta\sqrt{1-e^2}\cos\frac{S}{2}\right]\sin\frac{D}{2}. \end{aligned}$$

From the last relation, one easily obtains the evolution of the mean semi-major axis as

$$\dot{\overline{a}} = \overline{a}^{3/2}\frac{2}{\mu}\frac{\sqrt{\mu}}{\pi} C_r P_r \frac{\mathbb{A}}{\mathbb{M}}\left[\xi \sin\frac{S}{2} - \eta\sqrt{1-e^2}\cos\frac{S}{2}\right]\sin\frac{D}{2}. \tag{4.17}$$

Eq. (4.17) suggests that the difference between entrance and exit angles plays a significant role in the evolution of the mean semi-major axis. It is confirmed in Fig. 4.7 where both periods of semi-major axis and difference between cylindrical shadow exit and entrance mean longitudes are indeed close to each other. In Fig. 4.8, we report the evolution of the mean semi-major axis with the AMR equal to 5 m^2/kg. The differential equation (4.17) is integrated with the simple RK_4 integrator and tiny time steps (10^{-4} day$/2\pi$). The agreement between the osculating and mean semi-major axis is excellent and confirms the long term behaviour identified through the numerical integration.

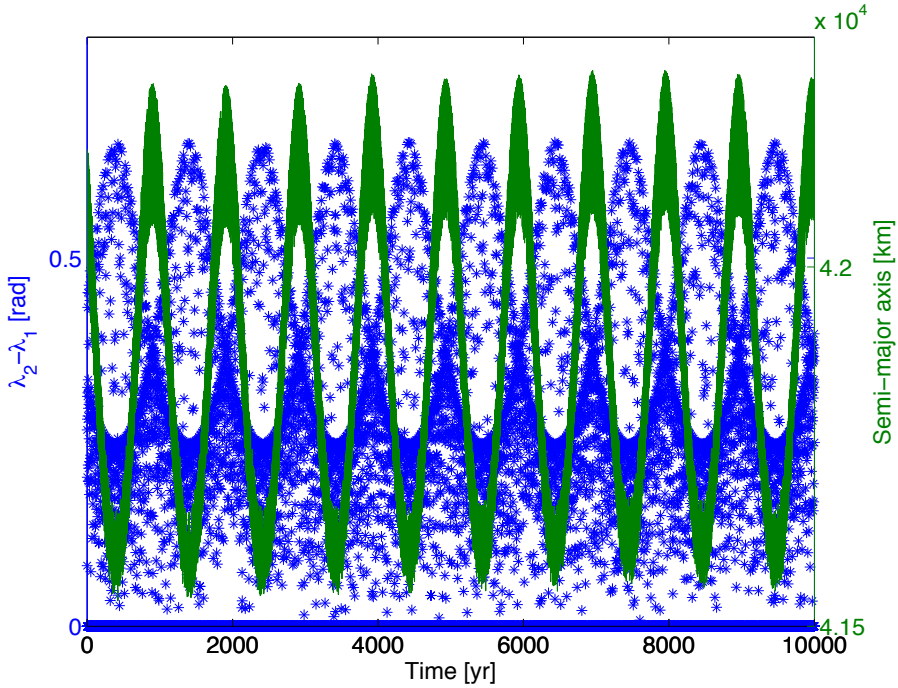

Figure 4.7 • *Comparison between the evolution of the semi-major axis and difference between shadow exit and entrance mean longitudes. Initial conditions are* $a = 42164.140$ *km,* $e = 0$, $i = \Omega = \omega = M = 0$ *rad, the initial time epoch is* 25 *January* 1991 *and the AMR is* 25 m^2/kg. *The* $SABA_4$ *integrator has been used with time steps equal to* 0.01 *day*$/2\pi$. *The model includes the gravitational attraction of the Earth as a mass point and the SRP with cylindrical Earth's shadows.*

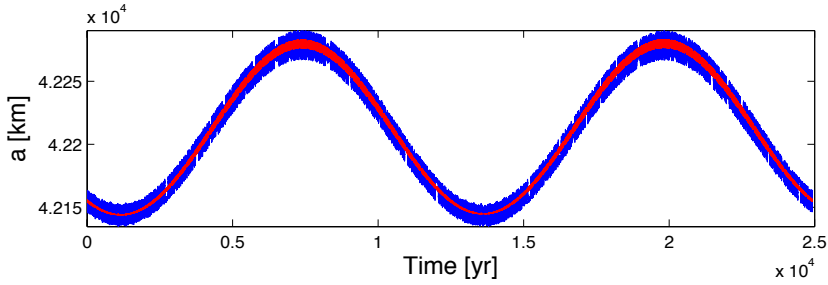

Figure 4.8 • *Semi-major axis evolutions obtained with the* $SABA_4$ *integrator (in blue) and the semi-analytical scheme (in red). Initial conditions are* $a = 42164.140$ *km,* $e = 0$, $i = \Omega = \omega = M = 0$ *rad and the AMR is* 5 m^2/kg. *Time steps are equal to* 10^{-4} *day*$/2\pi$. *The model includes the gravitational attraction of the Earth as a mass point and the SRP with cylindrical Earth's shadows.*

Using the same method, one directly obtains

$$\begin{aligned}
\frac{\partial \overline{\mathcal{H}}_{\text{debris}}}{\partial \overline{\omega}} &= \overline{\frac{\partial \mathcal{H}_{\text{debris}}}{\partial \omega}} \\
&= C_r P_r \frac{\mathbb{A}}{\mathbb{M}} \overline{a} \times \\
&\quad \sum_{j=1}^{3} \overline{r}_{\odot,j} \Big[-(\xi_{j,1} u + \eta_{j,1} v) \sin \overline{\omega} + (\xi_{j,2} u + \eta_{j,2} v) \cos \overline{\omega} \Big] \quad (4.18) \\
\frac{\partial \overline{\mathcal{H}}_{\text{debris}}}{\partial \overline{\Omega}} &= \overline{\frac{\partial \mathcal{H}_{\text{debris}}}{\partial \Omega}} \\
&= C_r P_r \frac{\mathbb{A}}{\mathbb{M}} \overline{a} \times \\
&\quad \sum_{j=1}^{3} \overline{r}_{\odot,j} \Big[-(\xi_{j,3} u + \eta_{j,3} v) \sin \overline{\Omega} + (\xi_{j,4} u + \eta_{j,4} v) \cos \overline{\Omega} \Big] \quad (4.19) \\
\frac{\partial \overline{\mathcal{H}}_{\text{debris}}}{\partial \overline{i}} &= \overline{\frac{\partial \mathcal{H}_{\text{debris}}}{\partial i}} \\
&= C_r P_r \frac{\mathbb{A}}{\mathbb{M}} \overline{a} \times \\
&\quad \sum_{j=1}^{3} \overline{r}_{\odot,j} \Big[-(\xi_{j,5} u + \eta_{j,5} v) \sin \overline{i} + (\xi_{j,6} u + \eta_{j,6} v) \cos \overline{i} \Big] \quad (4.20)
\end{aligned}$$

where

$$\begin{array}{lllllllll}
\xi_{1,1} &=& \cos \overline{\Omega} & \xi_{2,1} &=& \sin \overline{\Omega} & \xi_{3,1} &=& 0 \\
\xi_{1,2} &=& -\sin \overline{\Omega} \cos \overline{i} & \xi_{2,2} &=& \cos \overline{\Omega} \cos \overline{i} & \xi_{3,2} &=& \sin \overline{i} \\
\xi_{1,3} &=& \cos \overline{\omega} & \xi_{2,3} &=& \sin \overline{\omega} \cos \overline{i} & \xi_{3,3} &=& 0 \\
\xi_{1,4} &=& -\sin \overline{\omega} \cos \overline{i} & \xi_{2,4} &=& \cos \overline{\omega} & \xi_{3,4} &=& 0 \\
\xi_{1,5} &=& -\sin \overline{\Omega} \sin \overline{\omega} & \xi_{2,5} &=& \cos \overline{\Omega} \sin \overline{\omega} & \xi_{3,5} &=& 0 \\
\xi_{1,6} &=& 0 & \xi_{2,6} &=& 0 & \xi_{3,6} &=& \sin \overline{\omega}
\end{array}$$

and

$$\begin{array}{lllllllll}
\eta_{1,1} &=& -\sin \overline{\Omega} \cos \overline{i} & \eta_{2,1} &=& \cos \overline{\Omega} \cos \overline{i} & \eta_{3,1} &=& \sin i \\
\eta_{1,2} &=& -\cos \overline{\Omega} & \eta_{2,2} &=& -\sin \overline{\Omega} & \eta_{3,2} &=& 0 \\
\eta_{1,3} &=& -\sin \overline{\omega} & \eta_{2,3} &=& \cos \overline{\omega} \cos \overline{i} & \eta_{3,3} &=& 0 \\
\eta_{1,4} &=& -\cos \overline{\omega} \cos \overline{i} & \eta_{2,4} &=& -\sin \overline{\omega} & \eta_{3,4} &=& 0 \\
\eta_{1,5} &=& -\sin \overline{\Omega} \cos \overline{\omega} & \eta_{2,5} &=& \cos \overline{\Omega} \cos \overline{\omega} & \eta_{3,5} &=& 0 \\
\eta_{1,6} &=& 0 & \eta_{2,6} &=& 0 & \eta_{3,6} &=& \cos \overline{\omega}.
\end{array}$$

Let us remark that $\partial \overline{\mathcal{H}}_{\text{debris}} / \partial \overline{H}$ is provided by $\partial \overline{\mathcal{H}}_{\text{debris}} / \partial \overline{i}$ as

$$\frac{\partial \overline{\mathcal{H}}_{\text{debris}}}{\partial \overline{H}} = -\frac{\partial \overline{\mathcal{H}}_{\text{debris}}}{\partial \overline{i}} \frac{1}{\sqrt{\mu \overline{a} (1 - \overline{e}^2)} \sin \overline{i}}.$$

The computation of $\partial\overline{\mathcal{H}}_{\rm debris}/\partial\overline{G}$ turns out trickier. Choosing the first method (4.16), it gives

$$\begin{aligned}\frac{\partial\overline{\mathcal{H}}_{\rm debris}}{\partial\overline{G}} &= \frac{1}{2\pi}C_rP_r\frac{\mathbb{A}}{\mathbb{M}}\overline{a}\left[\frac{\partial\xi}{\partial\overline{G}}I+\frac{\partial\eta}{\partial\overline{G}}J+\xi\frac{\partial I}{\partial\overline{G}}+\eta\frac{\partial J}{\partial\overline{G}}\right]\\ &= \frac{1}{2\pi}C_rP_r\frac{\mathbb{A}}{\mathbb{M}}\overline{a}\left[\frac{\partial\xi}{\partial\overline{i}}\frac{\partial i}{\partial\overline{G}}I+\frac{\partial\eta}{\partial\overline{i}}\frac{\partial i}{\partial\overline{G}}J+\xi\frac{\partial I}{\partial\overline{e}}\frac{\partial\overline{e}}{\partial\overline{G}}+\eta\frac{\partial J}{\partial\overline{e}}\frac{\partial\overline{e}}{\partial\overline{G}}\right.\\ &\quad\left.+\xi\frac{\partial I}{\partial E_1}\frac{\partial E_1}{\partial\overline{G}}+\xi\frac{\partial I}{\partial E_2}\frac{\partial E_2}{\partial\overline{G}}+\eta\frac{\partial J}{\partial E_1}\frac{\partial E_1}{\partial\overline{G}}+\eta\frac{\partial J}{\partial E_2}\frac{\partial E_2}{\partial\overline{G}}\right] \quad (4.21)\end{aligned}$$

where

$$\begin{aligned}I &= -(1+\overline{e}^2)(\sin E_2-\sin E_1)-\frac{3}{2}\overline{e}\,(E_1-E_2)\\ &\quad -\frac{3}{2}\overline{e}\,2\,\pi+\frac{\overline{e}}{4}(\sin 2E_2-\sin 2E_1)\\ J &= \sqrt{1-\overline{e}^2}\left(\frac{\overline{e}}{4}(\cos 2E_1-\cos 2E_2)-(\cos E_1-\cos E_2)\right).\end{aligned}$$

The derivatives in (4.21) are easily obtained, at the exception of $\partial E_i/\partial\overline{G}$ which must be computed from relation (3.7). Indeed, $s_{\rm c}(\vec{r})$ is equal to zero when E_1 or E_2 are zero. Using u, v defined in eq. (4.5) and ξ, η described in (4.6) and (4.7), this condition can be written as

$$(u_i\xi+v_i\eta)+\sqrt{(1-e\cos E_i)^2-\frac{R_\oplus^2}{a^2}}=0 \quad (4.22)$$

where u_i and v_i are previous u and v functions with $E=E_i$, $i=1,2$. The partial derivative of (4.22) with respect to $\overline{G}$ is then given by

$$\begin{aligned}&\frac{\partial u_i}{\partial\overline{G}}\xi+\frac{\partial v_i}{\partial\overline{G}}\eta+u_i\frac{\partial\xi}{\partial\overline{G}}+v_i\frac{\partial\eta}{\partial\overline{G}}+\\ &\left((1-e\cos E_i)^2-\frac{R_\oplus^2}{a^2}\right)^{-1/2}(1-e\cos E_i)\left(-\frac{\partial\overline{e}}{\partial\overline{G}}\cos E_i+\overline{e}\frac{\partial E_i}{\partial\overline{G}}\sin E_i\right)=0,\end{aligned}$$

eventually yielding the following formulae for the derivatives of E_i

$$\begin{aligned}&\frac{\partial E_i}{\partial\overline{G}}\\ &= \left[-u_i\frac{\partial\xi}{\partial\overline{G}}-v_i\frac{\partial\eta}{\partial\overline{G}}+\frac{\partial\overline{e}}{\partial\overline{G}}\left(\xi+\eta\frac{\overline{e}}{\sqrt{1-\overline{e}^2}}\sin E_i+\frac{1-\overline{e}\cos E_i}{\sqrt{(1-\overline{e}\cos E_i)^2-R_\oplus^2/\overline{a}^2}}\cos E_i\right)\right]\\ &\quad\Big/\left[-\xi\sin E_i+\eta\sqrt{1-\overline{e}^2}\cos E_i+\frac{\overline{e}\sin E_i(1-\overline{e}\cos E_i)}{\sqrt{(1-\overline{e}\cos E_i)^2-R_\oplus^2/\overline{a}^2}}\right].\end{aligned}$$

To summarize, averaged elements can be computed by means of relations (4.17) and (4.16) coupled with (4.18)-(4.21). The comparison between the averaged and osculating elements is shown in Fig. 4.9. Even if some small descrepancies are noticible, both elements are in good agreement. Unfortunately, the eccentricity evolution is difficult to understand on a shorter time scale. For the sake of clarity, an enlargement of its evolution on a time span of 50 yr (arbitrarily chosen between 350 and 400 yr) is shown in Fig. 4.10. Clearly, the periodic motion is perfectly identified by the semi-analytical propagation. The simplified model and limited developments in eccentricity are responsible for the less accurate eccentricity amplitude and inclination and ascending node periods.

The semi-analytical model makes use of the canonical Delaunay's variables and classical orbital elements. Hence one should keep in mind that zero eccentricities and inclinations can cause undefined ascending node and argument of perigee values. To tackle this problem, one could use non-singular elements like the equinoctial ones used in Valk (2008) and presented in eq. (3.3). Unfortunately, analytical formulae become dramatically trickier with this set of elements. Obviously, this averaged model should not replace the numerical integration of the actual equations of motion. Anyway, it nicely confirms the precedent observations obtained with the numerical symplectic integration.

4.3 Conclusion

Numerical propagations performed with the symplectic integrator have been used to show that debris orbital elements (mainly the semi-major axis, eccentricity and inclination) are disturbed in a periodic way when only the SRP and Earth's shadow crossing perturbations are taken into account. The amplitude and frequency of this oscillatory motion clearly depend on the space debris AMR.

The study has been supported by an analytical study and a semi-analytical model. The latter has revealed that the period of the semi-major axis and eccentricity evolution is strongly bound to the period of the difference between the shadow exit and entrance anomalies. The agreement between the numerical simulations and the semi-analytical model is excellent and proves that the long-term orbit variations are not due to numerical errors in the symplectic scheme.

Even if the period of the semi-major axis and eccentricity seems very long for relatively small AMR, the amplitude shows that an important deviation from the initial trajectory is discernible on short time scales. However, one has to keep in mind that this long term influence appears when only the presence of the Sun is assumed. Other perturbations as the oblateness of the Earth and third body gravitational attractions obviously play a role and compete with the one that

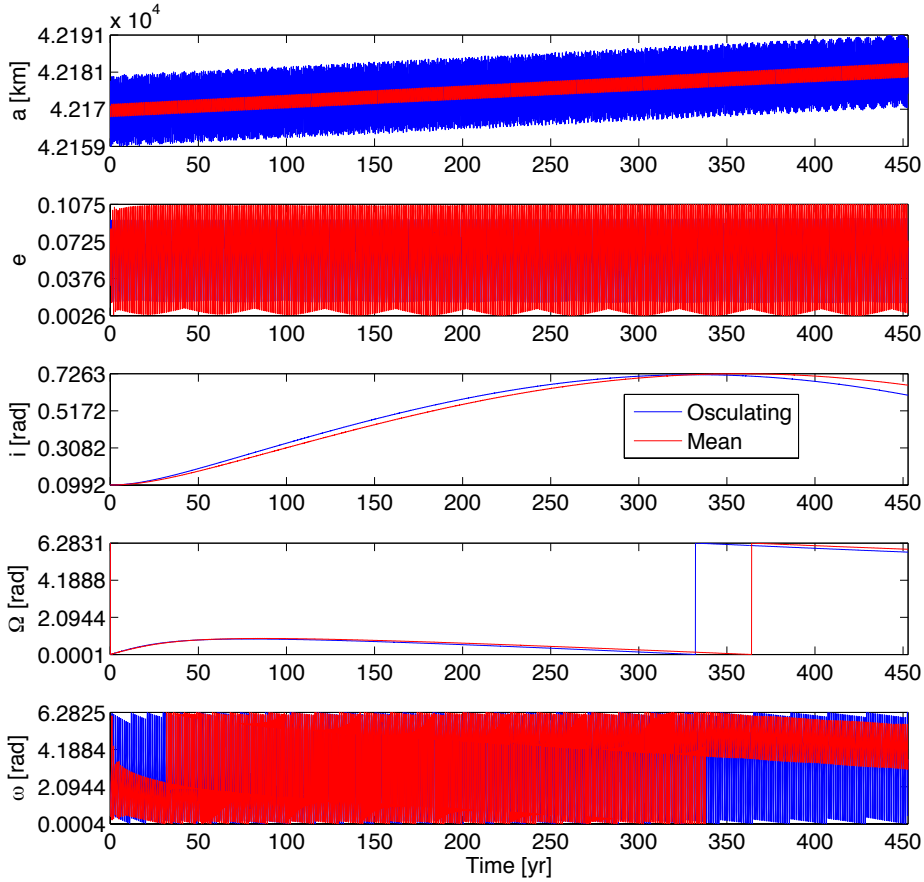

Figure 4.9 • *Comparison between the numerically and semi-analytically propagated orbits. Initial conditions are* $a = 42164.140$ *km,* $e = 0.01$, $i = 0.08$ *rad,* $\Omega = \omega = M = 0$ *rad, the initial time epoch is* 25 *January* 1991 *and the AMR is* 5 m^2/kg. *The* $SABA_4$ *integrator and fourth order Runge-Kutta integrator have been used with time steps equal to* 0.001 *day*$/2\pi$ *to obtain respectively the osculating and mean elements. The model includes the gravitational attraction of the Earth as a mass point and the SRP with Earth's shadows.*

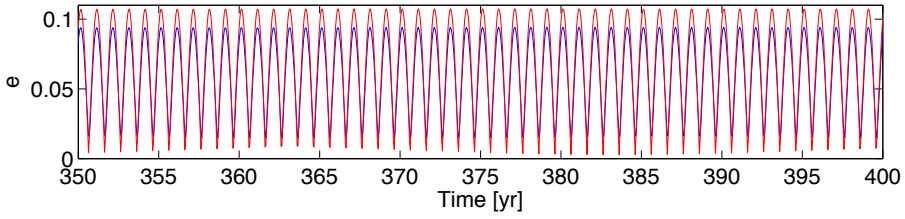

Figure 4.10 • *Enlargement of the eccentricity evolution in Fig. 4.9.*

has been described, strongly perturbing the periodic behaviour discussed in this chapter. Still, the larger the AMR, the higher the importance of the SRP and Earth's shadows perturbations.

This theory would be complete if the angle $D = E_2 - E_1$ could be analytically expressed in terms of orbital elements and not included in the formulae in an implicit way. Unfortunately, an explicit formulation could not be achieved. The difficulty comes from the polynomial Σ (3.6) which prevents us from finding explicit solutions. Several approaches and approximations have been made to handle this issue, without success. On the other hand, the hyperbolic tangent appearing in the shadow function (3.8) is really efficient from the numerical point of view but one can hardly expect simple analytical results from it.

It should be noted that secular variations of the semi-major axis can also originate from the asymmetry of solar light scattered by debris surface, as shown in Mikisha and Smirnov (1997) and Smirnov et al. (2001) with simulations of the evolution of geosynchronous satellites over 500 yr. Similarly, numerical propagations performed in Kuznetsov (2011) over 240 yr showed that the Poynting-Robertson effect could also be responsible for secular variations of the semi-major axis, depending on the AMR and motion of geosynchronous satellites (libration or circulation) in the $1 : 1$ gravitational resonance with the Earth. Lower order resonances were studied in Kuznetsov et al. (2012).

Chapter 5
Stability study

Contents

Understanding the behaviour of space debris orbits is a matter of great importance. Our contribution about the stability of high AMR debris motion is presented in this chapter. Different meanings are usually associated to the term *stability*. For example, one could consider an orbit as stable if its semi-major axis remained bounded throughout the entire propagation time span. In our case, unstable orbits correspond to *unpredictable* orbits, i.e. orbits which are very sensitive to initial conditions. In other words, two orbits starting infinitesimally close to each other would give completely different orbital behaviours. In the following, both terms unstable and chaotic will indifferently be used to characterize this kind of orbits.

Several detection techniques exist to study the regular or chaotic behaviour of orbits of Hamiltonian systems. In particular, we will work with well-known *Lyapunov*-like methods which are based on the resolution of the so-called variational equations giving the evolution of deviation vectors (i.e. infinitesimal displacements from a given orbit). These methods are essentially the Fast Lyapunov Indicator (FLI) (see Froeschlé et al. 1997), the Smaller Alignment Index (SALI) (Skokos 2001), the Mean Exponential Growth Factor of Nearby Orbits (MEGNO) (Cincotta et al. 2003) and the Generalized Alignment Index (GALI) (Skokos et al. 2007). Some preliminary studies (e.g. Mikkola et al. 2002) have been realized in order to solve the variational equations in a symplectic way, but considering low order integrators adapted to the study case. Hence we have developed our own tool, the *Global Symplectic Integrator* (for short the GSI), introduced in Libert et al. (2011). This is a general method allowing to numerically solve both Hamiltonian equations of motion and variational equations with the same symplectic integrator.

Two chaos indicators have been used. Initial developments were realized with the SALI but the MEGNO has been used extensively for space debris stability studies. Such a choice comes from the definition of the MEGNO whose computation requires the time evolution of a single deviation vector only. This advantage, with respect to the SALI that needs the knowledge of the evolution of two deviation vectors, becomes critical when considering a large amount of orbits on long time spans.

The beginning of this chapter is devoted to a description of the GSI algorithm (Sec. 5.1). Then, we discuss the influence of the choice of symplectic integrator on the accuracy of the GSI in Sec. 5.2. In Sec. 5.3, we present a summary of the MEGNO. Before applying the GSI to space debris dynamics (Sec. 5.5), we validate it through several study cases in Sec. 5.4. Following the same path as in previous chapters, we mention concluding thoughts in Sec. 5.6.

5.1 Global Symplectic Integrator

As in Chap. 2, let us consider an autonomous Hamiltonian system with N degrees of freedom $\mathcal{H}(\vec{p},\vec{q})$. The Hamiltonian vector field is written differently as

$$\dot{\vec{x}} = \mathcal{J}\vec{\nabla}_{\vec{x}}\mathcal{H} = W(\vec{x})\,, \tag{5.1}$$

where $\vec{x} = \begin{pmatrix} \vec{p} \\ \vec{q} \end{pmatrix} \in \mathbb{R}^{2N}$ and

$$\mathcal{J} = \begin{pmatrix} 0_N & -1_N \\ 1_N & 0_N \end{pmatrix} \tag{5.2}$$

is the standard symplectic matrix, 1_N is the $N \times N$ identity matrix and 0_N the $N \times N$ null matrix.

Chaos indicators like the FLI, the SALI, the MEGNO and more recently the GALI are based on the time evolution of deviation vectors. These vectors, $\vec{\delta} = (\vec{\delta}_p, \vec{\delta}_q) \in \mathbb{R}^{2N}$, satisfy the variational equations given by

$$\dot{\vec{\delta}} = D_{\vec{x}}W\vec{\delta}(t) = \mathcal{J}\nabla^2_{\vec{x}}\mathcal{H}\,\vec{\delta} \tag{5.3}$$

where $D_{\vec{x}}W$ is the Jacobian matrix of the vector field W and $\nabla^2_{\vec{x}}\mathcal{H}$ is the Hessian matrix of $\mathcal{H}$. Eq. (5.3) is also known as the *tangent map* and deviation vectors are also called *tangent* vectors. These ones describe infinitesimal displacements from an arc of an orbit of the flow W. More precisely[1], such an arc is defined as

$$\gamma(t) = \{\vec{x}(s,\vec{x}_0) \,:\, \vec{x}_0 \in M_h\,,\; 0 \le s < t\}$$

where M_h is the compact energy surface

$$M_h = \{\vec{x} \,:\, \mathcal{H}(\vec{p},\vec{q}) = h\} \subset \mathbb{R}^{2N}.$$

One easily proves that the vector field (5.3) is Hamiltonian, i.e. $D_{\vec{x}}W$ is Hamiltonian:

$$(D_{\vec{x}}W)^T\mathcal{J} + D_{\vec{x}}W\mathcal{J} = 0$$

where $(D_{\vec{x}}W)^T$ denotes the transpose of $D_{\vec{x}}W$. Indeed, a property of Hamiltonian systems (see e.g. Arnold 1989) states that $D_{\vec{x}}W$ is Hamiltonian if and only if there exists a symmetric matrix S such that $D_{\vec{x}}W = \mathcal{J}S$. By construction, $D_{\vec{x}}W = \mathcal{J}\nabla^2_{\vec{x}}\mathcal{H}$ and the Hessian matrix $\nabla^2_{\vec{x}}\mathcal{H}$ is symmetric. Hence the property holds and $D_{\vec{x}}W$ is an Hamiltonian matrix. It follows that the Hamiltonian vector field (5.3) is associated to the *variational* Hamiltonian given by

$$\mathcal{K}(\vec{x},\vec{\delta}) = \frac{1}{2}\vec{\delta}^T\nabla^2_{\vec{x}}\mathcal{H}(\vec{x})\vec{\delta}. \tag{5.4}$$

[1] We use notations from Cincotta et al. (2003).

The GSI was introduced in Libert et al. (2011)[2] to numerically integrate both systems of equations (5.4.1) and (5.3) in a symplectic way. The symplectic integrators described in Sec. 2.1.1 assume that $\mathcal{H}$ is split into two separately integrable parts. We impose the condition that A and B respectively depend on $\vec{p}$ and $\vec{q}$:

$$\mathcal{H}(\vec{p},\vec{q}) = A(\vec{p}) + B(\vec{q}). \tag{5.5}$$

Easy calculation shows that the variational equations (5.3) can be written as

$$\begin{pmatrix} \dot{\vec{\delta}}_p \\ \\ \dot{\vec{\delta}}_q \end{pmatrix} = \begin{pmatrix} 0 & -\nabla^2_{\vec{q}} B \\ \\ \nabla^2_{\vec{p}} A & 0 \end{pmatrix} \begin{pmatrix} \vec{\delta}_p \\ \\ \vec{\delta}_q \end{pmatrix} = \begin{pmatrix} -\nabla^2_{\vec{q}} B\, \vec{\delta}_q \\ \\ \nabla^2_{\vec{p}} A\, \vec{\delta}_p \end{pmatrix} = \begin{pmatrix} -\vec{\nabla}_{\vec{\delta}_q} \mathcal{B} \\ \\ \vec{\nabla}_{\vec{\delta}_p} \mathcal{A} \end{pmatrix} \tag{5.6}$$

and the variational Hamiltonian (5.4) becomes

$$\mathcal{K}(\vec{p},\vec{q},\vec{\delta}_p,\vec{\delta}_q) = \frac{1}{2}\vec{\delta}_p^T \nabla^2_{\vec{p}} A \vec{\delta}_p + \frac{1}{2}\vec{\delta}_q^T \nabla^2_{\vec{q}} B \vec{\delta}_q = \mathcal{A}(\vec{p},\vec{\delta}_p) + \mathcal{B}(\vec{q},\vec{\delta}_q)\,. \tag{5.7}$$

The notations introduced hereabove ($\mathcal{H} = A + B$ for the Hamiltonian and $\mathcal{K} = \mathcal{A} + \mathcal{B}$ for the variational Hamiltonian) will be used throughout this chapter. Let us stress that the term *global* in *Global Symplectic Integrator* does not mean that both dynamics of $\vec{x}$ and $\vec{\delta}$ are merged into one single Hamiltonian function. However, equations of motion and variational equations are integrated using the same symplectic scheme. Hence we take advantage of the convenient properties of the symplectic schemes to keep accurate integrations of the global dynamics.

5.2 Choice of symplectic integrator

Two families of symplectic integrators have been described in 2.1.1. We already pointed out that perturbed Hamiltonian systems are well handled by the family from Laskar and Robutel (2001), the error of the integrator being of order $\tau^{2n}\varepsilon + \tau^2\varepsilon^2$ where $\varepsilon \simeq |B|/|A|$. However, there is no a priori reason why the associated variational Hamiltonian $\mathcal{K}$ would be such that the ratio $|\mathcal{B}|/|\mathcal{A}|$ is small. Hence, the direct application of the above family of integrators is not suitable.

In Laskar and Robutel (2001), another solution is presented to get rid of the $\tau^2\varepsilon^2$ term in the integration error. An additional step (exponential operator, called *corrector*) is added. While this method really improves the preservation properties of the integrator, the error still depends on further powers of ε, which can become really important as time increases. This fact will be illustrated in Sec. 5.4. Moreover, this *corrector* requires A to be quadratic in $\vec{p}$ and B to only

[2]Another similar method was independently developed in Skokos and Gerlach (2010). Initial versions were made available online nearly at the same time: arXiv:1005.5611 and arXiv:1006.0154.

depend on $\vec{q}$. Hence, it imposes a restriction on the Hamiltonian model to be studied.

To tackle this problem, we have decided to rely on the class of symmetric and explicit symplectic integrators presented in Yoshida (1990). The latter is suitable whatever the importance of the perturbation. While this method turns out to be very efficient for the variational Hamiltonian $\mathcal{K}$ (since $|\mathcal{B}|/|\mathcal{A}|$ can be significant), it nevertheless does not take advantage of the structure of $\mathcal{H}$ as a perturbation of an integrable system.

5.3 MEGNO

The SALI was used in Libert et al. (2011) to describe the GSI. The simplicity of its definition first made it a good candidate to test our method. Indeed, it is easily computed as

$$\mathrm{SALI}(t) = \min\left(\left\|\frac{\vec{\delta_1}(\gamma(t))}{\|\vec{\delta_1}(\gamma(t))\|} + \frac{\vec{\delta_2}(\gamma(t))}{\|\vec{\delta_2}(\gamma(t))\|}\right\|, \left\|\frac{\vec{\delta_1}(\gamma(t))}{\|\vec{\delta_1}(\gamma(t))\|} - \frac{\vec{\delta_2}(\gamma(t))}{\|\vec{\delta_2}(\gamma(t))\|}\right\|\right)$$

where $\vec{\delta_1}$ and $\vec{\delta_2}$ are two linearly independent deviation vectors. A detailed analysis of this indicator is presented in Skokos et al. (2004).

However, given that the MEGNO only needs the time evolution of a single deviation vector, we decided to turn to this indicator for practical studies of space debris behaviour. For that reason, we will spend more time on its definition and computation.

5.3.1 Definition

According to Cincotta et al. (2003), the Mean Exponential Growth factor of Nearby Orbits is defined as

$$Y(\gamma(t)) = \frac{2}{t}\int_0^t \frac{\dot{\delta}(\gamma(s))}{\delta(\gamma(s))} s\, ds. \tag{5.8}$$

where $\delta = \|\vec{\delta}\|$. It is in fact very similar to the Lyapunov Characteristic Exponent (LCE) (Benettin et al. 1980). For a given orbit, the LCE is defined as

$$\sigma_\gamma(\gamma) = \lim_{t\to\infty} \frac{1}{t} \ln \frac{\delta(\gamma(t))}{\delta(\gamma(0))}.$$

It measures the mean exponential rate of divergence of nearby orbits. It can also be expressed as

$$\sigma_\gamma(\gamma) = \lim_{t\to\infty} \frac{1}{t} \int_0^t \frac{\dot{\delta}(\gamma(s))}{\delta(\gamma(s))} ds. \tag{5.9}$$

Both eq. (5.8) and (5.9) are close to each other. However, the LCE computation is more time consuming.

A useful indicator is given by the mean MEGNO, namely the time-average:

$$\overline{Y}(\gamma(t)) = \frac{1}{t} \int_0^t Y(s)\, ds. \tag{5.10}$$

While $Y(t)$ might neither converge nor admit a limit for $t \to \infty$, it has been proven by Cincotta et al. (2003) that the asymptotic value of $\overline{Y}$ provides a good characterization of the regular or chaotic nature of orbits.

5.3.2 Interpretation

In Cincotta et al. (2003), the asymptotic behaviour is shown for representative solutions of the deviation vectors.

Consider an orbit close to a quasi-periodic one. The Hamiltonian is assumed to be integrable with action-angle variables $(J_i, \theta_i)_{i=1,...,N}$. Each couple (J_i, θ_i) can be seen as a set of polar coordinates producing a circle. Hence, an N-dimensional torus is built from all action-action variables, defining a surface of constant energy in the $2N$-dimensional phase space. Quasi-periodic orbits mean that the frequencies W_i associated to the angles θ_i are not commensurable, i.e. we cannot find non zero integers $k_1, ..., k_N$ such that

$$k_1 W_1 + k_2 W_2 + ... + k_N W_N = 0.$$

The orbit will evolve on the torus without ever coming back to the origin. Such a torus is characterized as *irrational*. We also assume that the frequencies depend on the actions (i.e. the system is said *non-isochronous*). In this case, the norm of the deviation vector can be evaluated and the mean MEGNO is such that

$$\overline{Y}(\gamma) = \lim_{t\to\infty} \overline{Y}(\gamma(t)) = 2.$$

Even if this short analysis is more easily performed with action-angle variables, it should be noted that the MEGNO does not depend on a particular choice of variables for the Hamiltonian.

If γ is close to a stable periodic orbit, we can show that $Y(\gamma(t))$ oscillates about 2 and that $\overline{Y}(\gamma(t))$ asymptotically reaches 2. If γ coincides with a stable

orbit, $Y(\gamma(t))$ oscillates about 0 and $\overline{Y}(\gamma)$ equals 0. It comes directly from the isochronous property of the system.

Another possibility appears when γ is close to an unstable periodic orbit γ_u. In that situation $Y(\gamma(t))$ shows quasi-periodic oscillations coupled to periodic pulses. When γ is in a small neighbourhood of γ_u,

$$\delta(\gamma(t)) \simeq \delta(\gamma_u(t)) \simeq \delta(\gamma(0))e^{\sigma_u t}$$

with $\sigma_u > 0$. Outside this neighbourhood, $Y(\gamma(t))$ is expected to behave like the first case. The time-average $\overline{Y}(\gamma(t))$ behaves like $Y(\gamma(t))$ with decreasing pulse amplitudes as time increases. The closer γ to γ_u, the larger $\overline{Y}(\gamma)$. If γ coincides with γ_u, $\overline{Y}(\gamma(t))$ will grow linearly and $\overline{Y}(\gamma) >> 2$.

Eventually, let us consider irregular orbits. This means that

$$\delta(\gamma(t)) \simeq \delta(\gamma(0))e^{\sigma_\gamma t}$$

with σ_γ the LCN of γ. The associated MEGNO is given by

$$Y(\gamma(t)) \simeq \sigma_\gamma t + \tilde{\mathcal{O}}(\gamma(t))$$

where $\tilde{\mathcal{O}}$ is an oscillating function about 0. Over a sufficiently long time, the time-average becomes

$$\overline{Y}(\gamma(t)) \simeq \frac{1}{2}\sigma_\gamma t.$$

Hence, for chaotic orbits, $Y(\gamma(t))$ and $\overline{Y}(\gamma(t))$ increase linearly with time, the slope of $\overline{Y}(\gamma(t))$ being half of the orbit LCE.

Eventually, let us highlight two important differences between the LCN and MEGNO. First, the MEGNO can be expressed as a sum, whatever the considered orbit. The asymptotic behaviour of $\overline{Y}(\gamma(t))$ writes

$$\overline{Y}(\gamma(t)) \simeq a_\gamma t + d_\gamma$$

where $(a_\gamma, d_\gamma) \simeq (\sigma_\gamma/2, 0)$ for irregular orbits. However, $(a_\gamma, d_\gamma) \simeq (0, 2)$ for stable quasi-periodic orbits, $d_\gamma \lesssim 2$ for orbits close to periodic stable ones and $d_\gamma \gtrsim 2$ for orbits closed on unstable periodic ones. Second, one can show that $\lim_{t\to\infty} Y/t = \sigma_\gamma$ for chaotic orbits and that Y/t reaches 0 faster than the LCE does for regular orbits.

Interested readers can find a detailed analytical description of the evolution of the MEGNO in Cincotta et al. (2003) and a comparison between different chaos indicators in Maffione et al. (2013).

5.3.3 Computation

The computation of the MEGNO and its time-average requires both integrals (5.8) and (5.10) to be solved. Different methods are available.

A straightforward approach is based on the introduction of two auxiliary functions v_Y and $v_{\overline{Y}}$ such that

$$v_Y(t) = t\,Y(t) \quad \text{and} \quad v_{\overline{Y}}(t) = t\,\overline{Y}(t)\,,$$

whose time evolutions are directly given by the following differential equations:

$$\dot{v}_Y(t) = 2\frac{\dot{\delta}(t)}{\delta(t)}t = 2\frac{\dot{\vec{\delta}}\cdot\vec{\delta}}{\delta^2}t \quad \text{and} \quad \dot{v}_{\overline{Y}}(t) = Y(t) = \frac{v_Y(t)}{t}. \tag{5.11}$$

Obviously, (5.3) and (5.11) have to be computed with the same integrator (see e.g. Goździewski et al. 2001, Valk et al. 2009, Hinse et al. 2010, Maffione et al. 2011). In this case, the time step used to integrate eq. (5.3) is fixed by the integration of eq. (5.11). However, the use of auxiliary functions is less efficient within a symplectic integration scheme ((5.11) are not generally Hamiltonian equations of motion). In light of this, other alternatives have been considered.

In particular, it was observed in Breiter et al. (2005a) that a fixed step size integrator can be considered as equivalent to a discrete time map. Hence, using the definition of the MEGNO for discrete time dynamical systems (i.e. maps) given by Cincotta et al. (2003), it has been proposed to compute the MEGNO as

$$Y_*(t+\tau) = \frac{t}{t+\tau}Y_*(t) + 2\ln\frac{\delta(t+\tau)}{\delta(t)} + \mathcal{O}(\tau^2) \tag{5.12}$$

$$\overline{Y}_*(t+\tau) = \frac{t\overline{Y}_*(t) + \tau Y_*(t+\tau)}{t+\tau} + \mathcal{O}(\tau^2)\,, \tag{5.13}$$

τ being the integration step size and the subscript $*$ denoting the functions defined by Breiter et al. (2005a). Let us note that these formulae correspond to solving both integrals (5.8) and (5.10) with a simple rectangular quadrature method. On the other hand, a mixed scheme has been proposed in Goździewski (2003), that relies on the computation of the MEGNO by using the so-called trapezoidal rule [3] and then the discrete time approximation for the mean MEGNO.

In the present work, we develop further this idea. We propose to use the trapezoidal rule to compute both MEGNO and its time-average. First, we write

[3] Given a real-valued function f and an interval $[a,b]$, one has (Press et al. 2007)

$$\int_a^b f(x)dx = 0.5(b-a)[f(a)+f(b)] + \mathcal{O}(|b-a|^3|f''|)\,,$$

the second derivative being estimated on the interval $[a,b]$.

the MEGNO as

$$Y(t) = 2\log\delta(t) - \frac{2}{t}\int_0^t \log\delta(s)ds\,,$$

then using the trapezoidal rule we get

$$Y(t+\tau) = \frac{t}{t+\tau}Y(t) + \frac{2t+\tau}{t+\tau}\ln\frac{\delta(t+\tau)}{\delta(t)} + \mathcal{O}(\tau^3) \tag{5.14}$$

and

$$\overline{Y}(t+\tau) = \frac{1}{t+\tau}[t\overline{Y}(t) + 0.5\tau(Y(t)+Y(t+\tau))] + \mathcal{O}(\tau^3)\,. \tag{5.15}$$

The above formulae (5.14) and (5.15) improve the aforementioned ones corresponding to lower order approximations of the integrals defining MEGNO and mean MEGNO. The difference between both sets of formulae is more significant in the case of short time spans. As time increases, $Y(t)$ and $Y_*(t)$ computed respectively in (5.14) and (5.12) tend to the same values. Indeed, easy calculation shows that the difference between $Y(t)$ and $Y_*(t)$ is

$$Y(t) - Y_*(t) = -2\,\frac{\tau}{t}\ln\frac{\delta(t)}{\delta(0)} + \frac{t+\tau}{t-\tau}\,\mathcal{O}(\tau^2). \tag{5.16}$$

This quantity decreases with time for regular orbits and remains bounded for irregular ones. Let us also point out that, the less regular the orbit, the larger the difference between both formulae. Unfortunately, the differences occuring with the MEGNO time-average cannot be analyzed with such a simple formula.

One could wonder whether any higher order integration method would bring significant improvement to the computation of the MEGNO. To that end, let us consider the well-known *Simpson's rule* [4]. Using that method, (5.14) and (5.15) become

$$\begin{aligned} Y(t+\tau) \quad = \quad & \frac{t}{t+\tau}Y(t) + \frac{6t+\tau}{3(t+\tau)}\ln\frac{\delta(t+\tau)}{\delta(t)} \\ & + \frac{4\tau}{3(t+\tau)}\ln\frac{\delta(t+\tau)}{\delta(t+\tau/2)} \\ & + \mathcal{O}(\tau^5) \end{aligned} \tag{5.17}$$

[4] Given a real-valued function f and an interval $[a,b]$, one has (Press et al. 2007)

$$\int_a^b f(x)dx = (b-a)/6[f(a) + f((a+b)/2) + f(b)] + \mathcal{O}(|b-a|^5|f^{(4)}|)\,,$$

the fourth derivative being estimated on the interval $[a,b]$.

and

$$\begin{aligned}\overline{Y}(t+\tau) &= \frac{1}{t+\tau}\Big[t\overline{Y}(t) + \\ &+ \frac{\tau}{6}\left(Y(t)\frac{1}{4}Y(t+\tau/2) + Y(t+\tau)\right)\Big] \\ &+\mathcal{O}(\tau^5)\,. \end{aligned} \tag{5.18}$$

Naturally, the gain in accuracy requires the knowledge of the value of the deviation vector at the midpoint of the interval $[t\,,\ t+\tau]$. The usability of the Simpson's rule depends on the extent to which one can easily solve the variational equations for the time step $\tau/2$. One could obviously divide the time step by two but that would clearly lead to an increase in computation time. Given that the same number of evaluations are involved with the trapezoidal and rectangular quadrature methods, (5.14) and (5.15) seem to be a good compromise between accuracy and computation cost.

In the following, the GSI will be used with eq. (5.14) and (5.15), whereas eq. (5.11) will be used with the non-symplectic integrators. Let us also note that MEGNO values shown in the following stability maps are in fact asymptotic values of mean MEGNO i.e. mean MEGNO values at the end of the integration process.

5.4 Validation of the GSI

In this section, we aim to validate the GSI symplectic scheme. Well-known dynamical systems have been tested. First, we briefly summarize the results published in Libert et al. (2011) where a comparative study between the GSI and a typical non-symplectic scheme was performed using the SALI, based on the Hénon-Heiles system and restricted three-body problem (RTBP). Then, we spend more time on the validation of the GSI with the MEGNO. To that aim, we choose the tricky problem of slow diffusion in Hamiltonian systems (the so-called Arnold diffusion). Since it requires the evolution of orbits on very long time spans, the benefits from the GSI method with respect to a non-symplectic scheme are clearly visible. Moreover, as the GSI does not rely on the use of a specific symplectic integrator, we also discuss and compare some of them. The MEGNO is also used to show that the discrepancies appearing between propagations in Sec. 2.4.3 are explained by the irregularity of these orbits.

To emphasize the advantage of working completely in the framework of symplectic integrators, we decided to restrict our study to integrators of second and fourth orders. This allows us to reduce the amount of CPU times required to per-

form our numerical analysis without any loss of generality. Obviously, our method keeps its advantages also for higher order integrators. For example, a tenth order symplectic integrator and the well-known non-symplectic Bulirsch-Stoer (BS) integrator have been used in Libert et al. (2011) to study the RTBP.

5.4.1 Hénon-Heiles system

The Hénon-Heiles model was introduced in Hénon and Heiles (1964) to describe the planar motion of stars around a galactic center. It has already been widely used in literature as benchmark for various tests (see e.g. Cincotta et al. 2003, Skokos et al. 2004). The Hamiltonian is given by

$$\mathcal{H}_{\rm HH}(p_x, p_y, x, y) = \frac{1}{2}(p_x^2 + p_y^2) + \frac{1}{2}(x^2 + y^2) + x^2 y - \frac{1}{3}y^3$$

with one part depending only on momenta (p_x, p_y) and the other one depending on coordinates (x, y). Hence, the GSI can be applied without any difficulty. Usually the Hénon-Heiles phase space is presented in the two-dimensional plane (y, p_y) as a Poincaré surface section with $x = 0$ (we only keep orbit intersections with the $x = 0$ plane). As illustrated in Fig. 5.1, the phase-space is populated with regular and chaotic orbits. In particular, five orbits have been pointed out, corresponding to the different kinds detailed in Sec. 5.3.2. Initial conditions are chosen in the (y, p_y) plane, x is fixed to zero and p_x is chosen such as to keep $\mathcal{H}_{\rm HH} = 0.118$. The exact initial conditions are given in Cincotta et al. (2003) and correspond to an orbit close to a stable periodic (sp) orbit of period 1, a quasi-periodic (qp) stable orbit, a quasi-periodic orbit close to an unstable orbit (up) of period 4, an irregular orbit in a stochastic region (c1) and an irregular orbit in a large chaotic region (c2).

In Libert et al. (2011), based on a random choice of stable and unstable orbits to be correctly identified, the GSI has been compared to a non-symplectic integration of the equations of motion and variational equations 5.3. More precisely, the comparison involved the SABA_2 and SABA_4 integrators against the fixed step-size RK_4 integrator. The SALI was used as chaos indicator. In this work, the family of integrators from Yoshida (1990) had not yet been considered.

It was shown that the non-symplectic scheme tends to detect an excessive amount of chaotic orbits. In the same time, the GSI was able to identify correctly nearly all orbits with time-steps up to four times larger than the ones needed by the non-symplectic integrator. This can obviously be explained by the smaller energy loss observed with the GSI on long time-spans. The methodology that was followed in Libert et al. (2011) is very similar to the one explained with more details in Sec. 5.4.3, using the MEGNO indicator instead of the SALI.

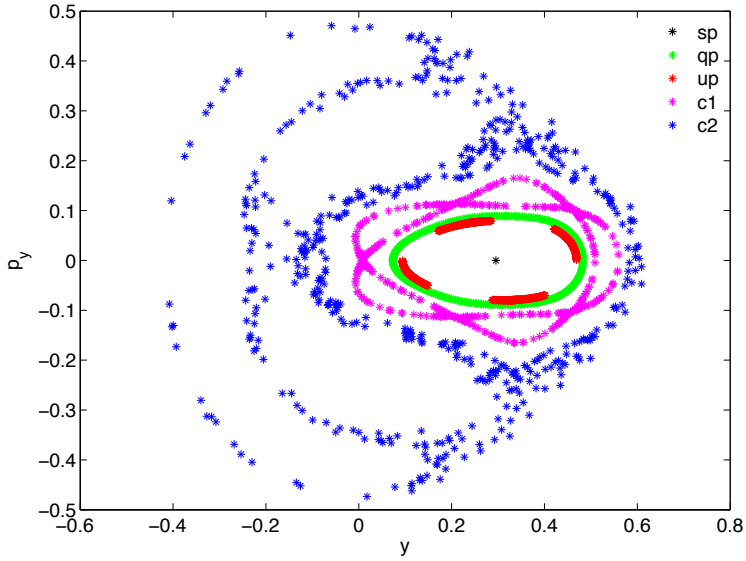

Figure 5.1 • *Hénon-Heiles Poincaré section with* $\mathcal{H}_{HH} = 0.118$. *Five types of orbits are illustrated. For each orbit, a point is plotted for each one of the* 500 *intersections with the* $x = 0$ *plane.*

5.4.2 Restricted three-body problem

Another study case presented in Libert et al. (2011) is the characterization of the Kozai resonance in the RTBP. The problem assumes that two bodies, one intermediate mass (e.g. Jupiter) and one massless body (e.g. an asteroid), evolve around the largest mass (e.g. the Sun). Jupiter evolves around the Sun on a circular orbit and the asteroid orbits between the Sun and Jupiter. In this configuration, it is known that the perturbation of Jupiter induces a coupled variation of the eccentricity and inclination of the highly inclined asteroid. Indeed, Kozai (1962) showed that the following quantity

$$\mathcal{E} = \sqrt{a_1(1-e_1^2)}\cos i_1$$

remains constant. The subscript 1 refers to the asteroid and 2 to Jupiter (see below). This dynamics is often referred to as *Kozai resonance* (see e.g. Libert and Henrard 2007). It is usually represented in the two-dimensional phase-space $(e_1\cos\omega_1, e_1\sin\omega_1)$ (see e.g. Thomas and Morbidelli 1996).

Orbital evolution and stability of the asteroid were investigated in Libert et al. (2011) by means of the *democratic heliocentric* Hamiltonian formulation of the

TBP (more details in Morbidelli 2002 and Duncan et al. 1998)

$$\mathcal{H}_{\rm TBP}(\vec{P}_1,\vec{P}_2,\vec{Q}_1,\vec{Q}_2) = \sum_{j=1}^{2}\left\{\frac{\|\vec{P}_j\|^2}{2m_j}-\mathcal{G}\frac{m_0 m_j}{\|\vec{Q}_j\|}\right\} + \frac{1}{2m_0}\left\|\sum_{j=1}^{2}\vec{P}_j\right\|^2 - \mathcal{G}\sum_{j=1}^{2}\sum_{i=1}^{j-1}\frac{m_i m_j}{\|\vec{Q}_i-\vec{Q}_j\|} \quad (5.19)$$

where $(\vec{Q}_1,\vec{Q}_2)$ and $(\vec{P}_1,\vec{P}_2)$ are respectively the canonical coordinates and momenta of the bodies of mass m_1 and m_2. The Sun's mass is denoted m_0. As for the Hénon-Heiles Hamiltonian $\mathcal{H}_{\rm HH}$, $\mathcal{H}_{\rm RTBP}$ can be split into two parts, each one depending only on momenta or coordinates. Another possibility, similar to what is proposed in Sec. 2.3, would be to isolate in the first term both Keplerian problems and leave the perturbation in the other part. This method is explained in Appx. D. However, it is not well adapted to the GSI and will not be used.

The RTBP phase space corresponding to $\mathcal{E} = 0.41833$ is shown in Fig. 5.2. Trajectories are plotted with initial conditions $a_1 = 0.35$ AU, $a_2 = 1$ AU, $e_2 = 0$, $i_2 = 0$ rad and along the $e_1 \sin\omega_1$ axis when $e_1\cos\omega_1 = 0$. Other initial Keplerian elements are zero. The SABA_{10} was used with small time steps $\tau = 10^{-3}$ yr. The fixed value of $\mathcal{E}$ means that the maximum inclination of the asteroid is $\pi/4$ rad. The phase space is divided into three distinct parts. Both stable Kozai equilibria are enclosed by the separatrix, the *eight-shaped* curve, and correspond to a libration of ω_1 around $\pi/2$ and $3\pi/2$ rad. As shown in Fig. 5.2, an asteroid with an initial circular orbit will start on the separatrix and stay close to it, suffering large eccentricity variations. These perturbations occur on very long time spans of the order of 10^4-10^5 yr and the ability of symplectic integrators to stay accurate on such a long period of time turns out an asset. While in the vicinity of the separatrix, the asteroid switches between the lower and upper parts of the separatrix, making the motion irregular.

The same phase space was then investigated with the GSI (SABA_{10}) and the SALI over 10^5 yr. Strong chaos was detected along the separatrix, while the Kozai equilibria were correctly identified as stable. For the variational Hamiltonian is not split in such a way that $\mathcal{B}(\vec{q},\vec{\delta}_q)$ is much smaller than $\mathcal{A}(\vec{p},\vec{\delta}_p)$, the integrations performed with SABA_{10} had to be made with extra small time steps $\tau = 10^{-5}$ yr.

Here we show the same phase space obtained by means of the GSI and S_6. As explained in Sec. 5.2, this integrator does not assume a particular form for the variational Hamiltonian and the error does not depend on the ratio $\mathcal{B}(\vec{q},\vec{\delta}_q)/\mathcal{A}(\vec{p},\vec{\delta}_p)$. Moreover, we replace the SALI by the MEGNO. Based on the same initial conditions and time span as in Libert et al. (2011), the chaos map is shown in Fig. 5.3.

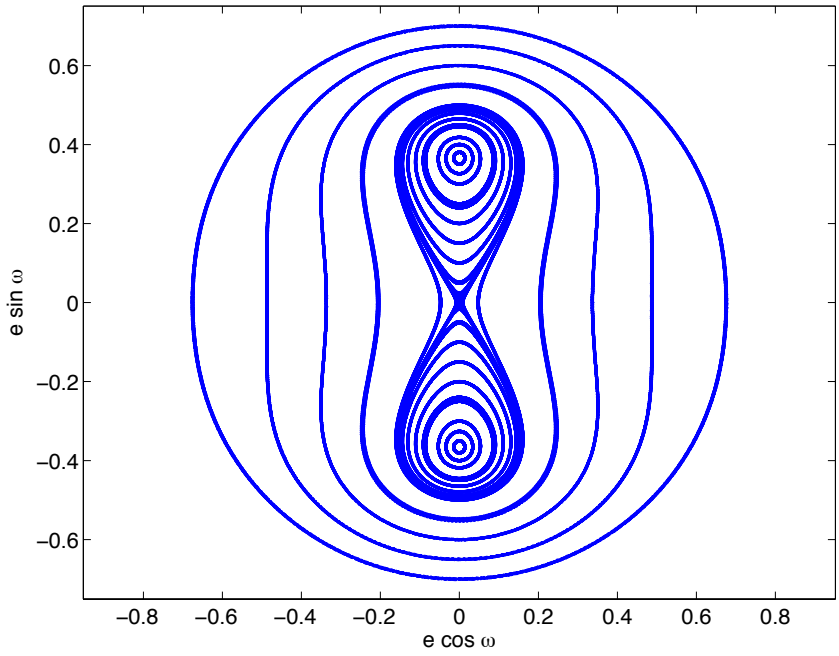

Figure 5.2 • *RTBP phase space corresponding to* $\mathcal{E} = 0.41833$ *obtained with the* $SABA_{10}$ *integrator and time steps* $\tau = 10^{-3}$ *yr. Initial conditions are* $a_1 = 0.35$, $a_2 = 1$, $e_2 = 0$, $i_2 = 0$ *rad.*

While S_6 lets us use larger time steps, the lower order with respect to $SABA_{10}$ prevents us to go higher. Results are in total agreement with what is presented in Libert et al. (2011).

As a point of comparison, we tried to reproduce the same results with a non-symplectic integrator. To that end, we resorted to the robust variable step-size BS integrator (see e.g. Hairer et al. 1993). With the accuracy parameter set to 10^{-8} (usually a suitable value), the BS needs up to three times more CPU time than the GSI with S_6. Moreover, the very slow chaotic diffusion along the separatrix is not well identified by the BS. We show in Fig. 5.4 the norm of deviation vectors as a function of time for orbits close to one stable equilibrium ($e_1 = 0.4$) and the unstable separatrix ($e_1 = 0.001$). Other initial conditions are similar to the ones used in the full phase space description. We compare the results obtained with the GSI ($SABA_{10}$ with small time steps, $\tau = 10^{-5}$ yr) and the BS integrator (with the parameter equal to 10^{-8}). Both schemes identify the stable orbit in the same way. While the norm of the deviation vector remains perfectly bounded with the GSI, a small but reasonable increase can be observed for the BS. As far as the other orbit is concerned, we clearly see a steady increase of the norm of the deviation vector

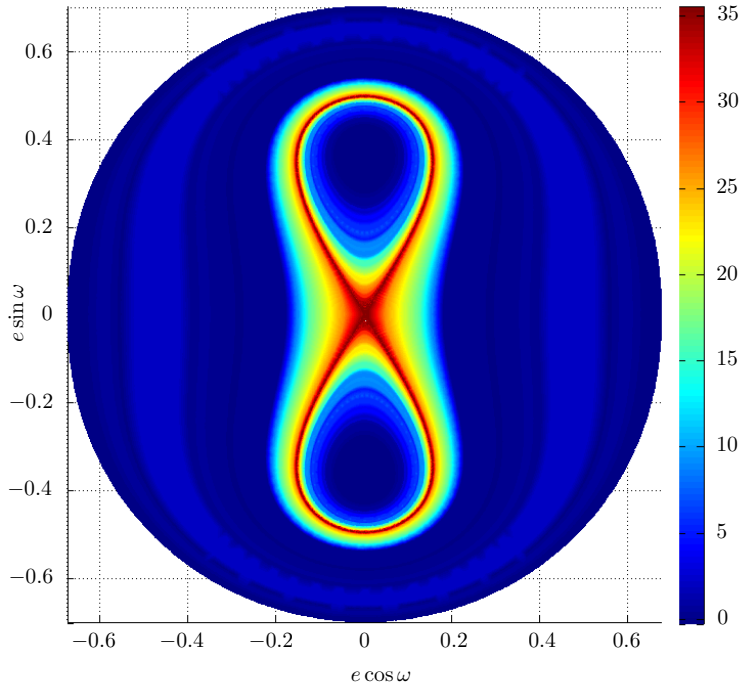

Figure 5.3 • *Stability analysis of the two-dimensional phase plane* $(e_1 \cos \omega_1, e_1 \sin \omega_1)$ *of the RTBP* ($E = 0.41833$) *represented using the GSI* (S_6) *and the MEGNO at* $t = 10^5$ *yr. Time steps are equal* $\tau = 10^{-4}$ *yr. Initial conditions are* $a_1 = 0.35$, $a_2 = 1$, $e_2 = 0$, $i_2 = 0$ *rad.*

with the GSI after some time. The situation is totally different for the BS which evolves nearly exactly as in the previous case. Each perturbation corresponds to an encounter of the orbit with the origin of the phase space $(e_1 \cos \omega_1, e_1 \sin \omega_1)$. The first switch between the lower and upper parts of the separatrix happens around 1.5×10^4 yr for the orbit propagated with the GSI. From that moment, the orbit is clearly identified as unstable. On the opposite, the BS integrator seems to remain insensitive to such events. The orbit never crosses the center of the phase space and remains on the lower part of the separatrix for the entire propagation. A tiny value of the accuracy parameter, namely 10^{-12}, is required to eventually detect chaos around the separatrix. This considerably increases the CPU time and reveals the importance of the GSI in studying dynamics acting on long time scales.

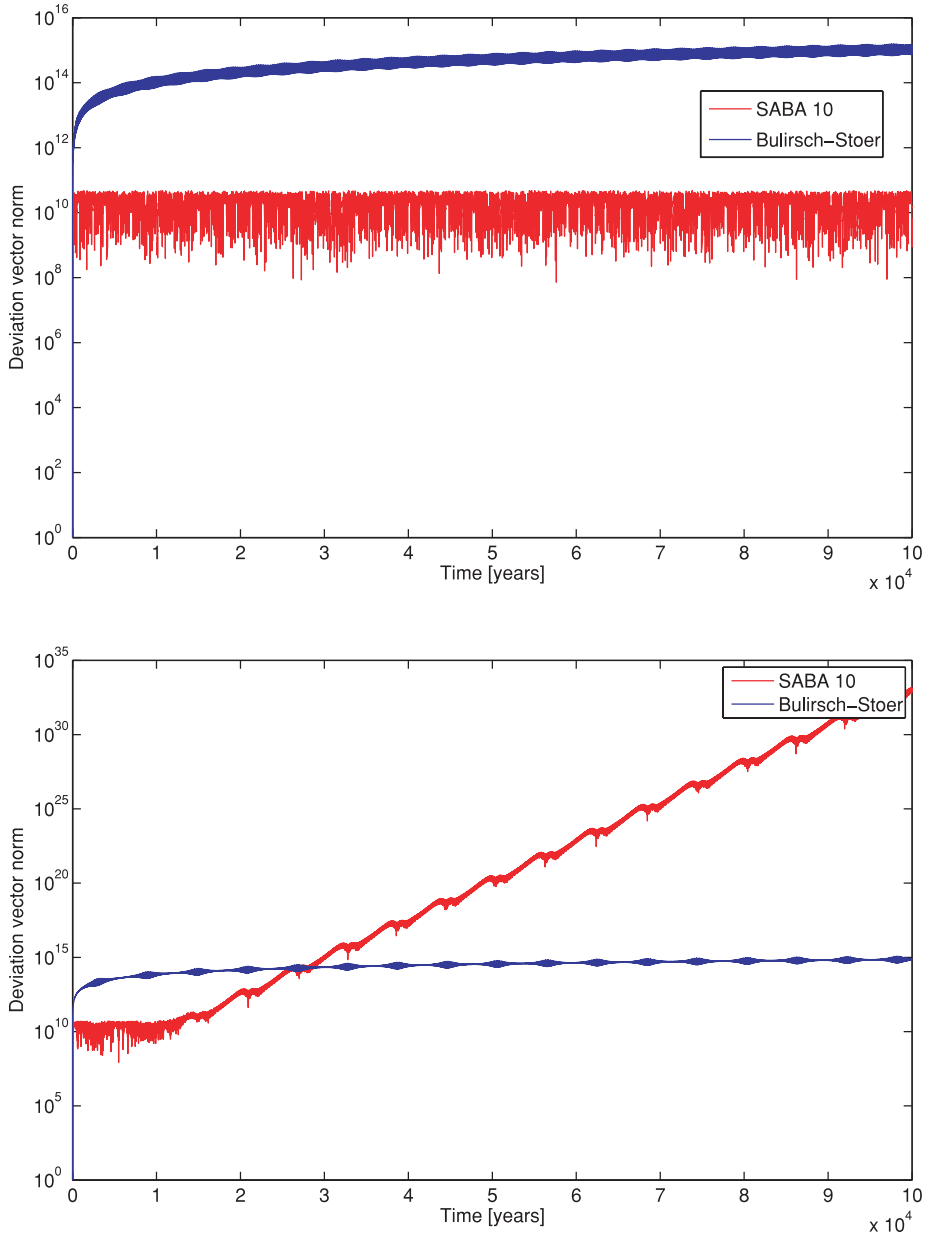

Figure 5.4 • *Deviation vector norm evolution of the RTBP ($\mathcal{E} = 0.41833$) obtained with the SABA$_{10}$ (in red) and BS (in blue) integrators. Initial conditions are $a_1 = 0.35$, $a_2 = 1$, $e_2 = 0$, $i_2 = 0$ rad. A stable orbit ($e_1 = 0.4$, top) and an orbit close to the unstable separatrix ($e_1 = 0.001$, bottom) are considered.*

5.4.3 Arnold diffusion

Model

A challenging application of our method is given by the following Hamiltonian system proposed by Lega et al. (2003):

$$\mathcal{H}_{\text{Arnold}}(I_1, I_2, I_3, \phi_1, \phi_2, \phi_3) = \frac{1}{2}(I_1^2 + I_2^2) + I_3 + \frac{\nu}{\cos(\phi_1) + \cos(\phi_2) + \cos(\phi_3) + 4} \tag{5.20}$$

where momenta $I_1, I_2, I_3 \in \mathbb{R}$ and coordinates $\phi_1, \phi_2, \phi_3 \in \mathbb{R}$ are canonically conjugate variables and ν is assumed to be a small parameter.

From eq. (5.20), we easily obtain the following relations

$$\dot{\phi}_1 = I_1 \ , \quad \dot{\phi}_2 = I_2 \quad \text{and} \quad \dot{\phi}_3 = 1.$$

Hence, each straight line

$$k_1 I_1 + k_2 I_2 + k_3 = 0 \ , \quad (k_1, k_2, k_3) \in \mathbb{Z}^3 \setminus \{0\} \tag{5.21}$$

on the two-dimensional plane (I_1, I_2) represents a resonance. As illustrated in Fig. 5.5, most relevant resonances are clearly visible on the plane (I_1, I_2), to form the so-called *Arnold Web*. Mean MEGNO values are shown for a grid of 600×600 equally spaced initial conditions in this plane. Other initial conditions are $I_3 = 1$ and $\phi_1 = \phi_2 = \phi_3 = 0$, and the parameter ν has been fixed to 0.007, as in the rest of this section. This value needs to be small in order to avoid resonances overlap. Besides, as pointed out in Lega et al. (2003), the smaller the perturbation, the slower the diffusion. The GSI has been used with S_4 integrator with a fixed time step $\tau = 0.01$ over 10^7 time units. Initial normalized deviation vectors $\vec{\delta}(0)$ are randomly chosen with uniform probability to avoid numerical artifacts in the computation of the MEGNO (Barrio et al. 2009).

The existence of instability in such close to integrable Hamiltonian systems was proven in Arnold (1963) and is often referred to as *Arnold diffusion*. A numerical proof of the existence of chaos along resonance lines for this particular Hamiltonian (5.20) was brought in Lega et al. (2003).

The exact reproduction of the Arnold web with respect to Lega et al. (2003) given in Fig. 5.5 is already a validation of our method of computation of the MEGNO within the GSI symplectic scheme. The analysis presented hereafter will be performed in the region delimited by $0.29 \leq I_1 \leq 0.33$ and $0.14 \leq I_2 \leq 0.18$, centered on the $I_1 = 2I_2$ resonance. This small region is enclosed in the box shown in Fig. 5.5. An enlargement of this box is presented in Fig. 5.6. Again, a grid of 600×600 equally spaced initial conditions has been numerically integrated using

the GSI with S_4 integrator up to 10^7 time units. Other initial conditions and parameters are the same as the ones used to produce Fig. 5.5. In the following analysis, we will consider several orbits around the top hyperbolic border (in brown in Fig. 5.6) of the resonance where diffusion is actually confined.

Numerical simulations performed with the GSI considering other values of ν and specific parts of the phase space have been published in Dvorak and Lhotka (2013).

Analysis

Similarly to Libert et al. (2011), we compare the results on the correct determination of regular or chaotic orbits behaviour obtained with the GSI and a non-symplectic integrator. Through an analysis of the maximum relative errors on the energy, percentage of correctly identified orbits and CPU time, we will show that our symplectic scheme outperforms the non-symplectic one and that Yoshida integrators family is more suitable for getting the solution of the variational equations.

To that end, we use and compare fourth-order integrators. This turns out to be a good compromise between reliability of the numerical results, as measured in term of relative energy loss, and number of evaluations of the vector fields, translated easily into required CPU time. On the one hand, we consider the RK_4 integrator. On the other hand, both symplectic integrator families presented in Sec. 2.1.1 have been tested. As far as only the Hamiltonian system (5.20) is concerned, SABA and SBAB integrator classes outperform Yoshida integrators. Indeed, the smallness of ν makes this system equal to an integrable one plus a small perturbation. Hence, the error $\mathcal{O}(\tau^{2n}\varepsilon + \tau^2\varepsilon^2)$ is smaller than Yoshida's one $\mathcal{O}(\tau^n)$. However, SABA and SBAB classes performances are limited for the variational Hamiltonian system. It is mainly due to the structure of $\mathcal{K}_{\mathrm{Arnold}}$. As time increases, the weight of the $\mathcal{B}$ part, say the perturbation, of $\mathcal{K}_{\mathrm{Arnold}}$ may become larger than the $\mathcal{A}$ part, see Fig. 5.7. This implies an increase of the error on the *variational* energy too. Naturally, the computation of both MEGNO and mean MEGNO suffers from this loss of precision. This is clearly shown in Fig. 5.8. The same orbit has been integrated and the MEGNO has been obtained with both the GSI and the non-symplectic scheme. Moreover, both S_4 and SBAB_4 symplectic integrators have been tested. While $\overline{Y}$ computed with RK_4 and with the GSI (S_4) are really close to each other and identify the orbit as a stable one, it diverges rapidly with the GSI coupled to the SBAB_4 integrator. The percentage study performed below will also highlight this problem occuring with SABA and SBAB families of integrators.

An attempt has been done to reduce the weight of the perturbation in the

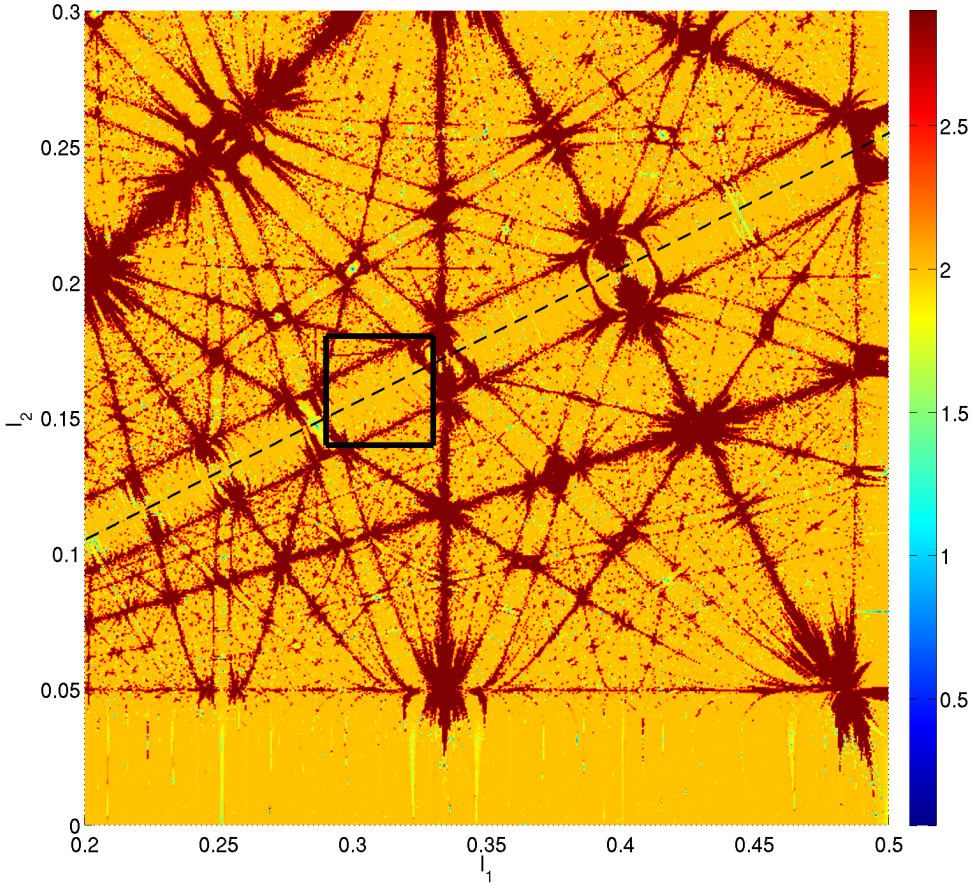

Figure 5.5 • *Arnold web. Stability analysis of the two-dimensional phase plane* (I_1, I_2) *represented using MEGNO values at* $t = 10^7$ *time units (the values greater than three have been fixed to three). A set of* 600×600 *uniformly distributed initial conditions has been integrated with* S_4 *(with time steps equal to* 0.01*). Other initial conditions are fixed to* $I_3 = 1$, $\phi_1 = \phi_2 = \phi_3 = 0$ *and* $\nu = 0.007$. *The dashed line represents the* $I_1 = 2I_2$ *resonance.*

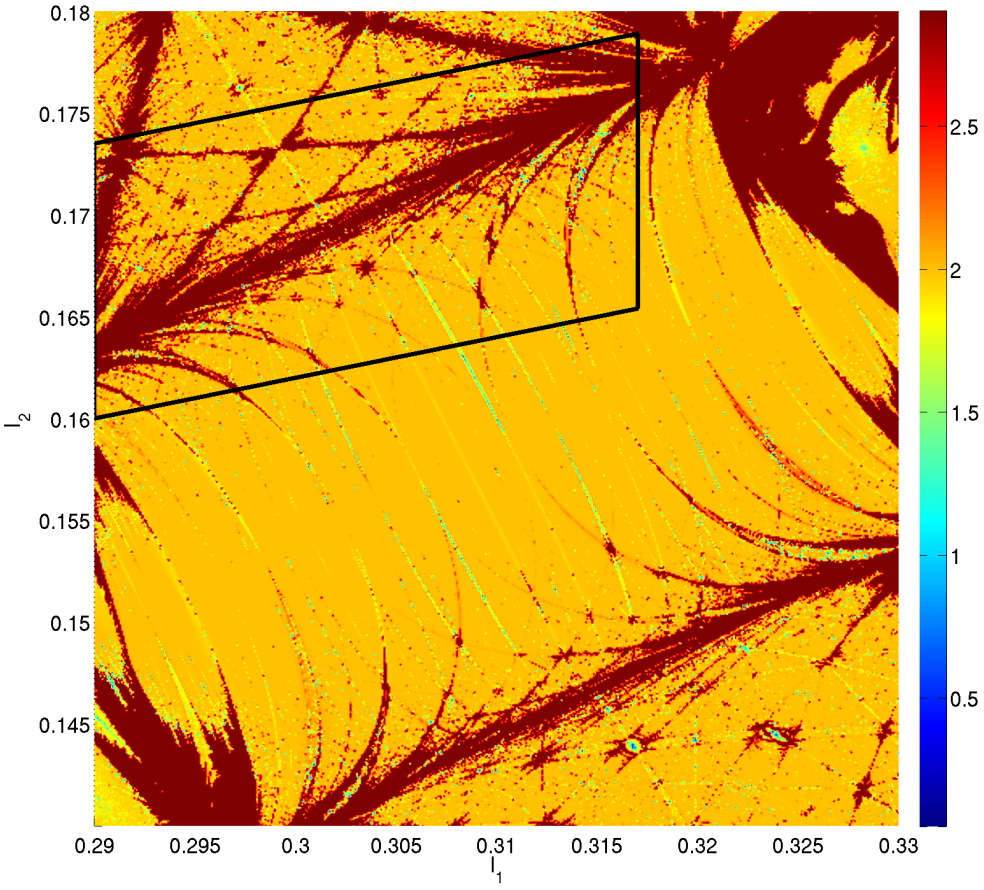

Figure 5.6 • *Magnification of the area enclosed in the box in Fig. 5.5. The parallelogram represents the region in which* 100 *initial conditions have been considered to compare the GSI to a non-symplectic integration scheme.*

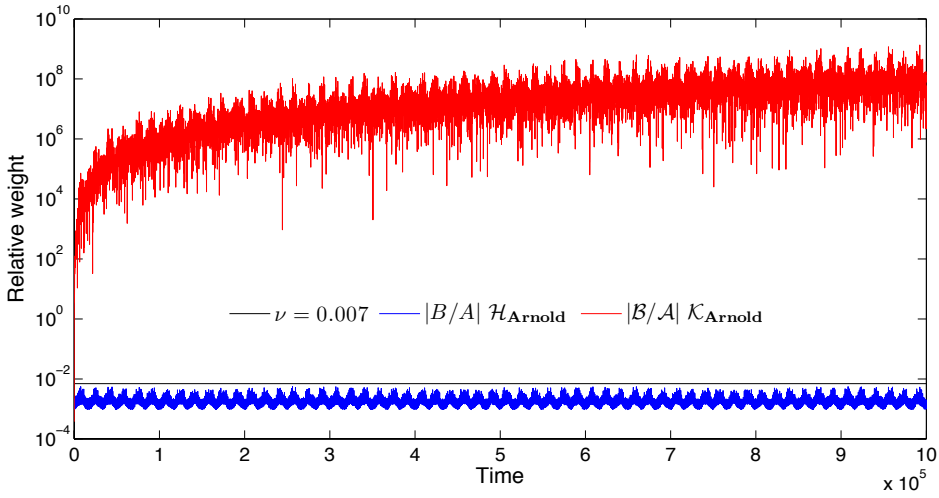

Figure 5.7 • *Relative weight of A and B parts (respectively $\mathcal{A}$ and $\mathcal{B}$), for both Hamiltonian systems $\mathcal{H}_{Arnold}$ and $\mathcal{K}_{Arnold}$. One generic orbit ($I_1 = 0.29$, $I_2 = 0.16$, $I_3 = 1$ and $\phi_1 = \phi_2 = \phi_3 = 0$) and the associated variational equations have been integrated with S_4 with a time step $\tau = 0.01$. The horizontal line corresponds to $\nu = 0.007$.*

variational Hamiltonian function by normalizing the deviation vector at each time step. However, given that the MEGNO (5.14) and its time-average (5.15) only depend on the norm of the deviation vector and not on its derivative (as in the definition (5.8)), the normalization is not suitable: as the MEGNO and mean MEGNO are initially set to zero, these two quantities will remain very close to zero whatever the nature of the orbit.

Our comparison has been performed considering 100 orbits whose initial conditions $(I_1(0), I_2(0))$ are uniformly distributed around the top hyperbolic border of the resonance (the parallelogram in Fig. 5.6). First, for each one of these orbits, a *reference* value of the mean MEGNO has been computed with S_4, a time step equal to $\tau = 0.01$ and over 2.5×10^6 time units. Afterwards the same orbits have been numerically integrated with both methods (GSI and RK_4) for time steps between 0.01 and 1 time units in order to obtain the corresponding MEGNO values. Eventually a comparison has been done with the reference MEGNO values to classify orbits as correctly identified or not. Orbits with MEGNO values respectively below and above 2.2 have been identified as stable and unstable. This 10 % margin above the theoretical value of 2 accounts for MEGNO values oscillating about 2 when the integration process is ended.

Meanwhile, CPU times and maximum relative errors in energy have been stored. For a given time step, the maximum relative error in energy over all

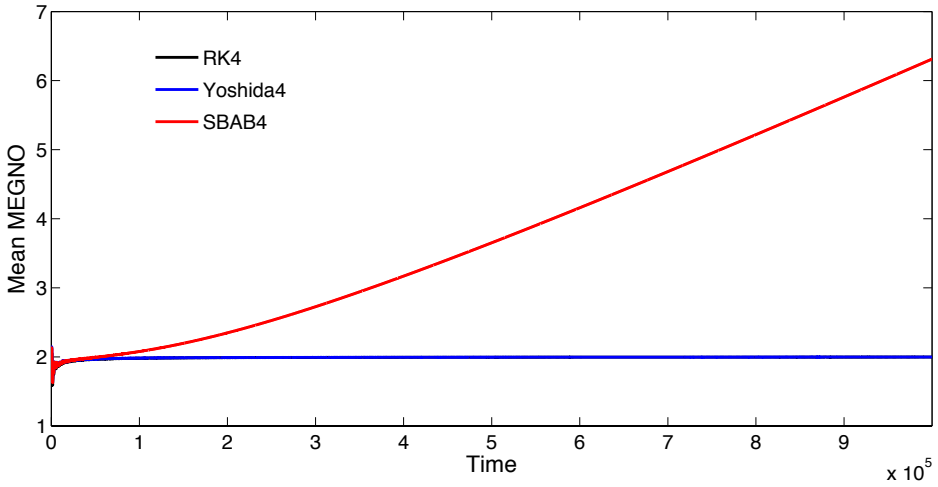

FIGURE 5.8 • *Mean MEGNO values obtained with different integration schemes. The same orbit as in Fig. 5.7 and the associated variational equations have been integrated with a time step* $\tau = 0.1$.

chosen orbits is computed as

$$\Delta E/E = \max_{\substack{0\leq t\leq 2.5\times 10^6 \\ i=1,\ldots,100}} |E_i(t) - E_i(0)|/|E_i(0)|\,, \tag{5.22}$$

$E_i(t)$ being the energy, i.e. the value of the Hamilton function $\mathcal{H}_{\text{Arnold}}$, at time t on the ith orbit. A second important indicator, related to the speed of the integration algorithm, is the total CPU time given by

$$T_{\text{CPU}} = \sum_{i=1}^{100} T^i_{\text{CPU}}\,, \tag{5.23}$$

T^i_{CPU} being the CPU time needed to integrate the ith orbit, the associated deviation vector and MEGNO for the defined time span and step.

Both indicators are reported in Fig. 5.9 as functions of the time step for the different integrators. As previously explained, the fourth order SBAB integrator performs well to integrate equations of motion and shows good energy preservation properties. This is due to the small parameter ν in the Hamiltonian function (5.20). When τ is smaller than 0.05, S_4 shows smaller energy loss than all other integrators. After that limit, $SBAB_4$ is the most precise one. It appears that S_4 always shows smaller energy loss than RK_4 integrator. Moreover, as time step increases, this difference becomes larger too. Also note that the maximum error becomes larger with RK_4 than with S_2 beyond $\tau \simeq 0.25$. That means that, even if S_2 is only a second order integrator, it is more reliable than RK_4 when using

big time steps. Another advantage of the GSI with S_2 or S_4 is the relatively low required CPU time (T_{CPU}) in comparison to RK_4. This is particularly important when considering lots of different initial conditions and long integration times as it will happen for the space debris stability study. Obviously, the lower-order S_2 asks less CPU time than S_4. The situation is different with the GSI coupled to the $SBAB_4$ integrator. The latter asking more evaluations of the exponential operators than S_4, the associated CPU time increases and is similar to the one needed by the RK_4 integrator.

From Fig. 5.10, one also concludes that the GSI with S_2 and S_4 correctly identifies more orbits than RK_4 does for large time steps. Indeed, MEGNO values computed by means of RK_4 are wrong for regular orbits when the time step is greater than 0.3. The percentage of well identified regular orbits even reaches zero while, at the same time, S_4 is still beyond 50%. This difference is less discernible for chaotic orbits: a small drift from such orbit and/or deviation direction does not provide a completely different behaviour. Let us also point out that the lower-order S_2 integrator manages to correctly identify approximately the same percentage of orbits as S_4. However, the GSI with $SBAB_4$ completely fails to detect regular orbits. This is another confirmation of the poor ability of the $SBAB_4$ to reliably integrate variational equations with large step sizes for this Hamiltonian system.

As a result, we have shown that the MEGNO criterion computed by the GSI with Yoshida's symplectic integrators is a powerful tool to characterize the regular or chaotic behaviour of orbits in Hamiltonian systems. It proves to be especially efficient for dynamics acting on long time scales like the Arnold diffusion problem.

5.4.4 Study case orbits

Before providing a stability analysis of geosynchronous space debris, we propose to apply it on three types of orbits already considered in Sec. 2.4.3. We especially focus on the MEO, XMM-like and INTEGRAL-like orbits propagated and shown in Fig. 2.8, 2.9 and 2.10. For these orbits, the comparison between $SBAB_8$ and LTOP propagations revealed differences between semi-major axis evolutions. We show in Fig. the corresponding MEGNO values obtained with the GSI (S_4) and time steps equal to 0.1 day/2π. The same perturbation model as in Sec. 2.4.3 has been used.

Each orbit is identified as chaotic. As far as the MEO is concerned, the mean MEGNO first seems to identify the orbit as stable but starts to increase after 100 yr (and keeps on increasing after 200 yr). A quick look at Fig. 2.8 shows that both orbits are indeed very close to each other at the beginning of the time span and

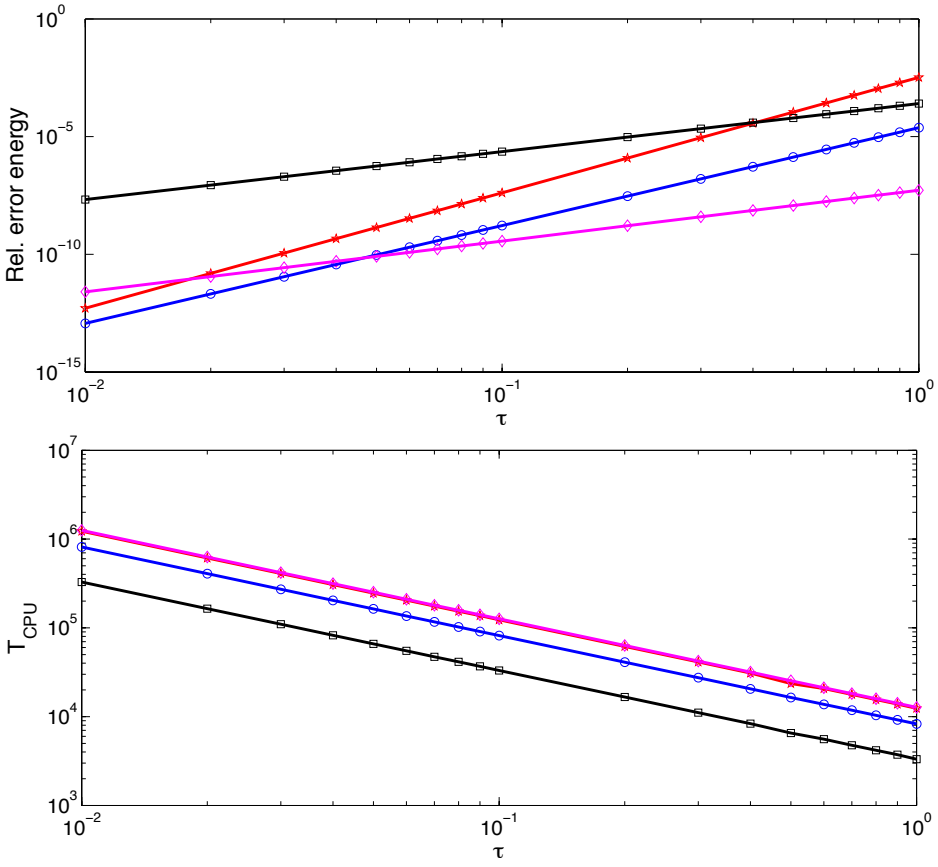

Figure 5.9 • *Maximum relative errors in energy $\Delta E/E$ (top panel) and CPU time T_{CPU} (bottom panel) as a function of the time step, in logarithmic scale. The integration time for this analysis has been set to 2.5×10^6 time units. The comparison involves 100 orbits whose initial conditions $(I_1(0), I_2(0))$ have been taken around the top hyperbolic border of the $I_1 = 2I_2$ resonance (see Fig. 5.6). Symbols are : (red) $*$ RK_4, (blue) $\bigcirc$ S_4, (black) $\square$ S_2 and (magenta) $\diamond$ $SBAB_4$.*

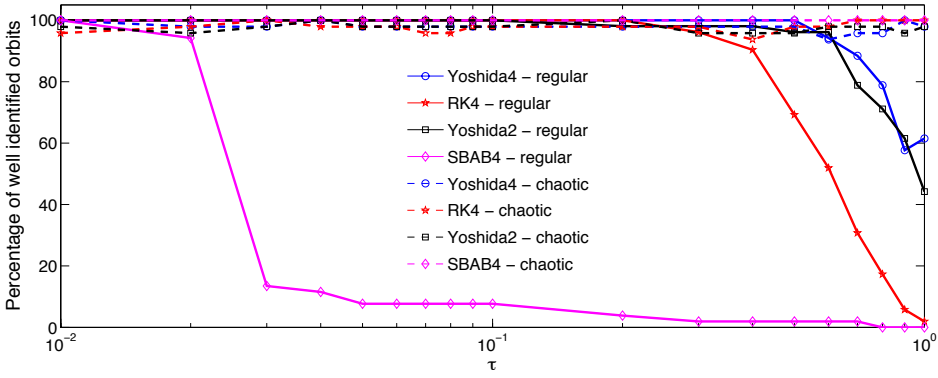

Figure 5.10 • *Percentages of correctly identified orbits with respect to time step in logarithmic scale. The comparison involves* 100 *orbits whose initial conditions* $(I_1(0), I_2(0))$ *have been taken around the top hyperbolic border of the* $I_1 = 2I_2$ *resonance (see Fig. 5.6). Solid lines and dashed lines represent respectively the identification of regular orbits and chaotic orbits.*

switch to different behaviours afterwards. Mean MEGNO values for both XMM- and INTEGRAL-like orbits increase rapidly and correspond to irregular orbits.

5.5 Geostationary space debris stability

Now that the GSI has been successfully tested in various situations, we can try to determine whether space debris situated in the near geostationary region are stable or not. First it is necessary to describe the global behaviour in this region without considering Earth's shadows. Then, we add shadow crossings into the model and discuss the results.

Similarly to Sec. 3.3, each MEGNO computation with shadow crossings is done with short time steps (0.01 day/2π). Indeed, typical shadow crossings at the geostationary altitude last less than one hour, representing only a small fraction of the complete orbital period. Let us also mention that either JPL ephemerides or an analytical model could be used to compute third body positions. However, due to compatibility issues with the computer cluster, chaos maps are performed using the analytical model described in Sec. 2.2. For the sake of completeness, both ephemerides have been tested separately on a single computer and gave the same results.

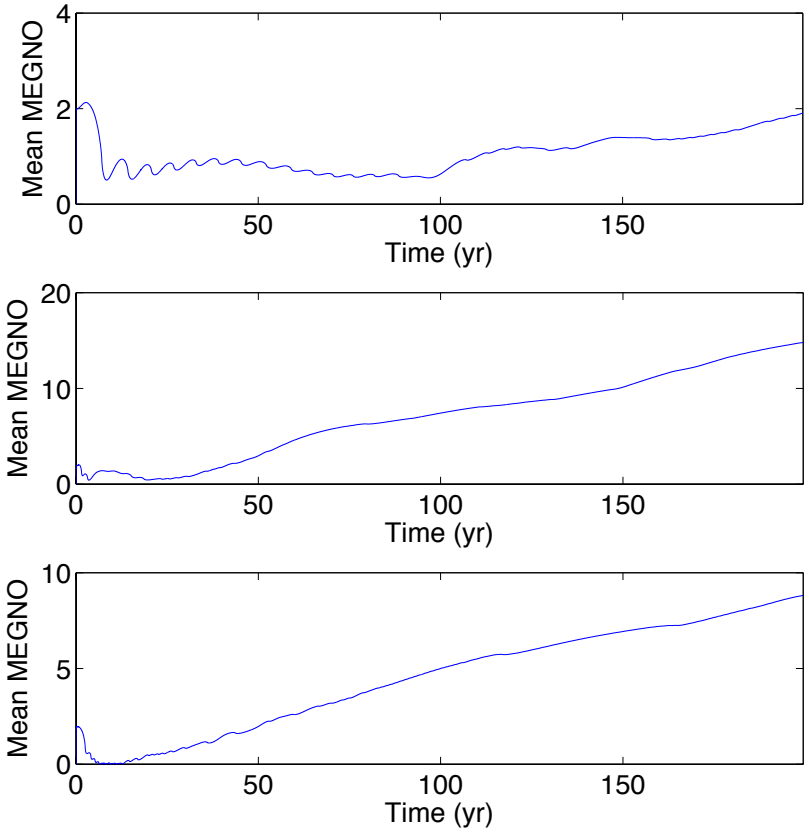

Figure 5.11 • *MEGNO computed with the GSI (S_4) for a MEO orbit (top), a XMM-like orbit (middle) and a INTEGRAL-like orbit (bottom). The perturbations and parameters correspond to the ones used in Sec. 2.4.3.*

5.5.1 Geostationary region

Each chaos map presented in this section is performed on a grid of initial osculating semi-major axes a and resonant angles $\sigma_{\rm res}$. As stated by Breiter et al. (2005b), the presence of the 1:1 mean motion resonance makes it a convenient choice. The resonant angle $\sigma_{\rm res}$ is defined as $\lambda - \theta$ where λ and θ are respectively the initial mean longitude and sidereal time. Around the geostationary altitude, both angle frequencies are very close to each other. Besides, the AMR will be fixed to 5 m^2/kg to enable comparisons with the map shown in Valk et al. (2009) (Fig. 6).

First, we reproduce the same map as in Valk et al. (2009) with the GSI (S_4) in Fig. 5.12. The model includes the central body attraction, the geopotential up to degree and order 2, luni-solar perturbations and SRP without Earth's shadows. As pointed out by Valk et al. (2009), this two-dimensional space $(\sigma_{\rm res}, a)$ is characterized by separatrices (already identified in Breiter et al. (2005b)) and an additional pattern inside the *eye of the resonance*. Due to the important amount of CPU time needed, we only plot a horizontal range of 160 deg. Hence we only see one eye of the typical double pendulum-like pattern related to the 1:1 resonance. The large AMR is responsible for the stochastic zones in the neighborhood of the separatrices. Based on both MEGNO criterion and frequency map analysis (Laskar 1990, Laskar 1995), the pattern inside the resonance has been explained by secondary resonances due to commensurabilities between the resonant angle and the ecliptic longitude of the Sun (Lemaitre et al. 2009). The fact that all these particular patterns are found back in Fig. 5.12 confirms that our method provides accurate stability results. The distorsion of the resonance eye can be explained by the use of osculating initial semi-major axes. Indeed, it is shown that mean initial semi-major axes get rid of this *short-period artifact* (Valk et al. 2009). As it does not prevent us from studying the influence of the Earth's shadow on such maps, we will keep using osculating initial conditions in this work.

Computing the MEGNO for such a huge number of initial conditions is excessively time consuming. Hence, propagations realized in Valk et al. (2009) usually stopped at 30 yr. Here we push it further and show the final values of the MEGNO after 300 yr in Fig. 5.13 (top). For the MEGNO scale is rather large, we show in Fig. 5.13 (bottom) the same map plotted with maximum MEGNO values equal to 3, i.e. all MEGNO values bigger than 3 are drawn with the same color. It lets us emphasize the presence of stable orbits when there is no umbra even after 300 yr.

In order to numerically check our conclusions about eq. (5.16) (referring to the difference between the MEGNO obtained with either the rectangular or trapezoidal quadrature method), the same map has been realized using (5.12)-(5.13) and (5.14)-(5.15) formulae. As already explained in Sec. 5.3.3, the difference between (5.12) and (5.14) should be higher for chaotic orbits and decrease as time

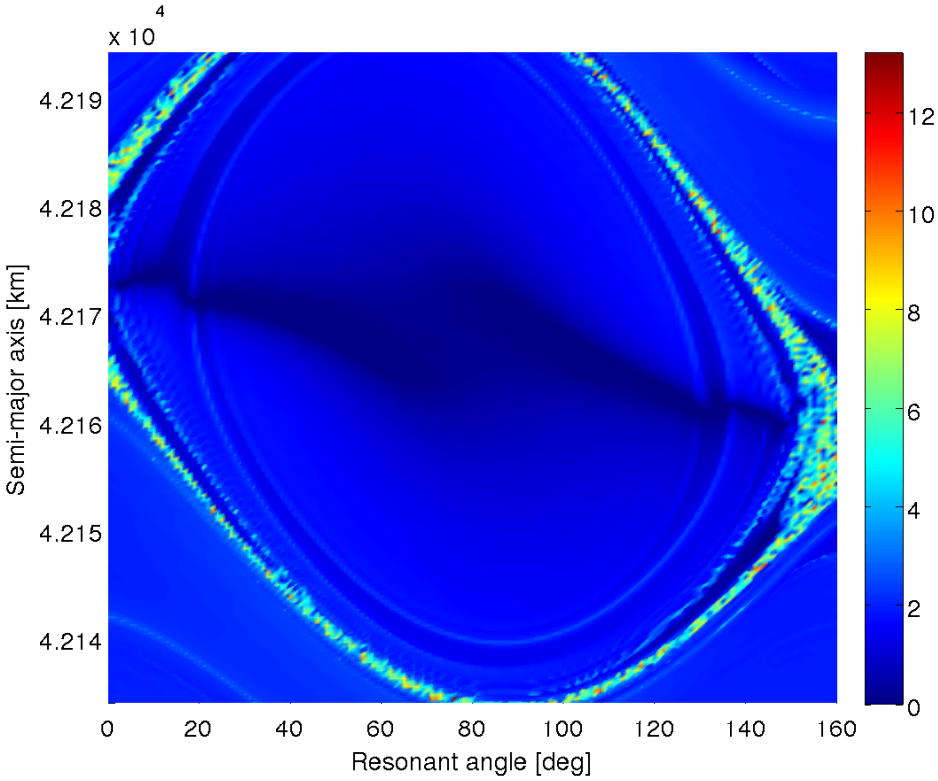

Figure 5.12 • *Stability analysis of the two-dimensional plane* (σ_{res}, a) *represented using MEGNO values at* 30 *yr without Earth's shadows. A set of* 160×160 *uniformly distributed initial conditions has been integrated with* S_4 *with time steps equal to* 0.05 *day*$/2\pi$*. Other initial conditions are fixed to* $e = 0.002$*,* $i = 0.004$ *rad and* $\Omega = \omega = 0$ *rad. The value of the initial sidereal time* θ *is determined by the initial time epoch at* 25 *January* 1991*. The model includes the central body attraction, the geopotential up to degree and order* 2*, luni-solar perturbations and SRP with the AMR equal to* 5 m^2/kg*. Same representation as in Valk et al. (2009)*

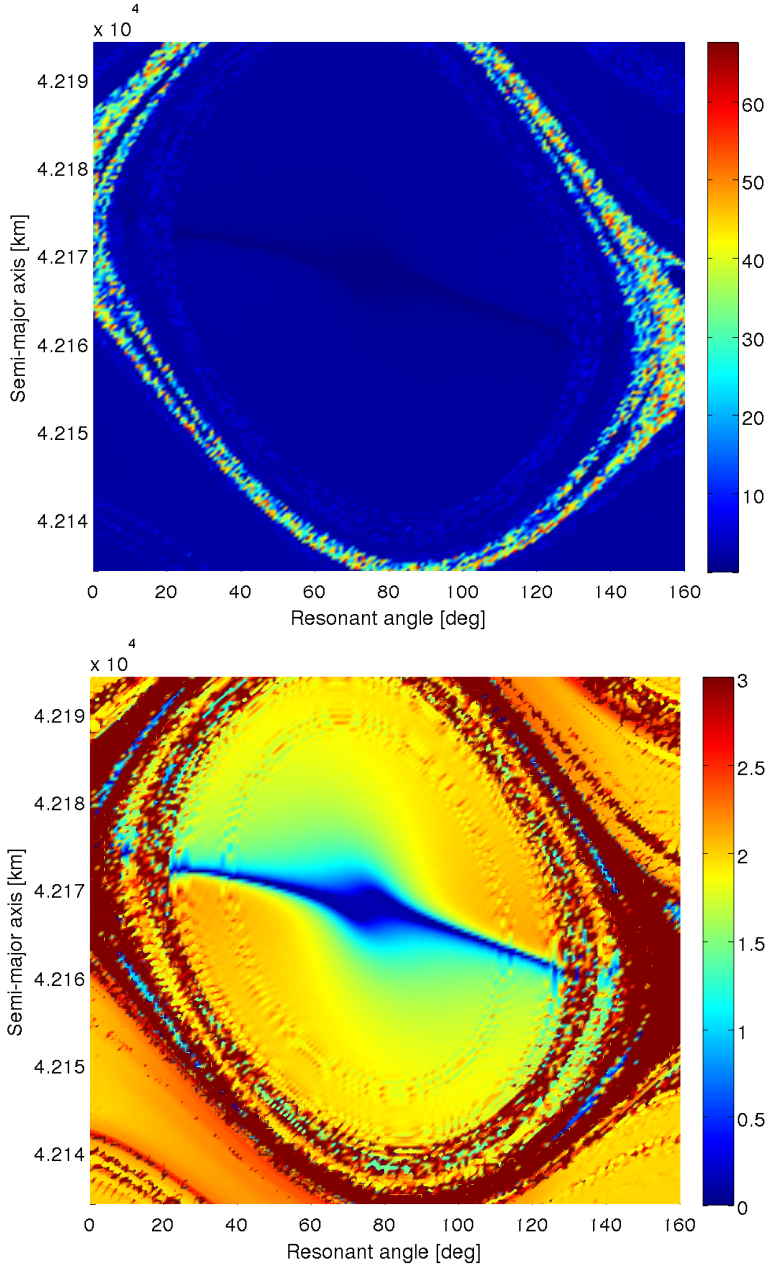

Figure 5.13 • *Stability analysis of the two-dimensional plane* (σ_{res}, a) *represented using real (top) and cut off (bottom) MEGNO values at* 300 *yr without Earth's shadows. A set of* 160×160 *uniformly distributed initial conditions has been integrated with* S_4 *with time steps equal to* 0.05 *day*$/2\pi$*. Other initial conditions are fixed to* $e = 0.002$*,* $i = 0.004$ *rad and* $\Omega = \omega = 0$ *rad. The value of the initial sidereal time* θ *is determined by the initial time epoch at* 25 *January* 1991*. The model includes the central body attraction, the geopotential up to degree and order* 2*, luni-solar perturbations and SRP with the AMR equal to* 5 m^2/kg*.*

increases. It can be observed in Fig. 5.14 that the same behaviour holds with the time-average MEGNO. Though relatively small, differences are larger on the separatrices than in other regions of the plane and are smaller in the center of the resonance. Moreover, it can be seen that differences between both methods are larger at 30 yr than at 300 yr. As a conclusion, even if the gain obtained with (5.14) and (5.15) does not seem to be so relevant on such long time scales (remember that one complete revolution is close to one sidereal day at this altitude), the fact that the trapezoidal and rectangular rules ask the same number of evaluations of the variational equations makes (5.14) and (5.15) suitable formulae.

5.5.2 Earth's shadowing effects

Earth's shadow crossings are modeled by multiplying $\vec{\nabla}_{\vec{r}}\mathcal{H}_{\rm srp}(\mathbf{r})$ by the shadow function $\nu(\mathbf{r})$ in space debris equations of motion. The shadow function $\nu(\mathbf{r})$ has been specifically designed as a smooth function so that variational equations can be safely computed. Considering both cylindrical and conical shadow models, we show in Fig. 5.15 the $(\sigma_{\rm res}, a)$ plane for an integration time of 30 yr. As already explained, smaller time steps (0.01 instead of 0.05 day$/2\pi$) are required in this case because of short shadow crossings. As a matter of fact, the chaos map obtained with the cylinder-shaped umbra leads to unrealistic results. The entire map is filled with chaotic orbits, at the exception of very few stable orbits located on the separatrices (Fig. 5.15, top). Since the cylindrical shadow makes $\nu(\mathbf{r})$ switch very rapidly between 1 or 0 values, one can reasonably assume that this succession of fast changes in both equations of motion and variational equations disturbes the evolution of the MEGNO criterion which is not able to correctly distinguish between regular and chaotic orbits. The Lyapunov time does not increase as we get closer to the center of the resonance eye. In light of this, the cylindrical shadow model should not be used to study the stability of space debris motion.

Fortunately, conical Earth's shadows are modeled by softer umbra-penumbra transition phases. In this case, the shadow function is smooth and is well handled by the MEGNO. As illustrated in Fig. 5.15 (bottom), the structure of the two-dimensional plane is preserved. However, chaotic regions around the separatrices are larger.

Then, we analyze the long term stability of space debris subject to conical Earth's shadows. To that end, Fig. 5.16 (top) gives MEGNO values obtained after 300 yr with conical shadows. While the long-term two-dimensional space without Earth's shadows remains mainly unchanged after 300 yr (see Fig. 5.13), the situation is totally different in the other case. Indeed, nearly all orbits are identified as chaotic. For the sake of clarity, the same map is plotted with MEGNO values cut off to 3 (Fig. 5.16 (bottom)). A close look to data shows that only 10 initial conditions lead to a final MEGNO value smaller than 2. Hence, the GSI

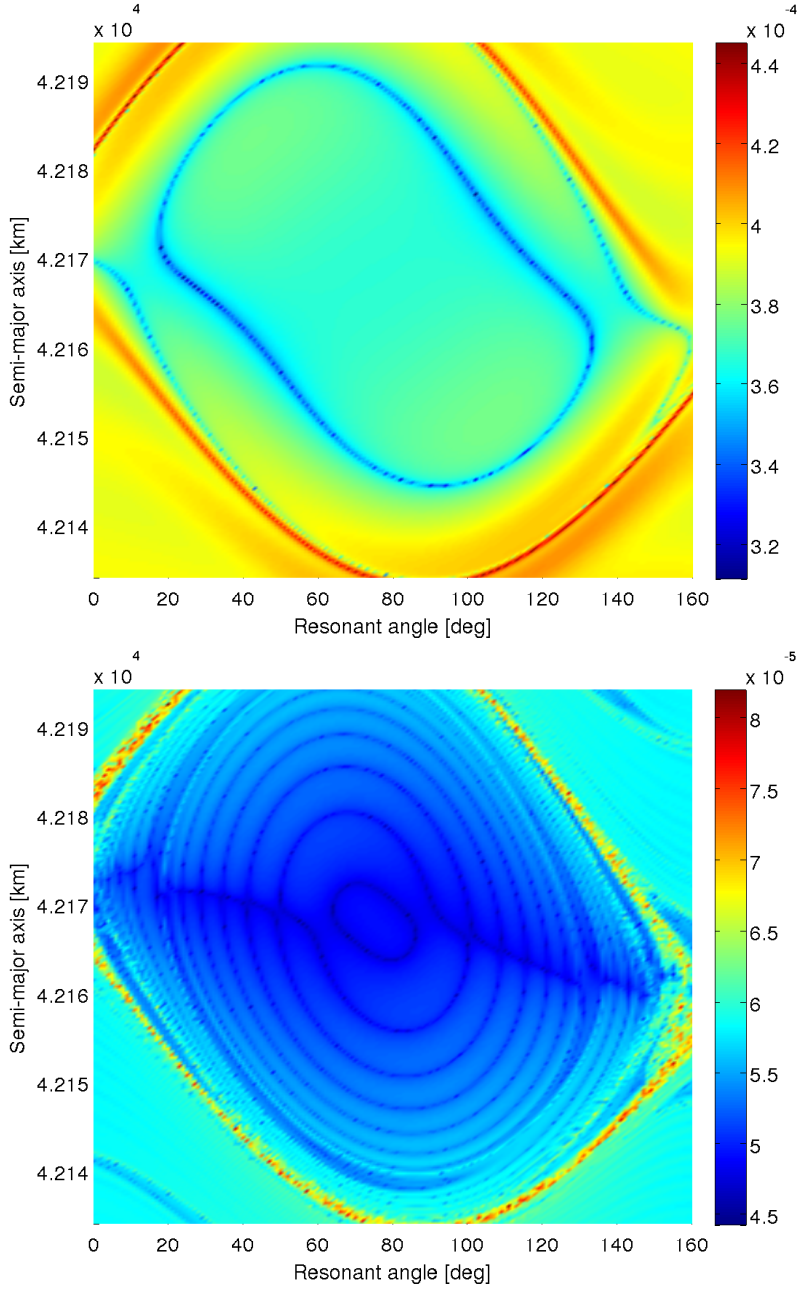

Figure 5.14 • *Stability analysis of the two-dimensional plane* (σ_{res}, a) *representing the difference between MEGNO values obtained by (5.13) and (5.15) methods at* 30 *yr (top) and* 300 *yr (bottom). Other initial conditions, perturbations model, time steps and integrator are chosen as in Fig. 5.12.*

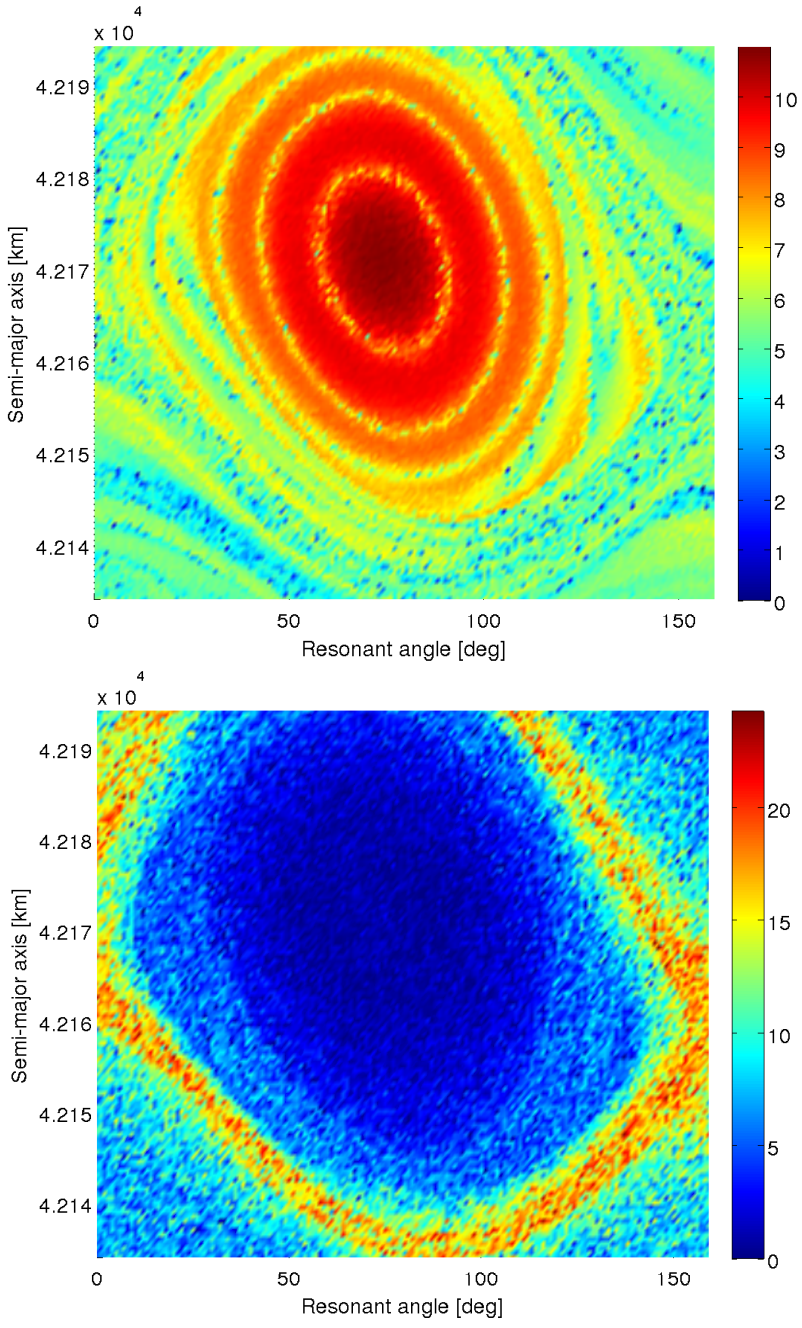

Figure 5.15 • *Stability analysis of the two-dimensional plane* (σ_{res}, a) *represented using MEGNO values at* 30 *yr (GSI) with Earth's shadows. Other initial conditions and integrator are chosen as in Fig. 5.12 with time steps equal to* 0.01 *day*$/2\pi$*. The model includes the central body attraction, the geopotential up to degree and order* 2*, luni-solar perturbations and SRP with the AMR equal to* 5 m^2/kg *with cylindrical (top) and conical (bottom) Earth's shadows.*

tells us that the introduction of Earth's shadowing effects greatly influence the behaviour of space debris orbits. As time increases, chaotic areas around the separatrices grow and even the center of the resonance seems to become unstable.

The robustness of our results with respect to the cone-shaped Earth's umbra model has been investigated further. Different values of the accuracy parameter δ defined in eq. (3.9) have been considered. The chosen reference value is $\delta = 8$, corresponding to the accuracy threshold $\sigma = 1 - \tanh\delta = 2.25 \times 10^{-7}$. First, relatively close values have been chosen. One percent difference gives two values of δ equal to 7.92 and 8.08, giving respectively $\sigma = 2.64\times10^{-7}$ and $\sigma = 1.91\times10^{-7}$. That leads to quasi-similar results (slightly lower and higher final MEGNO values respectively) and data are not reported. Choosing δ equal to 7 or 8 yields to one order of difference for the accuracy parameter: $\sigma = 1.66 \times 10^{-6}$ and $\sigma = 3.04 \times 10^{-8}$. We show in Fig. 5.17 the MEGNO values obtained in this case. Due to the large requested CPU time, it has been decided to only compute one portion of the two-dimensional plane $(\sigma_{\rm res}, a)$ ($\sigma_{\rm res} <= 70$ deg) with these new values. Maps obtained with δ equal to 7 or 8 are compared to the previous one (Fig. 5.16) obtained with $\delta = 8$. Even if differences are visible (mostly for $\delta = 9$ which tends towards a cylindrical model), the global behaviour of the stability map remains unchanged. We are pretty confident that the stability analysis reported here is not influenced by small variations of the shape of the shadow.

For comparison, the same analysis has been performed with two non-symplectic methods. Even if the long time span means a potential important loss of accuracy, such comparisons are helpful. First, we again resorted to NIMASTEP which was improved (version 6.11) to compute the Jacobian matrix of the piecewise shadow function of Montenbruck and Gill (2005) and enable the use the MEGNO indicator with conical shadows. This piecewise shadow function is computed from the angular separation and diameters of the Sun and the Earth. Distributions theory (Schwartz 1966) can be used to assess the derivatives of the function around the discontinuity points. The $\rm ABM_{10}$ integrator (Hairer et al. 1993) is used with time steps equal to 2 min and the initial conditions are the same as previously. MEGNO values after 300 yr (see Fig. 5.18) reveal that the entire $(\sigma_{\rm res}, a)$ plane is filled with chaotic orbits (a few number of stable orbits in the vicinity of the stable equilibrium excepted). The global behaviour is in agreement with our previous study.

The last comparison involves the BS integrator with the $\nu_{\rm p}$ (3.10) shadow function. This code is not included into NIMASTEP. Unfortunately, a small approximation was necessary to use BS with our model. Indeed, the JD (essential to call ephemeris subroutines) is currently passed as an argument at the beginning of the time step and updated for the next time step. However, the BS integrator works with a large number of substeps where the JD should be accordingly modified. Despite this approximation, the resulting MEGNO values (see Fig. 5.19, bottom) are in agreement with what is shown in Fig. 5.18 with NIMASTEP.

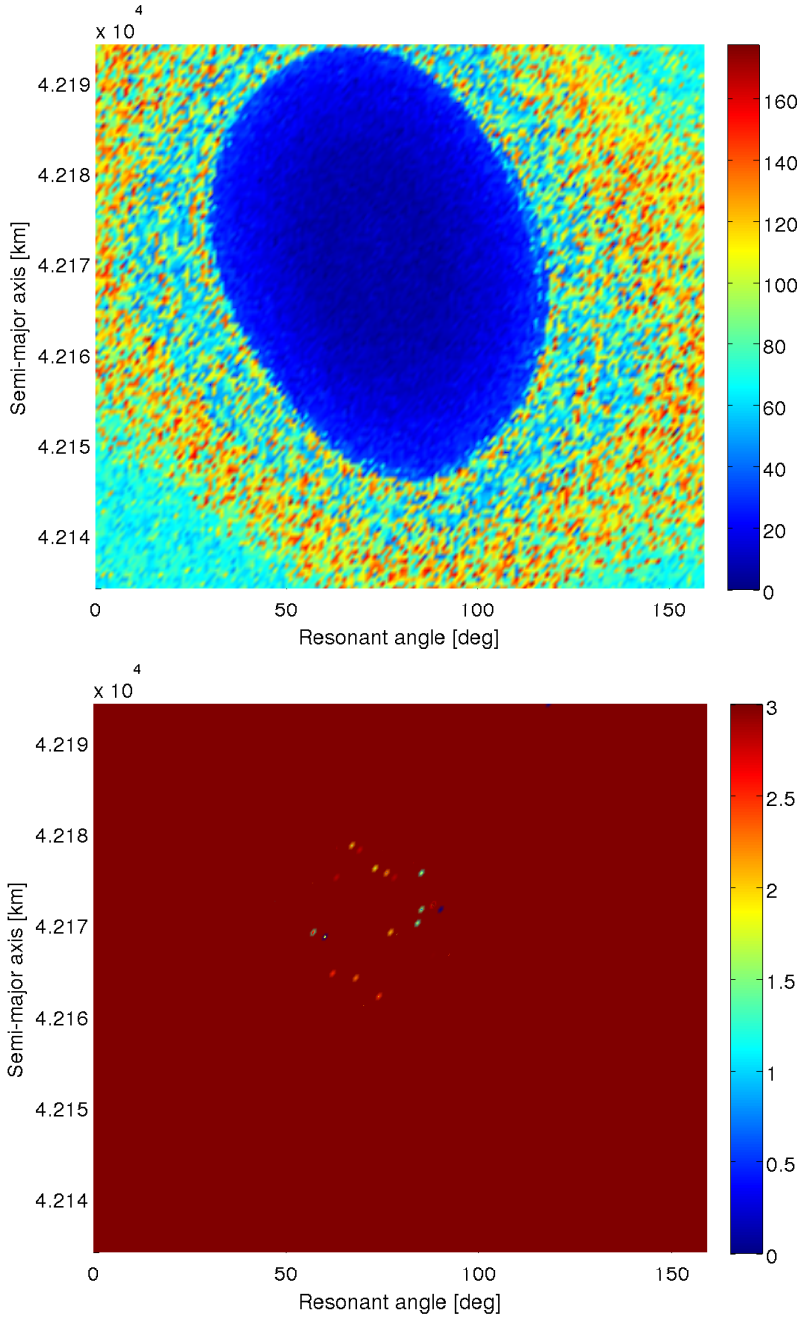

Figure 5.16 • *Stability analysis of the two-dimensional plane* (σ_{res}, a) *represented using real (top) and cut-off (bottom) MEGNO values at* 300 *yr (GSI). Other initial conditions, integrator and time steps are chosen as in Fig. 5.15. The model includes the central body attraction, the geopotential up to degree and order* 2*, luni-solar perturbations and SRP with the AMR equal to* 5 m^2/kg *with conical Earth's shadows.*

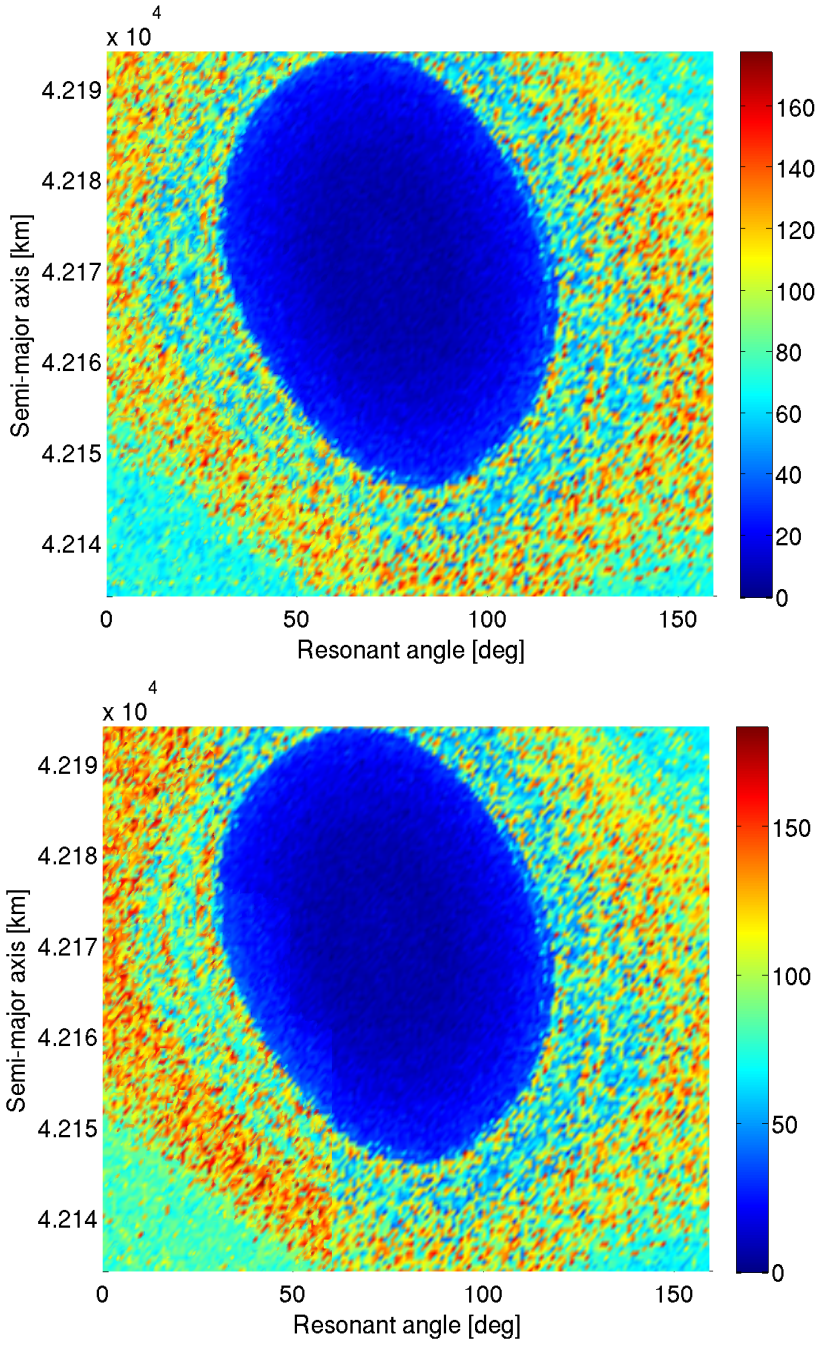

Figure 5.17 • *Stability analysis of the two-dimensional plane* (σ_{res}, a) *represented using MEGNO values at* 300 *yr without Earth's shadows. Portions of maps* ($\sigma_{res} <= 70$ *deg) obtained with values of* $\delta = 7$ *(top) and* $\delta = 9$ *(bottom) are compared to portions of maps obtained with* $\delta = 8$ ($\sigma_{res} > 70$ *deg). Other initial conditions, perturbations model, time steps and integrator are chosen as in Fig. 5.16.*

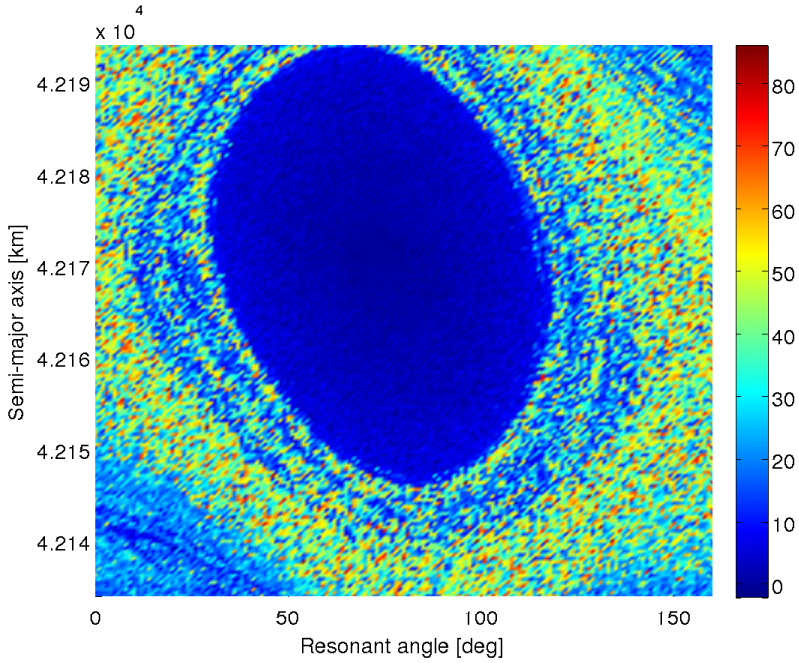

Figure 5.18 • *Stability analysis of the two-dimensional plane* (σ_{res}, a) *represented using MEGNO values at* 300 *yr. Other initial conditions are chosen as in Fig. 5.12. The NIMASTEP software* (ABM_{10}) *has been used with time steps equal to* 2 *min. The model includes the central body attraction, the geopotential up to degree and order* 2*, luni-solar perturbations and SRP with the AMR equal to* 5 m^2/kg *with conical Earth's shadows (Montenbruck's formulation).*

However stable orbits are identified right in the center of the resonance eye. This behaviour is similar to the one observed in Sec. 5.4.2 where the BS failed at identifying irregular orbits unless a very tiny accuracy parameter was chosen. As with the GSI, the rest of the two-dimensional plane is also identified as chaotic. Out of curiosity, the BS has also been tested with the adjusted time step method described in Appx. C. As shown in Fig. 5.19 (top), the MEGNO map is very analog to the results obtained with the GSI in Fig. 5.15 (top). It confirms that the cylindrical shadow model seems unfit to analyze the stability of space debris with shadow crossings. The vertical line appearing around $\sigma_{\text{res}} \simeq 35$ deg corresponds to missing data due to technical problems with the computer cluster.

Eventually, one could wonder if the same results hold for space debris with much lower AMR. A comprehensive and systematic approach showing stability results for increasing values of the AMR over 300 yr is unrealistic in terms of CPU time. However, one can reasonably suppose that, the lower the AMR, the more regular space debris orbits. More insight about this assumption is brought by

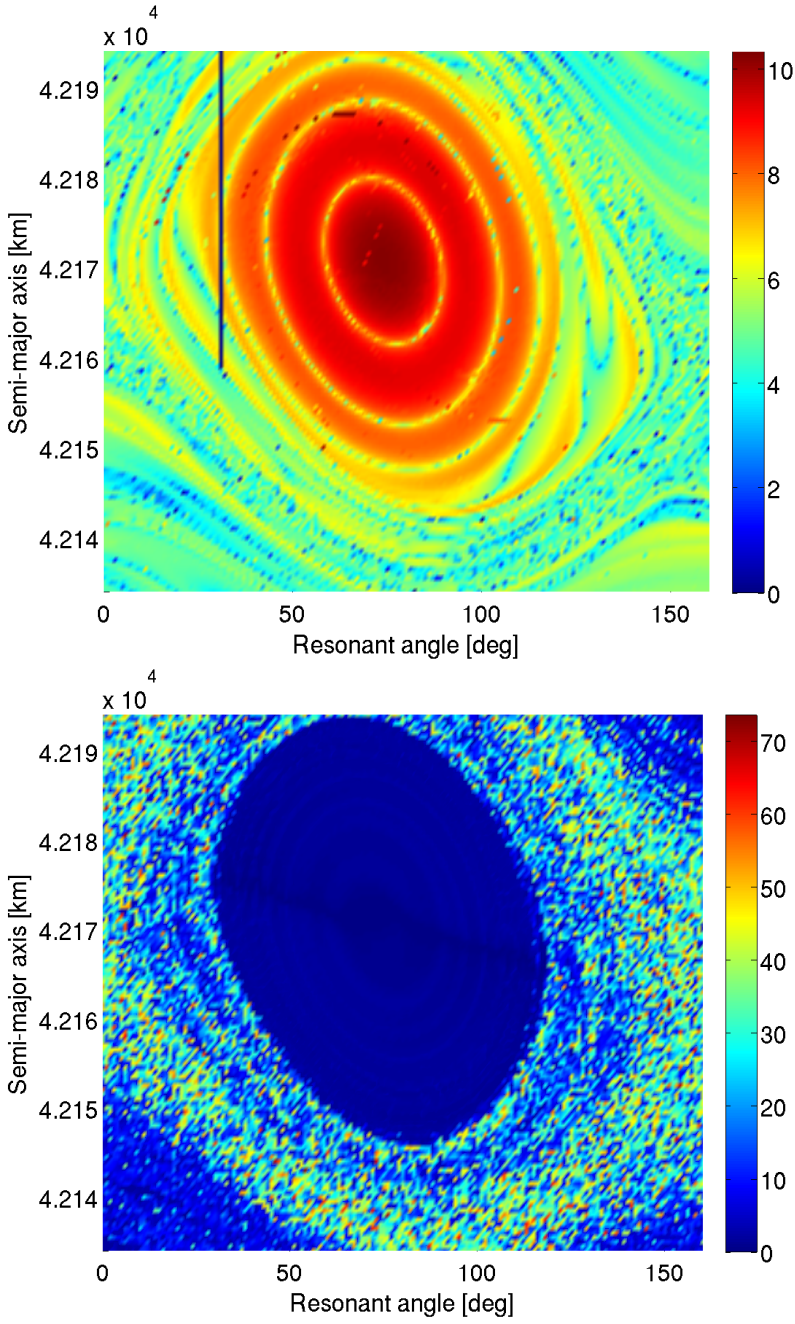

Figure 5.19 • *Stability analysis of the two-dimensional plane* (σ_{res}, a) *represented using MEGNO values at* 30 *yr (top) and* 300 *yr (bottom). Other initial conditions are chosen as in Fig. 5.12. The BS integrator has been used with the accuracy parameter equal to* 10^{-8}*. The model includes the central body attraction, the geopotential up to degree and order* 2*, luni-solar perturbations and SRP with the AMR equal to* 5 m^2/kg *with cylindrical (top) and conical (bottom) Earth's shadows.*

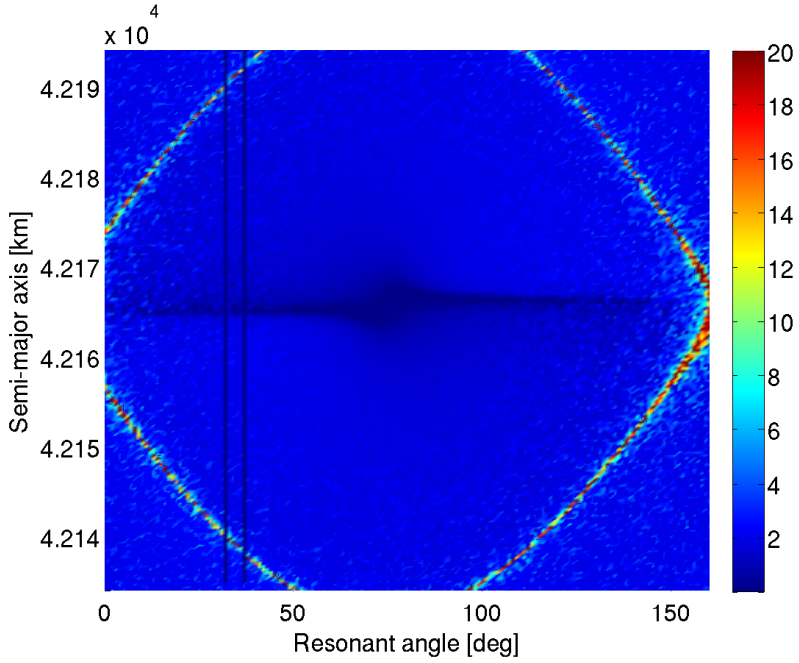

Figure 5.20 • *Stability analysis of the two-dimensional plane* (σ_{res}, a) *represented using MEGNO values at* 30 *yr (GSI). Other initial conditions, integrator time steps are chosen as in Fig. 5.16. The model includes the central body attraction, the geopotential up to degree and order* 2*, luni-solar perturbations and SRP with the AMR equal to* 0.01 m^2/kg *with conical Earth's shadows.*

means of a stability map realized with the AMR set to 0.01 m^2/kg. The results are shown in Fig. 5.20 after 30 yr. A quick look to Fig. 5.15 (bottom) confirms that the thick chaotic separatrix has given way to more constraint irregular motion. Again, both vertical lines appearing around $\sigma_{\rm res} \simeq 35$ deg and $\sigma_{\rm res} \simeq 40$ deg are due to missing data.

5.6 Conclusion

The GSI has been built to compute Lyapunov-like chaos indicators evolution on long time scales in the framework of symplectic integration schemes. Already introduced in Libert et al. (2011) and developed further to compute the MEGNO, it makes possible the simultaneous symplectic integration of both equations of motion and variational equations. Through several comparisons presented in Libert et al. (2011) and in this chapter, the GSI could be successfully validated and we

argue that the GSI with Yoshida's family of symplectic integrators is best suited to study the stability of dynamics associated to a generic Hamiltonian and acting on long time scales.

Then, the influence of Earth's shadowing effects on space debris dynamics has been investigated. Both adapted conical and cylindrical smooth shadow functions have been used. While the cylindrical model yields unreliable orbital behaviour, the conical model has proven to be well handled by the MEGNO. This more realistic umbra-penumbra transition model highlights that Earth's shadows greatly affect the stability of space debris with high AMR (5 m^2/kg). Due to shadow crossings, it has been shown that chaotic regions around the separatrices in the (σ_{res}, a) plane become larger as time evolves. The evolution of high AMR geostationary space debris turns out to be chaotic, the short-time resonance eye disappearing on long time scales. A last simulation has also shown that lower AMR values (namely 0.01 m^2/kg) greatly reduce the amount of chaotic orbits.

Different integrators and shadowing models have been compared to each other. While the same global unstable behaviour has been obtained, the center of the resonance eye has been identified as chaotic with the GSI and ABM but stable with BS. A lot of time has been spent on the validation of the GSI and we are pretty confident of its accuracy even on long time spans. Due to the huge number of orbital periods occuring over 300 yr in the GEO ring, the ABM and BS integrators lose precision as time increases. Moreover, the BS integrator had to be computed with a little approximation. In light of this, we believe that the GSI stability characterization is correct. One must stay careful though, as no analytical tool lets us discriminate between both possible situations.

Chapter 6
Conclusion

6.1 Synthesis

This thesis aimed to understand the long term evolution of space debris especially for near GEO characterized by high AMR. Due to the complexity of dealing with Earth's shadow crossings we mainly resorted to completely numerical or semi-analytical methods. In a first phase, we developed the necessary tools. Then the analysis of debris motion could be performed.

Given the targeted (extremely) long time span, it seemed pertinent to resort to symplectic integration schemes. Hence we first built our symplectic propagator. We have shown that several perturbations could be taken into account: Earth's geopotential, direct SRP and third body gravitational attractions. Through comparisons with other schemes, the accuracy of the integrator has been validated. The main advantage of our scheme lies in its excellent energy preservation properties which gives trustworthy propagations nearly regardless of the period of time. Moreover, orbits being nearly circular for near-geostationary orbits, bigger step sizes can be used with respect to other tested propagators.

An innovative analytical theory has been proposed to model both cylindrical and conical Earth's shadow crossings. It has been shown that the smooth shadow functions are well adapted to the symplectic scheme and do not yield any long term drift in the energy error (and hence on the semi-major axis). This method is also totally compatible with non symplectic integrators. Moreover, this method is suitable for stability studies requiring the computation of the variational equations.

Several tests with the symplectic propagator including Earth's shadows revealed unexpected long term periodic behaviour. Hence a semi-analytical method has been developed to understand the underlying dynamics. This model let us discover the strong link between the period of this peculiar motion and the angular evolution of the difference between Earth's shadow exit and entrance eccentric

anomalies. A comparison between the complete numerical propagation and semi-analytical model gave results in good agreement.

Then, we improved the GSI method (Libert et al. 2011) by discussing the right choice of symplectic integrator and proposing a convenient way to compute the fast and reliable MEGNO chaos indicator. This tool has been validated through several test cases showing its excellent ability to identify orbits behaviour even on long time scales. It has been applied to produce two-dimensional stability maps of the near-geostationary altitude. Both cylindrical and conical shadow models have been tested. Both the GSI and the non-symplectic scheme highlighted the poor usability of the cylindrical model in this framework. However, the conical shadow model seems well handled by the GSI. Simulations with a high AMR (5 m^2/kg) let us see the strong influence of shadow crossings on space debris stability. Chaotic zones around the separatrices of the 1:1 resonance (already present without shadows) grow and progressively fill the entire plane, destroying the resonant structure. It should be noted that the lower the AMR values (a simulation was performed with an AMR around 0.01 m^2/kg), the more regular the orbits in the plane. In this case, chaotic orbits are mainly confined around the thin separatrices.

Eventually, a brief presentation of our work in collaboration with the celestial mechanics team of the University of Pisa has been proposed. While this work is still in progress, it presents an elegant way to solve the Stark problem involving a typical Keplerian problem where the orbiting object is also subject to a constant force.

6.2 Limitations

It is well known that symplectic schemes do not easily handle variable step sizes. However, given the short time spent in shadow crossings, it would be particularly useful to be able to use larger time steps when not in shadow seasons or outside shadow crossings. Eccentric orbits also require smaller time steps. The other main drawback of our symplectic scheme is its current inability to add non conservative perturbations like the atmospheric drag. That makes LEO impossible to propagate.

The periodic motion discovered in Chap. 4 should be understood as a theoretical contribution to the understanding of space debris motion. It is obvious that the frequency highlighted in this part of our work only plays a small role in the complex set of all the perturbations acting on space debris motion. Moreover, we must keep in mind that the orbital behaviour of high AMR debris is identified as non predictable (see Chap. 5).

The semi-analytical model should not replace a more efficient numerical integration where the complete motion is actually taken into account. Moreover, near zero eccentricites and inclinations can lead to undefined orbital elements and break the numerical propagation.

Even if a lot of tests have been made to validate our tools, the stability results obtained about near-geostationary debris orbits should be carefully considered. Faced with the difficulty to assess such orbit behaviour in an analytical way, each result has been obtained numerically without any analytical background to support our claims. We have seen that slightly different results have been obtained with non symplectic methods. The shadow crossing model also plays a significant role.

6.3 Perspectives

Immediate perspectives arise from the aforementioned limitations. Based on the works already cited in Sec. 2.5, the variable step-size and atmospheric drag issues could be investigated further in this framework. The symplectic propagator would then become an extremely interesting propagator for nearly all types of orbits.

Another point of interest is the characterization of the difference between Earth's shadow exit and entrance eccentric anomalies. Such anomalies are solutions of the shadow function (3.6). Any bearable explicit form of (most likely the difference between) these angles would let us express our semi-analytical model in a more complete way and facilitate further analytical theories. It could lead to a way of computing the LCE for debris crossing Earth's shadows.

It is currently extremely difficult to have access to actual debris populations. Hence it turns out nearly impossible to confront any result obtained numerically to real debris positions. Building a synthetic space debris population would certainly be an interesting application of our propagation technique. Probabilistic methods developed at NAXYS to build a synthetic population of the Belgium population could be easily adapted to space debris framework. TLE could be used as a starting point. The evolution of each orbit and collision risk could be modelled in order to render an artificial population on which one could freely play and test our numerical models. Interesting related sources are Rossi (2005) and Klinkrad (2006).

Our stability investigations about near-geostationary debris could be extended to other types of orbits. While standard guidelines have been issued by the IADC for GEO disposal orbits, the situation is different for MEO on which GPS and

GALILEO navigation satellites stay. Existing works on this topic have already been published (among which one can cite Chao and Gick 2004, Saunders et al. 2005, Rossi 2008, Jenkin and McVey 2009, Anselmo and Pardini 2011 and Deleflie et al. 2011) and should be considered as a starting point.

Eventually, extending the study of the Stark problem to more complex models and adding shadow crossings could constitute a very interesting alternative to completely numerical propagation techniques.

Appendices

Appendix A

Units, acronyms and notations

This appendix gives detailed lists of units, acronyms and notations that are often used in this document.

A.1 Units

Notation	Meaning
deg	Degree
g	Gram
m	Meter
N	Newton
rad	Radian
s	Second
yr	Year
UD	Unit of Distance
UM	Unit of Mass
UT	Unit of Time

A.2 Acronyms

Acronym	Meaning
ABM	Adams-Bashforth-Moulton
AMR	Area-to-Mass Ratio
AU	Astronomical Unit
BS	Bulirsch-Stoer
CBH	Campbell-Baker-Hausdorff
CPU	Central Processing Unit
ESA	European Space Agency
ESOC	European Space Operations Centre
FLI	Fast Lyapunov Indicator
GALI	Generalized ALignment Index
GEO	Geostationary Orbit
GSI	Global Symplectic Integrator
GPS	Global Positioning System
GTO	Geostationary Transfer Orbit
IADC	Inter-Agency Space Debris Coordination Committee
JD	Julian Day
LCE	Lyapunov Characteristic Exponent
LEO	Low Earth Orbit
LTOP	Long-Term Orbit Propagator
MEGNO	Mean Exponential Growth Factor of Nearby Orbits
MEO	Medium Earth Orbit
MJD	Modified Julian Day
NIMASTEP	Numerical Integration of the Motion of Artificial Satellites orbiting a TElluric Planet
SALI	Smaller ALignment Index
SRP	Solar Radiation Pressure
SSN	US Space Surveillance Network
RK	Runge-Kutta
RTBP	Restricted Three-Body Problem
TLE	Two-Line Element

A.3 Notations

As the same notation sometimes appears in different contexts, we point out the chapters where the notation is valid. Temporary notations are not listed in the table.

Notation	Meaning	Chapter
$\mathbb{1}$	Identity operator	2
a	Semi-major axis	2, 3, 4, 5
A, B	Integrable parts of the Hamiltonian	2, 3,5
$\mathcal{A}$, $\mathcal{B}$	Integrable parts of the variational Hamiltonian	5
$\mathbb{A}$	Debris area	2, 3, 4, 5
$a_\odot$	1 AU	2, 4
α	Angle between the umbra cylinder and the umbra cone	3
β	Angle between the umbra cylinder and the penumbra cone	3
c_i, d_i	Symplectic integrator parameters	2,5
C_{nm}	Spherical harmonics coefficient	
C_r	Reflectivity coefficient	2, 4
$D = E_2 - E_1$	Difference of shadow exit and entrance eccentric anomalies	4
δ	Accuracy parameter	3
δ	Norm of $\vec{\delta}$	5
$\vec{\delta} = (\vec{\delta}_p, \vec{\delta}_q)$	Deviation vector	5
e	Eccentricity	2, 3, 4, 5
E	Eccentric anomaly	2, 3, 4
ϵ	Earth's obliquity	4
ε	Small parameter	2, 5
η	Auxilary function	4
E_1, E_2	Shadow entrance and exit eccentric anomalies	3, 4
f	True anomaly	2, 3
$(\vec{f}, \vec{g}, \vec{h})$	Equinoctial reference frame	3
$g = \omega$	Delaunay's angle	4
$G = L\sqrt{1-e^2}$	Delaunay's action	4
$\mathcal{G}$	Gravitational constant	2,5
γ	Precision parameter	3
$\gamma(t)$	Arc of an orbit of flow	5
$h = \Omega$	Delaunay's angle	4
$H = G\cos i$	Delaunay's action	4
$\mathcal{H}$	Hamiltonian	2
$h_e = e\sin(\Omega + \omega)$	Equinoctial element	3
i	Inclination	2, 3, 4, 5
(I_1, I_2, I_3)	Arnold Hamiltonian momenta	5
$\mathcal{J}$	Standard symplectic matrix	5

$\mathcal{K}$	Variational Hamiltonian	5
$k_e = e\cos(\Omega+\omega)$	Equinoctial element	3
κ	Constant parameter	4
$l = M$	Delaunay's angle	4
$L = \sqrt{\mu a}$	Delaunay's action	4
$\lambda = \Omega + \omega + M$	Mean longitude	2, 3
$\lambda_\odot$	Sun's mean longitude	4
Λ	Momentum associated to θ	2
$\Lambda_\odot$	Momentum associated to $\lambda_\odot$	4
$\mathbb{M}$	Debris mass	2, 3, 4, 5
m_0, m_1, m_2	Masses in the RTBP	5
M	Mean anomaly	2
$M_\oplus$	Earth's mass	2
$\mu = \mathcal{G}M_\oplus$	Standard gravitational coefficient	2, 4
μ_i	Standard gravitational coefficient for the ith body	2
n	Mean motion	2
$n_\odot$	Sun's mean motion	4
N	Number of degrees of freedom	2
ν	Small parameter	5
$\nu_{\rm c}$	Cylindrical shadow function	3, 4
$\nu_{\rm M}$	Conical shadow function Montenbruck and Gill (2005)	3
$\nu_{\rm p}$	Conical shadow function	3
Ω	Right ascension of the ascending node	2, 3, 4, 5
ω	Argument of pericenter	2, 3, 4, 5
$p = a(1-e^2)$	Semi-latus rectum	3
$p = -\varpi$	Non-singular Delaunay's coordinate	4
$P = L - G$	Non-singular Delaunay's momentum	4
$\vec{p} = (p_1, ..., p_N)$	Momenta vector	2, 5
$p_e = \tan(i/2)\sin\Omega$	Equinoctial element	3
$\mathcal{P}_{nm}$	Legendre function	2
P_r	Radiation pressure magnitude	2, 4
(P_1, P_2)	Canonical momenta for the democratic heliocentric formulation of the TBP	5
$p_e = \tan(i/2)\cos\Omega$	Equinoctial element	3
(p_x, p_y)	Hénon-Heiles momenta	5
ψ	Angle between $\vec{r}$ and $\vec{r}_\odot$	3, 4
(ϕ_2, ϕ_2, ϕ_3)	Arnold Hamiltonian coordinates	5
$q = -\Omega$	Non-singular Delaunay's coordinate	4
$Q = G - H$	Non-singular Delaunay's momentum	4
(Q_1, Q_2)	Canonical coordinates for the democratic heliocentric formulation of the TBP	5
$\vec{q} = (q_1, ..., q_N)$	Coordinates vector	2, 5
$\mathbb{R}$	Set of real numbers	2, 5
$\vec{r} = (x, y, z)$	Debris Cartesian coordinates	2, 3, 4

r	Norm of $\vec{r}$	2, 3, 4
$\vec{r}_\odot$	Sun's Cartesian coordinates	2, 3, 4
$r_\odot$	Norm of $r_\odot$	2, 3, 4
$\vec{r}_i$	ith body Cartesian coordinates	2
$\overline{r}_i$	ith normalized debris Cartesian coordinate	4
$\overline{r}_{\odot,i}$	ith normalized Sun's Cartesian coordinate	4
$R_\oplus$	Earth's equatorial radius	2, 3
$R_\odot$	Sun's radius	3
$\rho = r/r_\odot$	Small variable	3
$S = E_1 + E_2$	Sum of shadow entrance and exit eccentric anomalies	4
$SABA_n$, $SBAB_n$	Symplectic integrator of order n Laskar and Robutel (2001)	2, 3, 4, 5
S_n	Symplectic integrator of order n Yoshida (1990)	2, 5
S_{nm}	Spherical harmonics coefficient	2
σ	Small constant	3
$\sigma_{\text{res}} = \lambda - \theta$	Resonant angles	5
Σ	Shadow function	3
t	Real time	2
t_0	Initial real time	2
τ	Time step	2, 5
θ	Greenwich sidereal time	2
$u = \cos E - e$	Eccentricity function	4
$\vec{v}$	Debris Cartesian velocities	2
v	Norm of $\vec{v}$	2
$v = \sqrt{1-e^2}\sin E$	Eccentricity function	4
$V = \Omega + \omega + f$	True longitude	2, 3
V_{nm}	Cunningham's recursive function	2
$\varpi = \omega + \Omega$	Longitude of the pericenter	4
W	Hamiltonian vector field	5
$\mathcal{W}$	Canonical transformation generator	4
W_{nm}	Cunningham's recursive function	2
$\vec{x} = (x_1, ..., x_{2N})$	Momenta-coordinates vector	2, 5
(x, y)	Hénon-Heiles coordinates	5
(x_1, x_2)	Poincaré's coordinates	4
Y	MEGNO	5
$\overline{Y}$	MEGNO time average	5
(y_1, y_2)	Poincaré's momenta	4
ξ	Auxilary function	4
$\mathbb{Z}$	Set of integer numbers	5
ζ	Small constant	2

$L_{\mathcal{H}}\vec{J}$	Poisson brackets $\{\mathcal{H}, \vec{j}\}$

$\{\mathcal{H}, \vec{J}\}$	Poisson brackets of $\mathcal{H}$ w.r.t. $\vec{J}$
$[J, K] = JK - KJ$	Commutative operator
$\mathcal{O}(J)$	Term of order J
$\vec{\nabla}_{\vec{J}} K(\vec{J})$	Gradient vector of K w.r.t. $\vec{J}$
$D_{\vec{J}} \vec{K}(\vec{J})$	Jacobian matrix of $\vec{K}$ w.r.t. $\vec{J}$
$\nabla^2_{\vec{J}} K(\vec{J})$	Hessian matrix of K w.r.t. $\vec{J}$
$\vec{J} \cdot \vec{K}$	Dot product of $\vec{J}$ w.r.t. $\vec{K}$
$\dot{\vec{J}}$	Derivative of $\vec{J}$ w.r.t. time
$J'(K)$	Derivative of J w.r.t. K
$\partial_J K$	Partial derivative of K w.r.t. J

Appendix B
Recursive Cunningham's functions

Functions V_{nm} and W_{nm}, expressed in the fixed inertial geocentric frame, are detailed in Sec. B.1. Partial derivatives of the same functions with respect to coordinates $\vec{r}$ and θ are given in Sec. B.2. These functions and derivatives are used in Sec. 2.2.

B.1 Functions

Functions are recursively defined as

$$\begin{aligned} V_{mm} &= (2m-1) \\ &\quad \times \left\{ \frac{R_\oplus}{r^2}(x\cos\theta + y\sin\theta)V_{m-1,m-1} - \frac{R_\oplus}{r^2}(-x\sin\theta + y\cos\theta)W_{m-1,m-1} \right\} \\ W_{mm} &= (2m-1) \\ &\quad \times \left\{ \frac{R_\oplus}{r^2}(x\cos\theta + y\sin\theta)W_{m-1,m-1} + \frac{R_\oplus}{r^2}(-x\sin\theta + y\cos\theta)V_{m-1,m-1} \right\} \end{aligned}$$

and

$$\begin{aligned} V_{nm} &= \left(\frac{2n-1}{n-m}\right)\frac{zR_\oplus}{r^2}V_{n-1,m} - \left(\frac{n+m-1}{n-m}\right)\frac{R_\oplus^2}{r^2}V_{n-2,m} \\ W_{nm} &= \left(\frac{2n-1}{n-m}\right)\frac{zR_\oplus}{r^2}W_{n-1,m} - \left(\frac{n+m-1}{n-m}\right)\frac{R_\oplus^2}{r^2}W_{n-2,m}. \end{aligned}$$

Please note that $V_{n-2,m}$ and $W_{n-2,m}$ are set to zero in the right-hand sides of the above equations when $n = m + 1$. Initial conditions are

$$\begin{aligned} V_{00} &= \frac{R_\oplus}{\sqrt{x^2+y^2+z^2}} \\ W_{00} &= 0. \end{aligned}$$

B.2 Derivatives

Partial derivatives of the initial conditions are

$$\begin{aligned} \partial_x V_{00} &= \frac{-x}{(x^2+y^2+z^2)^{3/2}} R_\oplus \\ \partial_y V_{00} &= \frac{-y}{(x^2+y^2+z^2)^{3/2}} R_\oplus \\ \partial_z V_{00} &= \frac{-z}{(x^2+y^2+z^2)^{3/2}} R_\oplus \\ \partial_\theta V_{00} &= 0 \\ \partial_x W_{00} &= \partial_y W_{00} = \partial_z W_{00} = \partial_\theta W_{00} = 0 \end{aligned}$$

where we used $\partial_x f$ to denote $\partial f / \partial x$.

Then, one can recursively build partial derivatives of V_{nm} and W_{nm} functions, still keeping in mind that $V_{n-2,m}$ and $W_{n-2,m}$ are set to zero when $n = m + 1$:

$$\begin{aligned}
\partial_x V_{mm} &= (2m-1)\left\{ \frac{R_\oplus}{r^4}[r^2\cos\theta - 2x(x\cos\theta + y\sin\theta)]V_{m-1,m-1} + \frac{R_\oplus}{r^2}(x\cos\theta + y\sin\theta)\partial_x V_{m-1,m-1} \right. \\
&\left. -\frac{R_\oplus}{r^4}[-r^2\sin\theta - 2x(-x\sin\theta + y\cos\theta)]W_{m-1,m-1} - \frac{R_\oplus}{r^2}(-x\sin\theta + y\cos\theta)\partial_x W_{m-1,m-1} \right\} \\
\partial_y V_{mm} &= (2m-1)\left\{ \frac{R_\oplus}{r^4}[r^2\sin\theta - 2y(x\cos\theta + y\sin\theta)]V_{m-1,m-1} + \frac{R_\oplus}{r^2}(x\cos\theta + y\sin\theta)\partial_y V_{m-1,m-1} \right. \\
&\left. -\frac{R_\oplus}{r^4}[r^2\cos\theta - 2y(-x\sin\theta + y\cos\theta)]W_{m-1,m-1} - \frac{R_\oplus}{r^2}(-x\sin\theta + y\cos\theta)\partial_y W_{m-1,m-1} \right\} \\
\partial_z V_{mm} &= (2m-1)\left\{ \frac{R_\oplus}{r^4}[-2z(x\cos\theta + y\sin\theta)]V_{m-1,m-1} + \frac{R_\oplus}{r^2}(x\cos\theta + y\sin\theta)\partial_z V_{m-1,m-1} \right. \\
&\left. -\frac{R_\oplus}{r^4}[-2z(-x\sin\theta + y\cos\theta)]W_{m-1,m-1} - \frac{R_\oplus}{r^2}(-x\sin\theta + y\cos\theta)\partial_z W_{m-1,m-1} \right\} \\
\partial_\theta V_{mm} &= (2m-1)\frac{1}{r^2}\{R_\oplus(-x\sin\theta + y\cos\theta)V_{m-1,m-1} + R_\oplus(x\cos\theta + y\sin\theta)\partial_\theta V_{m-1,m-1} \\
&- (R_\oplus(-x\cos\theta - y\sin\theta)]W_{m-1,m-1} + R_\oplus(-x\sin\theta + y\cos\theta)\partial_\theta W_{m-1,m-1})\}
\end{aligned}$$

$$\begin{aligned}
\partial_x W_{mm} &= (2m-1)\left\{\frac{R_\oplus}{r^4}[r^2\cos\theta - 2x(x\cos\theta + y\sin\theta)]W_{m-1,m-1} + \frac{R_\oplus}{r^2}(x\cos\theta + y\sin\theta)\partial_x W_{m-1,m-1}\right. \\
&\left. + \frac{R_\oplus}{r^4}[-r^2\sin\theta - 2x(-x\sin\theta + y\cos\theta)]V_{m-1,m-1} + \frac{R_\oplus}{r^2}(-x\sin\theta + y\cos\theta)\partial_x V_{m-1,m-1}\right\}
\end{aligned}$$

$$\begin{aligned}
\partial_y W_{mm} &= (2m-1)\left\{\frac{R_\oplus}{r^4}[r^2\sin\theta - 2y(x\cos\theta + y\sin\theta)]W_{m-1,m-1} + \frac{R_\oplus}{r^2}(x\cos\theta + y\sin\theta)\partial_y W_{m-1,m-1}\right. \\
&\left. + \frac{R_\oplus}{r^4}[r^2\cos\theta - 2y(-x\sin\theta + y\cos\theta)]V_{m-1,m-1} + \frac{R_\oplus}{r^2}(-x\sin\theta + y\cos\theta)\partial_y V_{m-1,m-1}\right\}
\end{aligned}$$

$$\begin{aligned}
\partial_z W_{mm} &= (2m-1)\left\{\frac{R_\oplus}{r^4}[-2z(x\cos\theta + y\sin\theta)]W_{m-1,m-1} + \frac{R_\oplus}{r^2}(x\cos\theta + y\sin\theta)\partial_z W_{m-1,m-1}\right. \\
&\left. + \frac{R_\oplus}{r^4}[-2z(-x\sin\theta + y\cos\theta)]V_{m-1,m-1} + \frac{R_\oplus}{r^2}(-x\sin\theta + y\cos\theta)\partial_z V_{m-1,m-1}\right\}
\end{aligned}$$

$$\begin{aligned}
\partial_\theta W_{mm} &= (2m-1)\frac{1}{r^2}\{R_\oplus(-x\sin\theta + y\cos\theta)W_{m-1,m-1} + R_\oplus(x\cos\theta + y\sin\theta)\partial_\theta W_{m-1,m-1} \\
&+ R_\oplus(-x\cos\theta - y\sin\theta)]V_{m-1,m-1} + R_\oplus(-x\sin\theta + y\cos\theta)\partial_\theta V_{m-1,m-1}\}
\end{aligned}$$

$$
\begin{aligned}
\partial_x V_{nm} &= \left(\frac{2n-1}{n-m}\right)\left\{\frac{R_\oplus}{r^4}(-2xz)V_{n-1,m} + \frac{R_\oplus}{r^2}\,z\,\partial_x V_{n-1,m}\right\} \\
&\quad -\left(\frac{n+m-1}{n-m}\right)\left\{\frac{R_\oplus^2}{r^4}(-2x)V_{n-2,m} + \frac{R_\oplus^2}{r^2}\partial_x V_{n-2,m}\right\} \\
\partial_y V_{nm} &= \left(\frac{2n-1}{n-m}\right)\left\{\frac{R_\oplus}{r^4}(-2yz)V_{n-1,m} + \frac{R_\oplus}{r^2}\,z\,\partial_y V_{n-1,m}\right\} \\
&\quad -\left(\frac{n+m-1}{n-m}\right)\left\{\frac{R_\oplus^2}{r^4}(-2y)V_{n-2,m} + \frac{R_\oplus^2}{r^2}\partial_y V_{n-2,m}\right\} \\
\partial_y V_{nm} &= \left(\frac{2n-1}{n-m}\right)\left\{\frac{R_\oplus}{r^4}(r^2-2z^2)V_{n-1,m} + \frac{R_\oplus}{r^2}\,z\,\partial_z V_{n-1,m}\right\} \\
&\quad -\left(\frac{n+m-1}{n-m}\right)\left\{\frac{R_\oplus^2}{r^4}(-2z)V_{n-2,m} + \frac{R_\oplus^2}{r^2}\partial_z V_{n-2,m}\right\} \\
\partial_\theta V_{nm} &= \left(\frac{2n-1}{n-m}\right)\frac{zR_\oplus}{r^2}\partial_\theta W_{n-1,m} - \left(\frac{n+m-1}{n-m}\right)\frac{R_\oplus^2}{r^2}\partial_\theta V_{n-2,m}
\end{aligned}
$$

$$
\begin{aligned}
\partial_x W_{nm} &= \left(\frac{2n-1}{n-m}\right)\left\{\frac{R_\oplus}{r^4}(-2xz)W_{n-1,m} + \frac{R_\oplus}{r^2}\,z\,\partial_x W_{n-1,m}\right\} \\
&\quad -\left(\frac{n+m-1}{n-m}\right)\left\{\frac{R_\oplus^2}{r^4}(-2x)W_{n-2,m} + \frac{R_\oplus^2}{r^2}\partial_x W_{n-2,m}\right\} \\
\partial_y W_{nm} &= \left(\frac{2n-1}{n-m}\right)\left\{\frac{R_\oplus}{r^4}(-2yz)W_{n-1,m} + \frac{R_\oplus}{r^2}\,z\,\partial_y W_{n-1,m}\right\} \\
&\quad -\left(\frac{n+m-1}{n-m}\right)\left\{\frac{R_\oplus^2}{r^4}(-2y)W_{n-2,m} + \frac{R_\oplus^2}{r^2}\partial_y W_{n-2,m}\right\} \\
\partial_y W_{nm} &= \left(\frac{2n-1}{n-m}\right)\left\{\frac{R_\oplus}{r^4}(r^2-2z^2)W_{n-1,m} + \frac{R_\oplus}{r^2}\,z\,\partial_z W_{n-1,m}\right\} \\
&\quad -\left(\frac{n+m-1}{n-m}\right)\left\{\frac{R_\oplus^2}{r^4}(-2z)W_{n-2,m} + \frac{R_\oplus^2}{r^2}\partial_z W_{n-2,m}\right\} \\
\partial_\theta W_{nm} &= \left(\frac{2n-1}{n-m}\right)\frac{zR_\oplus}{r^2}\partial_\theta W_{n-1,m} - \left(\frac{n+m-1}{n-m}\right)\frac{R_\oplus^2}{r^2}\partial_\theta W_{n-2,m}
\end{aligned}
$$

Appendix C

Step size adjustment for shadow entrance and exit

We describe the algorithm to set the step size so that SRP is exactly switched off at the cylindrical shadow entrance and switched on at the exit (see Sec. 3.3 and 5.5.2). It uses a simple method. First the current debris mean anomaly (we could have worked with true or eccentric anomalies) is compared to the entrance and exit mean anomalies. Second the time step is adjusted by means of the mean motion which links time and mean anomaly values.

The algorithm is illustrated in Fig. C.1 and C.2. Different quantities are used:

M_0 = current mean anomaly

M = current mean anomaly modulo 2π

n = current mean motion

M_{in} = shadow entrance mean anomaly

M_{out} = shadow exit mean anomaly

t = current time

t_{in} = time until next shadow entrance

t_{out} = time until next shadow exit

h_0 = default time step

h = adjusted time step

srp = 1 (SRP must be considered) or 0 (SRP must be cancelled)

sun = true or false

The boolean quantity *sun* is used at the next step to determine if debris must be considered inside or outside Earth's shadows at the beginning of the time step.

Entrance and exit anomalies are computed (see Sec. 3.1.1) such that both M_{in} and M_{out} are between 0 and 2π. However, should M_{out} be smaller than M_{in}, 2π is added to M_{out}. In this way, M_{out} is always larger than M_{in}.

First, an initialization step is required to determine if debris initial position is inside cylindrical umbra or not (*srp* and *sun* variables are initialized). This step is explained in Fig. C.1.

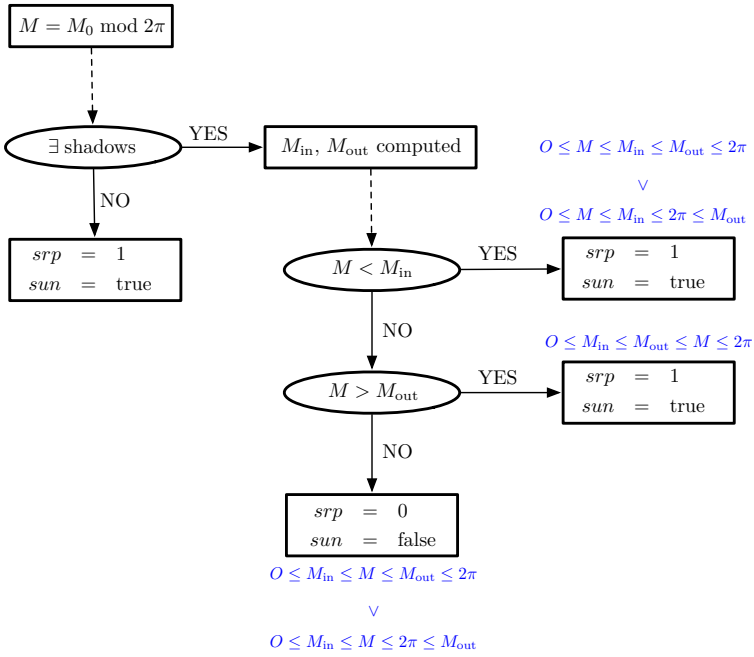

Figure C.1 • *Initialization step.*

Then, at each integration step, the time step is adjusted and *srp* and *sun* variables are updated. All details are shown in Fig. C.2.

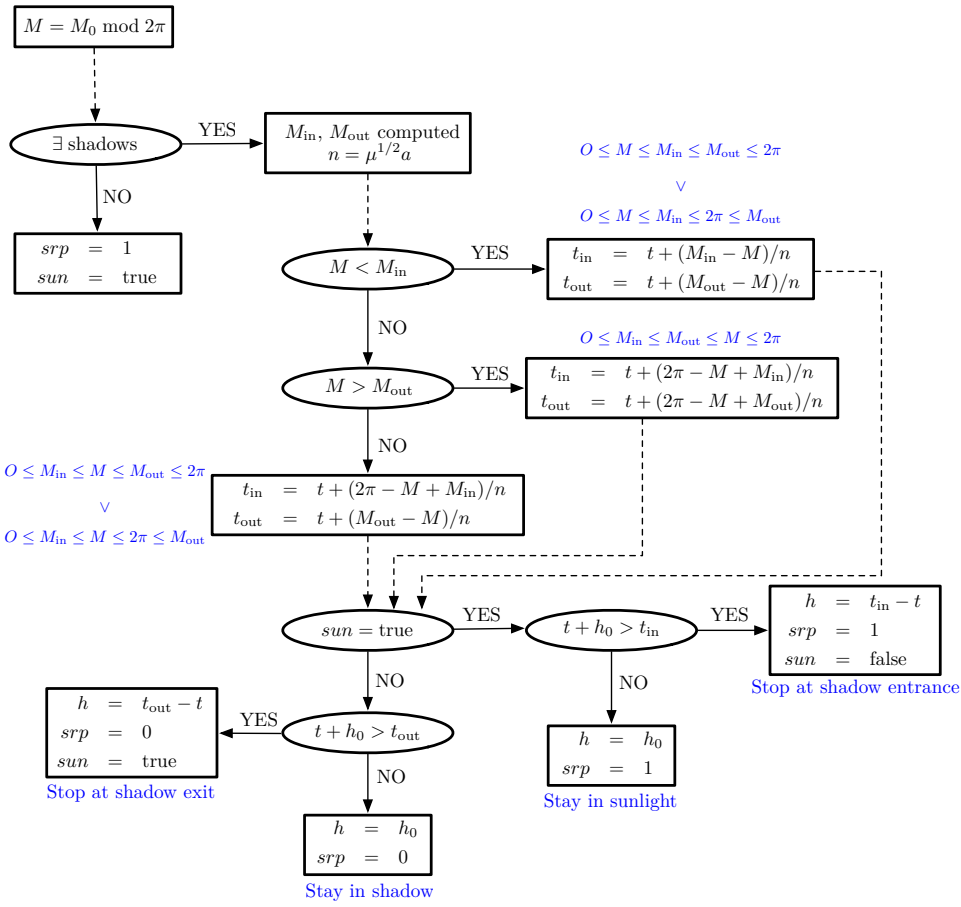

Figure C.2 • *General step.*

Appendix D
Symplectic integration of the TBP

This appendix presents an approach similar to Sec. 2.3 to solve the equations of motion associated to the Hamiltonian (5.19) (see Sec. 5.4.2).

The perturbed Hamiltonian (5.19) is written as

$$\begin{aligned}\mathcal{H}(\vec{P}_1,\vec{P}_2,\vec{Q}_1,\vec{Q}_2) &= \frac{\|\vec{P}_1\|^2}{2m_1} - \mathcal{G}\frac{m_0 m_1}{\|\vec{Q}_1\|} + \frac{\|\vec{P}_2\|^2}{2m_2} - \mathcal{G}\frac{m_0 m_2}{\|\vec{Q}_2\|} \\ &\quad + \|\vec{P}_1+\vec{P}_2\|^2 - \mathcal{G}\frac{m_1 m_2}{\|\,\vec{Q}_1-\vec{Q}_2\,\|} \\ &= A(\vec{P}_1,\vec{P}_2,\vec{Q}_1,\vec{Q}_2) + B(\vec{P}_1,\vec{P}_2,\vec{Q}_1,\vec{Q}_2).\end{aligned}$$

In the A-part, we find two non-interacting two-body problems. Hence, we will use the same algorithm as in Sec. 2.3.2 to numerically solve $\vec{x}_{k_i} = e^{c_i \tau L_A}\vec{x}^k$ where $\vec{x}^k$ represents $\vec{x} = (\vec{P}_1,\vec{P}_2,\vec{Q}_1,\vec{Q}_2)$ at the kth time step. The perturbation is present in the B-part of the Hamiltonian and stands for the mutual gravitational interaction between the two bodies. A new set of canonical variables is introduced to deal with the computation of $\vec{x}_{k_i} = e^{d_i \tau L_B}\vec{x}^k$.

The efficiency of the integration of this dynamics with SBAB_n or SABA_n symplectic integrators is analog to the one of the space debris propagator.

Different changes of variables are necessary. Let us assume that initial Keplerian elements for both bodies are known and noted

$$(a,e,i,\Omega,\omega,M)_1 \quad \text{and} \quad (a,e,i,\Omega,\omega,M)_2.$$

Respective heliocentric positions and velocities

$$(\vec{r}_1,\dot{\vec{r}}_1) \quad \text{and} \quad (\vec{r}_2,\dot{\vec{r}}_2)$$

can be computed as in Sec. 2.3.2. Then, the corresponding barycentric positions and velocities

$$(\vec{u}_1, \dot{\vec{u}}_1) \quad \text{and} \quad (\vec{u}_2, \dot{\vec{u}}_2)$$

are obtained by means of subroutines written by M.J. Duncan for SWIFT software (Levison and Ducan 1994). The last step consists in computing the canonical heliocentric positions and velocities. This is achieved as

$$\begin{aligned} \vec{Q}_i &= \vec{u}_i - \vec{u}_0 \\ \vec{P}_i &= m_i \dot{\vec{u}}_i \end{aligned}$$

where $\vec{u}_0$ is the barycentric position of the Sun. The inverse successive changes of variables are performed in the same way, noting that the barycentric position of the Sun is computed from canonical heliocentric coordinates as

$$\vec{u}_0 = -\frac{\sum_{j=1}^{k} m_j \vec{Q}_j}{\sum_{j=0}^{k} m_j}.$$

Sun's canonical coordinates are assumed to be $(\vec{P}_0, \vec{Q}_0) = (0, \vec{u}_0)$.

D.1 Computation of $e^{c_i \tau L_A} \vec{x}^k$

Both independent keplerian motions are computed as in section 2.3.2. However, we cannot directly use canonical heliocentric coordinates. If m_1 or m_2 are close to zero (which is the case for the restricted three-body problem), the corresponding canonical momenta will be near zero as well. From a numerical point of view, this yields very poor results. To tackle this issue, we use the intermediate state vector

$$\vec{x}_A^k = (\dot{\vec{u}}_1^k, \dot{\vec{u}}_2^k, \vec{Q}_1^k, \vec{Q}_2^k) = (\vec{P}_1^k/m_1, \vec{P}_2^k/m_2, \vec{Q}_1^k, \vec{Q}_2^k).$$

At each time step, $\vec{x}_A^k$ is computed from $\vec{x}^k$ and then each one of its parts is expressed in terms of keplerian elements by means of the aforementioned changes of variables:

$$\begin{aligned} (\vec{Q}_1^k, \dot{\vec{u}}_1^k) &\rightsquigarrow \mathcal{S}_1^k := (a, e, i, \Omega, \omega, M)_1^k \\ (\vec{Q}_2^k, \dot{\vec{u}}_2^k) &\rightsquigarrow \mathcal{S}_2^k := (a, e, i, \Omega, \omega, M)_2^k. \end{aligned}$$

Similarly to Sec. 2.3.2, $\mathcal{S}_1^{k_i}$ and $\mathcal{S}_2^{k_i}$ are computed analytically and the solution of both two-body problems $\vec{x}_A^{k_i}$ is given by

$$\begin{aligned} \dot{\vec{u}}_1^{k_i} &:= \dot{\vec{u}}_1(\mathcal{S}_1^{k_i}) \\ \dot{\vec{u}}_2^{k_i} &:= \dot{\vec{u}}_2(\mathcal{S}_2^{k_i}) \\ \vec{Q}_1^{k_i} &:= \vec{Q}_1(\mathcal{S}_1^{k_i}) \\ \vec{Q}_2^{k_i} &:= \vec{Q}_2(\mathcal{S}_2^{k_i}). \end{aligned}$$

The constant gravitational parameters μ_1 and μ_2 used in the computation of $M_1^{k_i}$ and $M_2^{k_i}$ (through third Kepler's law) are respectively equal to $\mathcal{G}(m_0+m_1)$ and $\mathcal{G}(m_0+m_2)$. Eventually, $\vec{x}^{k_i}$ is expressed in terms of the canonical heliocentric coordinates as

$$\vec{x}^{k_i} = (\vec{P}_1^{k_i}, \vec{P}_2^{k_i}, \vec{Q}_1^{k_i}, \vec{Q}_2^{k_i}) = (m_1\dot{\vec{u}}_1^{k_i}, m_2\dot{\vec{u}}_2^{k_i}, \vec{Q}_1^{k_i}, \vec{Q}_2^{k_i}).$$

Note that non-singular elements could be used, as explained in Sec. 2.3.2.

D.2 Computation of $e^{d_i\tau\, L_B}\vec{x}^k$

Let us recall that

$$B(\vec{P}_1, \vec{P}_2, \vec{Q}_1, \vec{Q}_2) = \|\vec{P}_1 + \vec{P}_2\|^2 - \mathcal{G}\frac{m_1 m_2}{\| \vec{Q}_1 - \vec{Q}_2 \|}.$$

From Arnold (1989), we know that the following change of coordinates

$$\vec{\mathcal{Q}}_1 = \vec{\mathcal{Q}}_1(\vec{Q}_1) \quad \text{and} \quad \vec{\mathcal{Q}}_2 = \vec{\mathcal{Q}}_2(\vec{Q}_2)$$

leads to a completely (i.e. time independent) canonical transformation if and only if the corresponding momenta are changed according to

$$(D_{\vec{Q}_1}\vec{\mathcal{Q}}_1)^T\vec{\mathcal{P}}_1 = \vec{P}_1 \quad \text{and} \quad (D_{\vec{Q}_2}\vec{\mathcal{Q}}_2)^T\vec{\mathcal{P}}_2 = \vec{P}_2 \tag{D.1}$$

where $D_{\vec{Q}_1}\vec{\mathcal{Q}}_1$ and $D_{\vec{Q}_2}\vec{\mathcal{Q}}_2$ are Jacobian matrices

$$(D_{\vec{Q}_1}\vec{\mathcal{Q}}_1)_{ij} = \frac{\partial \mathcal{Q}_{1i}}{\partial Q_{1j}} \quad \text{and} \quad (D_{\vec{Q}_2}\vec{\mathcal{Q}}_2)_{ij} = \frac{\partial \mathcal{Q}_{2i}}{\partial Q_{2j}}$$

and $\vec{\mathcal{P}}_1$, $\vec{\mathcal{P}}_2$ are the new momenta.

Then, let $\vec{\mathcal{Q}}_1$ and $\vec{\mathcal{Q}}_2$ be defined as

$$\vec{\mathcal{Q}}_1 = \vec{Q}_1 - \vec{Q}_2 \quad \text{and} \quad \vec{\mathcal{Q}}_2 = \vec{Q}_1.$$

By eq. (D.1), momenta are given by

$$\vec{\mathcal{P}}_1 = -\vec{P}_2 \quad \text{and} \quad \vec{\mathcal{P}}_2 = \vec{P}_1 + \vec{P}_2,$$

while the associated Hamiltonian can be written as

$$\mathcal{H}_{\text{TBP}}(\vec{\mathcal{P}}_1, \vec{\mathcal{P}}_2, \vec{\mathcal{Q}}_1, \vec{\mathcal{Q}}_2) = \frac{\|\vec{\mathcal{P}}_2\|^2}{2m_0} - \mathcal{G}\frac{m_1 m_2}{\|\vec{\mathcal{Q}}_1\|}.$$

Hence, equations of motion are

$$\begin{cases} \dot{\vec{\mathcal{P}}}_1 &= -\partial_{\vec{\mathcal{Q}}_1}\mathcal{H}_{\mathrm{TBP}} &= -\mathcal{G}\dfrac{m_1 m_2}{\|\vec{\mathcal{Q}}_1\|^3}\vec{\mathcal{Q}}_1 \\ \dot{\vec{\mathcal{P}}}_2 &= -\partial_{\vec{\mathcal{Q}}_2}\mathcal{H}_{\mathrm{TBP}} &= 0 \\ \dot{\vec{\mathcal{Q}}}_1 &= \partial_{\vec{\mathcal{P}}_1}\mathcal{H}_{\mathrm{TBP}} &= 0 \\ \dot{\vec{\mathcal{Q}}}_2 &= \partial_{\vec{\mathcal{P}}_2}\mathcal{H}_{\mathrm{TBP}} &= \dfrac{\vec{\mathcal{P}}_2}{m_0}. \end{cases}$$

Expressed in terms of old coordinates, $\bar{x}^{k_i} = e^{d_i\tau\, L_B}\bar{x}^k$ is numerically solved as

$$\begin{cases} \vec{P}_1^{k_i} &= \vec{P}_1^k - \mathcal{G}\dfrac{m_1 m_2}{\|\vec{Q}_1^k - \vec{Q}_2^k\|^3}(\vec{Q}_1^k - \vec{Q}_2^k)d_i\tau \\ \vec{P}_2^{k_i} &= \vec{P}_2^k + \mathcal{G}\dfrac{m_1 m_2}{\|\vec{Q}_1^k - \vec{Q}_2^k\|^3}(\vec{Q}_1^k - \vec{Q}_2^k)d_i\tau \\ \vec{Q}_1^{k_i} &= \vec{Q}_1^k + \dfrac{\vec{P}_1^k + \vec{P}_2^k}{m_0}d_i\tau \\ \vec{Q}_2^{k_i} &= \vec{Q}_2^k + \dfrac{\vec{P}_1^k + \vec{P}_2^k}{m_0}d_i\tau\,. \end{cases}$$

Appendix E
Stark problem

This appendix presents a joint work realized with Dr. Giovanni Federico Gronchi and Chiara Tardioli. This collaboration was made possible during a two-month stay at the Group of Celestial Mechanics, Department of Mathematics of the University of Pisa. Our work focused on the so-called *Stark problem*, also called *low-thrust* or *accelerated Kepler problem*. Several papers devoted to this problem have already been published. Here, we will mainly use Burns and Marshall (1968) and Lantoine and Russell (2011).

The Stark problem is the one where a satellite (or space debris) is under the combined influence of Keplerian and planar force fields. A Keplerian problem coupled to SRP perfectly fits this definition. This kind of problem has been known for a long time and finds analogous applications in different fields, like the radiation from hydrogen gas in an external planar electric field (Schrödinger 1926, Epstein 1926).

The main benefit of the Stark problem comes from the fact that complete closed-form solutions can be found, using parabolic coordinates, Hamilton-Jacobi equations and elliptic integrals as main tools. Initially, the aim of our work was to reproduce such solutions, add Earth's shadow crossings and check if any other perturbation (e.g. the oblateness of the Earth) could be added without destroying the integrability of the problem. Unfortunately, analytical and technical problems were encountered and a lot of time has been spent to the successful reproduction of results from Lantoine and Russell (2011). Further potential improvements could not be achieved for the moment and it is still a work in progress. This appendix aims to summarize the way to solve the Stark problem in a closed-form way (Sec. E.1) and to explain in Sec. E.2 the numerical methods that we used to practically solve it and highlight some difficult steps.

All notations used in this appendix are independent from the ones used in the rest of the manuscript. Elliptic functions and integrals are defined in Appx. F.

E.1 Closed-form solution

In the following developments, we arbitrarily assume that the SRP force, F, is fixed to the z-direction. Debris equations of motion are then given by

$$\begin{cases} \ddot{x} &= -\dfrac{\mu}{r^3}x \\ \ddot{y} &= -\dfrac{\mu}{r^3}y \\ \ddot{z} &= -\dfrac{\mu}{r^3}z + F \end{cases} \tag{E.1}$$

where μ is the gravitational parameter, $\ddot{x}$ denotes the second derivative of x with respect to time and r is the norm of $\vec{r} = (x, y, z)$. Another set of variables will be used to make the separation of the Hamiltonian possible. We introduce the parabolic coordinates (ξ, η, ϕ)

$$\begin{cases} x &= \xi\eta\cos\phi \\ y &= \xi\eta\sin\phi \\ z &= \dfrac{1}{2}(\xi^2 - \eta^2). \end{cases} \tag{E.2}$$

The associated Hamiltonian can be written as

$$\mathcal{H}_{\text{Stark}} = \frac{p_\xi^2 + p_\eta^2}{2(\xi^2+\eta^2)} + \frac{p_\phi^2}{2\xi^2\eta^2} - \frac{2\mu}{\xi^2+\eta^2} - \frac{1}{2}F(\xi^2 - \eta^2) \tag{E.3}$$

with the following momenta

$$\begin{cases} p_\xi &= (\xi^2+\eta^2)\dot{\xi} \\ p_\eta &= (\xi^2+\eta^2)\dot{\eta} \\ p_\phi &= \xi^2\eta^2\dot{\phi}. \end{cases}$$

Two methods have been investigated to solve equations of motion associated to $\mathcal{H}_{\text{Stark}}$. The first one, proposed in Burns and Marshall (1968) is based on the Hamilton-Jacobi equation. It is briefly described in Sec. E.1.1. The other one relies on two auxilary time variables and is studied with more details in Sec. E.1.2.

E.1.1 Hamilton-Jacobi equation

The Hamilton-Jacobi equation is written as

$$\frac{1}{2(\xi^2+\eta^2)}\left[\left(\frac{\partial S}{\partial \xi}\right)^2+\left(\frac{\partial S}{\partial \eta}\right)^2\right]+\frac{1}{2\xi^2\eta^2}\left(\frac{\partial S}{\partial \phi}\right)^2-\frac{2\mu}{\xi^2+\eta^2}-\frac{1}{2}F(\xi^2-\eta^2)+\frac{\partial S}{\partial t}=0 \tag{E.4}$$

where S is such that

$$\begin{cases} p_\xi &= \dfrac{\partial S}{\partial \xi} \\ p_\eta &= \dfrac{\partial S}{\partial \eta} \\ p_\phi &= \dfrac{\partial S}{\partial \phi}. \end{cases}$$

Solutions to the Hamilton-Jacobi equation are also solutions to the Stark problem.

We want to separate eq. (E.4) by finding a solution to this equation in the form

$$S(\xi,\eta,\phi,t)=W(\xi,\eta,\phi)-Et=l\phi+S_1(\xi)+S_2(\eta)-Et, \tag{E.5}$$

yielding

$$\frac{1}{2(\xi^2+\eta^2)}\left[\left(\frac{\partial S_1}{\partial \xi}\right)^2+\left(\frac{\partial S_2}{\partial \eta}\right)^2\right]+\frac{l^2}{2\xi^2\eta^2}-\frac{2\mu}{\xi^2+\eta^2}-\frac{1}{2}F(\xi^2-\eta^2)=E. \tag{E.6}$$

Let us mention that $p_\phi=\partial S/\partial\phi=l$ is constant. Multiplying eq. (E.6) by $(\xi^2+\eta^2)$ lets us write it as

$$\frac{1}{2}\left(\frac{\partial S_1}{\partial \xi}\right)^2+\frac{l^2}{2\xi^2}-\mu-\frac{F\xi^4}{2}-E\xi^2=-\frac{1}{2}\left(\frac{\partial S_2}{\partial \eta}\right)^2-\frac{l^2}{2\eta^2}+\mu-\frac{F\eta^4}{2}+E\eta^2, \tag{E.7}$$

the left and right hand sides respectively depending only on ξ and η. Given that ξ and η are independent coordinates and that this equality must hold for any combination (ξ,η), it must be constant. Hence, there exists a constant β such that

$$\begin{aligned} \beta &= \frac{1}{2}\left(\frac{\partial S_1}{\partial \xi}\right)^2-\frac{F\xi^4}{2}+\frac{l^2}{2\xi^2}-\mu+E\xi^2 \\ \beta &= -\frac{1}{2}\left(\frac{\partial S_2}{\partial \eta}\right)^2-\frac{F\eta^4}{2}-\frac{l^2}{2\eta^2}+\mu+E\eta^2 \end{aligned}$$

or

$$S_1 = \int_{\xi_0}^{\xi} \sqrt{Fs^4 + 2Es^2 - \frac{l^2}{s^2} + 2(\beta+\mu)}\, ds \tag{E.8}$$

$$S_2 = \int_{\eta_0}^{\eta} \sqrt{-Fs^4 + 2Es^2 - \frac{l^2}{s^2} - 2(\beta-\mu)}\, ds. \tag{E.9}$$

The function S (E.5) can now be fully expressed as

$$\begin{aligned} S(\xi,\eta,\phi,t) &= l\phi - Et + \int_{\xi_0}^{\xi} \sqrt{Fs^4 + 2Es^2 - \frac{l^2}{s^2} + 2(\beta+\mu)}\, ds \\ &\quad + \int_{\eta_0}^{\eta} \sqrt{-Fs^4 + 2Es^2 - \frac{l^2}{s^2} - 2(\beta-\mu)}\, ds. \end{aligned} \tag{E.10}$$

In addition, partial derivatives of S with respect to l, E and β respectively give three new constants

$$\begin{aligned} c_1 &= \phi - \frac{1}{2}\int_{\xi_0}^{\xi} \frac{ds}{s\sqrt{Fs^6 + 2Es^4 + 2(\beta+\mu)s^2 - l^2}} \\ &\quad -\frac{1}{2}\int_{\eta_0}^{\eta} \frac{ds}{s\sqrt{-Fs^6 + 2Es^4 - 2(\beta-\mu)s^2 - l^2}} \end{aligned} \tag{E.11}$$

$$\begin{aligned} c_2 &= -t + \int_{\xi_0}^{\xi} \frac{s^3 ds}{\sqrt{Fs^6 + 2Es^4 + 2(\beta+\mu)s^2 - l^2}} \\ &\quad + \int_{\eta_0}^{\eta} \frac{s^3 ds}{\sqrt{-Fs^6 + 2Es^4 - 2(\beta-\mu)s^2 - l^2}} \end{aligned} \tag{E.12}$$

$$\begin{aligned} c_3 &= \int_{\xi_0}^{\xi} \frac{s\, ds}{\sqrt{Fs^6 + 2Es^4 + 2(\beta+\mu)s^2 - l^2}} \\ &\quad - \int_{\eta_0}^{\eta} \frac{s\, ds}{\sqrt{-Fs^6 + 2Es^4 - 2(\beta-\mu)s^2 - l^2}}. \end{aligned} \tag{E.13}$$

Evaluating these equations at the initial time $t = t_0$ means that $\xi = \xi_0$ and $\eta = \eta_0$ and all integrals vanish. That lets us find that c_1 is the initial value of ϕ, $c_2 = -t_0$ and $c_3 = 0$. Hence we have obtained three relations linking ξ, η and ϕ to time. Unfortunately, it becomes extremely difficult to go one step further and express some coordinates as functions of the other ones. In Burns and Marshall (1968), a solution is found when the problem is restricted to a two-dimensional motion ($x - z$ plane, implying that $\phi = 0$). Choosing units and parameters conveniently, they manage to write two equations of the form

$$0 = \mathcal{U}_1(a_1, b_1, \xi_0; \xi) + \mathcal{U}_2(a_2, b_2, \eta_0; \eta) \tag{E.14}$$

$$t - t_0 = \mathcal{V}_1(a_1, b_1, \xi_0; \xi) + \mathcal{V}_2(a_2, b_2, \xi_0; \xi) \tag{E.15}$$

where a_1, b_1 and a_2, b_2 are respectively the roots of polynomials (divided by s^2 and adapted to the planar case) appearing inside the square roots of eqs. (E.11)-(E.13):

$$Fs^4 + 2Es^2 + 2(\beta + \mu) \quad \text{and} \quad -Fs^4 + 2Es^2 - 2(\beta - \mu).$$

The functions $\mathcal{U}_1, \mathcal{V}_1, \mathcal{U}_2$ and $\mathcal{V}_2$ are built as additions and substractions of inverted Jacobi's elliptic functions sn^{-1} and cn^{-1} described in Appx. F.

Even restricted to this two-dimensional case, we now have to cope with inversions of these functions to express for example ξ with respect to η from eq. (E.14) and then to replace this value in eq. (E.15) to get η as a function of time. However, we have no idea of the shape of these functions and of the best suited numerical tool to solve it[1]. Moreover, we still have to deal with the three-dimensional problem. Hence, this solution has not been investigated further. Some keypoints of this method have been used in the more efficient scheme of Lantoine and Russell (2011) though.

E.1.2 Auxiliary time variables

A different method is proposed in Lantoine and Russell (2011). In this work, the problem is solved in the planar case and a change of coordinates is used to express the solutions of the three-dimensional problem in terms of solutions of the two-dimensional one. Here we will directly describe the method in the three-dimensional problem.

Let us start again from the Hamiltonian $\mathcal{H}_{\text{Stark}}$ (E.3). Two fictitious time variables are introduced :

$$dt = (\xi^2 + \eta^2) d\tau_1 \tag{E.16}$$

$$dt = \xi^2 \eta^2 d\tau_2. \tag{E.17}$$

The momenta associated to $\mathcal{H}_{\text{Stark}}$ can then be expressed in terms of τ_1 and τ_2 as

$$\begin{cases} p_\xi = (\xi^2 + \eta^2)\dot{\xi} = \dfrac{\partial \xi}{\partial \tau_1} \\ p_\eta = (\xi^2 + \eta^2)\dot{\eta} = \dfrac{\partial \eta}{\partial \tau_1} \\ p_\phi = \xi^2 \eta^2 \dot{\phi} = \dfrac{\partial \phi}{\partial \tau_2}. \end{cases}$$

[1]It should be noted that no propagation computed from these formulae is presented in Burns and Marshall (1968).

As previously, the Hamiltonian can be separated into two parts and one obtains formulae equivalent to eq. (E.8) and (E.9):

$$d\tau_1 = \frac{\xi\, d\xi}{\sqrt{F\xi^6 + 2E\xi^4 + 2(\mu+\beta)\xi^2 - p_\phi^2}} = \frac{\xi\, d\xi}{\sqrt{P_\xi(\xi)}} \tag{E.18}$$

$$d\tau_1 = \frac{\eta\, d\eta}{\sqrt{-F\eta^6 + 2E\eta^4 + 2(\mu-\beta)\xi^2 - p_\phi^2}} = \frac{\eta\, d\eta}{\sqrt{P_\eta(\eta)}} \tag{E.19}$$

$$\phi - \phi_0 = p_\phi \tau_2. \tag{E.20}$$

We must now reduce eq. (E.18) and (E.19) to elliptic integral standard forms.

In the following, both polynomials P_ξ and P_η will be treated in a similar way. Hence, let us consider $P(X) = aX^6 + bX^4 + cX^2 + d$ where X can either be ξ or η and coefficients must be fixed accordingly. Two successive changes of variables are then defined:

$$Y = X^2 \tag{E.21}$$

$$\mathrm{sign}(a)\, Z^2 = Y - Y^*. \tag{E.22}$$

The first one makes P become a cubic polynomial which has at least one real root Y^*. Hence

$$P(X) = (Y - Y^*)Q(Y)$$

with Q a quadratic polynomial in Y. Integrals (E.18) and (E.19) can be expressed and solved in terms of Z. Then, it is easy to come back to $X^2 = Y^* + \mathrm{sign}(a)\, Z^2$.

Depending on the sign of the discriminant Δ of the cubic polynomial $P(Y)$, different cases have to be considered. It is computed as

$$\Delta = 4(b^2 - 3ac)^3 - (2b^3 - 9abc + 27a^2d^2)^2.$$

A discussion is made in Lantoine and Russell (2011) to determine which cases are physically possible. Here, we only describe the ones that actually correspond to feasible solutions.

If $\Delta > 0$, $P(Y)$ has three distinct real roots $Y^* = Y_1$, Y_2 and Y_3 such that the polynomial becomes

$$P(Y) = a(Y - Y^*)(Y - Y_2)(Y - Y_3)$$

and we define

$$Z_0^2 = \mathrm{sign}(a)(\xi_0^2 - Y^*)$$

$$Z_1^2 = \mathrm{sign}(a)(Y_2 - Y^*)$$

$$Z_2^2 = \mathrm{sign}(a)(Y_3 - Y^*).$$

Let us consider the case where $X = \xi$. The sign of a is positive and we choose the roots such that $Y_2 > Y_3 > Y^*$. One must distinguish two subcases $Z_0^2 < Z_2^2$ and $Z_0^2 > Z_1^2$ which will be refered to as ξ_1 and ξ_2. We start with the ξ_1 solution. Eq. (E.18) writes

$$\tau_1 - \tau_{1,0} = \tau_1 = \int_{Z_0}^{Z} \frac{ds}{\sqrt{Q(s)}}$$

where the initial value of $\tau_{1,0}$ is zero. Successive changes of variables yield

$$\begin{aligned}
\tau_1 &= \frac{1}{\sqrt{F}} \int_{Z_0}^{Z} \frac{ds}{\sqrt{(Z_1^2 - s^2)(Z_2^2 - s^2)}} \\
&= \frac{1}{\sqrt{F}} \int_{Z_0/Z_2}^{Z/Z_2} \frac{Z_2\, ds}{\sqrt{(Z_1^2 - Z_2^2 s^2)(Z_2^2 - Z_2^2 s^2)}} \\
&= \frac{1}{Z_1\sqrt{F}} \int_{Z_0/Z_2}^{Z/Z_2} \frac{ds}{\sqrt{(1 - (Z_2/Z_1)^2 s^2)(1 - s^2)}}.
\end{aligned}$$

Now, set the constant τ_{ξ_1} such that $Z(\tau_1 = \tau_{\xi_1}) = 0$. Then,

$$\begin{aligned}
\tau_{\xi_1} &= \frac{1}{Z_1\sqrt{F}} \int_{Z_0/Z_2}^{0} \frac{ds}{\sqrt{(1 - (Z_2/Z_1)^2 s^2)(1 - s^2)}} \\
&= -\frac{1}{Z_1\sqrt{F}} \int_{0}^{Z_0/Z_2} \frac{ds}{\sqrt{(1 - (Z_2/Z_1)^2 s^2)(1 - s^2)}} \\
&= -\frac{1}{Z_1\sqrt{F}} F_J(Z_0/Z_2; Z_2/Z_1) \qquad \text{(E.23)}
\end{aligned}$$

Hence, we can rewrite

$$\begin{aligned}
\tau_1 &= \frac{1}{Z_1\sqrt{F}} \int_{Z_0/Z_2}^{Z/Z_2} \frac{ds}{\sqrt{(1 - (Z_2/Z_1)^2 s^2)(1 - s^2)}} \\
&= \frac{1}{Z_1\sqrt{F}} \int_{0}^{Z/Z_2} \frac{ds}{\sqrt{(1 - (Z_2/Z_1)^2 s^2)(1 - s^2)}} \\
&\quad -\frac{1}{Z_1\sqrt{F}} \int_{0}^{Z_0/Z_2} \frac{ds}{\sqrt{(1 - (Z_2/Z_1)^2 s^2)(1 - s^2)}} \\
&= \frac{1}{Z_1\sqrt{F}} \int_{0}^{Z/Z_2} \frac{ds}{\sqrt{(1 - (Z_2/Z_1)^2 s^2)(1 - s^2)}} + \tau_{\xi_1}
\end{aligned}$$

and Z is obtained as

$$\begin{aligned}
& Z_1\sqrt{F}(\tau_1 - \tau_{\xi_1}) = \int_{0}^{Z/Z_2} \frac{ds}{\sqrt{(1 - (Z_2/Z_1)^2 s^2)(1 - s^2)}} \\
\Rightarrow \quad & Z = Z_2\, \mathrm{sn}(Z_1\sqrt{F}(\tau_1 - \tau_{\xi_1}); Z_2/Z_1).
\end{aligned}$$

An additional term is added in Lantoine and Russell (2011) to take into account the sign of the initial velocity. It is required for we assumed a positive sign for the square roots in eq. (E.18) and (E.19). More precisely,

$$\delta_{\xi_1} = \text{sign}(\dot{Z}_0 \,\text{cn}(-Z_1\sqrt{F}\tau_{\xi_1}; Z_2/Z_1)) \tag{E.24}$$

is computed to give the final expression for ξ :

$$\xi_1^2 = [Z_2 \,\text{sn}(Z_1\sqrt{F}(\delta_{\xi_1}\tau_1 - \tau_{\xi_1}); Z_2/Z_1)]^2 + Y^*. \tag{E.25}$$

A similar way is followed for the ξ_2 solution. In this case,

$$\tau_1 = -\frac{1}{Z_1\sqrt{F}} \int_{Z_1/Z_0}^{Z_1/Z} \frac{ds}{\sqrt{(1-(Z_2/Z_1)^2 s^2)(1-s^2)}} \tag{E.26}$$

$$\tau_{\xi_2} = \frac{1}{Z_1\sqrt{F}} F_J(Z_1/Z_0; Z_2/Z_1) \tag{E.27}$$

$$\delta_{\xi_2} = \text{sign}(\dot{Z}_0 \,\text{cn}(Z_1\sqrt{F}\tau_{\xi_2}; Z_2/Z_1)). \tag{E.28}$$

The solution can then be written as

$$\xi_2^2 = [Z_1/\text{sn}(-Z_1\sqrt{F}(\delta_{\xi_2}\tau_1 - \tau_{\xi_2}); Z_2/Z_1)]^2 + Y^*. \tag{E.29}$$

When $X = \eta$, the sign of a is different and the only possible solution turns out to be analog to ξ_1:

$$\eta_1^2 = -[Z_2 \,\text{sn}(-Z_1\sqrt{F}(\delta_{\eta_1}\tau_1 - \tau_{\eta_1}); Z_2/Z_1)]^2 + Y^*. \tag{E.30}$$

$$\tau_{\eta_1} = -\frac{1}{Z_1\sqrt{F}} F_J(Z_0/Z_2; Z_2/Z_1) \tag{E.31}$$

$$\delta_{\eta_1} = \text{sign}(\dot{Z}_0 \,\text{cn}(-Z_1\sqrt{F}\tau_{\xi_1}; Z_2/Z_1)) \tag{E.32}$$

The situation gets more complicated when $\Delta < 0$ which corresponds to a feasible solution for $X = \xi$, (denoted ξ_3). In this case Y^* is the real root and Y_2 and Y_3 are complex conjugate roots. Longer calculation and changes of variables

are needed to finally get[2]

$$\xi_3^2 = \left[\lambda \frac{C\,\mathrm{cn}(w_1;w_2) - \mathrm{sn}(w_1;w_2)}{C\mathrm{cn}(w_1;w_2) + \mathrm{sn}(w_1;w_2)}\right]^2 + Y^* \tag{E.33}$$

$$w_1 = -\sqrt{F}(\lambda + p)(\delta_{\xi_3}\tau_1 - \tau_{\xi_3}) \tag{E.34}$$

$$w_2 = \sqrt{1 - 1/C^4} \tag{E.35}$$

$$\alpha_0 = \left(\lambda + \sqrt{\xi_0^2 - Y^*}\right) / \left(\lambda - \sqrt{\xi_0^2 - Y^*}\right)$$

$$\tau_{\xi_3} = \frac{2\lambda}{B\sqrt{F}} F_J\left(\mathrm{sign}(\alpha_0) C / \sqrt{C^2 + \alpha_0^2}; w_2\right) \tag{E.36}$$

$$\delta_{\xi_3} = \mathrm{sign}(\dot{\xi}_0). \tag{E.37}$$

Auxilary variables are given by

$$\begin{aligned}
Y_r &= \mathrm{Re}(Y_2) - Y^* = \mathrm{Re}(Y_3) - Y^* \\
Y_i &= |\mathrm{Im}(Y_2)| = |\mathrm{Im}(Y_3)| \\
p &= \frac{1}{\sqrt{2}} \sqrt{\sqrt{Y_r^2 + Y_i^2} + Y_r} \\
q &= \frac{1}{\sqrt{2}} \sqrt{\sqrt{Y_r^2 + Y_i^2} - Y_r} \\
\lambda &= \sqrt{p^2 + q^2} \\
A &= (\lambda - p)^2 + q^2 \\
B &= (\lambda + p)^2 + q^2 \\
C &= \sqrt{B/A}
\end{aligned}$$

The numerical implementation of this method including technical difficulties is described in Sec. E.2.

[2]The described solution is different from the one appearing in Lantoine and Russell (2011). We believe that some mistakes are present in the formulae. Note that ξ_3 corresponds to the ξ 5 planar solution in the paper.

E.2 Numerical implementation

The code written by Dr. G.F. Gronchi, C. Tardioli and C. Hubaux is made of three main parts. First, initial Cartesian position and velocity and important constants are set. Then, the roots of $P_\xi(Y)$ and $P_\eta(Y)$ are computed. Finally, the loop on time is performed.

E.2.1 Initialization

Once the initial Cartesian position $\vec{r}_0 = r(0) = (x_0, y_0, z_0)$ and $\vec{v}_0 = v(0) = (v_{x,0}, v_{y,0}, v_{z,0})$ are chosen, the initial parabolic coordinates are computed as

$$\begin{cases} \xi_0 = \xi(0) = \sqrt{z_0 + r_0} \\ \eta_0 = \eta(0) = \sqrt{-z_0 + r_0} \\ \phi_0 = \phi(0) = \text{atan2}(y_0, x_0). \end{cases}$$

Note that a positive sign is assumed for ξ_0 and η_0 and that zero values of x_0, ξ_0 or η_0 must be considered to correctly compute ϕ_0. The atan2(y_0, x_0) function is an intrinsic Fortran 90 function computing the atan of y_0/x_0 in rad. The result is in $[-\pi, \pi]$. Both input signs are known so that the correct quadrant is computed for the output angle. The three main constants are given by

$$\begin{aligned} p_\phi &= l = x_0 v_{y,0} - y_0 v_{x,0} \\ E &= \frac{v_0^2}{2} - \frac{\mu}{r_0} - F z_0 \\ \beta &= -\left(E\xi_0^2 - \frac{1}{2}\left(r_0 v_{z,0} + \frac{\vec{r}_0 \cdot \vec{v}_0}{\sqrt{z_0 + r_0}} \right)^2 - \frac{p_\phi^2}{2\xi_0^2} + \mu + \frac{F\xi_0^4}{2} \right). \end{aligned}$$

E.2.2 Roots of $P_\xi(Y)$ and $P_\eta(Y)$

Roots of cubic polynomials can be computed in various ways. In this case, a subroutine developed at the University of Pisa has been used. Depending on the sign of the discriminant, three real roots or one real and two complex conjugate roots are obtained. Then, the correct type of ξ solution is identified and the corresponding constants are computed: respectively τ_{ξ_1}, δ_{ξ_1} for ξ_1, τ_{ξ_2}, δ_{ξ_2} for ξ_2 and τ_{ξ_3}, δ_{ξ_3} for ξ_3. Similarly, τ_{η_1} and δ_{η_1} are computed from the roots of P_η.

E.2.3 Loop on time

Step size

The same units as in the rest of the manuscript have been used. In our simulations, the time step has been set to $h = 10^{-2}$ day$/2\pi$. However, when r is small ($r \leq 0.1$ **UD**), the time step is reduced to 10^{-4} day$/2\pi$ to handle singularity crossings in quadrature methods used to compute τ_1 and τ_2. Then, at each time step, the following operations must be performed.

Computation of τ_1

The main part of each step consists in computing τ_1 corresponding to the current value of the time, t. We know from eq. (E.16) how to express t from τ_1. This relation must be inverted to obtain $\tau_1(t)$. Eq. (E.16) requires the value of $\xi(\tau_1)$ and $\eta(\tau_1)$ that can be computed easily thanks to the parameters set in the initialization step. Eq. (E.25), (E.29) and (E.33) are used for $\xi(\tau_1)$ and $\eta(\tau_1)$ is obtained from eq. (E.30).

Even if not theoretically proven, it turns out that the evolution of τ_1 with respect to t is monotonic and close to a linear function. Three examples are shown in Fig. E.1 for each ξ type of solution. The magnitude of the constant force is set to $F = 0.05$. Initial conditions are $\vec{r} = (1, 0, 0)$ **UD**, $\vec{v} = (0, 1, 0)$ **UD**/**UT** for (ξ_1, η_1), $\vec{r} = (1, 0, 1)$ **UD**, $\vec{v} = (-1, 0, 1)$ **UD**/**UT** for (ξ_2, η_1) and $\vec{r} = (1, 0, 1)$ **UD**, $\vec{v} = (0, 0.3, 1)$ **UD**/**UT** for (ξ_3, η_1).

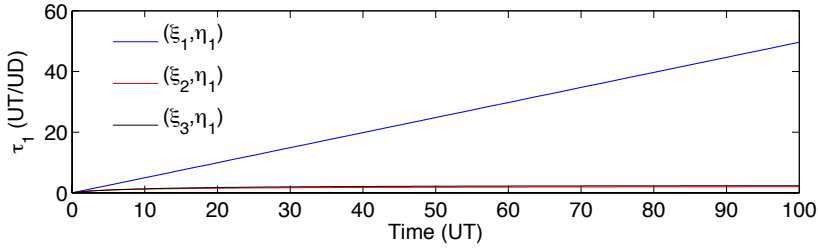

Figure E.1 • *Evolution of τ_1 with respect to t for each couple of feasible solutions.*

Given the shape of this function, the inversion is done by means of the fast *regula falsi* method. Given a general equation $f(\theta) = 0$, the algorithm to find θ with a precision threshold ϵ is the following:

choose a and b such that $f(a)\,f(b) \leq 0$
$c = [a\,f(b) - b\,f(a)]/[f(b) - f(a)]$
while $|f(c)| > \epsilon$
  if $f(a)\,f(c) > 0$ **then** $a = c$ $f(a) = f(c)$
  else $b = c$ $f(b) = f(c)$
  $c = [a\,f(b) - b\,f(a)]/[f(b) - f(a)]$

In our case, the function f is defined as

$$f(\theta) = h - \int_{\tau_{1,0}}^{\theta} [\xi^2(s) + \eta^2(s)]ds. \tag{E.38}$$

This relation is in agreement with eq. (E.16). Knowing the previous value of τ_1, denoted $\tau_{1,0}$, we need to find the current value of τ_1 associated to t. Instead of starting from $t_0 = 0$ and $\tau_{1,0} = 0$ at each time step, it is faster to start from the previous values of t (that explains the h variable in eq. (E.38)) and τ_1. One difficulty of this method is that one must already have a rough guess of the initial $[a, b]$ interval in which τ_1 lies. In the current version of our code, a is set to $\tau_{1,0}$ and b is computed iteratively. Starting from a, b is increased until $f(b)\,f(a) < 0$. This initialization step should be improved and be more efficient.

As for the previous roots solving problem, the quadrature is performed by means of a subroutine developed at the University of Pisa.
In Lantoine and Russell (2011), these integrals are solved analytically with Mathematica. However, we are sceptical about the accuracy of the proposed formulae. For example, the following relation is given, when Z corresponds to the ξ_1 solution:

$$\int Z^2 d\tau = \frac{Z_1}{\sqrt{F}\delta_{\xi_1}} \left[Z_1\sqrt{F}\delta_{\xi_1}\tau_1 - E_L(v_1; Z_2/Z_1) + E_L(v_0; Z_2/Z_1) \right] \tag{E.39}$$

with

$$\begin{aligned} v_0 &= -Z_1\sqrt{F}\tau_{\xi_1} \\ v_1 &= Z_1\sqrt{F}(\delta_{\xi_1}\tau_1 - \tau_{\xi_1}). \end{aligned}$$

The lack of limits to the integral is misleading. Indeed, when the correct limits are added, the formula is totally different and not equivalent to eq. (E.39) :

$$\begin{aligned} & \int_0^{\tau_1} Z^2(s)ds \\ = & \int_0^{\tau_1} Z_2^2\,\mathrm{sn}^2(Z_1\sqrt{F}(s - \tau_{\xi_1}); Z_2/Z_1)ds \\ = & \frac{Z_1}{\sqrt{F}\delta_{\xi_1}} [F_L(\mathrm{asin}(\mathrm{sn}(v_1; Z_2/Z_1)); Z_2/Z_1) - E_L(\mathrm{asin}(\mathrm{sn}(v_1; Z_2/Z_1)); Z_2/Z_1) \\ & -F_L(\mathrm{asin}(\mathrm{sn}(v_0; Z_2/Z_1)); Z_2/Z_1) + E_L(\mathrm{asin}(\mathrm{sn}(v_0; Z_2/Z_1)); Z_2/Z_1)]\,. \end{aligned}$$

The other solution types yield tricky formulae that could not be checked by hand. Hence we prefer to use a robust numerical quadrature method.

Once τ_1 is stored, $\tau_{1,0}$ is updated as $\tau_{1,0} = \tau_1$ for the next step.

Computation of τ_2

From eq. (E.17), it seems natural to compute τ_2 exactly like τ_1. However, that means that we should be able to express ξ and η with respect to τ_2. A much easier task is to express τ_2 as a function of τ_1. Indeed, eq. (E.16) and (E.17) directly give

$$d\tau_2 = \left(\frac{1}{\xi^2} + \frac{1}{\eta^2}\right) d\tau_1.$$

A simple quadrature leads to the value of τ_2 corresponding to the current real time:

$$\tau_2 = \tau_{2,0} + \int_{\tau_{1,0}}^{\tau_1} \left(\frac{1}{\xi^2(s)} + \frac{1}{\eta^2(s)}\right) ds.$$

Similarly to τ_1, $\tau_{2,0}$ is set equal to τ_2 for the next step.

Correct sign identification

Now that we have computed the fictitious times $\tau_1(t)$ and $\tau_2(t)$ that correspond to the real time, the parabolic coordinates can be evaluated. Nevertheless, an undetermined sign remains[3] in transformation (E.22):

$$X = \pm\sqrt{\text{sign}(a)\, Z^2 + Y^*}.$$

For we did not find any theoretical clue, the signs of ξ and η are determined in a numerical way. Storing the previous value of ξ and η, denoted respectively ξ_{prev} and η_{prev}, we follow this simple rule:

if $\xi_{\text{prev}} > 0$ **then**
  if $(\xi_{\text{prev}} + (\xi - \xi_{\text{prev}})/h < 0$ and $\xi > 0)$ **then**
    $\xi = -\xi$
  end
else
  if $(\xi_{\text{prev}} + (\xi - \xi_{\text{prev}})/h > 0$ and $\xi < 0)$ **then**
    $\xi = -\xi$

[3] This issue is skipped in Lantoine and Russell (2011).

```
    end
end
if η_prev > 0 then
    if (η_prev + (η − η_prev)/h < 0 and η > 0) then
        η = −η
    end
else
    if (η_prev + (η − η_prev)/h > 0 and η < 0) then
        η = −η
    end
end
```

Obviously, the efficiency of this process is limited. It proved to work well with sufficiently small time steps though.

Cartesian coordinates update

Cartesian position and velocity are parts of the output variables. This requires a conversion from parabolic coordinates. The Cartesian position is easily obtained from eq. (E.2). The Cartesian velocity involves derivatives of the parabolic coordinates with respect to the real time:

$$\begin{cases} \dfrac{dx}{dt} &= \left(\dfrac{d\xi}{dt}\eta + \xi\dfrac{d\eta}{dt}\right)\cos\phi - \xi\eta\dfrac{d\phi}{dt}\sin\phi \\ \dfrac{dy}{dt} &= \left(\dfrac{d\xi}{dt}\eta + \xi\dfrac{d\eta}{dt}\right)\sin\phi + \xi\eta\dfrac{d\phi}{dt}\cos\phi \\ \dfrac{dz}{dt} &= \xi\dfrac{d\xi}{dt} - \eta\dfrac{d\eta}{dt} \end{cases}$$

where

$$\begin{cases} \dfrac{d\xi}{dt} &= \dfrac{\partial\xi}{\partial\tau_1}\dfrac{\partial\tau_1}{\partial t} &= \dfrac{\partial\xi}{\partial\tau_1}\dfrac{1}{\xi^2+\eta^2} \\ \dfrac{d\eta}{dt} &= \dfrac{\partial\eta}{\partial\tau_1}\dfrac{\partial\tau_1}{\partial t} &= \dfrac{\partial\eta}{\partial\tau_1}\dfrac{1}{\xi^2+\eta^2} \\ \dfrac{d\phi}{dt} &= \dfrac{\partial\phi}{\partial\tau_2}\dfrac{\partial\tau_2}{\partial t} &= \dfrac{p_\phi}{\xi^2\eta^2}. \end{cases}$$

Depending on the type of ξ solution, the derivatives of ξ with respect to τ_1

are given by

$$\begin{aligned}
\frac{\partial \xi_1}{\partial \tau_1} &= Z_2^2 Z_1 \sqrt{F}\delta_{\xi_1} \mathrm{sn}\Big(Z_1\sqrt{F}(\delta_{\xi_1}\tau_1 - \tau_{\xi_1}); Z_2/Z_1\Big)\mathrm{cn}\Big(Z_1\sqrt{F}(\delta_{\xi_1}\tau_1 - \tau_{\xi_1}); Z_2/Z_1\Big) \\
&\quad \times \mathrm{dn}\Big(Z_1\sqrt{F}(\delta_{\xi_1}\tau_1 - \tau_{\xi_1}); Z_2/Z_1\Big) \Big/ \left[\mathrm{sign}(\xi_1)\sqrt{\xi_1^2}\right] \\
\frac{\partial \xi_2}{\partial \tau_1} &= \frac{Z_1^3\sqrt{F}\delta_{\xi_2}}{\mathrm{sn}^3\Big(-Z_1\sqrt{F}(\delta_{\xi_2}\tau_1 - \tau_{\xi_2}); Z_2/Z_1\Big)}\mathrm{cn}\Big(-Z_1\sqrt{F}(\delta_{\xi_2}\tau_1 - \tau_{\xi_2}); Z_2/Z_1\Big) \\
&\quad \times \mathrm{dn}\Big(-Z_1\sqrt{F}(\delta_{\xi_2}\tau_1 - \tau_{\xi_2}); Z_2/Z_1\Big) \Big/ \left[\mathrm{sign}(\xi_2)\sqrt{\xi_2^2}\right] \\
\frac{\partial \xi_3}{\partial \tau_1} &= \frac{2\lambda^2\sqrt{F}(\lambda+p)\delta_{\xi_3} C\,\mathrm{dn}(w_1;w_2)\Big(C\,\mathrm{cn}(w_1;w_2) - \mathrm{sn}(w_1;w_2)\Big)}{\mathrm{sign}(\xi_3)\sqrt{\xi_3^2}\Big(C\,\mathrm{cn}(w_1;w_2) + \mathrm{sn}(w_1;w_2)\Big)^3}
\end{aligned}$$

with w_1, w_2 defined in eq. (E.34), (E.35) and the sign of ξ determined as previously. Similarly, the derivative of η with respect to τ_1 is

$$\begin{aligned}
\frac{\partial \eta_1}{\partial \tau_1} &= Z_2^2 Z_1 \sqrt{F}\delta_{\eta_1} \mathrm{sn}\Big(-Z_1\sqrt{F}(\delta_{\eta_1}\tau_1 - \tau_{\eta_1}); Z_2/Z_1\Big)\mathrm{cn}\Big(-Z_1\sqrt{F}(\delta_{\eta_1}\tau_1 - \tau_{\eta_1}); Z_2/Z_1\Big) \\
&\quad \times \mathrm{dn}\Big(-Z_1\sqrt{F}(\delta_{\eta_1}\tau_1 - \tau_{\eta_1}); Z_2/Z_1\Big) \Big/ \left[\mathrm{sign}(\eta_1)\sqrt{\eta_1^2}\right].
\end{aligned}$$

E.2.4 Examples

Each type of solution is illustrated in Fig. E.2. The propagation is performed over 100 days/2π. The constant parameter F is set to 0.05. Initial conditions are the same as the aforementioned ones: $\vec{r} = (1,0,0)$ **UD**, $\vec{v} = (0,1,0)$ **UD**/**UT** for (ξ_1, η_1), $\vec{r} = (1,0,1)$ **UD**, $\vec{v} = (-1,0,1)$ **UD**/**UT** for (ξ_2, η_1) and $\vec{r} = (1,0,1)$ **UD**, $\vec{v} = (0,0.3,1)$ **UD**/**UT** for (ξ_3, η_1). While the first case corresponds to a bounded orbit[4], the other initial conditions lead to totally different motions. The relative error corresponding to the constants E and p_ϕ is equal to the double precision threshold in Fortran 90 on this time span. This error depends on the accuracy of the elliptic function evaluation, quadrature and roots solving subroutines

[4] A detailed analysis is presented in Lantoine and Russell (2011).

E.3 Conclusion

Two methods giving closed-form solutions to the Stark problem have been briefly described. The solution from Lantoine and Russell (2011) has been investigated further and technical details have been given about its practical numerical implementation. Some errors have been pointed out.

Even if some parts of the process should be improved, this method turns out efficient. Additional tests should be performed to assess the robustness of our implementation. One should also keep in mind that any traditional technique that could be used to numerically solve differential equations (E.1) has *in fine* been replaced by a quadrature method. In other words, we do not yet fully benefit from the explicit analytical form of the solution. In its current version, the accuracy of our code is closely bound to the one of the quadrature method.

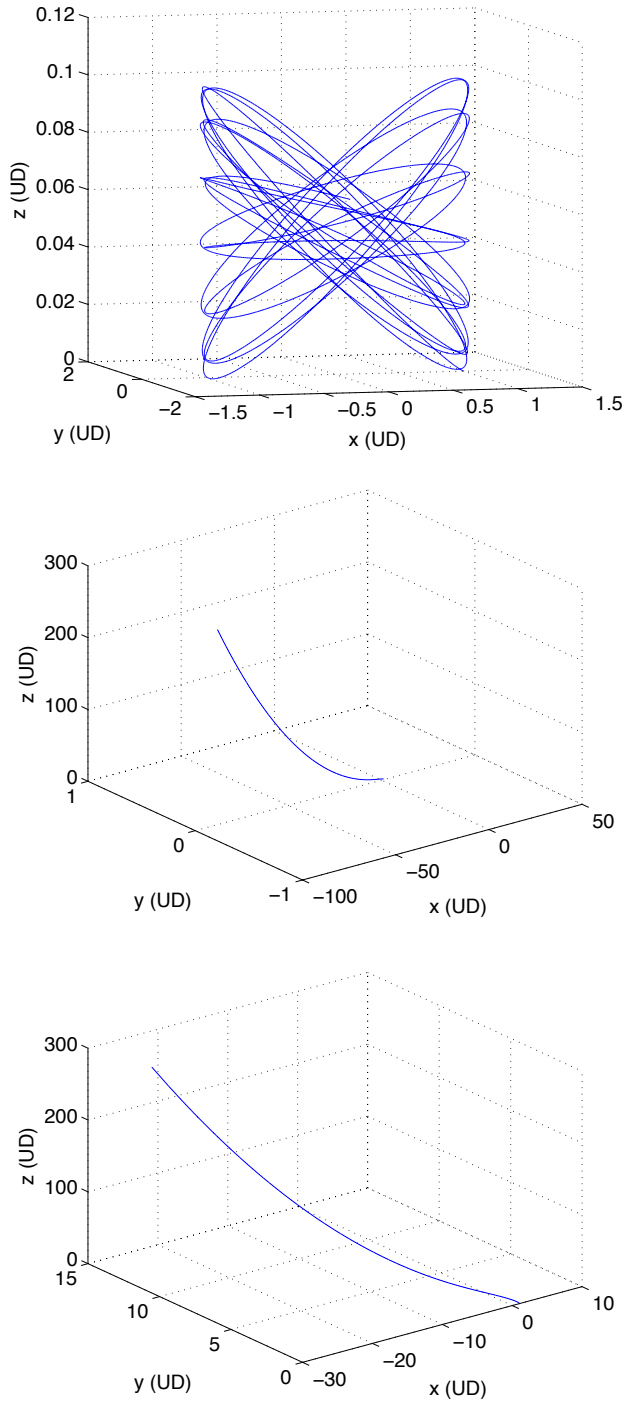

Figure E.2 • *Orbit evolution over* 100 *days*/2π *for each type of solution:* (ξ_1, η_1) *(top),* (ξ_2, η_1) *(middle) and* (ξ_3, η_1) *(bottom).*

Appendix F
Elliptic functions and integrals

The methods proposed in Appx. E to find solutions of the Stark problem heavily rely on elliptic functions. Dense literature exists about this topic and different definitions can be found, sometimes in contradiction with each other. Hence, it is necessary to give the definitions which will actually be used in this manuscript. Based on Appell and Lacour (1897) we present a summary of useful formulae.

Numerical evaluations of elliptic functions and integrals have been performed through Fortran 90 subroutines proposed in Press et al. (2007).

F.1 Elliptic integrals

Elliptic integrals of different kinds exist. The incomplete elliptic integral of the first kind, also known as the Legendre's elliptic integral of the first kind, is usually defined as

$$F_L(\phi;k) = \int_0^\phi \frac{ds}{\sqrt{1-k^2\sin^2 s}}.$$

This integral is said *complete* when $\phi = 1$. The variable k is called the *modulus* and is such that $0 < k^2 < 1$. Other definitions use the Jacobi's form given by

$$F_J(\phi;k) = \int_0^\phi \frac{ds}{\sqrt{(1-s^2)(1-k^2s^2)}} = F_L(\operatorname{asin}\phi;k).$$

Similarly, the (incomplete) Legendre's and Jacobi's elliptic integrals of the

second kind are

$$\begin{aligned} E_L(\phi;k) &= \int_0^\phi \sqrt{1-k^2\sin^2 s}\, ds \\ E_J(\phi;k) &= \int_0^\phi \frac{k^2 s^2\, ds}{\sqrt{(1-s^2)(1-k^2s^2)}} \\ &= \int_0^\phi \frac{ds}{\sqrt{(1-s^2)(1-k^2s^2)}} - \int_0^\phi \frac{1-k^2s^2}{\sqrt{(1-s^2)(1-k^2s^2)}}\, ds \\ &= F_J(\phi;k) - \int_0^\phi \frac{\sqrt{1-k^2s^2}}{\sqrt{1-s^2}}\, ds \\ &= F_L(\operatorname{asin}\phi;k) - E_L(\operatorname{asin}\phi;k). \end{aligned}$$

We do not define the elliptic integral of the third kind which will not be used.

F.2 Elliptic functions

The Jacobi's elliptic functions can be defined in terms of Jacobi's *theta functions*. However, a simpler definition is obtained by inverting the elliptic integrals. Indeed, the *amplitude* ϕ can be computed as

$$\phi = F_L^{-1}(u;k) \quad \text{where} \quad u = F_L(\phi;k).$$

Jacobi's elliptic functions sn, cn, and dn are then defined as

$$\begin{aligned} \operatorname{sn}(u;k) &= \sin\phi \\ \operatorname{cn}(u;k) &= \cos\phi = \sqrt{1-\operatorname{sn}^2(u;k)} \\ \operatorname{dn}(u;k) &= \sqrt{1-k^2\operatorname{sn}^2(u;k)}. \end{aligned}$$

Some useful formulae are

$$\begin{aligned} \operatorname{sn}^2(u;k) + \operatorname{cn}^2(u;k) &= 1 \\ \operatorname{dn}^2(u;k) + k^2\operatorname{sn}^2(u;k) &= 1 \end{aligned}$$

and

$$\begin{aligned} \frac{d}{du}\operatorname{sn}(u;k) &= \operatorname{cn}(u;k)\operatorname{dn}(u;k) \\ \frac{d}{du}\operatorname{cn}(u;k) &= -\operatorname{sn}(u;k)\operatorname{dn}(u;k) \\ \frac{d}{du}\operatorname{dn}(u;k) &= -k^2\operatorname{sn}(u;k)\operatorname{cn}(u;k). \end{aligned}$$

Bibliography

Aksnes, K. (1976). Short-period and long-period perturbations of a spherical satellite due to direct solar radiation. *Celest. Mech. Dyn. Astr.*, 13:89–104.

Anselmo, L. and Pardini, C. (2005). Orbital evolution of geosynchronous objects with high area-to-mass ratios. In *Danesy, D. (Ed), Proceedings of the Fourth European Conference on Space Debris, ESA SP-587. ESA Publications Division., Noordwijk, The Netherlands, pp. 79-284.*

Anselmo, L. and Pardini, C. (2011). Orbital evolution of the first upper stages used for the new European and Chinese navigation satellite systems. *Acta Astronaut.*, 68:2066–2079.

Appell, P. and Lacour, E. (1897). *Principes de la théorie des fonctions elliptiques et applications.* Gauthier-Villars et Fils, Paris.

Arnold, V. I. (1963). Proof of a theorem by A.N. Kolmogorov on the invariance of quasi-periodic motions under small perturbations of the Hamiltonian. *Russ. Math. Surv*, 18:9.

Arnold, V. I. (1989). *Mathematical Methods of Classical Mechanics.* Springer-Verlag, 2nd edition edition.

Barrio, R., Borczyk, W., and Breiter, S. (2009). Spurious structures in chaos indicators maps. *Chaos Soliton. Fract.*, 40:1697–1714.

Bendisch, J., Bunte, K., Klinkrad, H., Krag, H., Martin, C., Sdunnus, H., Walker, R., Wegener, P., and Wiedemann, C. (2004). The MASTER-2001 Model, Advances in Space Research, Vol. 34, No. 5, 2004, pp. 959-968. *Adv. Space Res.*, 34:959–968.

Benettin, G., Galgani, L., Giorgilli, A., and Strelcyn, J.-M. (1980). Lyapunov characteristic exponents for smooth dynamical systems and for Hamiltonian systems; a method for computing all of them, part 1: theory. *Meccanica*, 15:9–20.

Breiter, S. (1999). Explicit Symplectic Integrator for Highly Eccentric Orbits. *Celest. Mech. Dyn. Astron.*, 71:229–241.

Breiter, S., Melendo, B., Bartczak, P., and Wytrzyszczak, I. (2005a). Synchronous motion in the Kinoshita problem. *Astron. Astrophys.*, 437:753–764.

Breiter, S. and Métris, G. (1999). Symplectic mapping for satellites and space debris including nongravitational forces. *Celest. Mech. Dyn. Astr.*, 71:79–94.

Breiter, S., Wytrzyszczak, I., and Melendo, B. (2005b). Long-term predictability of orbits around the geosynchronous altitude. *Adv. Space Res.*, 35:1313–1317.

Burkardt, T. M. and Danby, J. M. A. (1983). The solutions of Kepler's equation. II. *Celest. Mech. Dyn. Astr.*, 31:317–328.

Burns, R. and Marshall, G. (1968). Motion of an artificial satellite under combined influence of planar and Keplerian force fields. Technical report, NASA technical note D-4622.

Chao, C. (2005). *Applied orbit perturbation and maintenance.* The Aerospace Press (El Segundo, California, American Institute of Aeronautics and Astronautics).

Chao, C. (2006). Analytical Investigation of GEO Debris with High Area-to-mass Ratio. In *AIAA paper No. AIAA-2006-6514, Presented at the 2006 AIAA/AAS Astrodynamics Specialist Conference, Keystone, CO.*

Chao, C. C. and Gick, R. A. (2004). Long-term evolution of navigation satellite orbits: GPS/GLONASS/GLONASS. *Adv. Space Res.*, 34:1221–1226.

Cincotta, P., Giordano, C., and Simó, C. (2003). Phase Space structure of multi-dimensional systems by means of the mean exponential growth factor of nearby orbits. *Physica D*, 182:151–178.

Cunningham, L. E. (1970). On the computation of the spherical harmonic terms needed during the numerical integration of the orbital motion of an artifical satellite. *Celest. Mech. Dyn. Astr.*, 2:207–216.

Danby, J. M. A. (1987). The Solution of Kepler's Equations - Part Three. *Celest. Mech. Dyn. Astr.*, 40:303–312.

Danby, J. M. A. and Burkardt, T. M. (1983). The solution of Kepler's equation. I. *Celest. Mech. Dyn. Astr.*, 31:95–107.

Deleflie, F. and et al. (2013). STELA: Semi-analytical Tool for End of Life Analysis. *Astron. Astrophys. Sup. S.*, Submitted.

Deleflie, F., Rossi, A., Portmann, C., Métris, G., and Barlier, F. (2011). Semi-analytical investigations of the long term evolution of the eccentricity of Galileo and GPS-like orbits. *Adv. Space Res.*, 47:811–821.

Delsate, N. and Compère, A. (2012). NIMASTEP: a software to modelize, study, and analyze the dynamics of various small objects orbiting specific bodies. *Astron. Astrophys.*, 540.

Deprit, A. (1969). Canonical transformations depending on a small parameter. *Celest. Mech. Dyn. Astr.*, 1:12–30.

Dufey, J. (2010). *Short-period effects in the rotation of Mercury.* PhD thesis, University of Namur (UNamur), Presses Universitaires de Namur.

Duncan, M., Levison, H., and Lee, M. (1998). A Multiple Time Step Symplectic Algorithm for Integrating Close Encounters. *Astron. J.*, 116:2067–2077.

Dvorak, R. and Lhotka, C. (2013). *Celestial Dynamics. Chaoticity and Dynamics of Celestial Systems.* Wiley-VCH Verlag GmbH.

Epstein, P. (1926). The Stark effect from the point of view of Schrödinger's quantum theory. *Phys. Rev.*, 28:695–710.

Escobal, P. (1976). *Methods of Orbit Determination.* Krieger, 2nd ed. edition.

Ferraz-Mello, S. (1964). Sur le problème de la pression de radiation dans la théorie des Satellites Artificiels. *C.R. Acad. Sc. Paris*, 258:463.

Ferraz-Mello, S. (1965). Action de la Pression de radiation sur le mouvement d'un satellite artificiel de la terre. In *Proc. 14th Intl. Astronaut. Congress-Paris, vol. IV, 1963, PWN, Warsaw, 41.*

Ferraz-Mello, S. (1972). Analytical study of the Earth's shadowing effects on satellite orbits. *Celest. Mech. Dyn. Astr.*, 5:80–101.

Flohrer, T., Krag, H., Klinkrad, H., Bastida Virgili, B., and Früh, C. (2009). Improving ESA's collision risk estimates by an assessment of the TLE orbit errors of the US SSN catalogue. In *Proceedings of the 5th European Conference on Space Debris, Darmstadt, Germany.*

Forest, E. and Ruth, R. (1990). Fourth-order symplectic integration. *Phys. D*, 43:105.

Fraysse, H., Morand, V., Le Fevre, C., Deleflie, F., Wailliez, S., Lamy, A., Martin, T., and Perot, E. (2012). Long term orbit propagation techniques developed in the frame of the french space act. *J. Aerospace Eng., Sci. Appl.*, 4:1–16.

Froeschlé, C., Lega, E., and Gonczi, R. (1997). Fast Lyapunov indicators. Applications to asteroidal motion. *Celest. Mech. Dyn. Astr.*, 67:41–62.

Goździewski, K. (2003). A dynamical analysis of the HD 37124 planetary system. *Astron. Astrophys.*, 398:315–325.

Goździewski, K., Bois, E., Maciejewski, A. J., and Kiseleva-Eggleton, L. (2001). Global dynamics of planetary systems with the MEGNO criterion. *Astron. Astrophys.*, 378:569–586.

Gronchi, G. (2005). An algebraic method to compute the critical points of the distance function between two Keplerian orbits. *Celest. Mech. Dyn. Astr.*, 93:295–329.

Hairer, E., Lubic, C., and Wanner, G. (2006). *Geometric Numerical Integration. Structure-preserving Algorithms for ordinary differential equations*. Berlin Heidelberg, 2nd ed. edition.

Hairer, E., Norsett, S., and Wanner, G. (1993). *Solving ordinary differential equations I: Nonstiff problems*. Springer-Verlag, New-York, 2nd edition edition.

Hénon, M. and Heiles, C. (1964). The applicability of the third integral of motion: Some numerical experiments. *Astron. J.*, 69:73.

Henrard, J. (1970). On a perturbation theory using Lie transform. *Celest. Mech. Dyn. Astr.*, 3:107–120.

Hinse, T. C., Christou, A. A., Alvarellos, J. L. A., and Goździewski, K. (2010). Application of the MEGNO technique to the dynamics of Jovian irregular satellites. *Mon. Not. R. Astron. Soc.*, 404:837–857.

Hoots, F. and Roehrich, R. (1980). Models for Propagation of NORAD Element Sets. Technical report, United States Department of Defense Spacetrack Report (3).

Hubaux, C. and Lemaitre, A. (2013). The impact of Earth's shadow on the long-term evolution of space debris. *Celest. Mech. Dyn. Astr.*, 116:79–95.

Hubaux, C., Lemaitre, A., Delsate, N., and Carletti, T. (2012). Symplectic integration of space debris motion considering several Earth's shadowing models. *Adv. Space Res.*, 49:1472–1486.

Hubaux, C., Libert, A.-S., Delsate, N., and Carletti, T. (2013). Influence of Earth's shadowing effects on space debris stability. *Adv. Space Res.*, 51:25–38.

IADC (2007). IADC Space Debris Mitigation Guidelines. Technical report, Steering Group and Working Group 4, IADC-02-01, Revision 1.

Jackson, A. (1996). A Symplectic Map for Geosynchronous Orbit Propagation. In *Spaceflight mechanics 1996; Proceedings of the 6th AAS/AIAA Spaceflight Mechanics Conference, Austin, TX, Feb. 12-15, 1996; San Diego, CA, Univelt, Inc. (Advances in the Astronautical Sciences. vol. 93, pt. 2), p. 1671-1682.*

Jenkin, A. B. and McVey, J. P. (2009). Constellation and "graveyard" collission risk for several MEO disposal strategies. In *Proceedings of the Fifth European Conference on Space Debris, ESA SP-672. ESA Publications Division., Noordwijk, The Netherlands.*

Kaula, W. M. (1966). *Theory of Satellite Geodesy: Applications of Satellites to Geodesy*. Blaisdell Publishing Company.

Klinkrad, H. (2006). *Space debris: models and risk analysis*. Springer, Praxis Publishing.

Kozai, Y. (1961). Effects of solar radiation pressure on the motion of an artificial satellite. *Smithsonian Astrophys. Obs. Spec. Rep*, 56:25–33.

Kozai, Y. (1962). Secular perturbations of asteroids with high inclination and eccentricity. *Astron. J.*, 67:591.

Kuznetsov, E. (2011). The effect of the radiation pressure on the orbital evolution of geosynchronous objects. *Sol. Syst. Res.*, 45:433–466.

Kuznetsov, E., Zakharova, P., Glamazda, D., Shagabutdinov, A., and Kudryavtsev, S. (2012). Light pressure effect on the orbital evolution of objects moving in the neighborhood of low-order resonances. *Sol. Syst. Res.*, 46:442–449.

Kwok, J. (1987). The Artificial Satellite Analysis Program (ASAP), Version 2.0, NPO-17522. Technical report, Jet Propulsion Laboratory, Pasadena, California, USA.

Lála, P. and Sehnal, L. (1969). The Earth's shadowing effects in the short-periodic perturbations of satellite orbits. *Bull. Astron. Inst. Czech.*, 20:327.

Lantoine, G. and Russell, R. (2011). Complete closed-form solutions of the Stark problem. *Celest. Mech. Dyn. Astr.*, 109:333–366.

Laskar, J. (1990). The chaotic motion of the solar system: a numerical estimate of the size of the chaotic zones. *Icarus*, 88:266–291.

Laskar, J. (1995). Introduction to frequency map analysis. In *Proceedings of 3DHAM95 NATO Advanced Institute, vol. 533, S'Agaro, pp. 134-150.*

Laskar, J. and Robutel, P. (2001). High order symplectic integrators for perturbed Hamiltonian systems. *Celest. Mech. Dyn. Astr.*, 80:39–62.

Lega, E., Guzzo, M., and Froeschlé, C. (2003). Detection of Arnold diffusion in Hamiltonian systems. *Physica D*, 182:179–187.

Lemaitre, A., Delsate, N., and Valk, S. (2009). A web of secondary resonances for large A/m geostationary debris. *Celest. Mech. Dyn. Astron.*, 104:383–402.

Lemoine, F., Kenyon, S., Factor, J., and et al. (1998). The development of the joint NASA GSFC and NIMA geopotential model EGM96. Technical report, NASA, TP-1998-206861.

Levison, H. and Ducan, M. (1994). The long-term dynamical behavior of short-period comets. *Icarus*, 108:18–36.

Libert, A.-S. and Henrard, J. (2007). Exoplanetary systems: The role of an equilibrium at high mutual inclination in shaping the global behavior of the 3-D secular planetary three-body problem. *Icarus*, 191:469–485.

Libert, A.-S., Hubaux, C., and Carletti, T. (2011). The Global Symplectic Integrator: an efficient tool for stability studies of dynamical systems. Application to the Kozai resonance in the restricted three-body problem. *Mon. Not. R. Astron. Soc.*, 414:659–667.

Liou, J.-C. and Weaver, J. (2005). Orbital dynamics of high area-to-mass ratio debris and their distribution in the geosynchronous region. In *Danesy, D. (Ed), Proceedings of the Fourth European Conference on Space Debris, ESA SP-589, ESA Publications Division, Noordwijk, The Netherlands, pp. 285-290.*

Lyddane, R. and Cohen, C. (1962). Numerical Comparison between Brouwer's Theory and Solution by Cowell's Method for the Orbit of an Artificial Satellite. *Astron. J.*, 3:176–177.

Maffione, N., Giordano, C., and Cincotta, P. (2011). Testing a fast dynamical indicator: the MEGNO. *Int. J. Nonlinear. Mech.*, 46:23–34.

Maffione, N. P., Darriba, L. A., Cincotta, P. M., and Giordano, C. M. (2013). Chaos detection tools: application to a self-consistent triaxial model. *Mon. Not. R. Astron. Soc.*, 429:2700–2717.

McMahon, J. and. Scheeres, D. (2010). Secular orbit variation due to solar radiation effects: a detailed model for BYORP. *Celest. Mech. Dyn. Astr.*, 106:261–300.

McMahon, J. and Scheeres, D. (2010). New solar radiation pressure force model for navigation. *J. Guid. Control. Dynam.*, 33:1418–1428.

Meeus, J. (1988). *Astronomical Formulae for Calculators.* Willmann-Bell Inc, 4th ed Enlarged and Revised.

Mikisha, A. and Smirnov, M. (1997). The influence of solar light pressure to GEO objects. Evolution aspects. In *Proceedings of the Second European Conference on Space Debris, ESA SP-393, pp. 323-325.*

Mikkola, S. and Innanen, K. (1999). Symplectic Tangent Map for Planetary Motions. *Celest. Mech. Dyn. Astr.*, 74:59–67.

Mikkola, S., Palmer, P., and Hashida, Y. (2002). An Implementation of the Logarithmic Hamiltonian Method for Artificial Satellite Orbit Determination. *Celest. Mech. Dyn. Astron.*, 82:391–411.

Milani, A. and Gronchi, G. (2009). *Theory of orbit determination.* Cambridge University Press, 1st edition.

Montenbruck, O. and Gill, E. (2005). *Satellite Orbits.* Springer.

Morbidelli, A. (2002). *Modern Celestial Mechanics: Dynamics in the Solar System.* CRC Press.

Mueller, A., Scheifele, G., and Starke, S. (1979). An analytical orbit predictor for near-Earth satellites. In *17th Aerospace Sciences Meeting, New Orleans, La., paper No 79-0122.*

Murray, C. and Dermott, S. (1999). *Solar system dynamics.* Cambridge University Press.

NASA (2013). *Orbital Debris Quarterly News*, 17.

Press, W. H., Teukolsky, S. A., Vetterling, W. T., and Flannery, B. P. (2007). *Numerical Recipes, The Art of Scientific Computing*. Cambridge University Press.

Rosengren, A. and Scheeres, D. (2012). Long-term dynamics of HAMR objects in HEO. In *Paper presented at the AIAA/AAS Astrodynamics Specialist Meeting, Minneapolis*.

Rosengren, A. andScheeres, D. (2011). Averaged dynamics of HAMR objects: effects of attitude and Earth oblateness. In *Paper No. AAS 11-594 presented at the 2011 AAS/AIAA Astrodynamics Specialist Meeting, Girdwood, Alaska*.

Rossi, A. (2005). Population models of space debris. In *Z. Knežević and A.Milani Ed., Proceedings of the IAU Colloquium No. 197, Dynamics of population of planetary systems, pp. 427-438*.

Rossi, A. (2008). Resonant dynamics of Medium Earth Orbits: space debris issues. *Celest. Mech. Dyn. Astr.*, 100:267–286.

Rossi, A. and Valsecchi, G. B. (2006). Collision risk against space debris in Earth orbits. *Celest. Mech. Dyn. Astr.*, 95:345–356.

Saunders, C. J., E., M. C., and Lewis, H. G. (2005). Disposal orbit characteristics for GALILEO including orbit propatation techniques. In *Danesy, D. (Ed), Proceedings of the Fourth European Conference on Space Debris, ESA SP-587. ESA Publications Division., Noordwijk, The Netherlands, pp. 79-284*.

Scheeres, D. (2012). Orbit mechanics about asteroids and comets. *J. Guid. Control. Dynam.*, 35:987–997.

Schildknecht, T., Früh, C., Herzog, A., Hinze, J., and Vananti, A. (2010). AIUB Efforts to Survey, Track, and Characterize Small-Size Objects at High Altitudes. In *Proceedings of 2010 AMOS Technical Conference, 14-17 September, Maui, Hawaii, USA*.

Schildknecht, T., Musci, R., Flury, W., Kuusela, J., de Leon, J., and de Fatima Dominguez Palmero, L. (2005). Optical observations of space debris in high-altitude orbits. In *Danesy, D. (Ed), Proceedings of the Fourth European Conference on Space Debris, ESA SP-587, ESA Publications Divison, Noordwijk, The Netherlands, pp. 113-118*.

Schrödinger, E. (1926). *Ann. Physik*, 80:457.

Schwartz, L. (1966). *Théorie des Distributions*. Hermann, Paris.

Skeel, R. and Biesiadecki, J. (1994). Symplectic integration with variable stepsize. *Ann. Num. Math.*, 1:191–198.

Skeel, R. and Gear, C. (1992). Does variable step size ruin a symplectic integrator ? *Phys. D*, 60:311–313.

Skokos, C. (2001). Alignment indices: A new, simple method for determining the ordered or chaotic nature of orbits. *J. Phys. A*, 34:10029–10043.

Skokos, C., Antonopoulos, C., Bountis, T., and Vrahatis, M. (2004). Detecting order and chaos in Hamiltonian systems by the SALI method. *J. Phys. A*, 37:6269–6284.

Skokos, C., Bountis, T., and Antonopoulos, C. (2007). Geometrical properties of local dynamics in Hamiltonian systems. *Physica D*, 231:30–54.

Skokos, C. and Gerlach, E. (2010). Numerical integration of variational equations. *Phys. Rev. E*, 82.

Smirnov, M., Mikisha, A., Novikova, E., and Rykhova, L. (2001). Secular variations of semimajor axis of debris particles near GEO due to solar radiation pressure. In *Proceedings of the Third European Conference on Space Debris, ESA SP-473 , pp. 403-406.*

Standish, E. (1998). JPL planetary and lunar ephemeris, DE405/LE405. Technical report, JPL Interoffice Memorandum IOM 312. D-98-048.

Thomas, F. and Morbidelli, A. (1996). The Kozai Resonance in the Outer Solar System and the Dynamics of Long-Period Comets. *Celest. Mech. Dyn. Astr.*, 64:209–229.

Valk, S. (2008). *Global dynamics of geosynchronous space debris with high area-to-mass ratios.* PhD thesis, FUNDP Namur.

Valk, S., Delsate, N., Lemaitre, A., and Carletti, T. (2009). Global dynamics of high area-to-mass ratios GEO space debris by means of the MEGNO indicator. *Adv. Space Res.*, 43:1509–1526.

Valk, S. and Lemaitre, A. (2008). Semi-analytical investigations of high area-to-mass ratio geosynchronous space debris including Earth's shadowing effects. *Adv. Space Res.*, 42:1429–1443.

Valk, S., Lemaitre, A., and Anselmo, L. (2008). Analytical and semi-analytical investigations of geosynchronous space debris with high area-to-mass ratios. *Adv. Space Res.*, 41:1077–1090.

Vokrouhlický, D., Farinella, P., and Mignard, F. (1993). Solar radiation pressure perturbations for Earth satellites. I. A complete theory including penumbra transitions. *Astron. Astrophys.*, 280:295–312.

Vokrouhlický, D., Farinella, P., and Mignard, F. (1994a). Solar radiation pressure perturbations for Earth satellites. II. An approximate method to model penumbra transitions and their long-term orbital effects on LAGEOS. *Astron. Astrophys.*, 285:333–343.

Vokrouhlický, D., Farinella, P., and Mignard, F. (1994b). Solar radiation pressure perturbations for Earth satellites. III. Global atmospheric phenomena and the albedo effect. *Astron. Astrophys.*, 290:324–334.

Vokrouhlický, D., Farinella, P., and Mignard, F. (1996). Solar radiation pressure perturbations for Earth satellites. IV. Effects of the Earth's polar flattening on the shadow structure and the penumbra transitions. *Astron. Astrophys.*, 307:635–644.

Wnuk, E., Wytrzyszczak, I., Golembiewska, J., and Klinkrad, H. (2010). Orbit Prediction Tool for Different Classes of Space Debris Orbits. In *PEDAS1-0024-10, 38th COSPAR Scientific Assembly, 2010, Bremen, Germany.*

Yoshida, H. (1990). Construction of higher order symplectic integrators. *Phys. Lett. A*, 150:262–268.